



University  
of Glasgow

Tabouillot, Victor (2025) *Functionalisation of metamaterials and their applications in novel chiral biosensing technologies*. PhD thesis.

<https://theses.gla.ac.uk/84951/>

Copyright and moral rights for this work are retained by the author

A copy can be downloaded for personal non-commercial research or study, without prior permission or charge

This work cannot be reproduced or quoted extensively from without first obtaining permission in writing from the author

The content must not be changed in any way or sold commercially in any format or medium without the formal permission of the author

When referring to this work, full bibliographic details including the author, title, awarding institution and date of the thesis must be given

Enlighten: Theses

<https://theses.gla.ac.uk/>  
[research-enlighten@glasgow.ac.uk](mailto:research-enlighten@glasgow.ac.uk)

# Functionalisation of Metamaterials and Their Applications in Novel Chiral Biosensing Technologies



University of Glasgow

Victor Tabouillot

Submitted in fulfilment of the requirements for the Degree of Doctor of Philosophy

School of Chemistry  
College of Science and Engineering  
University of Glasgow  
February 2025

# Abstract

---

*Nanotechnologies have the potential to transform our society, offering unprecedented control over matter and enabling a multitude of applications across a wide range of scientific disciplines. Scaling materials down to the nanoscale presents a significant challenge, necessitating evermore complex manufacturing techniques. Despite extensive research on the enhanced properties of nanoscale materials, most of the real-world applications have yet to see widespread adoption. In this thesis, the extraordinary optical properties of metamaterials will be explored and applied to the development of next-generation ultrasensitive chiral sensors. Metamaterials, in this context, are engineered periodic arrays of subwavelength-scale plasmonic structures that produce optical responses unmatched with naturally occurring materials.*

*The chemical functionalisation of these metamaterials is a critical step in numerous applications such as sensing, photovoltaic and optical technologies. In this PhD research, a novel selective functionalisation technique has been developed, enabling control over the chemical selectivity of plasmonic nanostructures. This is possible using a thermoresponsive polymer with a functional end group that can be switched on and off using the heat directly generated by the nanostructures through thermoplasmonic effects.*

*The application of chiral metamaterials in chiral sensing is a focal point in this thesis, where several techniques are studied for the detection and characterisation of chiral molecules. In the first project, plasmonic circularly polarised luminescence is used to probe the near field of a chiral metamaterial and detect a monolayer of a de novo peptide, which cannot be achieved with a light scattering technique in the far field. A second study focuses on surface enhanced Raman spectroscopy applied to the discrimination of chiral helicoid nanoparticles using a chiral metamaterial. This is possible through the enantio-dependent intensity of the electromagnetic hotspots, which is “hotter” for matching combinations and “colder” for mismatching ones. The final research project in this PhD exploits chiral metamaterials in the infrared, where the vibrational modes of a single molecular layer of amino acid can be detected. Enantiomeric discrimination of multilayers of this molecule was also achieved by enhancing vibrational circular dichroism effects using the same chiral plasmonic metamaterial.*

# Table of contents

---

|          |   |           |
|----------|---|-----------|
| <b>0</b> | <b>Front matter</b>                                 | <b>2</b>  |
| <b>1</b> | <b>Introduction and Structure</b>                   | <b>12</b> |
| <b>2</b> | <b>Background and Theory</b>                        | <b>16</b> |
| 2.1      | Maxwell's equations                                 | 17        |
| 2.1.1    | Gauss's law for electric field                      | 17        |
| 2.1.2    | Gauss's law for magnetic field                      | 18        |
| 2.1.3    | Faraday's law                                       | 18        |
| 2.1.4    | Ampère-Maxwell law                                  | 19        |
| 2.2      | Electromagnetic wave                                | 20        |
| 2.2.1    | Polarisation of light                               | 21        |
| 2.3      | Chirality   | 24        |
| 2.4      | Optical activity                                    | 26        |
| 2.4.1    | Optical rotation                                    | 26        |
| 2.4.2    | Circular dichroism                                  | 27        |
| 2.4.3    | Cotton effect                                       | 29        |
| 2.4.4    | Optical Chirality and Superchirality                | 30        |
| 2.5      | Fundamentals of plasmonics                          | 33        |
| 2.5.1    | Plasmonic oscillations                              | 33        |
| 2.5.2    | Surface plasmon polariton                           | 36        |
| 2.5.3    | Localised Surface Plasmon Resonance                 | 37        |
| 2.5.4    | Plasmonic hybridisation in coupled nanoparticles    | 40        |
| 2.5.5    | Refractive index-based sensing                      | 41        |
| 2.6      | Thermoplasmonics                                    | 41        |
| 2.6.1    | Physics of Plasmonic Heating                        | 42        |
| 2.7      | Metamaterials                                       | 44        |
| 2.7.1    | Origin and definition                               | 44        |
| 2.7.2    | Chiral metamaterials                                | 45        |
| 2.7.3    | Metamaterials applied to biosensing                 | 47        |
| <b>3</b> | <b>Nanofabrication and Characterisation Methods</b> | <b>50</b> |
| 3.1      | Nanofabrication Methods                             | 51        |
| 3.1.1    | Fabrication of ordered arrays of nanostructures     | 51        |
| 3.1.2    | Shuriken metafilm fabrication                       | 60        |
| 3.2      | Characterisation methods                            | 66        |
| 3.2.1    | Atomic force microscopy                             | 66        |
| 3.2.2    | Scanning electron microscopy                        | 68        |
| 3.2.3    | Ellipsometry  | 71        |
| 3.3      | Spectroscopic measurements                          | 72        |
| 3.4      | Simulation model and methods                        | 74        |



|          |  |            |
|----------|--|------------|
| 3.4.1    | Finite element method _____  | 74         |
| 3.4.2    | Wave optics module _____   | 75         |
| 3.4.3    | Heat transfer module _____   | 77         |
| 3.4.4    | 3D Simulation model _____  | 78         |
| <b>4</b> | <b>Selective Functionalisation of Metamaterials _____</b>          | <b>81</b>  |
| 4.1      | Introduction _____   | 82         |
| 4.2      | Background _____   | 83         |
| 4.2.1    | Pulse laser photothermal effects _____                             | 83         |
| 4.2.2    | Thermoresponsive polymers _____                                    | 84         |
| 4.3      | Methods _____  | 86         |
| 4.3.1    | Nanostructures and thermoresponsive polymer _____                  | 86         |
| 4.3.2    | Pulsed laser heating setup _____                                   | 90         |
| 4.3.3    | Simulation model _____   | 92         |
| 4.4      | Results and discussion _____                                       | 94         |
| 4.4.1    | Optical properties of the nanorod arrays _____                     | 94         |
| 4.4.2    | Experiment 20 mW _____   | 97         |
| 4.4.3    | Experiment 10 mW _____   | 103        |
| 4.4.4    | Simulation results _____   | 106        |
| 4.5      | Selective QD functionalisation _____                               | 113        |
| 4.6      | Conclusion _____   | 116        |
| <b>5</b> | <b>Plasmonic Luminescence for Enhanced Bio-Detection _____</b>     | <b>118</b> |
| 5.1      | Introduction _____   | 119        |
| 5.2      | Background _____   | 119        |
| 5.2.1    | Plasmonic enhanced photoluminescence _____                         | 119        |
| 5.2.2    | Photoluminescence chiroptical spectroscopic measurements _____     | 122        |
| 5.3      | Methods _____  | 123        |
| 5.3.1    | Sample and analyte _____   | 123        |
| 5.3.2    | Measurement setups _____   | 126        |
| 5.3.3    | Simulation model _____   | 128        |
| 5.4      | Results and discussion _____                                       | 131        |
| 5.4.1    | Far field measurements _____                                       | 131        |
| 5.4.2    | Near Field measurements _____                                      | 135        |
| 5.5      | Conclusion _____   | 143        |
| <b>6</b> | <b>Enantiomeric Discrimination of Helicoid Nanoparticles _____</b> | <b>145</b> |
| 6.1      | Introduction _____   | 146        |
| 6.2      | Background _____   | 147        |
| 6.2.1    | Basic principle of vibrational spectroscopy _____                  | 147        |
| 6.2.2    | Theory of Raman spectroscopy _____                                 | 148        |
| 6.2.3    | Surface enhanced Raman spectroscopy (SERS) _____                   | 151        |
| 6.2.4    | Raman optical activity (ROA) _____                                 | 152        |

|          |  |            |
|----------|--|------------|
| 6.3      | Method   | 154        |
| 6.3.1    | Sample and analyte                                       | 154        |
| 6.3.2    | Simulation modelling                                     | 155        |
| 6.4      | Results and discussion                                   | 157        |
| 6.4.1    | Sample optical properties                                | 157        |
| 6.4.2    | SERS measurements  | 158        |
| 6.4.3    | Simulation results                                       | 160        |
| 6.5      | Conclusion   | 170        |
| <b>7</b> | <b>Plasmonics for Enhanced Vibrational Bio-Detection</b> | <b>172</b> |
| 7.1      | Introduction   | 173        |
| 7.2      | Background   | 174        |
| 7.2.1    | IR spectroscopy theory                                   | 174        |
| 7.2.2    | Surface-enhanced infrared absorption                     | 175        |
| 7.2.3    | Surface enhanced vibrational circular dichroism          | 176        |
| 7.3      | Methods  | 178        |
| 7.3.1    | Sample and analyte                                       | 178        |
| 7.3.2    | FTIR transmission spectroscopy setup                     | 180        |
| 7.3.3    | Vibrational circular dichroism setup                     | 181        |
| 7.3.4    | Simulation model   | 183        |
| 7.4      | Results and discussion                                   | 185        |
| 7.4.1    | Cysteine on bare silicon                                 | 185        |
| 7.4.2    | IR plasmonic detection of cysteine monolayer             | 187        |
| 7.4.3    | VCD of thick cysteine layer                              | 195        |
| 7.5      | Conclusion   | 209        |
| <b>8</b> | <b>Summary and outlook</b>                               | <b>211</b> |
|          | <b>References</b>  | <b>217</b> |
|          | <b>Appendix A</b>  | <b>234</b> |
|          | <b>Appendix B</b>  | <b>236</b> |
|          | <b>Appendix C</b>  | <b>240</b> |
|          | <b>Appendix D</b>  | <b>242</b> |
|          | <b>Appendix E</b>  | <b>243</b> |

# List of Abbreviations

---

|                |  |
|----------------|--|
| AFM            | Atomic force microscopy                            |
| ATR            | Attenuated total reflection                        |
| BPDT           | Biphenyl-4,4'-dithiol                              |
| BSA            | Bovine serum albumin                               |
| BSE            | Backscattered electrons                            |
| CAD            | Computer-aided design                              |
| <i>cc-Hept</i> | $\alpha$ -helical coiled coils heptamer            |
| CD             | Circular dichroism                                 |
| CID            | circular intensity difference                      |
| CPL            | Circularly polarised light                         |
| D              | Dextrogyre   |
| DI             | Deionised water                                    |
| EBL            | Electron beam lithography                          |
| EF             | Enhancement factor                                 |
| EM             | Electromagnetic                                    |
| FEM            | Finite-element method                              |
| FTIR           | Fourier transform infrared                         |
| FWHM           | Full width at half maximum                         |
| HBS            | Hepes Buffered Saline                              |
| HEPES          | 4-(2-hydroxyethyl)-1-piperazineethanesulfonic acid |
| HNP            | Helicoid nanoparticle                              |
| IP             | Isoelectric point                                  |
| IPA            | Isopropyl alcohol                                  |
| IR             | Infrared   |
| JWNC           | James Watt Nanofabrication Centre                  |
| KK             | Kramers–Kronig                                     |
| L              | Levogyre   |
| LCP            | Left circularly polarised                          |
| LCST           | Lower critical solution temperature                |
| LDOS           | Local density of optical states                    |
| LH             | Left-handed  |
| LP             | Linear polariser                                   |

|                 |   |
|-----------------|---|
| LSPR            | Localised surface plasmon resonance                           |
| MIBK            | Methyl isobutyl ketone  |
| MIP             | Molecularly imprinted polymers                                |
| MIR             | Mid-infrared  |
| MSE             | Mean squared error  |
| NA              | Numerical aperture  |
| NIR             | Near-infrared   |
| NP              | Nanoparticle  |
| OR              | Optical rotation  |
| ORD             | Optical rotatory dispersion                                   |
| PBS             | Phosphate-buffered saline                                     |
| PCPL            | Plasmonic circularly polarised luminescence                   |
| PCM             | Planar chiral metamaterials                                   |
| PEG             | Polyethylene glycol   |
| PEM             | Photo-elastic modulator                                       |
| PL              | Photoluminescence   |
| PML             | Perfectly matched layer                                       |
| PMMA            | Poly-methyl methacrylate                                      |
| PM-IRRAS        | Polarization modulation IR reflection-absorption spectroscopy |
| <i>p-NIPAAm</i> | Poly(N-isopropylacrylamide)                                   |
| QD              | Quantum dot   |
| QWP             | Quarter wave plate  |
| R               | Rectus  |
| RCP             | Right circularly polarised                                    |
| RH              | Right-handed  |
| ROA             | Raman optical activity  |
| S               | Sinister  |
| SAM             | Self-assembled monolayer                                      |
| SE              | Secondary electrons   |
| SEM             | Scanning electron microscopy                                  |
| SEIRA           | Surface-enhanced infrared absorption                          |
| SEROA           | Surface enhanced Raman optical activity                       |
| SERS            | Surface enhanced Raman spectroscopy                           |
| SG              | Savitzky-Golay  |
| SPP             | Surface plasmon polariton                                     |

|      |                                     |
|------|-------------------------------------|
| TPS  | Template plasmonic substrate        |
| UCST | Upper critical solution temperature |
| UV   | Ultraviolet                         |
| VCD  | Vibrational circular dichroism      |
| VOA  | Vibrational optically active        |

# Acknowledgements

---

*First and foremost, I would like to extend my profound thanks to Professor Malcolm Kadowala, who allowed me to embark on this PhD under his supervision and guided me throughout these four years. His unwavering support and invaluable expertise were instrumental in the completion of the work presented in this thesis. I am also deeply grateful to have been co-supervised by Dr. Affar Karimullah, from whom I have learnt so much over the years. I always looked forward to our idea exchanges, which greatly enriched my research. I feel exceptionally fortunate to have shared this journey with my colleagues from the Chemical Nanophotonics group, whose enthusiasm made the long hours in the office both productive and enjoyable.*

*I extend my sincere thanks to the staff at the James Watt Nanofabrication Centre (JWNC) at the University of Glasgow. Their training on state-of-the-art equipment and their expertise in nanofabrication significantly advanced my work during this PhD. I am also grateful to the many collaborators from the School of Chemistry, whose insights and support created a stimulating research environment and provided me with the skills and passion to teach undergraduate students during numerous lab demonstrations.*

*I am particularly thankful to Professor Ewan Blanch and Dr. Jeremy Landry for welcoming me to the Royal Melbourne Institute of Technology (RMIT) University. This collaboration was a true highlight of my PhD, teaching me adaptability and offering a valuable experience within a different research environment and producing exciting results that are discussed in this thesis.*

*Finally, I am profoundly grateful to my parents and siblings for their unwavering support and encouragement, always inspiring me to strive for excellence. To my father, Denis, who gave me his life philosophy and his values of respect, duty, and love, and to my mother, Stéphanie, whose devotion and uplifting words, along with her positive attitude, have been a constant source of motivation. To my brother, Clément, whose determination, intelligence, and sense of humour make us inseparable, and to my sister, Eugénie, for her artistic creativity, passion for science, and admiration. Lastly, to all my friends, whether from Glasgow, France, or around the world, thank you for helping me grow as a person.*



# Author's declaration

---

I declare that, except where explicit reference is made to the contribution of others, that this dissertation is the result of my own work and has not been submitted for any other degree at the University of Glasgow or any other institution.

**Printed Name:** Victor TABOUILLOT

**Signature:** \_\_\_\_\_

# Published work

---

- Tabouillot V, Kumar R, Lalaguna PL, Hajji M, Clarke R, Karimullah AS, Thomson AR, Sutherland A, Gadegaard N, Hashiyada S, Kadodwala M. Near-field probing of optical superchirality with plasmonic circularly polarized luminescence for enhanced bio-detection. *ACS photonics*. 2022 Oct 20;9(11):3617-24.
- Kartau M, Skvortsova A, Tabouillot V, Chaubey SK, Bainova P, Kumar R, Burtsev V, Svorcik V, Gadegaard N, Im SW, Urbanova M. Chiral metafilms and surface enhanced Raman scattering for enantiomeric discrimination of helicoid nanoparticles. *Adv. Opt. Mater.* 2023 May;11(9):2202991.
- Chaubey SK, Kumar R, Lalaguna PL, Kartau M, Bianco S, Tabouillot V, Thomson AR, Sutherland A, Lyutakov O, Gadegaard N, Karimullah AS. Ultrasensitive Raman detection of biomolecular conformation at the attomole scale using chiral nanophotonics. *Small*. 2024 Nov;20(45):2404536.



# Chapter 1

---

Introduction and Structure

Light is a propagating electromagnetic wave that can interact with matter in various ways, forming the basis of many sensing techniques. Light-based sensors take advantage of these interactions to detect and measure the physical, chemical and biological properties of a wide array of analytes.

In recent years, new advanced materials, known as metamaterials, have emerged as a disruptive force in the field of optics, owing to their extraordinary abilities to manipulate light. An increasing endeavour has been put on the research of new applications for metamaterials, notably in the field of chiral sensing, which has the potential to disrupt the pharmaceutical industry.

Enantiomers, the two non-superimposable mirror image forms of chiral molecules, are ubiquitous in biology, engulfing many naturally occurring biomolecules, including proteins, amino acids and sugars. Furthermore, around half of the drugs commercialised are chiral molecules, where the majority are sold as racemates, consisting of an equal proportion of the two enantiomers. Although enantiomers have the same chemical structure, their pharmacological and toxicological properties can be drastically different, justifying the need for chiral segregation. This is a challenging feat due to the weak light-matter interactions of chiral molecules, resulting in the need for a large quantity of analyte in traditional chiroptical techniques (micrograms) [1].

This thesis is centred around the functionalisation of metamaterials and their application in the field of chiral sensing by exploiting plasmonic effects. Plasmonics describes the interaction between electromagnetic fields and free electrons in metals. When subwavelength metallic structures interact with light, the collective oscillations of the confined electron cloud will result in localised electromagnetic field enhancement [2]. These fields provide an incisive probe to the surrounding environment, where a minute amount of molecular analyte can be detected and characterised. In 2010, the work of Tang and Cohen [3] demonstrated the existence of superchiral fields, which interact more with chiral molecules than regular circularly polarised light used in traditional spectroscopic techniques. It was then shown by Hendry et al. [4] that chiral metamaterials have the ability to generate a large chiroptical response, enabling the ultrasensitive detection of monolayer amounts of chiral analytes (picograms). Following these studies, researchers have discovered a plethora of useful techniques leveraging the exotic properties of metamaterials for the sensing of chiral molecules.

The chemical functionalisation of metamaterials is a key challenge in producing novel sensing techniques. This process involves the incorporation of specific molecular functionalities at the metasurface, making it selective to the target analytes. Spatially functionalising nanostructures is commonly done through low-throughput techniques such as dip-pen lithography or inkjet printing [5,6]. These approaches are inherently “top-down” methods, limited to small substrate areas (micron scale), and suffering from their complexity and cost. In this thesis, a new selective chemical functionalisation technique is presented, involving the use of a thermoresponsive polymer adsorbed at the

metamaterial surface. The molecular conformation of this polymer is directly controlled by the heat generated through thermoplasmonic effects in the metallic nanostructure, covering a large sample area. When the temperature reaches a threshold level, the polymer will collapse. This will cause the chemical functional group at its end to be buried, resulting in the passivation of the sample's surface. Thermoplasmonics is an emerging field at the frontier between plasmonics and thermal physics. When a nanoparticle is subjected to a plasmonic excitation, heat can be generated through non-radiative decay of the oscillations of free electrons in the metal (plasmons). This heat will be delivered in a highly localised volume around the nanostructure, allowing the control of the thermoresponsive polymer. This thermal effect has been used by researchers in numerous applications such as photothermal cancer therapy [7], drug delivery [8], photocatalysis [9] and photovoltaics [10].

This thesis contains a chapter dedicated to the relevant theory surrounding metamaterials and their application in the field of biosensing. The general methods employed during this PhD are then presented, including detailed nanofabrication protocols, an overview of characterisation techniques and a description of the numerical simulation strategy. The main part of this thesis is divided into four result chapters, containing the relevant background and methodology specific to each one.

**Chapter 4** explores the selective chemical functionalisation of metamaterials. Two aspect ratios of gold nanorods are exposed to a nanosecond pulse laser to control the molecular conformation of a thermoresponsive polymer through thermoplasmonic effects. Despite a very similar shape, these different rods can exhibit large temperature differences while being irradiated by the same pulsed laser. This technique can precisely control the chemical activity of large arrays of plasmonic nanostructures with a high throughput. Two experiments conducted at different powers will be presented, followed by the simulation results.

**Chapter 5** introduces a novel biosensing technique using photoluminescence to probe the near field environment of plasmonic metamaterials. This technique achieves greater sensitivity than traditional light-scattering methods, detecting a monolayer of *de novo* peptide adsorbed on the metamaterial surface. The small size of this molecule relative to the spatial extent of the electromagnetic near field makes it particularly difficult to detect using conventional methods. In this chapter, this new near-field sensing technique, named plasmonic circularly polarised luminescence, is compared to the traditional far-field strategy.

**Chapter 6** provides a detailed description of the simulation work involved in the understanding of a new application of metamaterials in surface enhanced Raman spectroscopy. By using an achiral Raman molecular reporter to link chiral helicoid nanoparticles to a chiral metamaterial surface, diastereomeric combinations of identical and opposite symmetry are formed. These different combinations generate distinctive

electromagnetic field enhancements, allowing the enantiomeric discrimination of these nanoparticles.

Finally, **Chapter 7** discusses the use of chiral metamaterials in the infrared range to detect the molecular vibrational modes of an amino acid. A first technique uses classic Fourier-transform infrared spectroscopy, where an unpolarised beam passes through the metamaterial surface. The successful detection of vibration modes from a self-assembled monolayer amount of analyte is observed and discussed. A second method uses a vibrational circular dichroism instrument, which measures the difference in absorbance between both handedness of circularly polarised incident light. In this experiment, two enantio-sensitive plasmonic phenomena are described, achieving chiral discrimination of a deposited layer of the amino acids.

In summary, this thesis presents innovative strategies for the functionalisation of metamaterials and their application in the field of chiral sensing, contributing to the advancement of ultrasensitive biosensors. By leveraging plasmonic and thermoplasmonic effects, new avenues for high-throughput chemical functionalisation and enhanced molecular detection are explored. These advancements not only offer improvements in existing sensing techniques but also introduce novel methods for overcoming the challenges of weak light-matter interactions, thus pushing the boundaries of what is achievable in the field of biosensing. Ultimately, this work extends the current understanding of metamaterial-based sensing and lays the foundation for future applications in pharmaceutical and biomedical industries.

# Chapter 2

---

Background and Theory

In this chapter, the theory forming the basis of this thesis will be presented with the goal of placing this work in context with the broad landscape of nanophotonics applied to metamaterials. This will include an introduction to Maxwell's equations and the theory of electromagnetic waves, followed by a description of chirality and how chiral materials interact with light through a property called optical activity. A section will then be dedicated to plasmonics, which describes the interaction between free electrons in metals and electromagnetic fields. Finally, a brief review of plasmonic-based optical biosensors will be provided.

## 2.1 Maxwell's equations

In the early 1860s, a Scottish physicist named James Clerk Maxwell published his work unifying previous theories on electricity and magnetism, laying the foundation for the field of modern electromagnetism [11]. Maxwell, through his set of equations, described for the first time light as a propagating electromagnetic wave. The four Maxwell's equations are known as [12]:

1. Gauss's law for electric fields
2. Gauss's law for magnetic fields
3. Faraday's law
4. Ampère-Maxwell law

These equations are used to model the behaviour of the electric and magnetic fields and their generation by charges and currents. The general form of Maxwell's equations will be introduced and explained here [13–15].

### 2.1.1 Gauss's law for electric field

There are two kinds of electric fields in Maxwell's equations: the electrostatic field and the induced electric field, which are produced by an electric charge and a changing magnetic field, respectively. Gauss's law for electric field relates the spatial behaviour of the electrostatic field to the charge distribution. It can be written in its integral form, giving the following equation:

$$\oint_S \mathbf{E} \cdot \hat{\mathbf{n}} da = \frac{q_{enc}}{\epsilon_0}. \quad (2.1)$$

Which describes the flux of the electric field  $\mathbf{E}$  passing through a closed surface  $S$ , with the outwardly directed normal unit vector  $\hat{\mathbf{n}}$  and an infinitesimal element of area  $da$ . It states that the electric flux is equal to the enclosed charge  $q_{enc}$  over the permittivity of free space  $\epsilon_0$ . Permittivity is a fundamental property in electrodynamics, it can be

understood as the resistance of a medium against the formation of an electric field. In free space, this is a constant equal to  $\epsilon_0 = 8.85 \times 10^{-12} \text{ F.m}^{-1}$ .

This first equation of Maxwell can also be expressed in its differential form by application of the divergence theorem:

$$\nabla \cdot \mathbf{E} = \frac{\rho}{\epsilon_0}. \quad (2.2)$$

Where  $\nabla \cdot \mathbf{E}$  is the divergence of the electric field and  $\rho$  is the electric charge density.

This version of Maxwell's first equation describes the divergence of the electric field, which can be understood as the flow of a vector field at a point in space. For a positive value, the point acts as a source, and for a negative value, it behaves as a sink. Thus, this equation states that the electric field diverges from positive charges and converges to negative charges.

## 2.1.2 Gauss's law for magnetic field

Maxwell's second equation describes the magnetic field  $\mathbf{B}$  in any closed surface  $S$  and can be expressed in its integral form as:

$$\oint_S \mathbf{B} \cdot \hat{n} \, da = 0. \quad (2.3)$$

This second law states that the total magnetic flux through the surface  $S$  is always null. This rule implies that magnetic monopoles are impossible. The divergence form of this equation gives:

$$\nabla \cdot \mathbf{B} = 0. \quad (2.4)$$

The divergence of the magnetic field is null at any point in space, which here again, means that magnetic monopoles or magnetic charges cannot exist.

## 2.1.3 Faraday's law

This third equation explains the phenomenon of electromagnetic induction, which describes how a changing magnetic field around a circuit will induce an electric field. The integral form of the Maxwell-Faraday equation is given as:

$$\oint_C \mathbf{E} \cdot d\mathbf{l} = -\frac{\partial}{\partial t} \int_S \mathbf{B} \cdot \hat{n} \, da. \quad (2.5)$$

The left side of this equation represents the circulation of the induced electric field  $\mathbf{E}$  around a closed loop  $C$ , where  $d\mathbf{l}$  is an infinitely small length along this path. The right side is the rate of change of the magnetic flux through the open surface  $S$ , which is bounded by the closed path  $C$ .

The differential form of Faraday's law is obtained by application of Stokes' theorem and is written as:

$$\nabla \times \mathbf{E} = -\frac{\partial \mathbf{B}}{\partial t}. \quad (2.6)$$

This expression states that the *curl* of the electric field  $\mathbf{E}$ , which quantifies the circulation of the field vector around a point, is produced by a changing magnetic field.

## 2.1.4 Ampère-Maxwell law

This final equation is based on Ampère's law, which states that an electric current will generate a magnetic field. Maxwell theorised that Ampère's law couldn't hold outside of magnetostatics (for steady currents) and was therefore missing a term. The integral form of Ampère's law, fixed by Maxwell, is formulated as:

$$\oint_C \mathbf{B} \cdot d\mathbf{l} = \mu_0 \left( I_{enc} + \varepsilon_0 \frac{d}{dt} \int_S \mathbf{E} \cdot \hat{\mathbf{n}} da \right). \quad (2.7)$$

Where  $\mu_0$  is the permeability of free space. This property is analogous to the permittivity but is related to the magnetic field. It can be understood as the ability of a medium to support the formation of a magnetic field within it. The vacuum magnetic permeability is a physical constant, which is equal to  $\mu_0 = 1.26 \times 10^{-6} \text{ N} \cdot \text{A}^{-2}$ . Here,  $I_{enc}$  is the enclosed electric current. Mirroring Faraday's law, this equation states that an electric current or a fluctuating electric flux through a surface enclosed in a boundary  $C$  will generate a circulating magnetic field around that path. This equation can be rewritten in a differential form by applying the Stokes' theorem; it now reads:

$$\nabla \times \mathbf{B} = \mu_0 \left( \mathbf{J} + \varepsilon_0 \frac{\partial \mathbf{E}}{\partial t} \right). \quad (2.8)$$

Here, the Ampère-Maxwell law states that a circulating magnetic field is produced by an electric current and/or by a time-varying electric field.



## 2.2 Electromagnetic wave

Maxwell, from his set of equations, postulated that the oscillation of a charge will produce a moving electric field, which will in turn generate a changing magnetic field, mutually producing each other. This time-varying electric and magnetic field would propagate away from the source as two in-phase waves perpendicular to each other, known as an electromagnetic (EM) wave (see **Figure 2.1**).

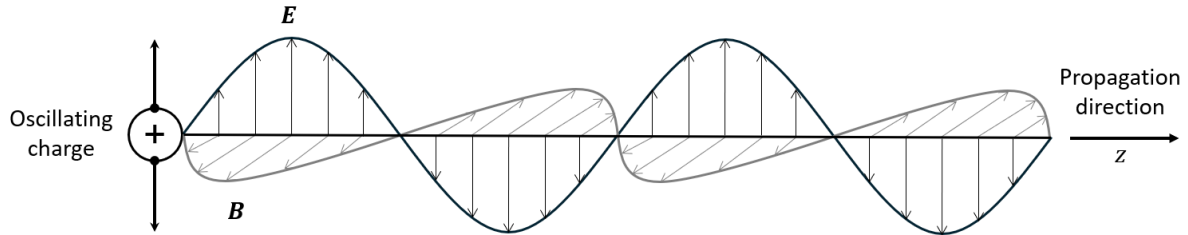


**Figure 2.1: Schematic of a propagating electromagnetic wave emanating from the oscillation of a charge.**

Maxwell defined this propagating EM wave by applying the *curl* operator to Faraday's law (in equation (2.6)), giving the following equation [13]:

$$\frac{\partial^2 \mathbf{E}}{\partial t^2} - \frac{1}{\mu_0 \epsilon_0} \nabla^2 \mathbf{E} = 0. \quad (2.9)$$

From this formula, the speed  $c$  of this propagating electromagnetic wave, is given as:

$$c = \frac{1}{\sqrt{\mu_0 \epsilon_0}}. \quad (2.10)$$

Earlier, in 1856, Weber and Kohlrausch experimentally measured the physical constants  $\mu_0$  and  $\epsilon_0$ . When these values were used, the result was close to the speed of light  $\approx 2.998 \times 10^8 \text{ m/s}$ . This observation led Maxwell to conclude that "light is an electromagnetic disturbance propagated through the field according to electromagnetic laws" [16].

## 2.2.1 Polarisation of light

Before Maxwell, the research of Augustin-Jean Fresnel in optics established consensus on the wave theory of light. He explained polarisation phenomena by demonstrating that light is constituted of transverse waves. Fresnel later introduced and defined the different polarisation states of light, namely the *linear*, *circular* and *elliptical* polarisation [17].

Light, as defined in the electromagnetic model, is characterised by the electric and magnetic vectors, oscillating in-phase and orthogonal to one another. The polarisation state of light is defined by the time-varying direction and amplitude of the electric vector [18]. If the electric field vector oscillates in a specific plane, the resulting electromagnetic wave will be *plane polarised* or *linearly polarised* light, and can be expressed as:

$$\mathbf{E} = E_0 \cos(kz - \omega t). \quad (2.11)$$

Where  $\mathbf{E}$  describes the electric field at time  $t$ ,  $E_0$  is the amplitude of the electric field,  $k$  is the wave number,  $\omega$  is the angular frequency and  $z$  is the direction of propagation.

The plane of propagation of the electric field can be expressed by the sum of two components  $E_x$  and  $E_y$  oscillating in-phase (see **Figure 2.2**), following this equation:

$$\mathbf{E} = (E_{x,0} + E_{y,0}) \cos(kz - \omega t). \quad (2.12)$$

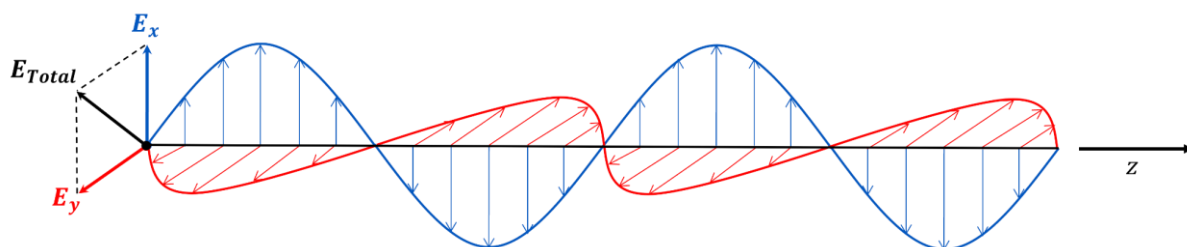


**Figure 2.2: Linearly polarised light propagating in the z direction, represented as the sum of the components in the x and y axis.**

In the case where  $E_{x,0}$  is equal to  $E_{y,0}$ , the resulting wave is polarised linearly in a  $45^\circ$  angle between the x- and y-axes (see **Figure 2.2**).

If the two components of the electric field are out-of-phase by  $\pi/2$ , the electric field vector will rotate perpendicularly around the axis of propagation of the light at a constant rate (see **Figure 2.3**). This is called *circular* polarisation; it can be either left- or right-handed depending on the sense of rotation of the vector and the convention applied. In Chemistry, the point of view of the receiver is privileged, with the right-handedness rotating clockwise. The electric field of circularly polarised light (CPL) can be described by the following equation:

$$\mathbf{E} = E_{x,0}\cos(kz - \omega t) + E_{y,0}\cos(kz - \omega t \pm \pi/2). \quad (2.13)$$

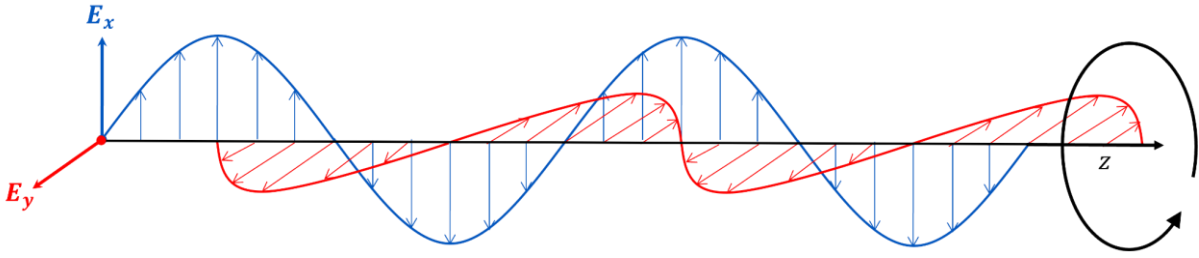


**Figure 2.3: Electric field components of left-handed circularly polarised light propagating in the z direction.**

Interestingly, if both handedness of CPL are superposed in-phase, the resulting wave will be linearly polarised [18]:

$$\mathbf{E}_{LCP} + \mathbf{E}_{RCP} = 2E_{x,0}\cos(kz - \omega t). \quad (2.14)$$

The *elliptical* polarisation arises from two orthogonal waves of unequal amplitude and/or out-of-phase by an arbitrary angle (see **Figure 2.4**). It is the most common and general case of polarisation, with the *linear* and *circular* polarisations being special instances of *elliptical* polarisation [19]. This polarisation state of light will be discussed in more detail in the following section.

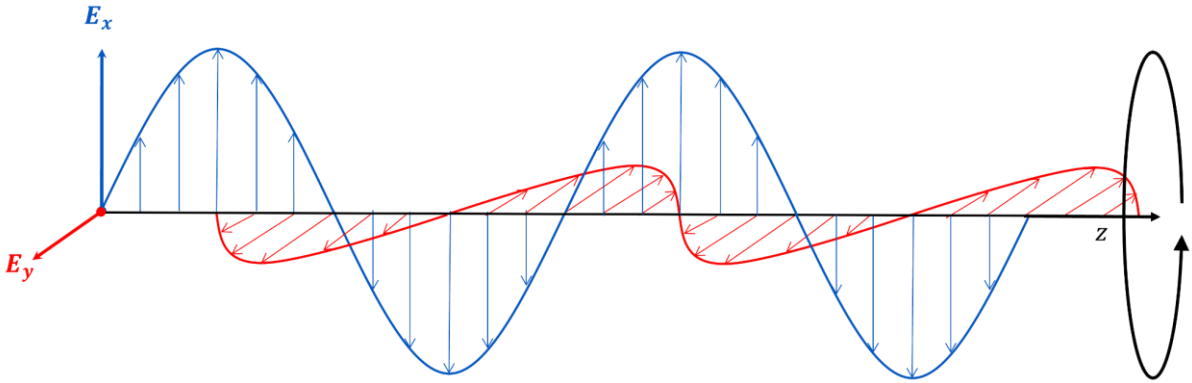


**Figure 2.4: Electric field components of left-handed elliptically polarised light propagating in the z direction.**

These three cases of light polarisation are summarised in **Figure 2.5**, where the sum of the electric fields  $E_x$  and  $E_y$  is visible in the black line, which is projected onto the  $xy$  plane as a line, a circle and an ellipse.

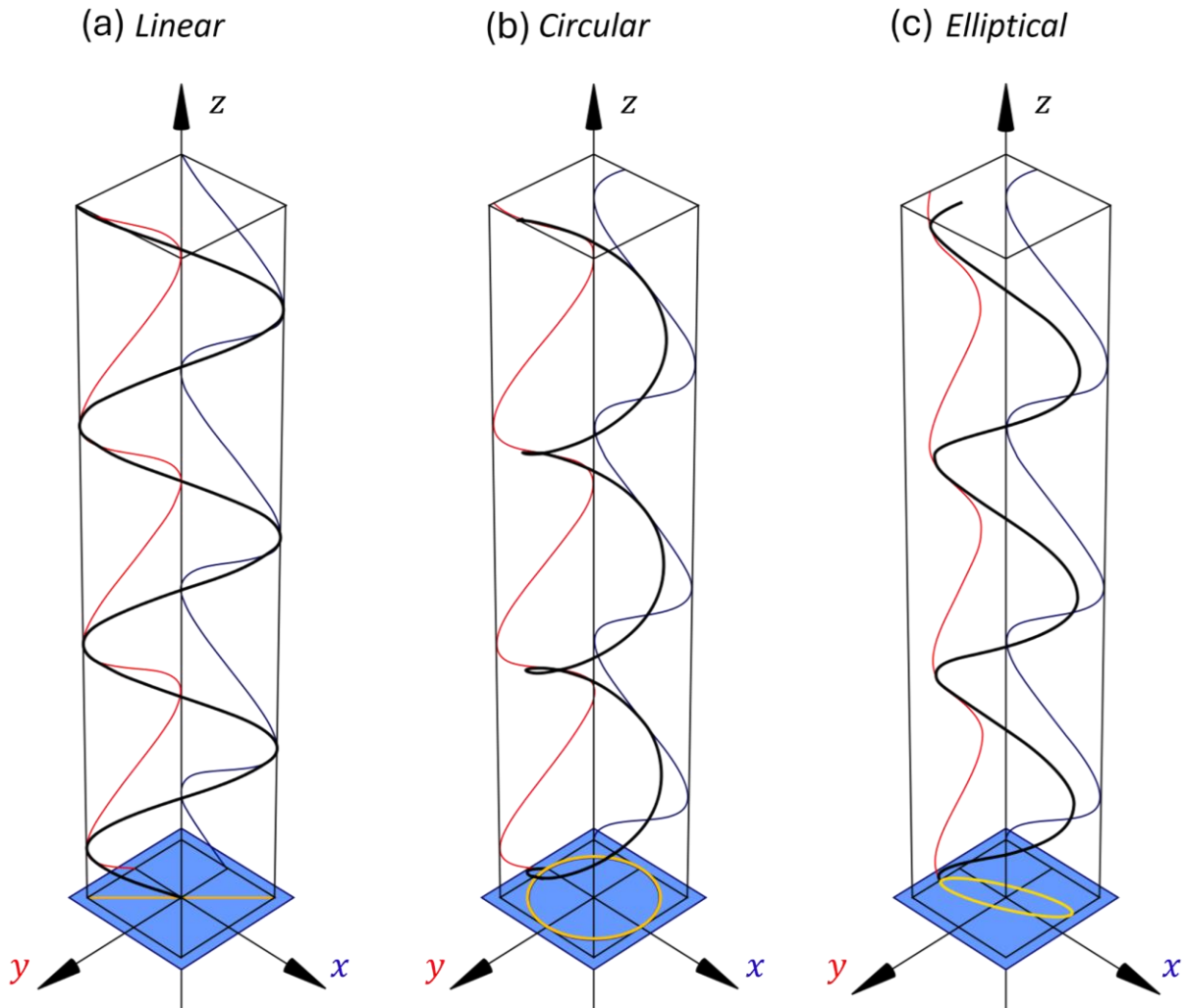


**Figure 2.5: 3D visualisation of the different polarisation states of light, with (a) linearly, (b) circular and (c) elliptical polarised light, with their electric field vector projected in yellow on the  $xy$  plane. The two electric field vector components  $E_x$  (blue) and  $E_y$  (red) are projected on the  $xz$  and  $yz$  planes, respectively.**

The combination of several waves, produced by numerous incoherent sources, will lead to *unpolarised* light. This is the case for the sun's rays or incandescent light bulbs, which are producing light of random polarisation.

## 2.3 Chirality

The word “chiral” takes its roots from the ancient Greek word “ $\chi\epsilon\iota\rho$ ” (*kheir*), meaning hand. It refers to an object that is not identical to its image in the mirror (non-superimposable), a hand is a good example of a chiral object. This term was first introduced in 1893 in a Robert Boyle lecture on the molecular tactics of a crystal at Oxford University by Sir William Thomson, later Lord Kelvin, professor of Natural Philosophy at the University of Glasgow [20]. Today, his statue sits near the campus, **Figure 2.6**. A quote is available in the Baltimore Lectures, containing a definition of chirality by Lord Kelvin [21]:

*“I call any geometrical figure or group of points chiral and say it has chirality, if its image in a plane mirror, ideally realised, cannot be brought to coincide with itself.”*



**Figure 2.6: Statue of Lord Kelvin in Kelvingrove park near the University of Glasgow.**

Objects that are symmetrical and identical with their mirror image are called achiral. A chiral object and its mirror image are called enantiomorphs, or enantiomers in the case of molecules (also optical isomers). These enantiomorphs are differentiated by their different handedness in reference to the example of the hand [22].

In optical chirality, the handedness of a molecule is defined from the way it rotates *linearly* polarised light. If the rotation is clockwise, then the molecule is right-handed, for an anticlockwise rotation the molecule is left-handed [23]. This property was first discovered in 1815 by Jean-Baptiste Biot at the College of France [24]. In 1848, Louis Pasteur demonstrated in one of his experiments that different forms of tartaric acid salt

crystals were rotating the plane of polarised light in opposite directions [25]. These discoveries laid the foundation for stereochemistry, which is the study of the three-dimensional structure of molecules.

Chiral molecules are frequently encountered in biology. For instance, proteins, peptides and DNA are all chiral. In some cases, a molecule is homochiral, which means that only one enantiomer is found in nature. Chiral molecules are referred to as dextrogyre (D) and levogyre (L) depending on the direction they rotate polarised light, clockwise for D and anticlockwise for L molecules [26]. Another common nomenclature is the R/S system, also known as the Cahn-Ingold-Prelog, which designated each chiral centre in a molecule independently, where R and S stand for *Rectus* (right) and *Sinister* (left), respectively [27]. These enantiomers can have drastically different properties, even though they share the same atomic composition. An example of this is carvone, which is naturally found in two enantiomeric forms. (R)-carvone is the molecule responsible for the distinctive smell of mint leaves, (S)-carvone is found in caraway seeds and has a very different odour (see **Figure 2.7**).

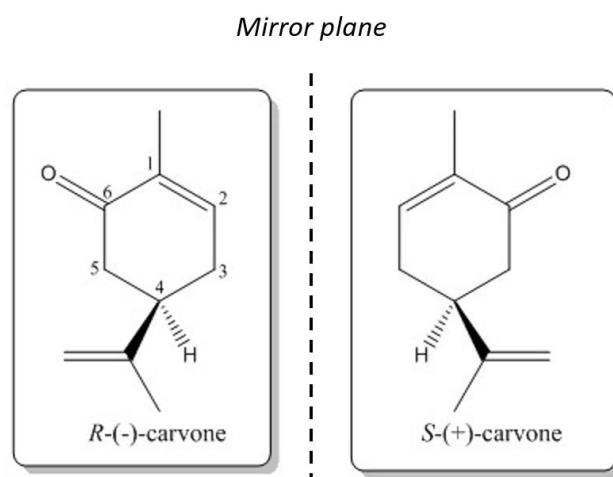


**Figure 2.7:** Carvone (R)- and (S)-enantiomers, with its chiral centre on the 4<sup>th</sup> carbon atom.

This change in properties between enantiomers is very important in the pharmaceutical industry. Indeed, optical isomers can have different affinity at a receptor site, for example, at a protein binding site, which implies that they are metabolised differently. Despite this, drugs are often used as racemates (or racemic) molecules, which is an equal mixture of the two enantiomers. Tuning the ratio of enantiomers in the drug or selecting only one optical isomer could have far reaching benefits, including decreased toxicity and increased efficacy [28].

It is challenging to differentiate enantiomers due to their similar physical properties (same mass, solubility, boiling point). But thanks to a phenomenon called optical activity, enantiomers can be discriminated through their different interactions with *circularly* polarised light, which is also a chiral entity with a left and right handedness.

## 2.4 Optical activity

Chiral molecules can rotate the plane of *linearly* polarised light thanks to a property called optical activity. This effect has deep implications in many fields such as molecular biology, analytical chemistry, and crystallography [29]. Optical activity encompasses two phenomena: *optical rotation* and *circular dichroism*.

### 2.4.1 Optical rotation

As discussed previously in Section 2.2.1, *circularly* polarised light (CPL) is characterised by the constant rotation rate of the electromagnetic field perpendicularly to the direction of propagation of the light. This CPL is right-handed (RH) if the electric field vector rotates clockwise from the point of view of the receiver, and left-handed (LH) if the rotation appears counterclockwise (see **Figure 2.8** (a)). *Linearly* polarised light is made by the superposition of both LH and RH CPL of equal amplitude. The orientation of the plane of polarisation is obtained by the sum of the electric field vectors of both handedness of CPL (see **Figure 2.8** (a)). In an optically active medium, both handedness of the CPL will not propagate at the same velocity, resulting in an *optical rotation* (OR) of the plane of polarisation, defined by the angle  $\theta$  (see **Figure 2.8** (b)) [30].

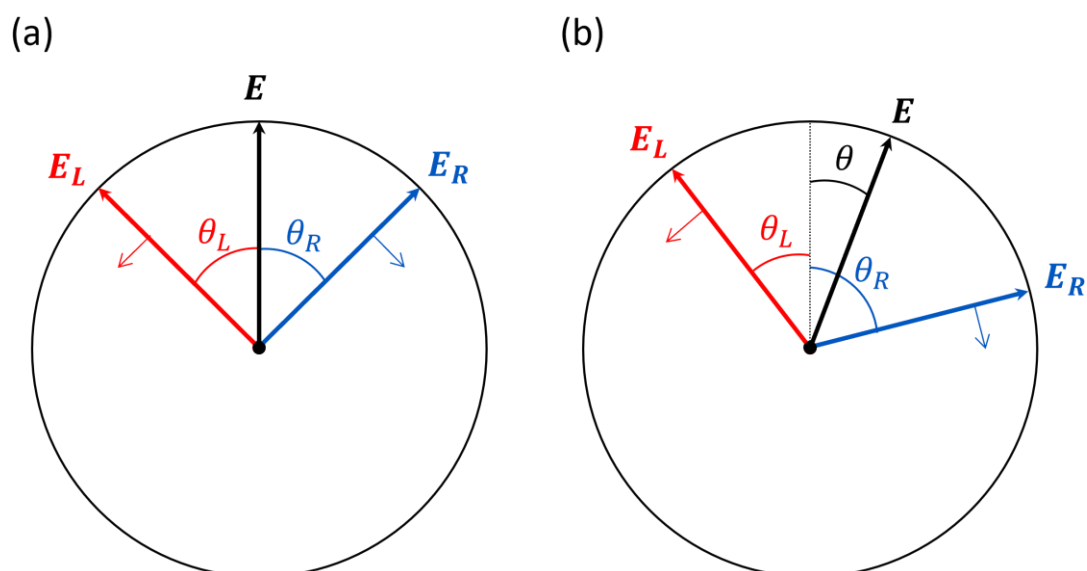


**Figure 2.8:** Linearly polarised light, viewed from the receiver in the propagation axis with electric field vectors of left (red) and right (blue) handed CPL propagating through (a) an achiral medium and (b) an optically active chiral medium with a rotation  $\theta$  of the vector  $E$  of the plane polarised light.

The difference in velocity between these two opposite handedness of CPL will cause a phase shift. This rotation angle  $\theta$  is given by:

$$\theta = \frac{1}{2}(\theta_L + \theta_R). \quad (2.15)$$

If the velocity of LH and RH components is  $v_L$  and  $v_R$ , respectively and the angular frequency of the *linearly* polarised beam is  $\omega = 2\pi c/\lambda$ , then the angles  $\theta_L$  and  $\theta_R$  are [30]:

$$\theta_L = \frac{2\pi cl}{\lambda v_L} \text{ and } \theta_R = \frac{2\pi cl}{\lambda v_R}. \quad (2.16)$$

Where  $c$  is the speed of light in vacuum and  $l$  is the length of the optically active medium. From these equations, the optical rotation angle  $\theta$  in equation (2.15) becomes:

$$\theta = \frac{\pi cl}{\lambda} \left( \frac{1}{v_L} - \frac{1}{v_R} \right). \quad (2.17)$$

The speed of light in any medium is determined by the refractive index  $n$ , which is simply the ratio of the speed of light in free space to that in the medium [31]. Finally,  $\theta$  is given by:

$$\theta = \frac{\pi}{\lambda} (n_L - n_R). \quad (2.18)$$

Here, there are two different values of  $n$  depending on the handedness of the circular polarisation components of the incident light. This is an optical property encountered in chiral materials called circular birefringence [32].

*Optical rotatory dispersion* (ORD) measures the optical rotation as a function of the wavelength. This measurement technique provides more information than the monochromatic measurement of the optical rotation, traditionally taken at 589.3 nm using a sodium-vapour lamp [33].

## 2.4.2 Circular dichroism

*Circular dichroism* (CD) arises from the difference in absorption between the LH and RH components of an incident *linearly* polarised beam when passing through an optically active medium. Unlike *optical rotation*, where the plane polarisation rotates, here, the difference in absorption causes a mismatch in amplitude between both components of the electric field vectors  $\mathbf{E}_L$  and  $\mathbf{E}_R$ , making the light elliptically polarised (see **Figure 2.9** (b)) [34].



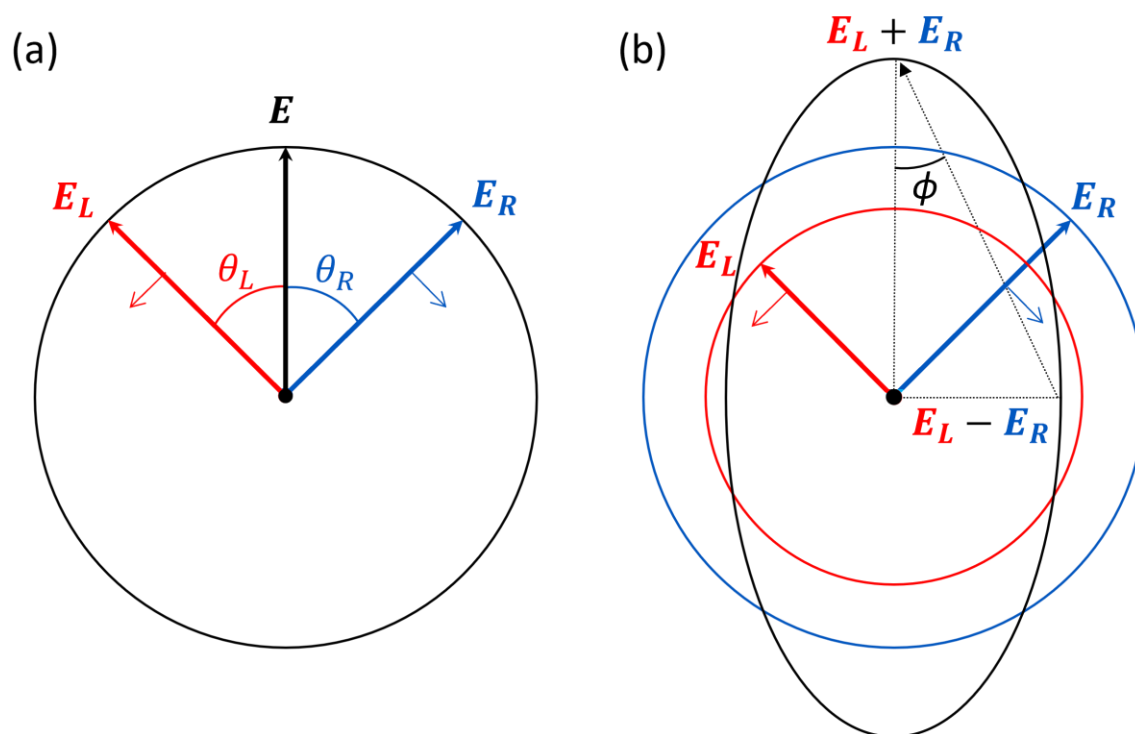


**Figure 2.9: Linearly polarised light, viewed from the receiver in the propagation axis with electric field vectors of left (red) and right (blue) handed CPL propagating through (a) an achiral medium and (b) an optically active chiral medium, generating an elliptically polarised light with specific angle  $\phi$ .**

CD spectroscopy measures the degree of elliptical polarisation of light after interacting with the chiral analyte. The ellipticity of light is given by the angle  $\phi$ , which is obtained by:

$$\phi = \tan^{-1} \left( \frac{E_L - E_R}{E_L + E_R} \right). \quad (2.19)$$

This effect is usually small in molecular analytes, measured in millidegrees, but it is nonetheless a powerful technique that is routinely used to determine the absolute conformation of molecules. The qualitative and even semi-quantitative analysis of the polypeptide backbone of proteins (secondary structure) is possible using CD in the UV-visible range [35].

### 2.4.3 Cotton effect

When *linearly* polarised light interacts with an optically active medium, ORD and CD will generally be observed simultaneously. This is because these effects are linked to the complex refractive index of the chiral material. As discussed in the previous section (2.4.1 and 2.4.2), ORD is determined by the real part of the refractive index, while CD depends on the absorption of light, which is related to the imaginary part, called the *extinction coefficient* [36]. *Linearly* polarised light will therefore be rotated and *elliptically* polarised after interacting with a chiral medium (see **Figure 2.10**).

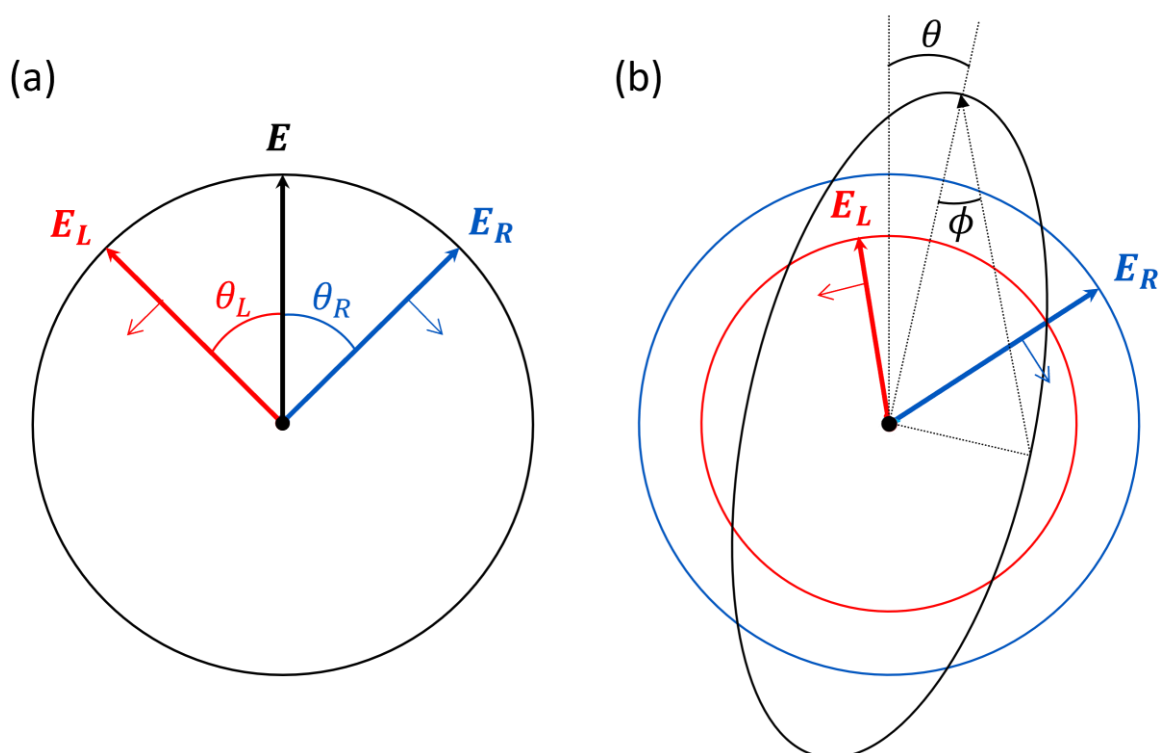


**Figure 2.10:** Linearly polarised light, viewed from the receiver in the propagation axis with electric field vectors of left (red) and right (blue) handed CPL propagating through (a) an achiral medium and (b) an optically active chiral medium, causing OR and CD simultaneously.

The ORD and CD spectra are linked at the absorption band by the *Cotton* effect, which shows that maximum ellipticity on the CD spectrum is equal to the point of zero rotation on the ORD curve (see **Figure 2.11**). Furthermore, ORD spectra are always of equal amplitude and mirror each other for optically identical enantiomers [37]. The *Cotton* effect is said to be positive when the maximum ORD value is at a long wavelength (see example in **Figure 2.11**), and it is negative for a maximum value at a short wavelength. A molecular substance is defined as dextrogyre (D) for a positive *Cotton* effect and levogyre (L) for a negative *Cotton* effect.

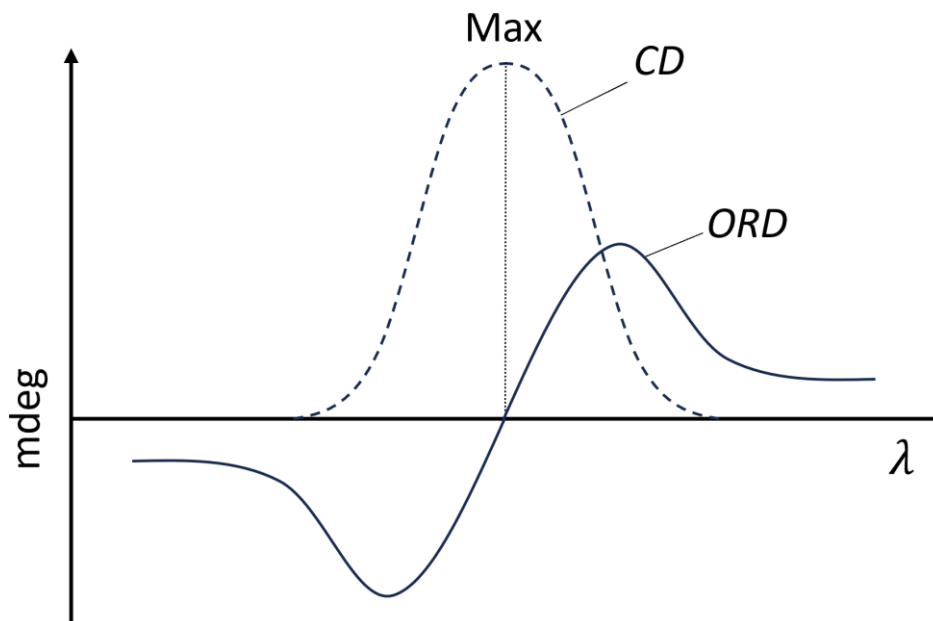


Figure 2.11: Example of CD and ORD spectra related by the positive Cotton effect.

The real and imaginary parts of complex optical functions are linked by the *Kramers–Kronig* (KK) relationship, which allows the calculation of a CD spectrum from ORD spectrum and vice versa. The two expressions of the KK relationship used to calculate the angles  $\theta_{KK}$  and  $\phi_{KK}$  at the wavelength  $\lambda$  from the experimental spectra of  $\phi$  and  $\theta$  at wavelength  $\lambda'$  are [38,39]:

$$\theta_{KK}(\lambda) = \frac{2}{\pi} \int_0^{\infty} [\phi(\lambda')] \frac{\lambda'}{(\lambda^2 - \lambda'^2)} d\lambda' \quad (2.20)$$

$$\phi_{KK}(\lambda) = -\frac{2}{\pi\lambda} \int_0^{\infty} [\theta(\lambda')] \frac{\lambda'}{\lambda^2 - \lambda'^2} d\lambda'. \quad (2.21)$$

#### 2.4.4 Optical Chirality and Superchirality

Chirally sensitive spectroscopic techniques using ORD and CD effects are based on the difference in light-matter interaction between LH and RH CPL. But this asymmetry is usually weak and necessitates a large quantity of molecules to be detected ( $> \mu g$ ) [40]. This limitation is mostly due to the small size of the molecules being analysed such as proteins and viruses, which are far smaller than the wavelength of the light. The rotation of CPL over the size of the chiral analyte is therefore insignificant, leading to an inherent weakness of enantioselective measurements. The dissymmetry between the interaction of both handedness of CPL and the chiral analytes is often characterised by the dissymmetry factor  $g$ :

$$g = \frac{A_{LCP} - A_{RCP}}{\frac{1}{2}(A_{LCP} + A_{RCP})}. \quad (2.22)$$

Where  $A_{LCP/RCP}$  is the absorption of LCP and RCP light, respectively. A  $g$ -factor equal to 2 or  $-2$  expresses total selectivity of CPL handedness for LH and RH respectively. In practice, the values observed for small enantiopure molecules are  $< 10^{-2}$  [41].

It was long thought that the maximum chiral dissymmetry was obtained using CPL, but recent work by Tang and Cohen suggested the new concept of “superchiral light” [3]. These superchiral fields possess a higher degree of helicity compared to standard CPL, which translates to a much faster rotation of their electric field vector compared to CPL for the same distance.

The foundation of this concept was first introduced by Daniel Lipkin in 1964, who used Maxwell’s equations to find the “*Existence of a new conservation law in electromagnetic theory*”. Lipkin named this new conserved quantity “zilch”, unaware of its physical meaning [42]. This quantity was later referred to as “optical chirality” by Tang and Cohen, parameterised as  $C$ . The time-dependent form is given by the following equation [3]:

$$C = \frac{1}{2} \left\{ \varepsilon_0 \mathbf{E} \cdot (\nabla \times \mathbf{E}) + \frac{1}{\mu_0} \mathbf{B} \cdot (\nabla \times \mathbf{B}) \right\}. \quad (2.23)$$

Where  $\mathbf{E}$  and  $\mathbf{B}$  are the complex time-varying electric and magnetic fields, respectively. This equation describes the ‘twist’ of the EM field by adding the contribution from the electric and magnetic fields. The time average form is given by:

$$C = -\frac{\varepsilon_0 \omega}{2} \text{Im}(\mathbf{E}^* \cdot \mathbf{B}). \quad (2.24)$$

Here  $\mathbf{E}$  and  $\mathbf{B}$  are the complex amplitudes of the electric and magnetic fields, respectively, and  $\omega$  is the angular frequency. The value of  $C$  is normalised to CPL, where the field vectors undergo one revolution per wavelength, giving  $C = 1$  for LH and  $C = -1$  for RH CPL. If  $|C| > 1$ , the EM field is called ‘superchiral’.

Optical chirality is a conserved quantity that can be exchanged with electrical currents inside chiral materials through losses. The time derivative of equation (2.23) gives [3]:

$$\frac{\partial C}{\partial t} + \frac{1}{\mu_0} \nabla \cdot \mathbf{F} = -\frac{1}{2} \{ \mathbf{j} \cdot \nabla \times \mathbf{E} + \mathbf{E} \cdot \nabla \times \mathbf{j} \}. \quad (2.25)$$

Where  $\mathbf{j}$  is the current density and  $\mathbf{F}$  is the optical chirality flux, that represents the flow of optical chirality through space, expressed by:

$$\mathbf{F} = \{ \mathbf{E} \times (\nabla \times \mathbf{B}) - \mathbf{B} \times (\nabla \times \mathbf{E}) \} / 2. \quad (2.26)$$

These equations show that, in free space, optical chirality is conserved and that the currents in a material can act as a source or sink of optical chirality [43].

To physically understand how light can be superchiral, it is useful to visualise the electric field vector at a snapshot in time. **Figure 2.12** compares the field vector of a propagating LH CPL (see **Figure 2.12** (a)) to an example of a superchiral wave of equal frequency (see **Figure 2.12** (b)).

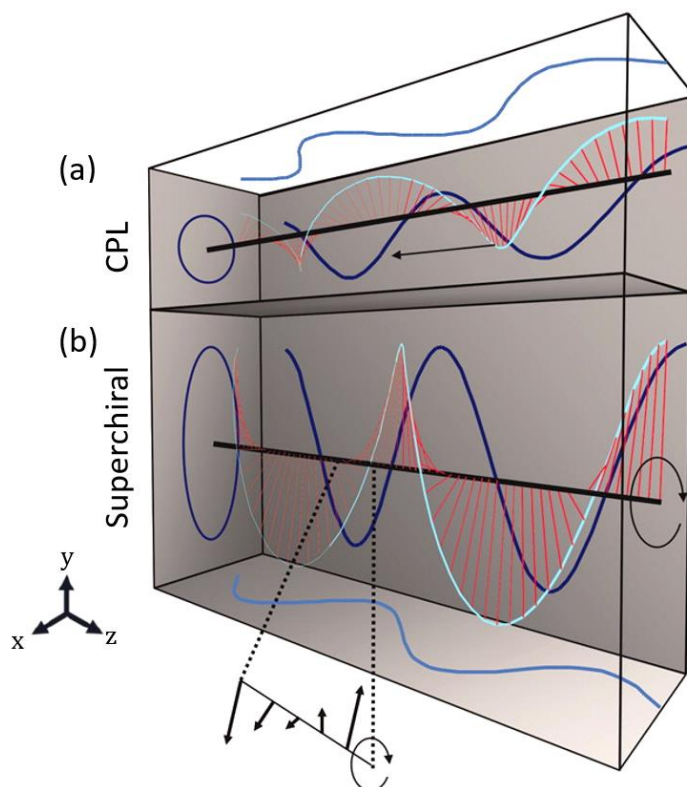


**Figure 2.12:** Electric field vector of a) a LH CPL propagating along the direction of the black arrow and b) a superchiral light. The field projections are plotted in blue onto the planes  $xy$ ,  $xz$  and  $yz$  (from [44]).

In the case of a CPL beam, the field vector (red lines) rotates at a constant rate around the propagation axis, exhibiting a constant optical chirality and energy density throughout space. The projection of its electric field vector onto the  $xy$  plane is a circle. For the case of a superchiral wave, the electric field rotates around its axis but doesn't propagate. This standing wave can undergo a greater rotation rate compared to CPL over the same distance at a spot called a '*superchiral node*'. An example of rotation of the electric field vector at a *superchiral node* is presented at the bottom of **Figure 2.12**, where the field rotates  $180^\circ$  over a distance much shorter than  $\lambda/2$ . If a chiral molecule is located at this *superchiral node*, it will see a greater twist than with CPL, increasing the enantioselectivity of CD spectroscopy [44].

Following their work on optical chirality, Tang and Cohen demonstrated an 11-fold enhancement in enantioselectivity using superchiral light over regular CPL in CD. This superchiral configuration was created from the interference between counterpropagating CPL beams of opposite handedness with a slight mismatch in their

amplitude. They adapted the equation of the dissymmetry factor to include the optical chirality parameter  $C$  [44]:

$$g = g_{CPL} \left( \frac{cC}{2U_e\omega} \right). \quad (2.27)$$

Where  $g_{CPL}$  is the dissymmetry factor obtained with CPL and  $C$  is the optical chirality parameter as seen in the equation (2.22) and (2.23), respectively. Here,  $c$  is the speed of light and  $U_e$  is the electric energy density. The term  $g_{CPL}$  is purely dependent on the molecular analyte, while  $(cC/2U_e\omega)$  is electrodynamic in nature, describing the chirality of the incident EM field. This formula implies that an enhancement of the dissymmetry factor  $g$  is possible by increasing  $C$ .

Following the establishment and definition of optical chirality in the electrodynamic frame, researchers have exploited plasmonic metamaterials to confine light at the nanoscale and enhance  $C$  in the near field [45]. The molecular analytes can be strategically placed in these regions of high optical chirality to drastically increase CD effects and achieve ultrasensitive sensing capabilities [4].

## 2.5 Fundamentals of plasmonics

Plasmonics is a subfield of nanophotonics that encompasses the excitation and manipulation of the collective oscillation of electrons at the metal-dielectric interface, referred to as surface plasmons. These oscillations of electronic charges are caused by the interaction of EM fields with the free electron cloud in metals, known as plasma. This phenomenon is linked to the intrinsic properties of metals, which have an equal number of ions (positive charges) and electrons (negative charges) at equilibrium.

Plasmonic processes have the potential to disrupt many industries, with applications in chemistry, communication, medical diagnosis and treatment. Amongst them, biosensing holds a focal point in this thesis, where plasmonic metamaterials are employed to confine light at the nanoscale to amplify optical phenomena such as ORD and CD viewed in Section 2.4 [46]. Plasmonics can be divided into two categories that will be presented in the following parts: propagating plasmonic modes and localised plasmonic modes [47].

### 2.5.1 Plasmonic oscillations

An EM field can cause a collective motion of the electrons around the rigid ionic lattice of the metal. The displacement of this electron gas will cause an asymmetry in the repatriation of the charges in the metal. When the metal is no longer subjected to the

excitation of the incident EM wave, the core ions will attract back the negative charges, which will keep oscillating thanks to the conservation of momentum.

The response of free electrons to light excitation is described by the complex dielectric function of the metal  $\varepsilon(\omega)$ , which is derived from the *Drude* model of electrical conduction [48]:

$$\varepsilon(\omega) = 1 - \frac{\omega_p^2}{\omega^2 + \gamma^2} + i \frac{\omega_p^2 \gamma}{\omega(\omega^2 + \gamma^2)}. \quad (2.28)$$

Where  $\omega$  is the angular frequency of light,  $\gamma$  is the damping constant of the metal or the electron collision rate in the material and  $\omega_p$  is the bulk plasma frequency. This frequency  $\omega_p$  is given by [49]:

$$\omega_p = \sqrt{\frac{Ne^2}{m\varepsilon_0}}. \quad (2.29)$$

With  $N$  the conduction electron density,  $e$  the charge of an electron of mass  $m$  and  $\varepsilon_0$  the permittivity of free space.

For frequencies in the visible range  $\omega \gg \gamma$ . The real and imaginary parts of the dielectric function can therefore be simplified to:

$$\varepsilon_1(\omega) = 1 - \frac{\omega_p^2}{\omega^2} \quad (2.30)$$

$$\varepsilon_2(\omega) = i \frac{\omega_p^2}{\omega^3}. \quad (2.31)$$

The real part  $\varepsilon_1(\omega)$  of the dielectric function is the relative permittivity of the material, describing the ability of the electrons in a material to polarise under an applied electromagnetic field. The imaginary part  $\varepsilon_2(\omega)$  represents the dissipation of energy in the material.

From equations (2.30) and (2.31), if  $\omega < \omega_p$ , then the real part is negative, consequently, the EM wave decays exponentially as it penetrates the metal and light is reflected in this frequency range. For the case where  $\omega = \omega_p$ , the real part is null, and the electrons will be oscillating in-phase at this frequency throughout the material. Finally, if  $\omega > \omega_p$ , the reflectivity decreases, and the wave propagates in the metal, which becomes transparent [50].

The *Drude* model can accurately predict the optical response of metals at low frequencies, but it faces major limitations at high frequencies. This is due to the inherent simplification of this model, which assumes free electron charges and neglects electron-electron and electron-ion interactions [51]. Photons with a higher energy than the band gap of the material can initiate an interband transition of electrons from a low-energy *d*-band to a high-energy *sp* conduction band.

For gold and silver, which are the two metals most widely used in the field of plasmonics, interband transition effects occur in the visible to near-IR region. As a result, the *Drude* model (see solid line in **Figure 2.13**) doesn't hold beyond  $\sim 1$  eV, or below  $\lambda \approx 1000$  nm, where it deviates from experimental observations (see red dots in **Figure 2.13**) [52].

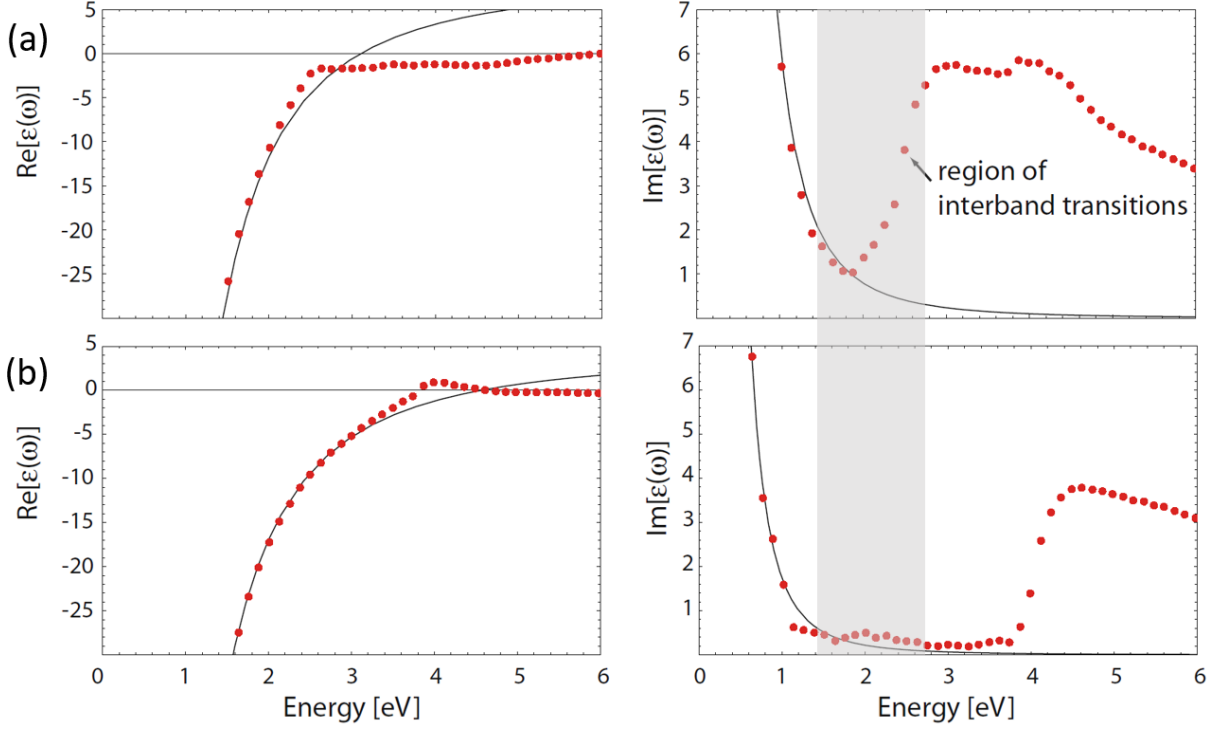


**Figure 2.13:** Real and imaginary part of the dielectric function  $\epsilon(\omega)$  of a) gold and b) silver as modelled by the *Drude* model (solid line) and experimental data from Johnson and Christy [53] (red dots). Image from [51].

These interband transitions happening at high photon energy can be accounted for by the *Lorentz* model, which describes the response of bound electrons to an EM wave. This model assumes that the positively charged nucleus is connected by electrostatic interactions to a negatively charged electron through a spring constant  $k$ . The *Lorentz* model can be combined with the *Drude* model to fit the optical properties of materials in a broader wavelength range. In the *Drude-Lorentz* model, the dielectric function becomes [54]:

$$\epsilon(\omega) = 1 + \frac{\omega_p^2(\omega_0^2 - \omega^2)}{(\omega_0^2 - \omega^2) + \gamma^2\omega^2} + i \frac{\gamma\omega_p^2\omega}{(\omega_0^2 - \omega^2)^2 + \gamma^2\omega^2} \quad (2.32)$$

$$\omega_0 = \sqrt{\frac{k}{m}} \quad (2.33)$$



$$\omega_p = \sqrt{\frac{N'e^2}{m\epsilon_0}}. \quad (2.34)$$

Where  $\omega_0$  is the resonant frequency of the harmonic oscillator and  $\omega_p$  is the new plasma frequency, considering the density of bond electrons  $N'$ .

As seen in **Figure 2.14**, the *Drude-Lorentz* model shows much more consistency with the measured values for gold.

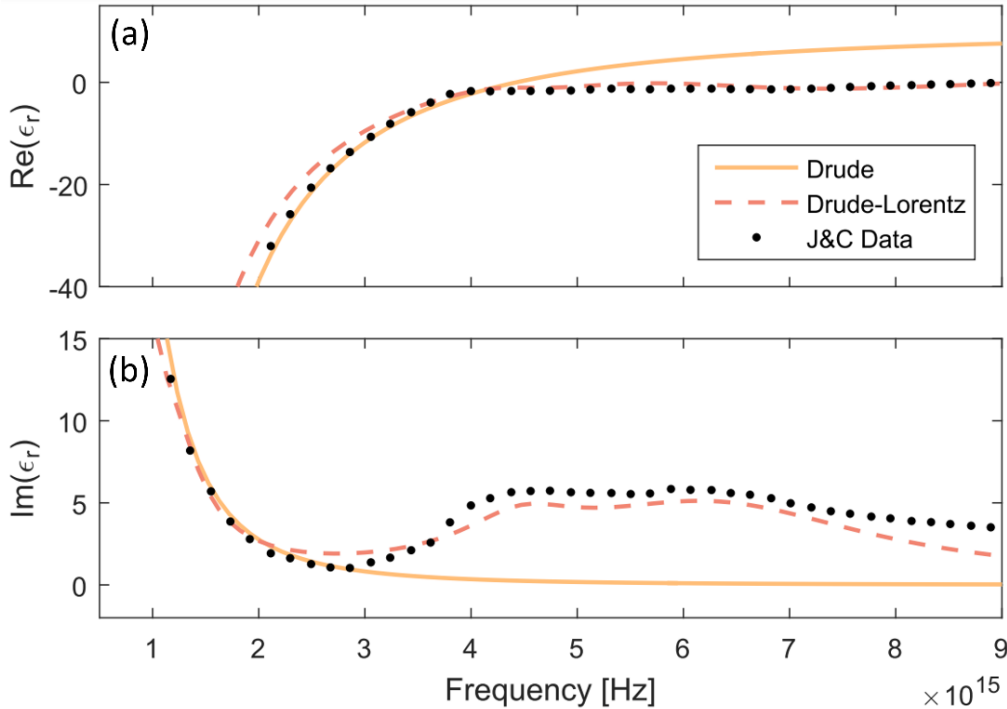


**Figure 2.14:** a) Real and b) imaginary part of the dielectric function  $\epsilon(\omega)$  of gold from the Drude model (orange solid line) compared to the Drude-Lorentz model (dashed red line) with the experimental data from Johnson and Christy [53] (black dots). Image from [55].

## 2.5.2 Surface plasmon polariton

The coupling of an incident electromagnetic wave with the electron plasma in the metal can excite a plasmonic phenomenon called a surface plasmon polariton (SPP) at the metal-dielectric interface. This excitation propagates along the interface between the metal and the dielectric medium. The associated electric field decays exponentially perpendicular to the surface into the dielectric, creating an evanescent wave. Within the metal, this field is associated with the surface plasmon, while in the adjacent dielectric medium, it forms the polariton (see **Figure 2.15** (a)) [56]. The propagation length, or the distance over which the plasmonic excitation travels before decaying is important, particularly in applications such as surface plasmon resonance (SPR) imaging, where it directly influences the lateral resolution of the system.

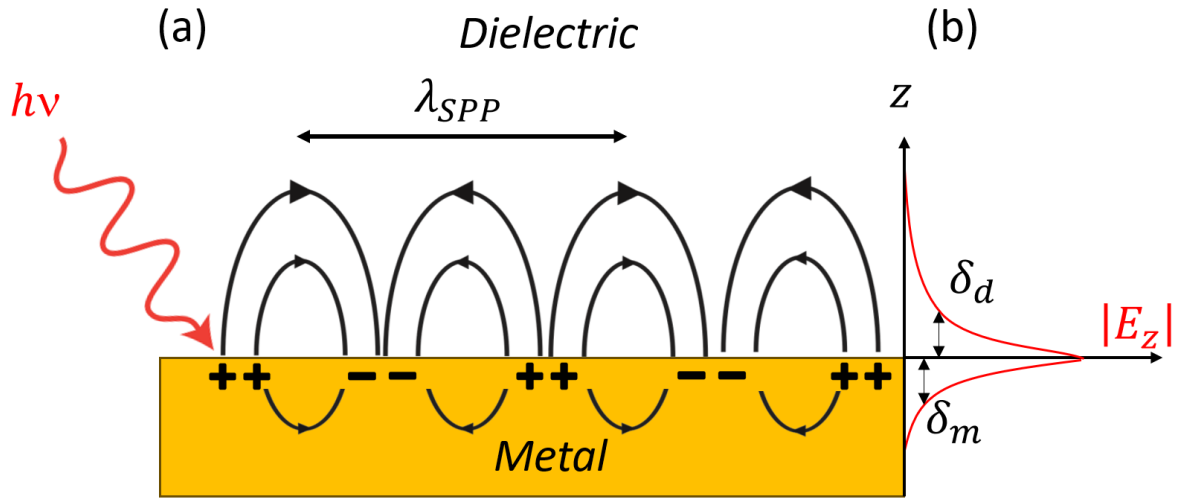


Figure 2.15: a) Surface charges propagating along a metal–dielectric interface after being excited by an electromagnetic wave. b) Penetration depth profile of SPP into both media [57].

The frequency of the oscillation of surface plasmon polaritons  $\omega_{spp}$  is different from the bulk plasma frequency in the metal from equations (2.29) and (2.34), it now becomes:

$$\omega_{spp} = \frac{\omega_p}{\sqrt{1 + \epsilon_d}}. \quad (2.35)$$

With the bulk plasma frequency as  $\omega_p$  and the relative permittivity of the dielectric medium  $\epsilon_d$ .

As seen from this equation, the SPP frequency is lower than the bulk frequency, making it possible for lower energy to excite the SPP mode. The EM field intensity of SPP is dependent on the depth relative to the interface in both media. It decreases exponentially with the distance from the surface, decaying quicker for the metal compared to the dielectric due to a stronger absorption (see Figure 2.15 (b)). For an incident light of 630 nm, surface plasmon polariton at a gold/water interface has penetration depths of 29 nm for  $\delta_m$  in the metal and 162 nm for  $\delta_d$  in the dielectric [58].

### 2.5.3 Localised Surface Plasmon Resonance

When plasmon oscillations are confined to a metallic nanostructure, they are called localised surface plasmon resonances (LSPR) and are, by definition, non-propagating waves. These nanoparticles generally need to be far smaller than the wavelength of the incident EM wave. The electron gas inside the nanostructure will oscillate, driven by the EM radiation, while being bound by the positively charged metallic core (see Figure 2.16).

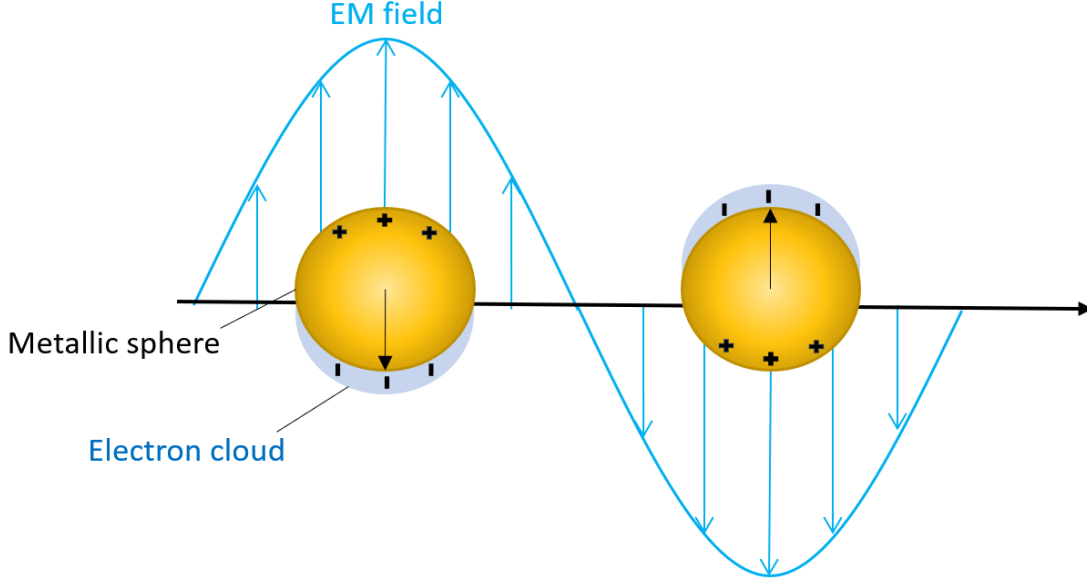


**Figure 2.16: Conduction band electrons oscillating in a metallic nanoparticle irradiated by an incident EM wave (adapted from [59]).**

At the resonance frequency, the nanoparticle exhibits strong absorption and scattering, with an electric field around its surface enhanced by many orders of magnitude compared to the intensity of the incident EM field [60]. In the electrostatic approximation, the polarisability  $\alpha$  of a nanosphere of radius  $r \ll \lambda$  and dielectric constant  $\varepsilon$ , placed in an isotropic and non-absorbing dielectric medium ( $\varepsilon_d$ ), is given by [51]:

$$\alpha = 4\pi r^3 \frac{\varepsilon - \varepsilon_d}{\varepsilon + 2\varepsilon_d}. \quad (2.36)$$

This equation shows that LSPR is size dependent, scaling to the cube of the nanosphere's radius. It also demonstrates that the LSPR varies with the material properties of the nanostructure and its surrounding medium. When  $Re[\varepsilon(\omega)] = -2\varepsilon_d$ , the polarisability is maximised, and there is a plasmonic resonance. This is called the *Fröhlich* condition. The frequency of the LSPR  $\omega_0$  can be derived by using the approximation of equation (2.30) to solve the *Fröhlich* condition:

$$1 - \frac{\omega_p^2}{\omega_0^2} = -2\varepsilon_d \quad (2.37)$$

and finally:

$$\omega_0 = \sqrt{\frac{\omega_p^2}{1 + 2\varepsilon_d}}. \quad (2.38)$$

The extinction cross-section of the nanoparticle  $C_{ext} = C_{sca} + C_{abs}$ , is characterised by the efficacy with which the plasmonic nanostructure scatters and absorbs light and is proportional to the polarisability  $\alpha$ . The scattering ( $C_{sca}$ ) and absorption ( $C_{abs}$ ) cross-sections are given by [51]:

$$C_{sca} = \frac{k^4}{6\pi} |\alpha|^2 = \frac{8\pi}{3} k^4 r^6 \left| \frac{\varepsilon - \varepsilon_d}{\varepsilon + 2\varepsilon_d} \right|^2 \quad (2.39)$$

$$C_{abs} = k \text{Im}[\alpha] = 4\pi k r^3 \text{Im} \left[ \frac{\varepsilon - \varepsilon_d}{\varepsilon + 2\varepsilon_d} \right]. \quad (2.40)$$

Where  $k = 2\pi/\lambda$  is the wave number. As seen in these equations, the scattering cross-section will be proportional to  $r^6$  while the absorption cross-section will scale with  $r^3$ . For very small particles with  $r \ll \lambda$ , the absorption of light will dominate compared to the scattering of light.

The resonance of the polarisability  $\alpha$  under the *Fröhlich* condition can only predict the optical behaviour of very small nanoparticles ( $< 100$  nm). These plasmonic nanostructures act as electric dipoles when resonating with an EM wave, both absorbing and scattering light. For larger dimensions, this model is not sufficient due to the phase-changes of the incident EM field over the volume of the particle [51]. The quasi-static approach employed previously is not sufficient anymore, and an electrodynamic solution is necessary. In 1908, Gustav Mie solved Maxwell's equations to describe the scattering of an EM wave by a spherical nanoparticle [61]. The extinction cross-section  $\sigma_{ext}$  from Mie theory is [62,63]:

$$\sigma_{ext} = \frac{\lambda}{2\pi} \sum_{n=0}^{\infty} (2n+1) \text{Re}\{a_n + b_n\}. \quad (2.41)$$

Where  $a_n$  and  $b_n$  are the Mie coefficients, which are complex functions described by two parameters:  $m$  and  $x$ , where  $m$  is the ratio of the refractive index of the particle  $n_p$  relative to that of the dielectric medium  $n_d$  as  $m = n_p/n_d$ . The second parameter  $x$  is the ratio of the circumference of the nanosphere to the wavelength of the incident light ( $\lambda$ ) in the dielectric surrounding it, as  $x = 2\pi r/(\lambda/n_d)$ .

Mie theory is valid for a wide range of nanoparticles' sizes of any refractive indices, but it is limited only to spheres far away from each other. Indeed, when plasmonic nanostructures are close together, their LSPR can couple, drastically changing the optical properties of the system compared to the case of an isolated particle.

## 2.5.4 Plasmonic hybridisation in coupled nanoparticles

When plasmonic modes of individual nanostructures interact with one another, they can couple, leading to plasmonic hybridisation. The collective response of a plasmonic assembly has been modelled using the property of a single nanoparticle, similar to the molecular orbital theory [64,65]. In chemistry, the molecular orbital theory describes the hybridisation of the electronic structure of atoms in proximity, forming bonds.

If two particles with plasmonic resonances  $\omega_1$  and  $\omega_2$  are cross-coupling weakly at a frequency  $\omega_{cc} \ll |\omega_1 - \omega_2|$ , then the individual resonances  $\omega'_1$  and  $\omega'_2$  will be slightly shifted, following [66]:

$$\omega'_1 = \omega_1 + \frac{\omega_{cc}}{4(\omega_1 - \omega_2)} \quad (2.42)$$

$$\omega'_2 = \omega_2 - \frac{\omega_{cc}}{4(\omega_1 - \omega_2)}. \quad (2.43)$$

This will result in a small shift in the position of the resonances (see **Figure 2.17** (a)). In the case of a strong coupling, with  $\omega_{cc} \gg |\omega_1 - \omega_2|$ , the formation of the new hybrid modes  $\omega_+$  and  $\omega_-$  will arise. These resonances will split symmetrically between the two initial resonances (see **Figure 2.17** (b)), as follows [66]:

$$\omega_{\pm} = \frac{\omega_1 + \omega_2}{2} \pm \frac{\omega_{cc}}{2}. \quad (2.44)$$

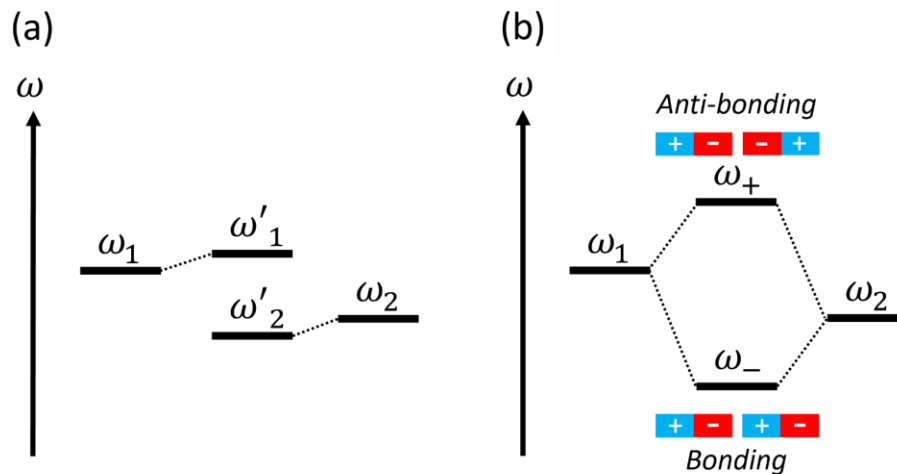


**Figure 2.17:** Schematic of the hybridisation of two plasmonic resonances  $\omega_1$  and  $\omega_2$  when (a) they are weakly coupled and (b) strongly coupled, with a representation of the dipolar symmetric and anti-symmetric plasmonic modes of two nanorods in proximity (adapted from [66]).

In a simple example, where a nanorod dimer is close enough to couple strongly, the plasmonic modes can oscillate in-phase or out-of-phase. If they are in-phase, a lower-energy ‘bonding’ mode (symmetric) will result, exhibiting a higher EM enhancement. The out-of-phase ‘anti-bonding’ mode (anti-symmetric) will have a higher energy due to the addition of electrostatic energy caused by the charge accumulations of the system (see **Figure 2.17** (b)) [67]. These modes are often referred to as ‘bright’ and ‘dark’ modes due to their respectively strong and weak interaction with light.

## 2.5.5 Refractive index-based sensing

The LSPR extinction wavelength ( $\lambda_{Max}$ ) is sensitive to the dielectric constant  $\epsilon_d$ , or refractive index  $n_d$  (with  $\epsilon = n^2$ ) of the medium surrounding the plasmonic nanostructure. The introduction of molecular species in the near field environment of the plasmonic surface will cause a shift in the resonance peak  $\lambda_{Max}$ . This shift  $\Delta\lambda$  can be calculated by [59]:

$$\Delta\lambda = m\Delta n \left( 1 - \exp\left(\frac{-2d}{l_d}\right) \right). \quad (2.45)$$

Where  $m$  is a coefficient representing the sensitivity of the nanoparticle to a change in refractive index,  $\Delta n$  is the variation in the refractive index due to the introduction of molecules,  $d$ , the effective thickness of the molecular layer, and  $l_d$ , the evanescent field decay length normal to the surface.

Thanks to a small decay length ( $1/e$ ) of  $\sim 5-10$  nm compared to  $\sim 200$  nm for SPP at the surface of gold, the change in refractive index is detected when the molecules are in direct proximity to the nanoparticle (or adsorbed) [68]. By measuring the shift induced by an adsorbed layer of molecular analytes, it is possible to estimate their optical properties, which can also be used to detect conformational changes in proteins [69]. This phenomenon is at the core of LSPR-based sensors.

## 2.6 Thermoplasmonics

The field of thermoplasmonics defines the physics behind heat generation in plasmonic nanoparticles following light excitation [70]. Once considered an unwanted consequence of plasmonic effects, this property of metallic nanoparticles is now the focus of study in numerous applications. Thermoplasmonic effects were first employed in 1999 for fast denaturation of proteins by using gold nanoparticles illuminated with a pulsed laser [71]. This strategy proved to be advantageous over the use of traditional techniques

involving an absorber dye, which is prone to photobleaching and does not exhibit comparable temperature increases. Since then, a myriad of other useful applications have been explored, notably in the field of biomedicine, with biomolecule photothermal imaging and novel cancer treatments through photothermal therapy [72,73]. Amongst other applications worth mentioning, photothermal chemistry uses the heat generated by plasmonic nanoparticles to enable the spatial confinement of chemical reactions [74]. Thermophotovoltaics is also a field where plasmonic nanoparticles offer promising solutions. Turning all the sun rays into heat using a plasmonic absorber and converting this heat into thermal emission close to the bandgap of a photovoltaic cell would theoretically enable an increase in the yield beyond 80% [75].

## 2.6.1 Physics of Plasmonic Heating

When an electromagnetic wave induces LSPR in a nanoparticle, the collective oscillation of the electron cloud is amplified, and the frequency of collisions with atoms in the metal lattice is increased, resulting in Joule heating [76]. If we consider a metallic nanoparticle of complex relative permittivity  $\varepsilon(\omega)$  illuminated by a monochromatic light of angular frequency  $\omega$  surrounded by a dielectric medium (such as water), then the heat source density from Joule effects  $q(\mathbf{r})$  in the nanoparticle is [77]:

$$q(\mathbf{r}) = \frac{1}{2} \text{Re}[\mathbf{J}^*(\mathbf{r}) \cdot \mathbf{E}(\mathbf{r})]. \quad (2.46)$$

Here  $\mathbf{J}(\mathbf{r})$  is the complex amplitude of the electronic current density in the plasmonic nanostructure and  $\mathbf{E}(\mathbf{r})$  is the complex amplitude of the electric field inside the nanoparticle. We can express  $\mathbf{J}(\mathbf{r})$  as  $\mathbf{J}(\mathbf{r}) = i\omega\mathbf{P}(\mathbf{r})$ , with the polarisation in the material  $\mathbf{P}(\mathbf{r}) = \varepsilon_0\varepsilon(\omega)\mathbf{E}(\mathbf{r})$ , leading to the following formulation:

$$q(\mathbf{r}) = \frac{\omega}{2} \text{Im}(\varepsilon(\omega))\varepsilon_0 |\mathbf{E}(\mathbf{r})|^2. \quad (2.47)$$

The heat generated inside the metallic nanoparticle is therefore proportional to the square of the electric field. The distribution of heat depends strongly on the size of the nanoparticle, as well as its shape, and can vary inside the structure [77].

The total heat power  $Q$  delivered by the plasmonic nanoparticle can be expressed by the integration over the heat source density in the volume ( $V$ ):

$$Q = \int_V q(\mathbf{r}) d^3\mathbf{r}. \quad (2.48)$$

This phenomenon is also dictated by the absorption cross section of the system, while the scattering cross-section defines the energy reflected from the nanoparticles in the form of light [78]. The heat power in the nanoparticle can be expressed as a function of the absorption cross-section  $\sigma_{abs}$  of the plasmonic system as:

$$Q = \sigma_{abs} I . \quad (2.49)$$

Where  $I$  is the irradiance of the incident light (in  $W$  per unit area), for a plane wave  $I = nc\varepsilon_0|\mathbf{E}_0|^2/2$ . This approach is viable when the nanoparticle studied has a simple shape such as a sphere or an ellipsoid, and  $\sigma_{abs}$  is obtained analytically.

The process behind thermoplasmonics is the result of a cascade of energy exchanges happening at different time scales. When a pulsed electromagnetic wave reaches the nanoparticle at the LSPR frequency, a dipolar oscillation of electrons in the conduction band arises, creating hot electron-hole pairs (**Figure 2.18 (a)**). To relax this excited state, the energy is dispersed either through radiative photon re-emission or non-radiative generation of energetic charge carriers (electron-hole pair) via Landau damping (see **Figure 2.18 (b)**) [79]. In quantum mechanics, Landau damping is a process that transfers a quantum of plasma oscillation into a single electron-hole pair excitation within  $1 fs$  to  $100 fs$  [80]. The relaxation of these “hot” carriers takes place in a timeframe of several hundred femtoseconds, during which electron equilibration is reached through electron-electron scattering processes (see **Figure 2.18 (c)**). This step is followed by the thermalisation of the metal lattice via electron-lattice scattering over a few picoseconds. The heat locally generated within the NP is thereafter distributed to the dielectric media of the surroundings (see **Figure 2.18 (d)**). The timescale varies from  $100 ps$  to  $10 ns$  depending on the material properties of the NP and its environment, as well as the size of the NP and if LSPR are coupled with other NPs in the vicinity [81].

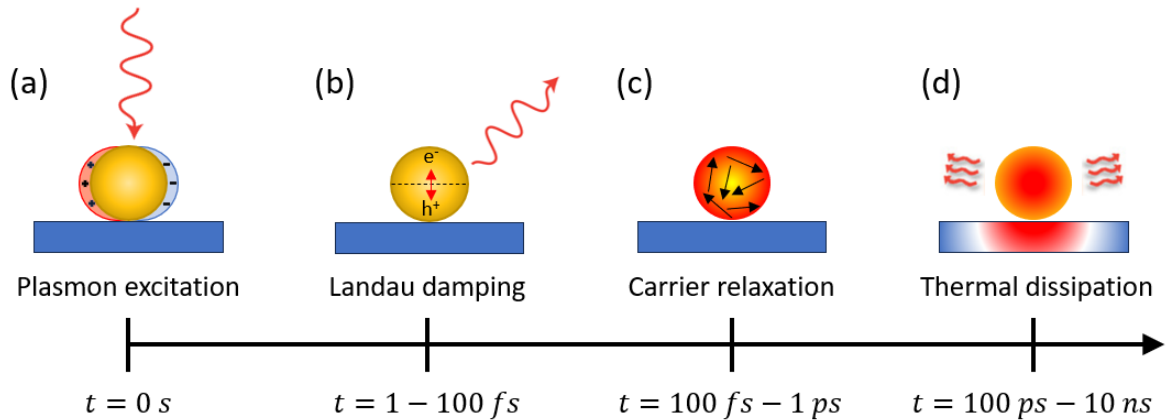


**Figure 2.18: Thermoplasmonics effect time scale (adapted from [82]).**

Hot carrier generation can be optimised by tuning the geometry of the NP, hence its LSPR properties. It also depends on the electronic structure and density of states of the material employed [83].



## 2.7 Metamaterials

### 2.7.1 Origin and definition

The word ‘metamaterial’ refers to artificially engineered structures that are designed to have different properties compared to the bulk material they are made of. The prefix “meta” translates to “beyond” in Greek, referring to their unusual properties. The concept of metamaterials was first introduced as “left-handed materials” in 1968 by Veselago, who theoretically proposed the existence of materials with negative electric permittivity and magnetic permeability simultaneously [84]. These metamaterials, often based on plasmonic phenomena, would possess optical properties that are not found in nature, such as a negative refractive index, reversed Doppler shift and backward wave propagation [85]. It was only in 1996 that experimental evidence of a negative permittivity in wire medium was provided [86], followed by the discovery of an artificial magnetic plasma with a negative permeability in 1999 [87]. In 2000, Smith et al. published their seminal paper on a sample with negative permittivity and permeability, that they named “Metamaterial” [88]. If in a given frequency range  $\epsilon(\omega)$  and  $\mu(\omega)$  are negative, the refractive index will also be negative, with  $n = \sqrt{\mu\epsilon} = \sqrt{(-1)^2|\mu||\epsilon|} = -\sqrt{\mu\epsilon}$  [51]. This negative sign of  $n$  is consistent with Maxwell’s equations and translates to refracted light in the negative-index medium in the opposite direction it usually follows in a positive-index material (see **Figure 2.19**).

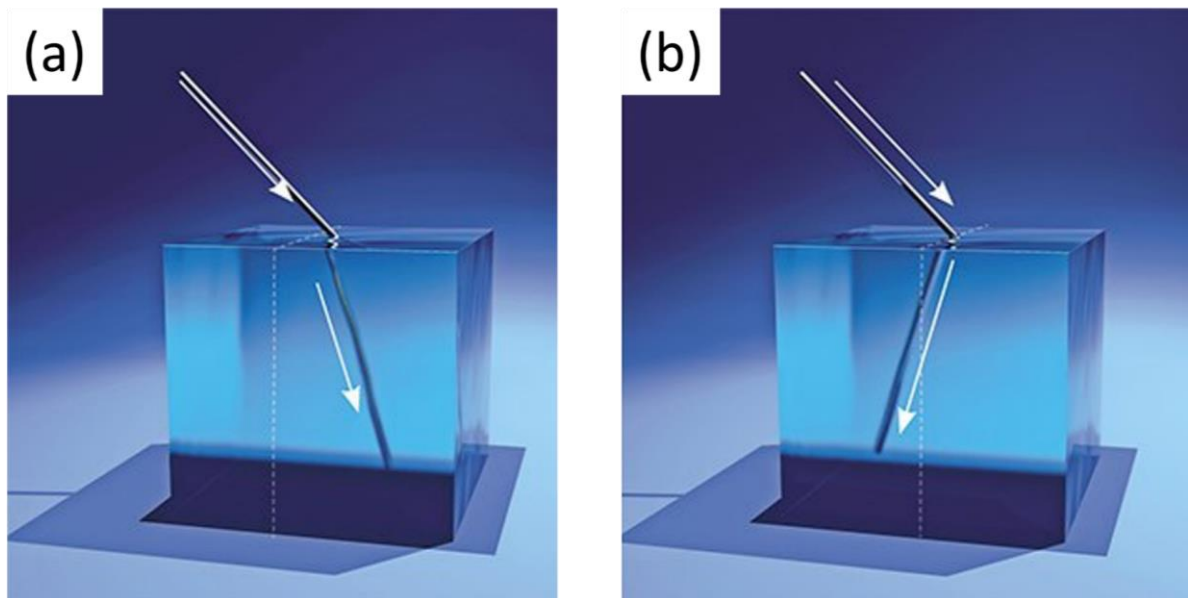


**Figure 2.19:** Illustration of the path of refracted light inside (a) a conventional positive-index material and (b) a negative-index material (from [89]).

This property was initially the focus of metamaterial research, with potential applications in the development of perfect lenses, which would not limit the sharpness of the image to the wavelength of light (see **Figure 2.20 (a)**) [90]. Another application of negative-index metamaterials is the development of invisibility cloaking. This technology operates by manipulating the material's optical properties to reduce or redirect the scattered light around an object, effectively making it undetectable to observers (see **Figure 2.20 (b)**) [91,92]. The later work explored their unprecedented electromagnetic properties in other applications, such as optical sensing, novel waveguides and photonic nanocircuits [93].

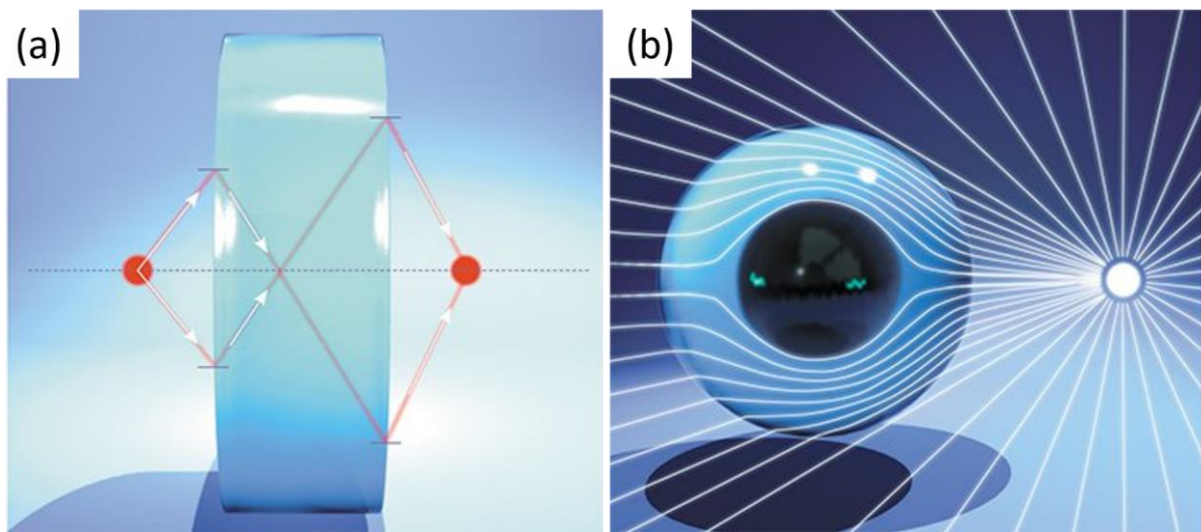


**Figure 2.20: Illustration of the light paths going through (a) a perfect lens and (b) in a metamaterial shell around an object, rendering it invisible (from [89]).**

## 2.7.2 Chiral metamaterials

Metamaterials are generally made of periodic structural units, sometimes referred to as “meta-atoms”, with dimensions under the wavelength of the incident light. Advances in nanofabrication techniques have given researchers the means to manufacture complex structural designs with high reproducibility and tailored properties. Chiral metamaterials are a subcategory of these exotic materials exhibiting strong optical activity. There are many ways to fabricate chiral metamaterials, with two main strategies [94]: the elements constituting the periodic structure can have a chiral shape, or an assembly of achiral patterns can be orientated in a handed way.

An example of the first type is the 3D helix (or corkscrew), which was fabricated using direct laser writing into a polymer photoresist and electrochemical deposition of gold (see **Figure 2.21**) [95].

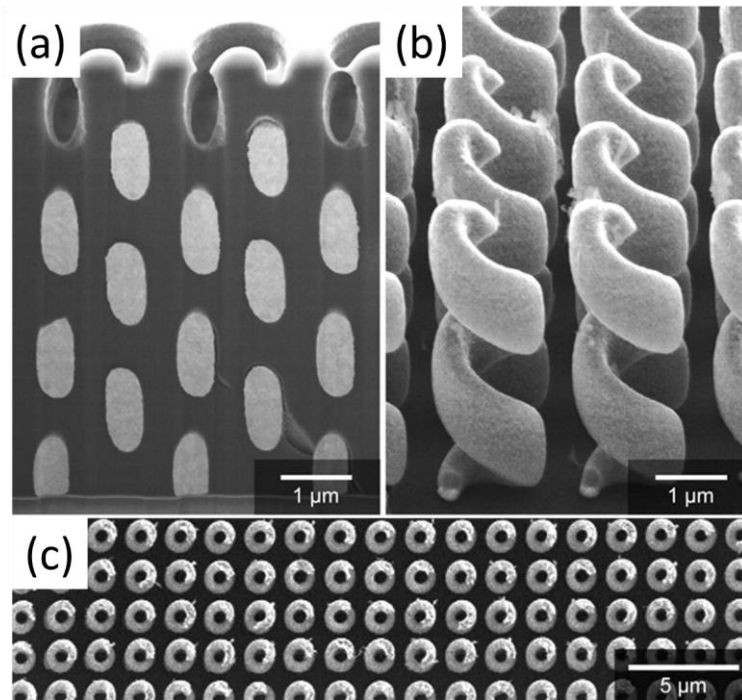


**Figure 2.21:** 3D helix metamaterial SEM images with (a) side view of the sliced polymer filled with gold, (b) oblique view of a LH helix array without the polymer and (c) top view of the metamaterial surface (image from [95]).

The second type of chiral metamaterial can be obtained by stacking two identical achiral layers of gold nanoholes (called Moiré patterns) and operating an in-plane rotation of the top structure (see **Figure 2.22**) [96].

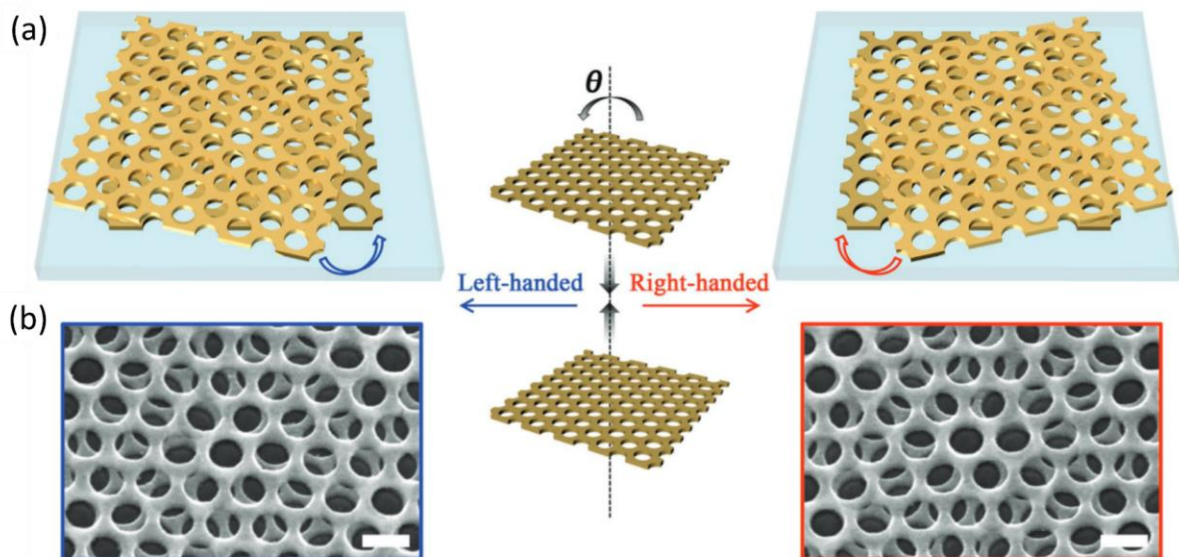


**Figure 2.22:** (a) Schematic illustration of a Moiré chiral metamaterial of both handedness and (b) top view SEM images (image from [96]).

### 2.7.3 Metamaterials applied to biosensing

In the past decade, extensive attention has been put on the development of ever more sensitive chiral biosensing metamaterials based on LSPR. Following the study of Tang and Cohen on superchiral EM fields [3], Hendry and colleagues pioneering work demonstrated that the detection and characterisation of minute amounts of chiral material ( $\sim$ picograms) was possible using planar chiral metamaterials (PCMs) [4]. The samples used in this study were arrays of LH and RH gold chiral ‘gammadion’ shaped structures on quartz slides. These PCMs exhibit a strong CD response at the LSPRs, which is equal and opposite between both gammadion handedness (see **Figure 2.23** (a)). Three modes are visible on the CD spectra, where mode I is located at around 550 nm, mode II at 650 nm and the mode III, the largest, at 800 nm. When chiral molecules are introduced at the very surface of the PCMs, the CD spectra show an asymmetry between both gammadion handedness. This different response is visible at the position of the LSPRs, where a different magnitude of the red shift  $\Delta\lambda_{RH/LH}$  is observed after the adsorption of the chiral molecules (see **Figure 2.23** (b)). As seen in Section 2.5.5, this shift in the position of the LSPR ( $\lambda$ ) is the basis of the biosensing ability of plasmonic materials. The average shift between both PCMs handedness  $\Delta\lambda_{Av}$  obtained for all the molecules studied is shown in **Figure 2.23** (c), providing insight on the thickness of the adsorbed layer. The asymmetry observed was parametrised by  $\Delta\Delta\lambda = \Delta\lambda_{RH} - \Delta\lambda_{LH}$  for all three LSPRs (see **Figure 2.23** (d)).

The technique described was shown to be sensitive to the secondary structure of the proteins studied here. Indeed, the macromolecules with high proportions of  $\beta$ -sheets (outer membrane protein A, concanavalin A and  $\beta$ -lactoglobulin) have all high  $\Delta\Delta\lambda$  values. Conversely, proteins with a high proportion of  $\alpha$ -helices (BSA, myoglobin and haemoglobin) exhibit smaller  $\Delta\Delta\lambda$  values (see **Figure 2.23** (d)).

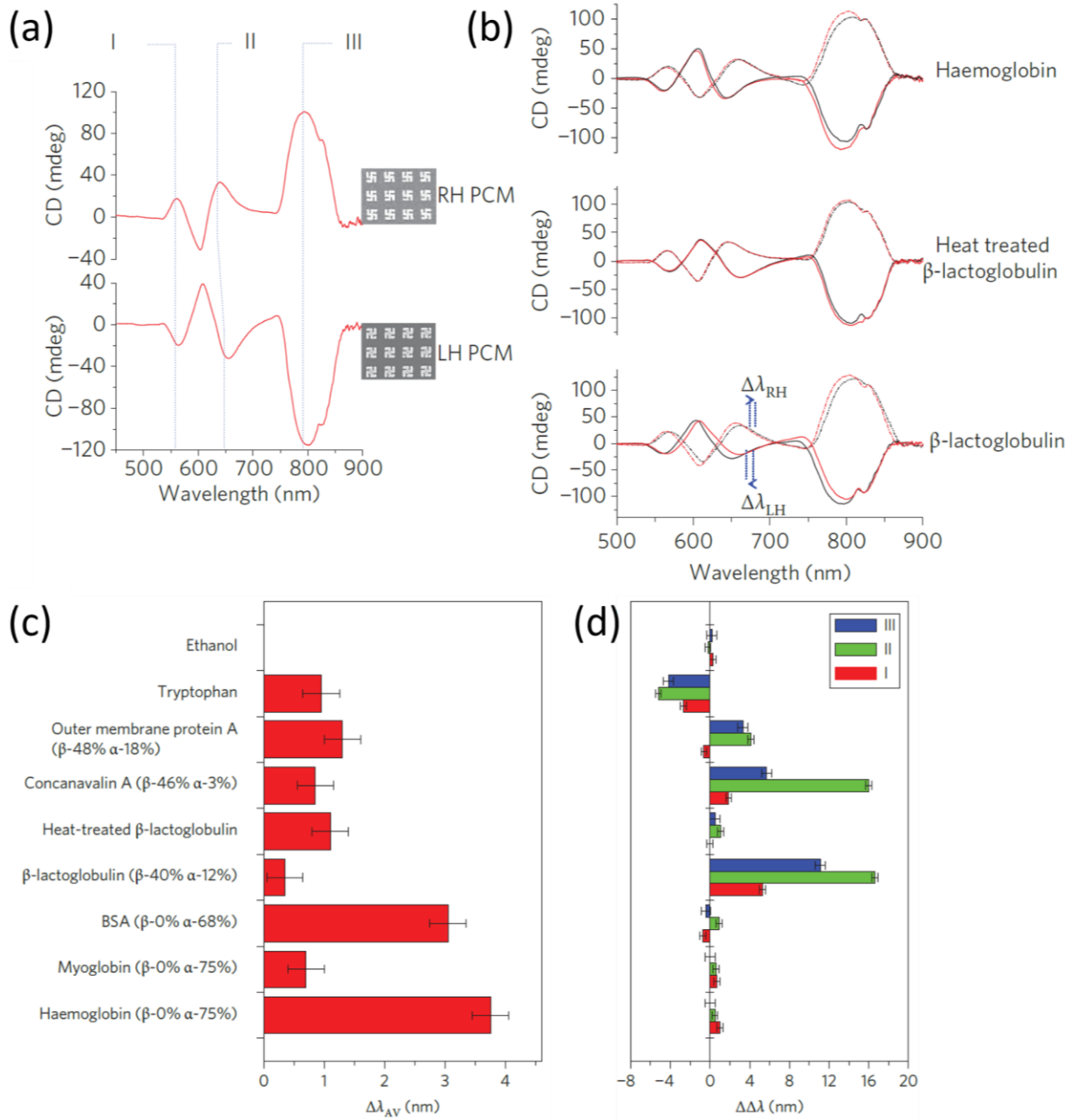


**Figure 2.23:** (a) CD spectra of the RH and LH gammadion in water on the top and bottom, respectively, and (b) CD spectra of both gammadion handedness taken in Tris buffer in red, and adsorbed with haemoglobin, heat-treated  $\beta$ -lactoglobulin and  $\beta$ -lactoglobulin in black. (c) Average shift  $\Delta\lambda_{AV}$  in the LSPR (I) for ethanol (achiral) and all the chiral analytes, with (d) the corresponding values of  $\Delta\Delta\lambda$  for modes I, II and III (from [4]).

This ultrasensitive detection and characterisation of a single molecular layer quantity of chiral analyte was achieved by harvesting the superchiral EM fields generated in the near field of the PCMs. This hypothesis was supported by numerical simulation performed on the gammadion geometry, showing a strong enhancement of the electric field and an enhanced optical chirality  $C$  close to the surface of the plasmonic structure (see **Figure 2.24** (a) and (b)).





**Figure 2.24:** Simulated maps of (a) the electric field strength relative to the incident electric field ( $E_0$ ) and (b) the local optical chirality  $C$  at mode III (from [4]).

Countless other metamaterial designs were developed and tested since then, but the question around the necessity for a plasmonic substrate to be itself chiral to enhance the weak molecular CD is still debated in the literature. The two strategies are equally represented, with achiral substrates [97] providing experimental results on par with chiral designs [98]. The main advantage of an achiral platform is the absence of a far-field CD signal from the structures, which could overshadow the weak CD signal from the molecular analytes [99,100]. Regarding chiral platforms, they can be designed to offer a stronger chiral-specific selectivity [101,102]. The theoretical work of Tang and Cohen [3], with the later addition of Schäferling et al. [103] suggests that the main condition required to observe enhancement of the CD signal is obtained when the fields  $\mathbf{E}$  and  $\mathbf{H}$  are not orthogonal inside the plasmonic hotspots.

The study presented in this section is the starting point of a myriad of successful projects conducted in the Kadodwala group, including the research work presented in this thesis.

# Chapter 3

---

Nanofabrication and  
Characterisation Methods

## 3.1 Nanofabrication Methods

This chapter describes how the samples studied in this work were manufactured. Two different types of metamaterial samples were nanofabricated using tailored protocols. These complex processes involved the use of electron beam lithography (EBL) and injection moulding, among other techniques. All the nanostructure arrays were manufactured inside the James Watt Nanofabrication Centre (JWNC) at the School of Engineering (University of Glasgow). This cleanroom facility is equipped with state-of-the-art nanofabrication instruments as well as a particle filtration system in a pressurised atmosphere to ensure the best sample quality.

### 3.1.1 Fabrication of ordered arrays of nanostructures

The main type of sample manufactured during this PhD was made on a silicon wafer using the EBL technique, followed by metal evaporation. The end goal of this process is to obtain a periodic array of metallic nanostructures, deposited at the surface of the silicon substrate. An exemplar sample manufactured with this technique can be seen on the **Figure 3.1**, obtained by atomic force microscopy (AFM).

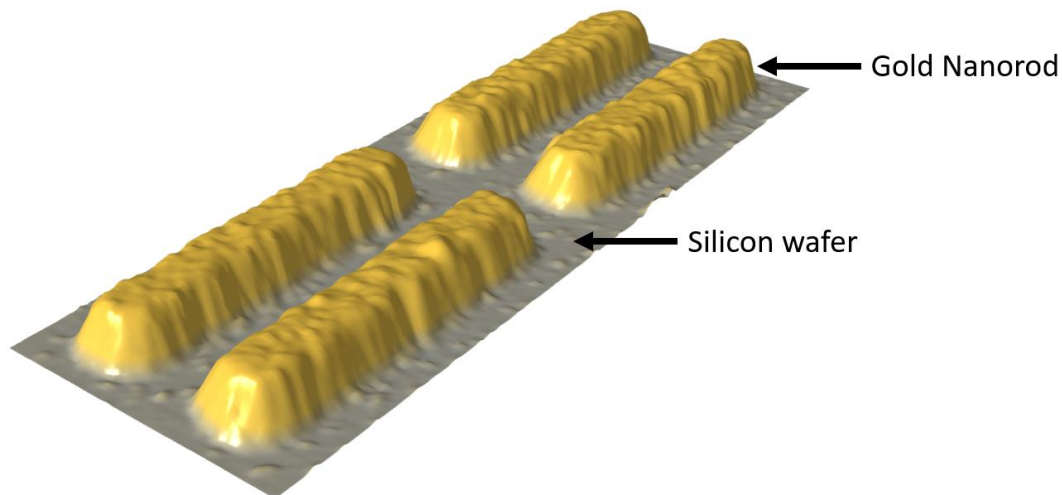


**Figure 3.1:** 3D image of a gold nanostructure array fabricated on a silicon wafer by EBL and metal evaporation. Here the nanorods are 100 nm high and 750 by 150 nm large.

The shape of the nanostructures obtained eventually varied depending on the requirements of the experiment; both chiral and achiral shapes were manufactured in different sizes. To maintain the best quality in the shortest fabrication time, the protocols were adapted and optimised, depending on the size of the desired pattern. The complete process flow using EBL is described in the following sections.



## Sample cleaning

The silicon wafer cleaning process is done using a succession of solvents, namely acetone, methanol and isopropyl alcohol (IPA). Acetone gets rid of any organic contaminants and can also dissolve most resists that may have been used in a previous failed attempt at the EBL process. When dried, acetone will leave a thin layer of non-volatile compounds. To remove it, methanol is used. Finally, the silicon wafer is submerged in an IPA bath to dry the surface [104]. The wafer is thereafter dried using a N<sub>2</sub> air gun. The succession of solvents was poured into a beaker containing the wafer and placed in a mega-sonic bath for 5 minutes each. Acoustic waves in the megahertz range can generate vacuum bubbles as small as 10 µm moving at a high speed, which can remove particles of a few hundred nanometres [105,106].

After this step, the substrate is cleaned using oxygen plasma ashing for 2 minutes at 120 W with a G1000 CE VLF machine by *Yield Engineering Systems Inc.* During this operation, the wafer is put on a metallic tray in a vacuum chamber. The ambient air is evacuated, and the chamber is filled with oxygen gas. High power radio waves at 40 kHz ionise the gas into reactive species and emit near-UV radiation [107], effectively removing any organic compounds left at the surface. This method has significant benefits compared to wet chemistry processes, which are mostly used for contaminant layers above 10 µm thick. Plasma cleaning is easy, safe and inexpensive. In addition, it does not produce chemical waste [108].

These steps ensure that the surface is free from any organic residue and dust particles that would jeopardise the rest of the manufacturing process. Furthermore, oxygen plasma treatment increases the wettability of the surface by introducing hydroxyl groups [109,110], which is important in the coating of the electrosensitive resist involved in the next step of the fabrication.

## Spin coating

The spin coating process is routinely employed in lithography to spread a thin film of photosensitive (or electrosensitive) resist uniformly at the surface of wafers. During the spin coating process, the wafer is held by a vacuum chuck, and the resist is spread uniformly at the surface thanks to the centrifugal force (see **Figure 3.2**). The spin coater used in this step of the manufacturing process is a PWM 32 model by Headway. To avoid flairs, waves, or other defects on the resist layer, it is important to spin coat on a clean and flat surface, obtained with the protocol discussed previously.

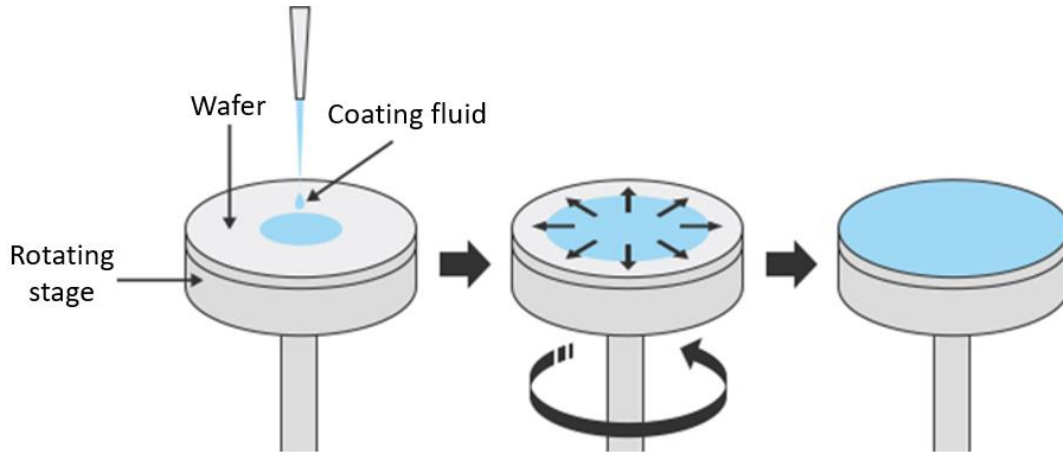


**Figure 3.2** Description of the spin coating process, where the wafer is securely mounted on a vacuum chuck and the resist is deposited before initiating the rotation.

Resists are liquid solutions of molecules that will chemically react upon interaction with photon or electron radiation, which will result in a change of solubility to a solvent known as a developer. The E-beam process is used to locally expose negative or positive resist to an electron beam in a desired pattern. With positive E-beam resist, the area exposed to high-energy electrons becomes more soluble by breaking molecular chains. The exposed zones are thereafter dissolved, and washed away, in a developer bath (resist solvent). For the negative E-beam resist, it is the opposite, the exposed resist is 'cured', causing cross-linking of the molecular chains, making the resist less soluble in the developer solution [111]. This patterned resist will later act as a mask for the deposition of metal to form the arrays of plasmonic nanostructures.

The resist used for all the samples made by EBL throughout this thesis was chosen to be poly-methyl methacrylate (PMMA), a high-resolution positive resist. This molecule is a long polymer chain that can be between 10 kDa and 1000 kDa [112], with a maximum resolution of around 5 nm [113]. The exposure to an electron beam will result in a de-crosslinking of the PMMA polymer chains, locally increasing the solubility of the resist layer in the developer solution.

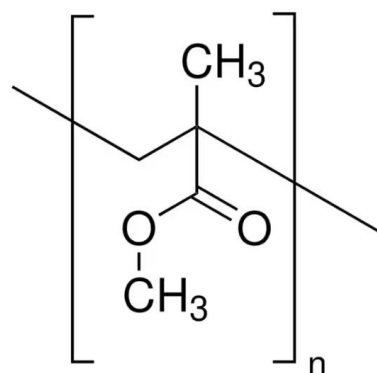


**Figure 3.3:** Poly-methyl methacrylate (PMMA) resist monomer.

Gold plasmonic nanostructures can be manufactured using a bi-layer lift-off technique, which has several advantages over the use of a single layer, amongst which a better resolution and improved edge definition. During this process, two consecutive layers of chemically different products must be spin coated. A first layer of 632.12 50K PMMA in anisole solvent is coated onto the silicon substrate and is then covered by an upper layer of 649.04 200K PMMA in ethyl lactate. The reason for the use of two different solvents is because the second layer would otherwise dissolve the first one upon contact. There are many important parameters involved in spin coating. The acceleration, the maximum speed, and the time of spinning are all very important parameters to determine the thickness of the final layer. Usually, these parameters are given by the resist manufacturer, but it is useful to test and verify the thickness of the coated layer. This can be done in the JWNC using a height profiler tool, such as a Bruker Dektak XT Stylus Profiler, or an ellipsometer M-2000XI machine.

Immediately after spin coating the resist, it is essential to do a 'softbake' in an oven or on a hotplate. This step will allow the solvent in the resist to evaporate, hardening the layer and leaving the surface non-sticky. It is also a necessary step to enable chemical reactions inside the resist layer once exposed to a photon or electron beam [114]. This step will also influence the thickness of the resist layer and needs to be included in the metrological examination of the thickness of the film. The temperature and the duration of the bake are both very important parameters for this step. For the first layer, a bake of 5 minutes at 180 °C was conducted, and 10 minutes for the second one at the same temperature.

## Computer-aided design (CAD) Mask design

Several pieces of software have been required in order to design and submit the pattern to the E-beam equipment. The first one is *L-edit*. It is used to design the pattern of nanostructures and replicate it to form an array. The design presented in **Figure 3.4** is a chiral shuriken shape of 1  $\mu\text{m}$  arm-to-arm dimension. Multiple nanostructure arrays of different designs have been made with various sizes and pitches during this project. The typical array size was set to 500  $\mu\text{m}$ , which corresponds approximately to the field of view of most optical measurements performed in this work.

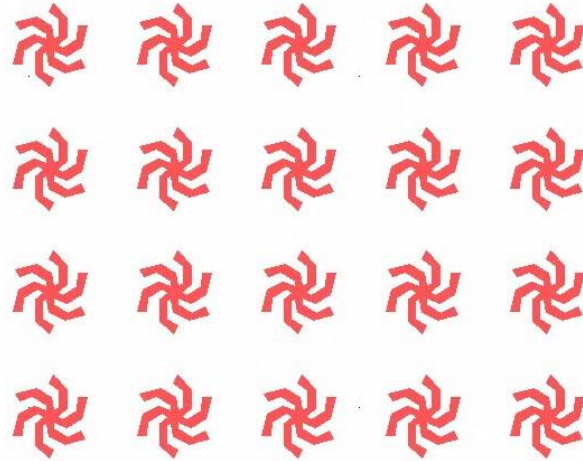


**Figure 3.4:** CAD mask of a shuriken array designed on *L-edit*.

After *L-edit*, it is necessary to use *Beamer* to fracture the patterns and remove the overlaps in the design. It was also used to set the step and resolution size (both  $0.01 \mu\text{m}$ ). Then the *.gpf* file is transferred to the Patterns folder. The next software in the process flow is *Cjob*. It is being used to set the position of the pattern on the wafer as well as the EBL parameters, like the electron exposure dose and the beam current. Prior to exposing the sample containing various sizes of the nanostructure patterns, it is important to do a dose and beam current test. By varying the dose and beam current on the smallest and biggest structures, it is possible to choose the best combination to use for the sample exposure. A visual examination using SEM allows to choose the best parameters. Finally, it is important to check and minimise the exposure time. After this step, it is necessary to send the *Cjob* file to the JWNC server. The *Belle* portal is used for this purpose. The final step includes submitting the job on the JWNC portal, along with a representation of the clamped sample for the operator.

## Electron beam lithography

The samples are made on a crystalline silicon wafer, which is a semiconductor, allowing the electrons to dissipate during the EBL process. This is important to avoid charging the insulator PMMA resist, which would distort the pattern's shape [115].

EBL is a maskless process that utilises a focused beam of electrons instead of photons used in classic lithography techniques. The electrons are generally coming from a thermal field emission source and have a very small wavelength ( $0.01 \text{ nm}$ ), enabling this process to achieve an ultra-high special resolution (under  $10 \text{ nm}$ ) [111,116]. EBL uses several electromagnetic lenses to focus the beam onto the coated resist, and to move it following the CAD mask pattern submitted in the previous section. The E-beam tool used in this work was an EBP 5200 model by Raith. (see **Figure 3.5**).

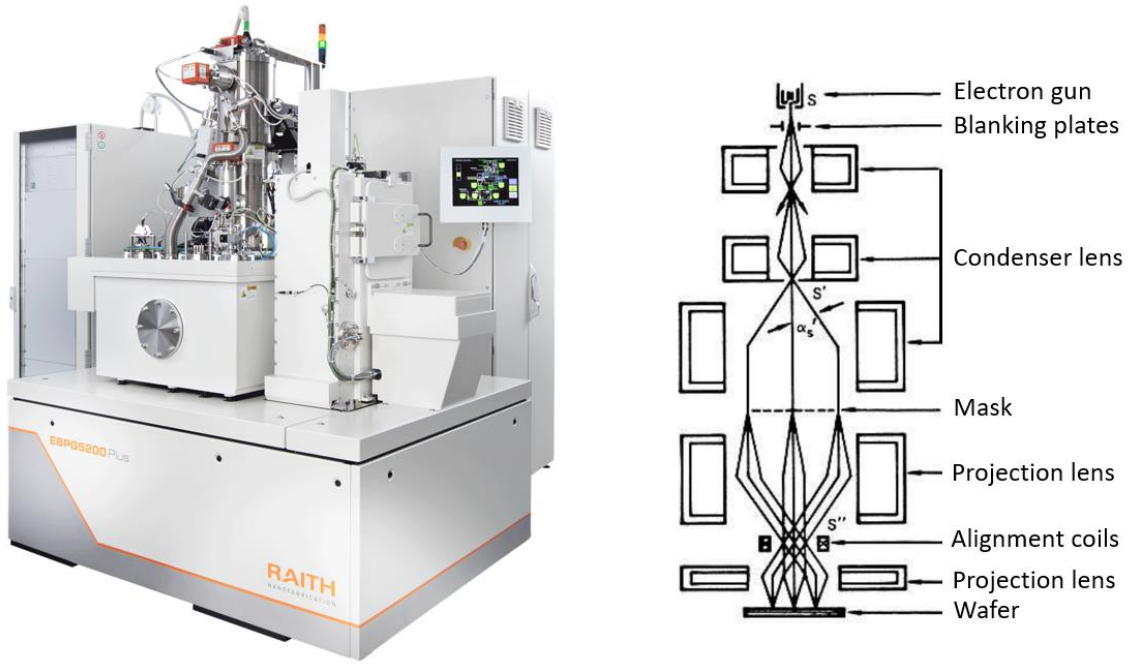


**Figure 3.5** Photo of the EBL machine on the left and cross view of the components on the right (adapted from [117]).

When the electron beam irradiates the positive PMMA resist, the polymer chains will be broken into smaller molecular fragments, of which the size will depend on the dose of the beam [118,119]. The average molecular weight of these fragments ( $M_f$ ) is given by [120]:

$$M_f = \frac{M_n}{1 + \eta}. \quad (3.1)$$

With  $M_n$ , the average molecular weight before interaction with the electron beam and  $\eta = g\varepsilon M_n / \rho N_A$  the average number of chain splitting events per molecule,  $g$  is the number of chain scissions per unit of energy dissipated per unit of volume,  $\varepsilon$  is the absorbed energy density, which is proportional to the dose,  $\rho$  is the resist density and  $N_A$  is the Avogadro's number. This leads to a simplified expression:

$$M_f = \frac{\rho N_A}{g\varepsilon}. \quad (3.2)$$

One can note that this formula does not depend on the initial molecular weight of the initial resist ( $M_n$ ), therefore, the solubility, and performance of different molecular weights of PMMA resists will be similar. When  $\varepsilon$  increases (dose increases), the size of the chains irradiated will tend to decrease, making it more soluble in the developer solution.

The E-beam exposition process can be long, depending on the area being exposed, as such, it is generally expensive. But the high resolution and absence of a physical mask

make this technique suitable for the research and prototyping of small plasmonic nanostructures presented in this PhD thesis.

## Development

Once exposed by the E-beam tool, the PMMA resist has become highly soluble in a developer solution of methyl isobutyl ketone (MIBK). This developer was used for all the nanofabricated samples diluted in IPA. The ratio of dilution of the developer in IPA is important since it determines the rate at which the solvent penetrates the resist as well as the dissolution of the polymer, which is controlled by the molecular weight of the solvent (kinetically) [121]. As seen in **Figure 3.6**, for an equal dose, the exposed PMMA resist was removed at different rates depending on the dilution of the developer. This is because MIBK dissolves PMMA very strongly, and mixing it with IPA has a weakening effect on the development process [122,123]. Consequently, the 3:1 (IPA:MIBK) dilution requires more dose or more development time to give the same result as 2:1, but has the advantage of showing a greater contrast with more defined patterns.

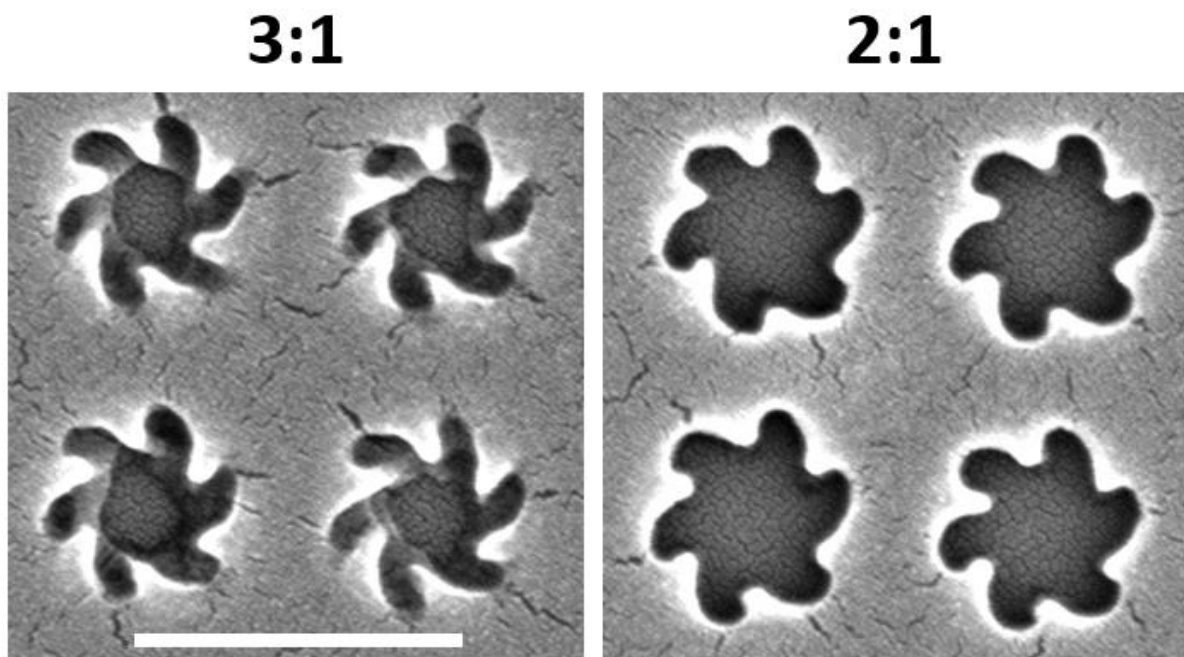


**Figure 3.6** SEM images comparing the pattern obtained after developing 250 nm large shuriken arrays with different dilutions of IPA:MIBK developer submerged for 1 min (exposed with a 2 nA beam at 400  $\mu\text{C}/\text{cm}^2$ ). The scale bar is 400 nm large.

The temperature of the solution is also a critical factor in obtaining the right development rate, with a cooler solution slowing down the development rate [120]. According to the data collected by the JWNC, a change of 0.1  $^{\circ}\text{C}$  in the developer solution

causes a 4% shift in the dose. This impacts greatly the reproducibility of the nanofabrication; therefore, the process window for the dose must be chosen by accounting for about a 10% variation. With all these variables, dose tests and development tests are necessary to choose the correct parameters.

The protocol for the development that was found to give the best results was by using the 3:1 solution for one minute at 23.2 °C, then plunging the wafer for 5 s in IPA to finish by a N<sub>2</sub> drying. An O<sub>2</sub> plasma descum of 80 W for 10 s is then conducted to remove the resist that may still be present on the Si surface and make sure that the silicon surface is clean and dry.

## Metallisation and bi-layer lift off

The bi-layer technique involves using two different resists spin coated successively. The bottom one is not reactive to the electron beam and is soluble in the developer solution, while the surface layer is an electrosensitive resist. This top layer can be patterned with high precision by the EBL process. The bottom layer is undercut by slightly increasing the development time. The developer will isotropically dissolve the underlayer, making the edge profile suitable for metallisation.

Once the silicon wafer is exposed to air, where the resist was removed, the metal can now be deposited to form plasmonic nanostructures. An adhesion layer of Ti alloy of 5 nm is first deposited by a metal evaporator (Plassys instrument), then a 95 nm layer thick of gold can be added by the same tool [124]. Finally, both resist layers can be removed by dissolving the bottom layer in a 50°C acetone bath for a minimum of 2 hours (see **Figure 3.7**) [125]. The final sample is then rinsed in a sonic bath of IPA, and plasma cleaned at 100 W for 1 minute.

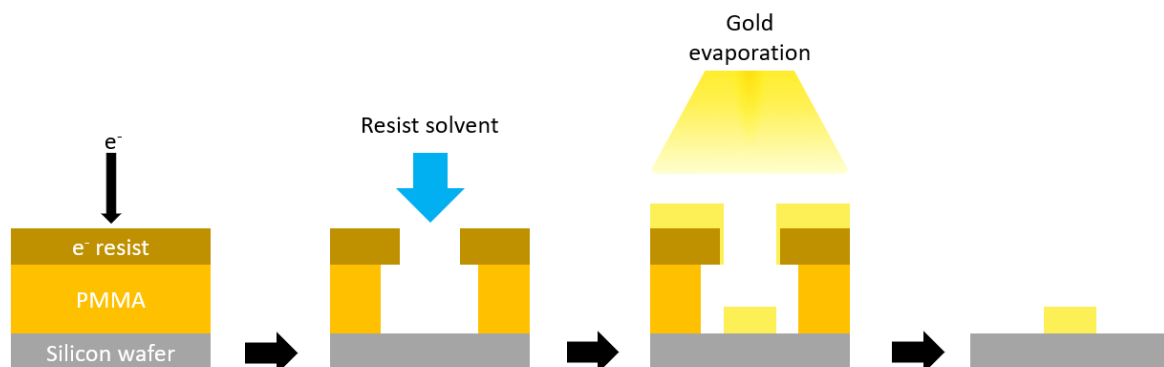


**Figure 3.7:** Summary of the bi-layer lift-off EBL process, where the wafer is coated with two chemically different resists before EBL exposure and subsequent development step, leaving the wafer exposed to air for metal evaporation.

## Protocol summary: bi-layer lift off process

The process flow used for E-beam nanofabrication is summarised as follows:

- **Wafer cleaning:** 5 min sonic bath in acetone, methanol and IPA, N<sub>2</sub> drying.
- **O<sub>2</sub> Plasma ash:** 100 W for 2 min.
- **Spin coating:** 1<sup>st</sup> layer of 632.12 50K PMMA at 4000 rpm for 1 min followed by a 5 min bake at 180 °C. 2<sup>st</sup> layer of 649.04 200k PMMA is coated with the same parameters as the first one, and baked for 10 min at 180 °C.
- **EBL:** 8 nA beam (spot size of 12 nm and beam step size of 10 nm) with a dose of 900  $\mu\text{C}/\text{cm}^2$ .
- **Resist development:** 1 min in a bath of MIBK 3:1 at 23.2 °C followed by 5 s in pure IPA and finishing by N<sub>2</sub> drying.
- **O<sub>2</sub> Plasma descum:** 80 W for 10 s.
- **Metallisation:** 5 nm Ti adhesion layer then 95 nm Au layer.
- **Lift-off:** leave for 2 h in 50 °C acetone, remove the metal film with a pipette. Rinsed with IPA and dried with N<sub>2</sub> gas.

## Fabrication protocol optimisation

The protocol presented so far is adapted for small structures that require high spatial resolution. It was used for the manufacturing of nanorods, which are separated by 150 nm from each other. But it is not optimised for larger structures such as the 1000 nm shuriken arrays, which have a pitch of 1500 nm. In an attempt to reduce the time of fabrication, especially the E-beam exposure step, new protocol parameters were tested.

The electron beam current employed to expose the larger structures was set at 64 nA, giving a theoretical size of 40 nm and necessitating a beam step size set at 25 nm. A single layer of 649.04 200k PMMA was coated on a clean wafer at 4000 rpm for 60 s, and baked at 180 °C for 10 min. The wafer is then ready to be submitted for the EBL job. Using a single layer resist over a bi-layer reduces the risk of spin coating defects, and does not impact the quantity of large scale structures (>1000 nm).

A dose test is required to find the right dose for this new protocol. The large shuriken arrays have been exposed to doses ranging from 300 to 500  $\mu\text{C}/\text{cm}^2$  with a 50 increment. The wafer was then developed with a 2:1 MIBK solution and then coated with a 6 nm layer of gold using a sputter coater instrument. This metallic layer allows us to observe the negative structures in the PMMA using an SEM, avoiding charging effects that cause distortion of the image. At a dose of 400  $\mu\text{C}/\text{cm}^2$ , the PMMA is still present at the bottom of the pit, whereas for a dose slightly higher of 450, the silicon wafer is completely exposed (see **Figure 3.8**). The best dose was chosen to be 500  $\mu\text{C}/\text{cm}^2$ . Using a bigger



beam to expose an array of large shuriken reduces the time of exposure significantly, going from a time of 7 minutes 25 s to expose one million shuriken structures with the 8 na beam, to 2 minutes 26 s for the 64 na beam, a 67% time reduction.

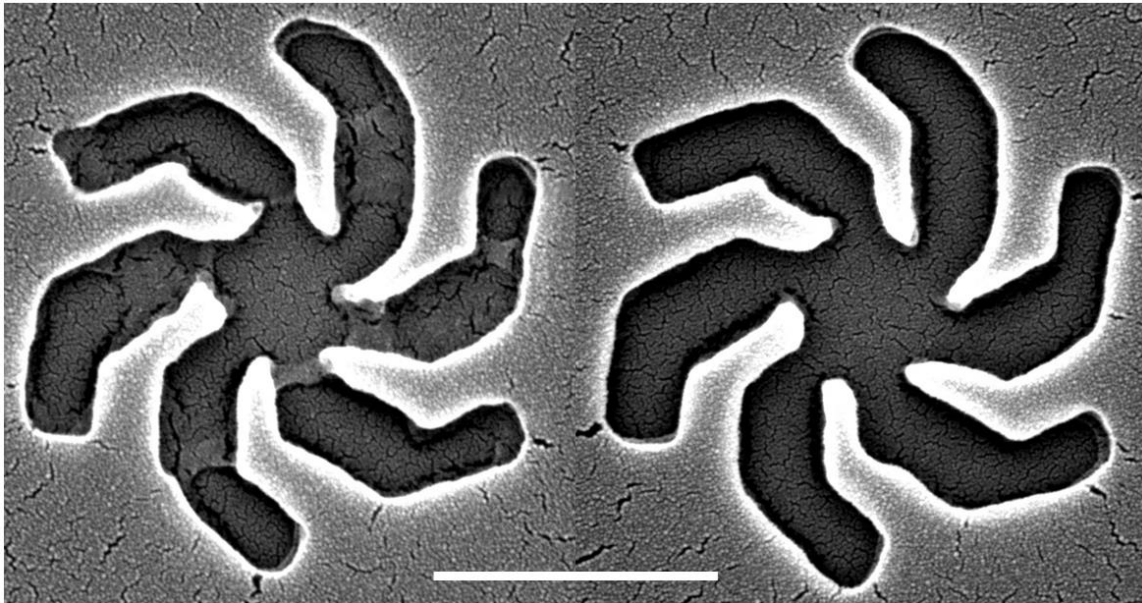


**Figure 3.8:** SEM images of 1000 nm large LH shuriken exposed with the 64 na beam and a different dose of  $400 \mu\text{C}/\text{cm}^2$  for the left structure and 450 for the right one. The scale bar represents 500 nm.

### 3.1.2 Shuriken metafilm fabrication

Another type of sample manufactured during this PhD work was a shuriken metafilm. This sample is made of arrays of opposite handedness shuriken shapes, indented on a polycarbonate substrate and coated with a 100 nm thick gold film (see **Figure 3.9**). The indented polycarbonate template is made by injection moulding and is referred to as a template plasmonic substrate (TPS). This technique allows a high fabrication throughput for a low cost by reusing a master pattern called a shim. This shim can be used to make thousands of polycarbonate substrates before it needs to be replaced.

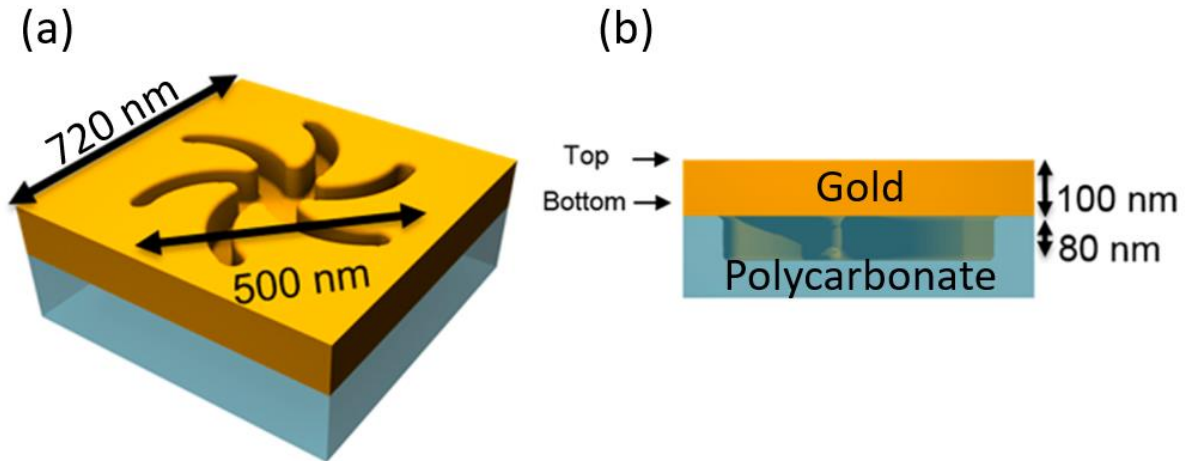


**Figure 3.9:** Shuriken plasmonic template, with (a) orthogonal view of the 500 nm large shuriken and (b) the side view showing the indented polycarbonate substrate with a 100 nm of gold film evaporated on top [126].

## Shim fabrication process

The shim master shape used for the moulding of the TPS polycarbonate substrate is made by EBL, which is one of the few techniques that can reach the desired resolution of the structures. The mask for the shim was designed using the same method as described previously in Section 3.1.1, with an adapted protocol. In a first step, a monolayer of PMMA is spin coated on a silicon wafer. The thickness of this layer is important since it will determine the depth of the structures in the TPS. To obtain a depth of 100 nm, a PMMA layer of 120 nm thick is needed to account for a 20 nm loss in the following part of the fabrication process. A monolayer of 649.04 200k PMMA was coated on a clean wafer at 5000 rpm for 60 s. The wafer is then baked in a 180°C oven for 10 minutes to evaporate the solvent in the resist, thus hardening the monolayer layer. The thickness of this layer has been measured to be 124.7 nm using a Bruker Dektak XT Stylus Profiler on the surface scratched beforehand.

A dose test and development test were conducted on two separate wafers, one was developed using a 2:1 IPA:MIBK solution, and the other was developed with a 3:1 ratio. Several shuriken diameters were tested, starting from 200 nm to 550 nm with a 50 nm increment. Doses ranging from 200 to 1000  $\mu\text{C}/\text{cm}^2$  were tested, with a step of 100. The 2 nA and 4 nA beams were tested on the smallest shuriken structures (from 200 to 350 nm) and the 8 nA and 16 nA beams were tested on the larger ones. This protocol could not resolve the arms of the smallest size (200 nm) regardless of the dose, developer concentration, or beam current (see Figure 3.10). The 250 nm large structure was the smallest structure that could resolve arms and therefore achieve a chiral shape (see Figure 3.6). The beam current did not significantly impact the quality of the structures, while the developer concentration of 3:1 gave slightly sharper structures but

necessitated a dose  $100 \mu\text{C}/\text{cm}^2$  higher than the 2:1. The minimal dose was  $400 \mu\text{C}/\text{cm}^2$  for the 3:1 developer solution. Below this value, the PMMA resist was still present on the silicon wafer.

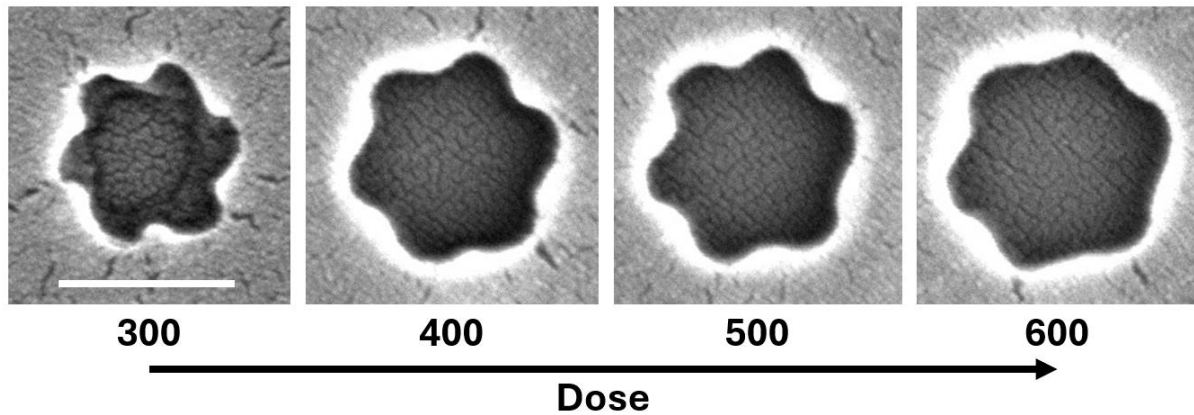


**Figure 3.10: Effect of the electron beam dose on the 200 nm LH shuriken shape with a 2 nA beam developed in a 2:1 solution of MIBK.**

Shuriken with various sizes of achiral and both chiral handedness shapes were designed in square arrays of  $400 \mu\text{m}$  dimensions with five variations of the pitch. The different diameters of the shuriken structures were set to 400, 450, 500, 550, 1000, 1500 and 2000 nm, with one dimension per row. The period of the shuriken array was set to fit a ratio between the diameter and the pitch equal to 0.72. Four other values of the pitch were selected, two were set to 20 and 40 nm larger and the other two were smaller by the same amount (see **Figure 3.11**). This variety of dimensions allows for a lot of different plasmonic responses in a wide wavelength range to be studied on the same sample template.

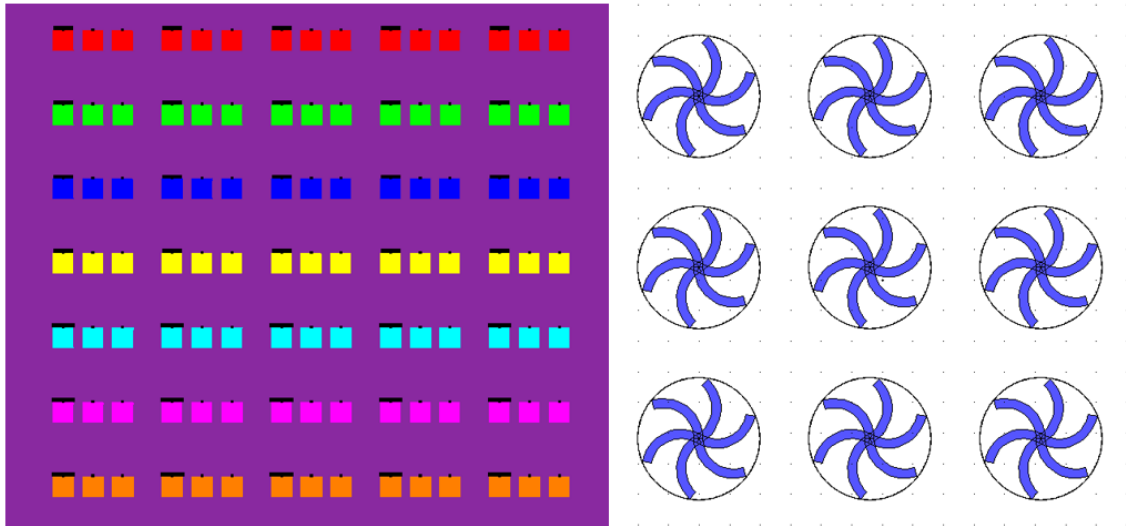


**Figure 3.11: CAD file of the E-beam job submitted for the exposure of the Shim wafer, with on the left side, an overview of a full set of shuriken arrays and on the right, a zoomed-in image of an LH 500 nm large shuriken array with a pitch equal to 360 nm.**

The nanostructure shapes are then written by the E-beam machine with a dose of  $600 \mu\text{C}/\text{cm}^2$  using an 8 nA beam for shuriken shapes below 1000 nm, and 64 nA for the larger ones. Three iterations of the entire set of structures were exposed on the same 4" wafer, for a total E-beam job of about 8 hours. The patterns in the resist were developed in the 3:1 IPA and MIBK solution for 1 minute, then quickly rinsed in IPA for 5 seconds and dried with  $\text{N}_2$ .

A 1 mm nickel layer was then electroplated on the wafer to transfer the patterns. This step was conducted by *Temicon*, a professional company. Acetone is used to dissolve the monolayer and release the nickel shim. Nickel is an ideal choice for injection moulding thanks to its large thermal conductivity, which allows it to cool down the polymer, but also its low surface roughness, which enables the nanostructure indentations to be well defined in the substrate.

## Polycarbonate injection moulding

The shim manufactured can now be used in an injection moulding machine; in our case, the Engel Victory 28 hydraulic moulder was used (see **Figure 3.12**). Polycarbonate granules are heated above the glass transition temperature at  $280 \text{ }^\circ\text{C}$  and then pressed into the shim mould by a screw system through the nozzle [127]. The mould cavity is kept at  $140 \text{ }^\circ\text{C}$  to ensure the liquid polymer stays in its vitreous state. Once the process is complete, the chamber opens, and the piece is left to cool at room temperature before

being removed from the shim. This process can be iterated hundreds of times during a single day, producing a large quantity of templates at a very inexpensive production cost.

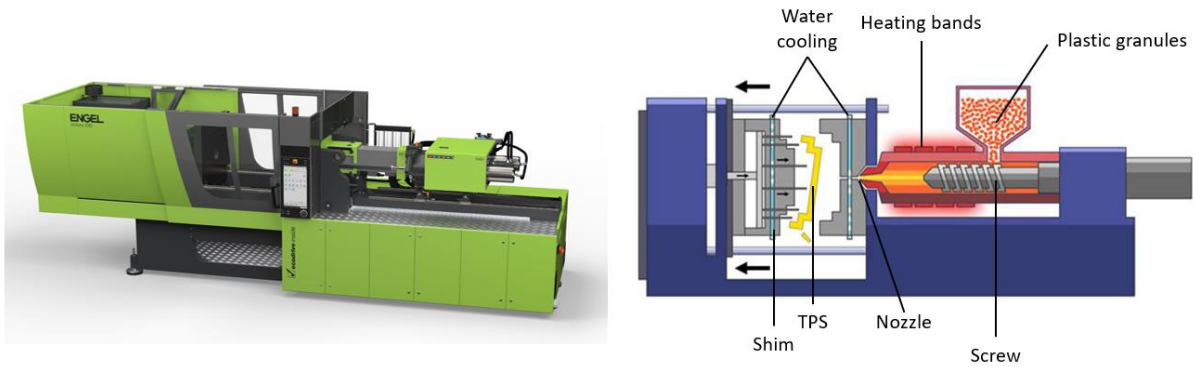


**Figure 3.12: Engel Victory injection moulding machine on the left, and a schematic of the main components on the right (images from the manufacturer's website).**

## Gold metafilm deposition

The polycarbonate TPSs can now be cleaned with methanol and IPA and coated with the desired metal thin film in order to generate plasmonic effects and be studied. In this thesis, a 100 nm gold layer was deposited by the E-beam evaporator MEB550S machine from Plassys.

## Protocol summary: shim and shuriken metafilm fabrication

The process flow used for master Shim, and subsequently the shuriken metafilm is summarised as follows:

### **Shim fabrication:**

- **Wafer cleaning:** 5 min sonic bath in acetone, methanol and IPA, N<sub>2</sub> gun drying.
- **O<sub>2</sub> Plasma ash:** 100 W for 2 min.
- **Spin coating:** 649.04 200k PMMA at 5000 rpm for 1 min followed by a 10 min bake at 180 °C.
- **EBL:** Use of an 8 nA beam (spot size of 12 nm and beam step size of 10 nm) for the smallest structures, and 16 na beam (same parameters as for the 8 na) for shuriken arrays 1000 nm and above, with a constant dose of 600 μC/cm<sup>2</sup>.
- **Resist development:** 1 min in a bath of MIBK 3:1 at 23.2 °C followed by 5 s in pure IPA and finishing by N<sub>2</sub> drying.
- **O<sub>2</sub> Plasma descum:** 80 W for 10 s.
- **Electroplating:** 1 mm nickel layer added on top of the patterned wafer.
- **Lift-off:** Acetone bath to remove the resist and detached the Shim.

### **Metafilm fabrication:**

- **TPS cleaning:** 5 min sonic bath in methanol and IPA, N<sub>2</sub> gun drying.
- **Metal evaporation:** E-beam evaporation of a 100 nm gold layer at a rate of 0.3 nm/s ± 0.02 nm/s.
- **Final cleaning:** IPA wash, N<sub>2</sub> gun drying and O<sub>2</sub> plasma ash of 80 s for 1 min.

## 3.2 Characterisation methods

To verify the quality of the nanofabrication process or analyse samples, it is essential to observe the structures at the nanoscale. A variety of metrological instruments are available at the JWNC to fulfil this goal. The main types of microscopic machines are atomic force microscopy (AFM), which is relevant to determine the height of the structures and assess the quality of the metal evaporation step, and scanning electron microscopy (SEM), which is required to visualise the lateral dimensions of the nanostructures and determine if they match the CAD model exposed by EBL.

### 3.2.1 Atomic force microscopy

AFM is a scanning probe microscopy technique; it uses a sharp tip attached to a cantilever to record the position between the sample and the probe in a raster pattern (see **Figure 3.13**). When the cantilever is brought close to the substrate, the coulombic (short range) and van der Waals (long range) forces will respectively repel and attract the tip (see **Figure 3.14**). By monitoring the movement of the probe using a laser beam reflected off the cantilever and recorded by a photodetector, a 3D map of the surface is generated.

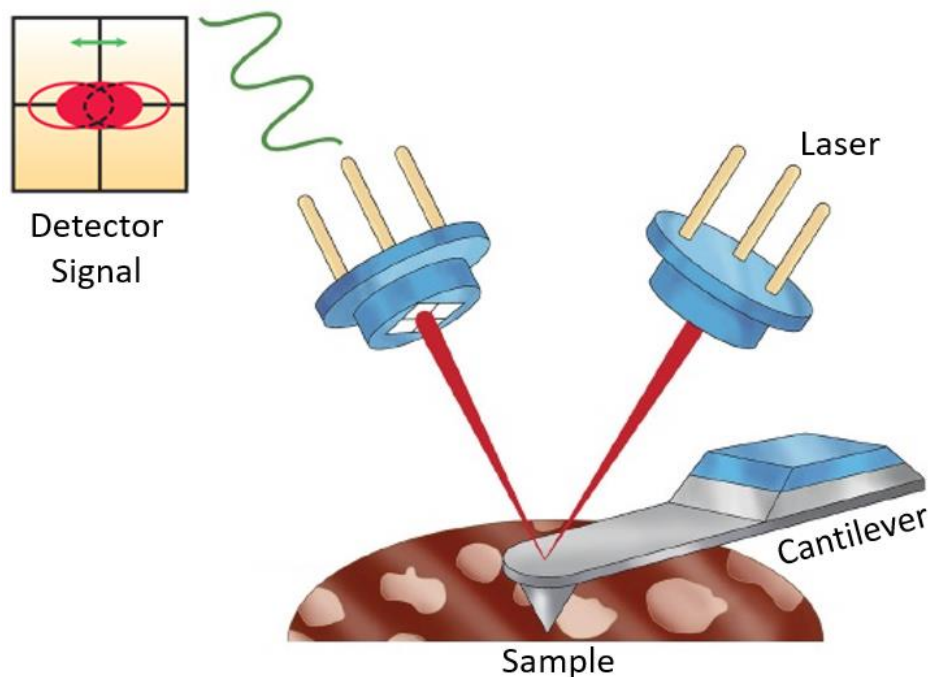


**Figure 3.13: Working principle of an atomic force microscope, using as laser to monitor the position of the cantilever probing the surface of the sample with the AFM tip (adapted from Bruker's documentation).**

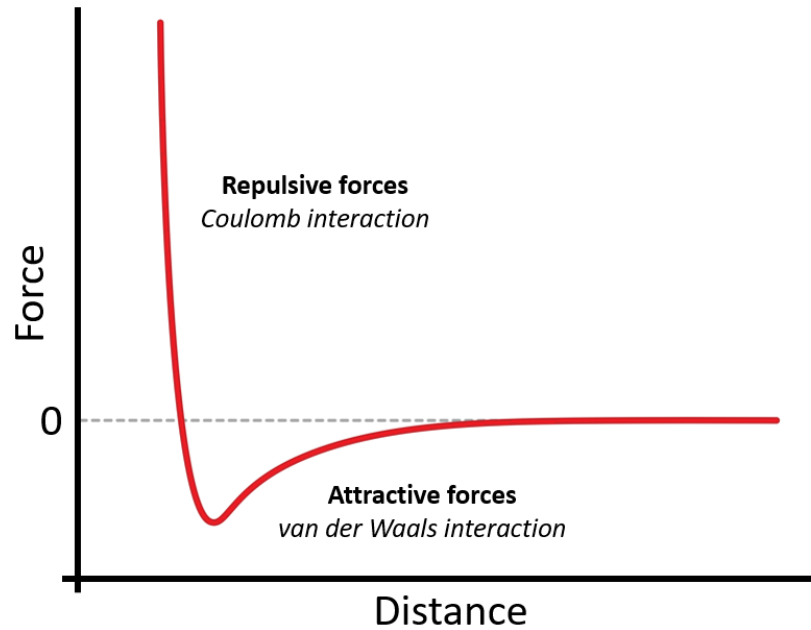


**Figure 3.14:** Force between the probe and the surface of the sample as a function of the distance (reproduced from [128]).

The vertical resolution of this technique is limited by the thermal noise on the deflection detection system. Commercial AFM machines can achieve vertical sensitivity as low as 0.01 nm. This sub-Ångström vertical resolution gives AFM an advantage over every other surface analysis technique [129].

The lateral resolution of AFM is strongly related to the tip dimensions and is defined in the context of optical microscopy as the minimum distance detectable between two sharp peaks of different heights. This distance ( $d$ ) is related to the radius of curvature of the tip ( $R$ ) and the vertical resolution ( $\Delta z$ ). If the relative height ( $\Delta h$ ) between the two objects is small:

$$d = \sqrt{2R}(\sqrt{\Delta z} + \sqrt{\Delta z + \Delta h}) . \quad (3.3)$$

In the case of a sharp tip, AFM can reach subnanometer resolution [129]. With tall nanostructures ( $\sim 100$  nm), the surface features will appear larger because the resolution is limited by the finite sharpness of the tip. This is referred to as the convolution effect, and it manifests as a positive slope on the vertical side walls of the nanostructures [130].

The AFM technique is used in a variety of modes that will suit different kinds of samples. In static mode, the probe and the sample are kept at the same distance; hence, the force will also be unchanged. This mode is not adapted to biological samples, which are too soft to withstand the lateral force exerted by the probe. Instead, a contactless mode will be more adaptable. With this technique, the cantilever will oscillate vertically near its resonance frequency while the tip approaches the sample in the attractive interaction regime [128].



Our samples are made of silicon and metal, which are hard enough for the contact mode to be suitable. This mode was used to obtain information about the thickness of the gold layer deposited on all the samples as well as create 3D models for simulation purposes. **Figure 3.15** shows an example of AFM data obtained on an array of gold nanorods in the *ProfilMOnline* software (<https://www.profilmonline.com/>). The height of the structures can be accessed through a vertical slice operation, and the 3D model can be exported to an *.stl* file to design a model in the *COMSOL* software.

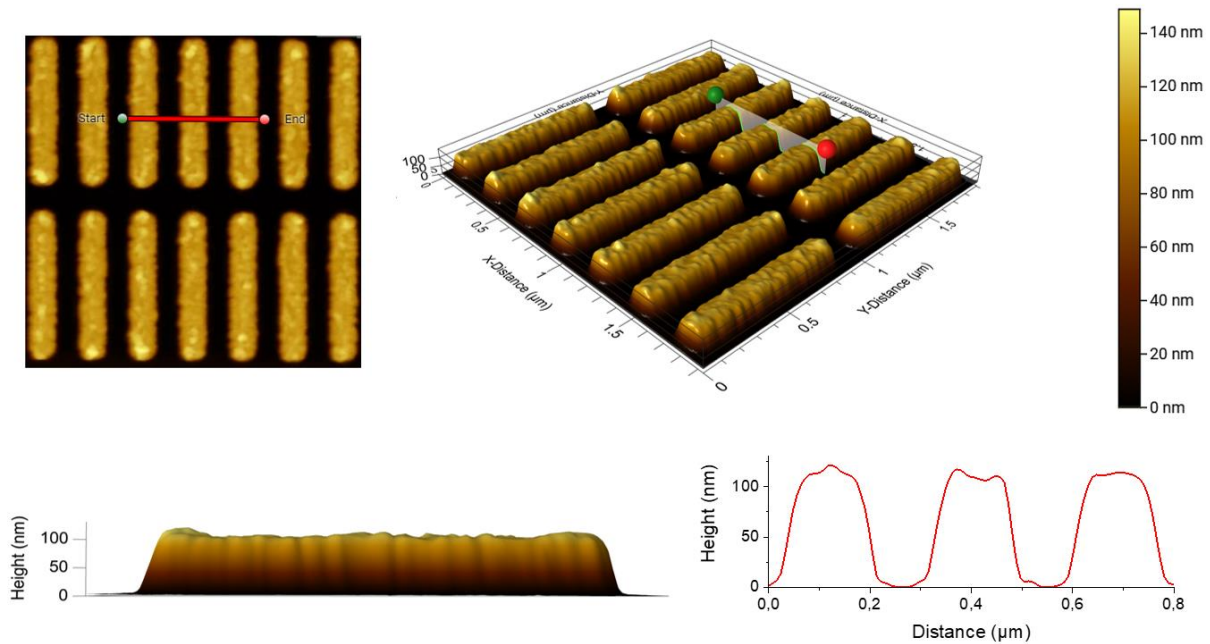


**Figure 3.15: Atomic force microscopy images of an array of gold nanorods made by EBL on a silicon substrate. A vertical cut profile has been added to the 3D maps (top panels) to measure the height of the rods (bottom right plot).**

The AFM instrument used in this work is a Dimension Icon made by Bruker, available in the JWNC cleanroom.

### 3.2.2 Scanning electron microscopy

Observing structures manufactured at the nanoscale requires a technique with a far better resolution than conventional optical microscopy, this last one being limited by diffraction of the wavelength of the light in the visible range (limit of resolution of  $\sim 2,000$  Å) [131]. In contrast, SEM uses an electron beam with a much smaller wavelength. The De Broglie wavelength is used to define the wavelength of objects in quantum mechanics, it follows this equation [132]:

$$\lambda = h/\sqrt{2meV} . \tag{3.4}$$

Where the wavelength of the particles is  $\lambda$ ,  $h$  is the Planck's constant,  $m$  is the mass and  $e$  is the charge of an electron. Here,  $V$  is the acceleration voltage applied to the electron gun. This gives a wavelength value of  $0.172 \text{ \AA}$  for an electron beam accelerated by a 5 kV voltage. SEM is therefore capable of reaching a theoretical maximum resolution of 0.5 nm and a maximum magnification of  $\times 500\,000$  [133].

An SEM is operated in an ultra-high vacuum chamber where the electrons are focused on the sample using several electrostatic lenses (see **Figure 3.16**). The electron beam is generated by the thermionic emission of a source, generally a tungsten filament cathode (heated at about 2800 K). The SEM equipment employed all throughout this PhD was a Hitachi model SU8240. This setup uses a cold field emission electron source, which offers a far better resolution than its counterparts ( $\sim 0.8 \text{ nm}$ ) and has a better signal-to-noise ratio. This beam is focused using electrostatic lenses made of current-carrying coils, which focus the beam on the sample, thus determining the final resolution of the image.

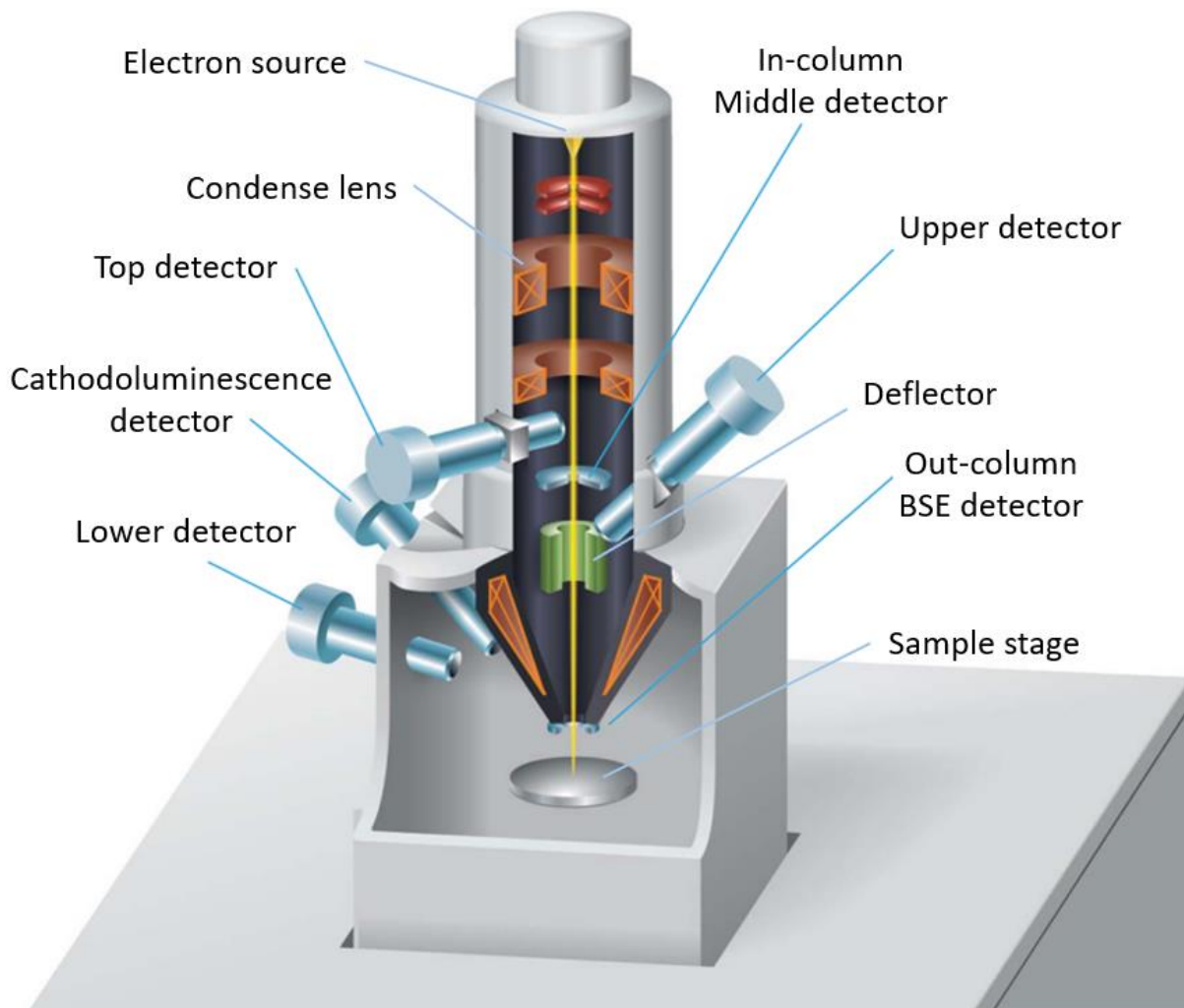


**Figure 3.16: Scanning electron microscope schematic with the electron beam (yellow) generated from the source, focused on the sample using electrostatic lenses (adapted from Hitachi's documentation).**

The electron beam will interact with the electrons of the atoms at the surface of the sample, resulting in the production of secondary electrons (SE) and backscattered electrons (BSE). SE are generated by inelastic collisions between the incoming beam and the electrons of the sample. Their energies are lower than 50 eV, thus only the electrons close to the surface will manage to “escape” the sample to be detected (mean free path length around 10 Å). Thanks to this property, SE is used to generate high resolution topographic images. Regarding the BSE, they are electrons of the focused beam that are scattered elastically by the atoms of the surface. They experience minimal loss and can thus originate from a greater depth (10 to 100 nm) and be differentiated from SE. These BSE are employed to visualize the sample surface composition thanks to the property that heavier elements deflect more electrons, resulting in a higher amount of BSE [133].

A variety of other signals can be detected, such as characteristic X-rays, which are generated when vacancies left by SE are filled by outer shell electrons, producing photons of energy specific to the atomic element. Other sources of topological information include Auger electrons, generated after the recombination of the vacancy left by SE, and cathodoluminescence, obtained after the recombination of an electron hole pair, releasing a photon in the visible range of light. These different signals are detected by specific detectors, adapted to the nature of each one. Their respective depths with respect to the surface are depicted in **Figure 3.17**.

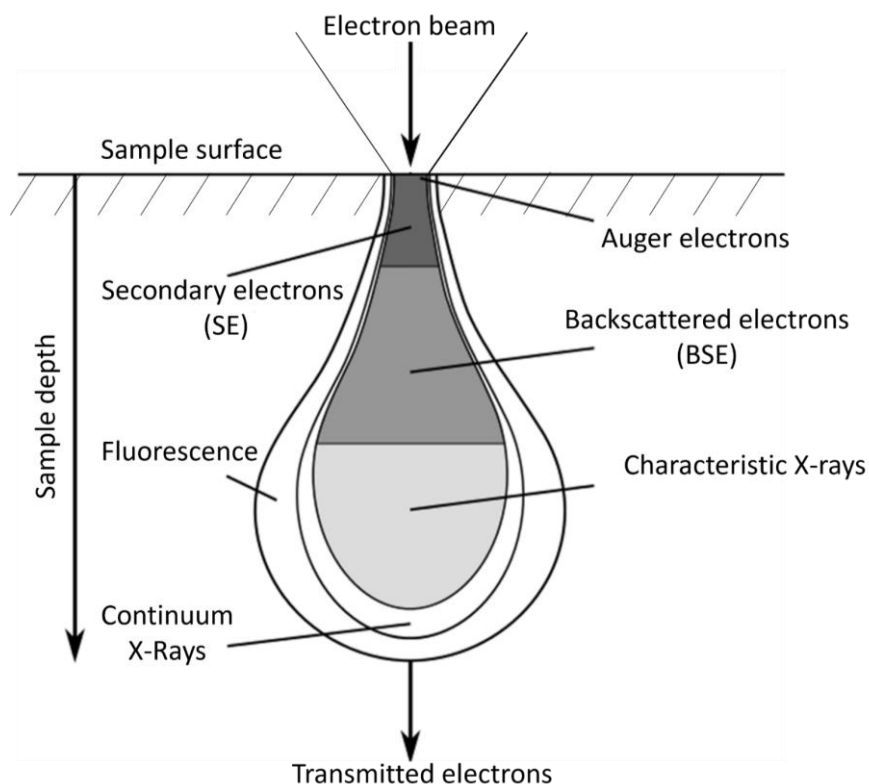


**Figure 3.17: Electron beam characteristic depth profile in the sample, where the SE are more sensitive to the surface compared to the BSE and other photon signals (adapted from [134]).**

### 3.2.3 Ellipsometry

Ellipsometry is a technique that is used to characterise the thickness of thin films and their optical properties. The fundamental principle behind spectroscopic ellipsometry is that an incident light of known polarisation will undergo changes after interacting with a sample. These changes are measured, and the properties of the thin film can be derived. The ellipsometer machine used for all the measurements in this PhD was a M-2000XI by J.A. Woollam.

A monochromatic or broadband source will emit a light beam that will pass through a linear polariser, the electric field vector will subsequently have components both parallel (p) and perpendicular (s) to the incident plane. This incident beam will be directed at the surface of the sample at a known inclination angle that can be varied. When the light interacts with the material of the thin film, the polarisation state will be changed, and the beam will become elliptically polarised. The reflected light will pass through another polariser called an analyser, and the beam will then reach a detector (see **Figure 3.18 (a)**) [135].

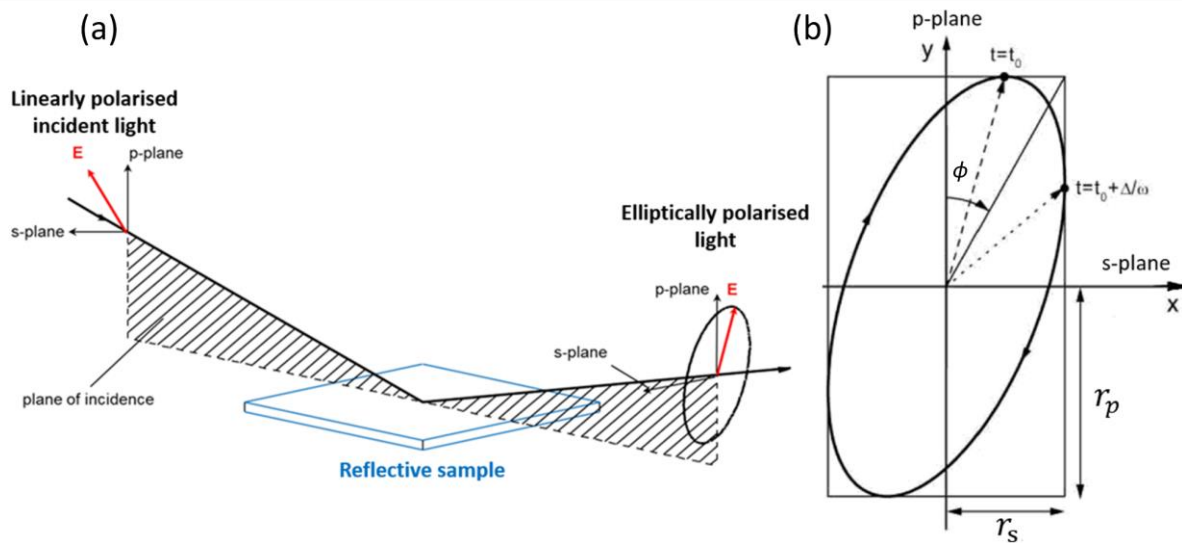


**Figure 3.18:** (a) Working principle of ellipsometry, illustrating the change in polarisation of an incident light reflected from the surface of the sample and (b) schematic of the resulting elliptical polarization, showing the angles  $\phi$  and  $\Delta$  (adapted from [136]).

The polarisation changes of the light are measured in terms of amplitude ratio ( $\phi$ ) and phase difference ( $\Delta$ ). The amplitude of the reflected light components  $r_p$  and  $r_s$ , along the p and s planes, respectively, is measured and normalised to the values of the incident beam (see **Figure 3.18 (b)**). The ratio of these values is called the complex reflectance ratio  $\rho$ , and is defined by [136]:

$$\rho = \frac{r_p}{r_s} = \tan(\phi) e^{i\Delta}. \quad (3.5)$$

The weakness of this technique is that the measurement of  $\phi$  and  $\Delta$  is an indirect way to obtain information about the thin film properties and necessitates data modelling analysis.

The data was fitted using the *CompleteEASE* software, in which a model of the sample's layer structure is constructed, or a default model is chosen from the ones available, such as 'silicon with absorbing film'. The thickness and optical properties of each layer is estimated by the user or taken from the software directly. Then *CompleteEASE* calculates the theoretical values of  $\phi$  and  $\Delta$ , and iteratively adjusts the parameters set in the model to the ellipsometry data taken experimentally. The quality of the fit is assessed by the mean squared error (MSE) obtained between the calculated and experimental data, where the best fit model corresponds to the estimated thickness and optical properties of the film. This technique can accurately determine the thickness of ultra-thin film, however, below a certain thickness, the sensitivity to the index of the film will degrade [137].

### 3.3 Spectroscopic measurements

The far-field ORD measurements were carried out using a polarisation microscope (see **Figure 3.19**). This custom-built instrument can record ORD (polarisation angle  $\theta$ ) and reflectivity spectra. The light is generated by a 50W tungsten halogen light source from Thorlab, the beam passes through a nanoparticle polariser (Thorlab) and is then sent to a beam splitter (Thorlab 50:50 700 nm-1000 nm CCM-1BS014/M). The light is then diverted and its polarisation changes by  $90^\circ$ , which goes to the  $10\times$  lens with 0.3 numerical aperture Olympus UPlanFLN. The reflected light from the sample passes through the beam splitter and traverses another calcite polariser (output polariser). The beam of light passes through a second beam splitter to reach a camera (Thorlab CMOS camera DCC1645C) and the spectrometer (Ocean Optic USB 4000). Using Thorlab camera software, it is possible to focus on the nanostructure arrays and align the sample to the linearly polarised incident beam.

To obtain an ORD spectrum, the angle of this last polariser is set to  $0^\circ, 45^\circ, 90^\circ$  and  $135^\circ$  (Stokes angles). It is then possible to use the program *LabVIEW* to calculate the ORD spectrum from the intensity ( $I$ ) recorded at the Stokes angles with this formula [138]:

$$ORD = \frac{1}{2} \tan^{-1} \frac{(I_{45} - I_{135})}{(I_0 - I_{90})}. \quad (3.6)$$

To record the reflectance spectra, the output polariser is set to 0° and the spectrum obtained on the nanostructures is divided by the spectrum reflected from the substrate background:

$$Reflectance = \frac{I_{nanostructure}}{I_{background}}. \quad (3.7)$$

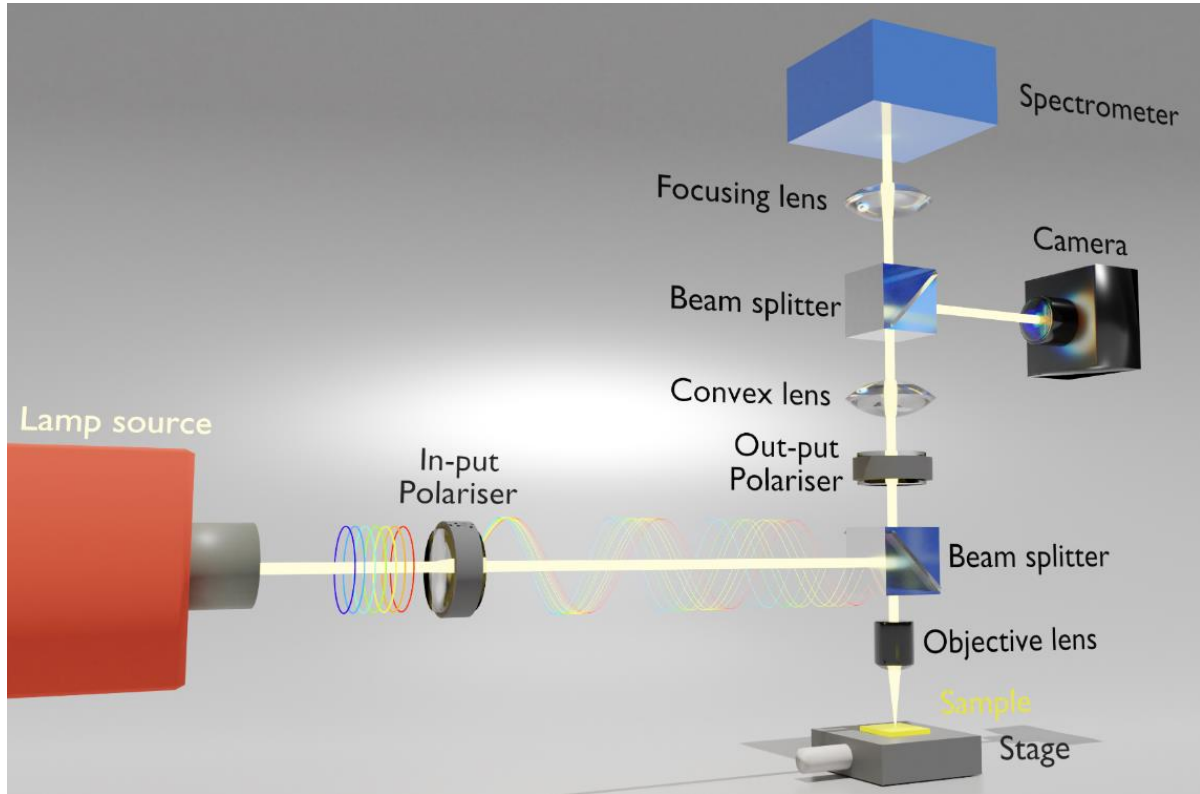


**Figure 3.19: Polarisation microscope setup, consisting of a broadband light source that is polarised linearly, and an out-put polariser that enables the measurement of the ORD of the reflected light ([139]).**

## 3.4 Simulation model and methods

*“All models are wrong, but some are useful”*, famously said the British statistician George E. P. Box. This is also valid for numerical simulations, which are currently unable to capture all of reality and only give approximations. The validation of experimental observation through simulation modelling is nonetheless crucial to describe complex phenomena and support results through the understanding of theory.

The modelling of the interaction of light with plasmonic nanomaterials in this work was conducted on the commercial software *COMSOL Multiphysics*, using the finite element method.

### 3.4.1 Finite element method

The finite element method (FEM) is used to solve differential equations encountered in virtually all problems in engineering sciences, such as thermodynamics, mechanics and electromagnetics. It is achieved by the discretisation of the system into smaller pieces called elements. These simple elements can have different shapes. For 2D problems, the triangle shape is often used, and the tetrahedron is most widely employed for 3D models, but other shapes can also be considered (see **Figure 3.20**). Neighbouring elements share nodes at their boundaries, where the solutions of the differential equations will be constant. This ensemble of elements forms the ‘mesh’ of the model. The more elements, the finer the mesh and therefore the more reliable the results will be, but this comes at the cost of more time and computation resources. Known boundary conditions can be applied to the outmost nodes of the mesh, such as a fixed temperature or a non-reflective boundary. The solutions of all the nodes are compiled into larger global equations that will be solved to derive the unknowns at each node [140].

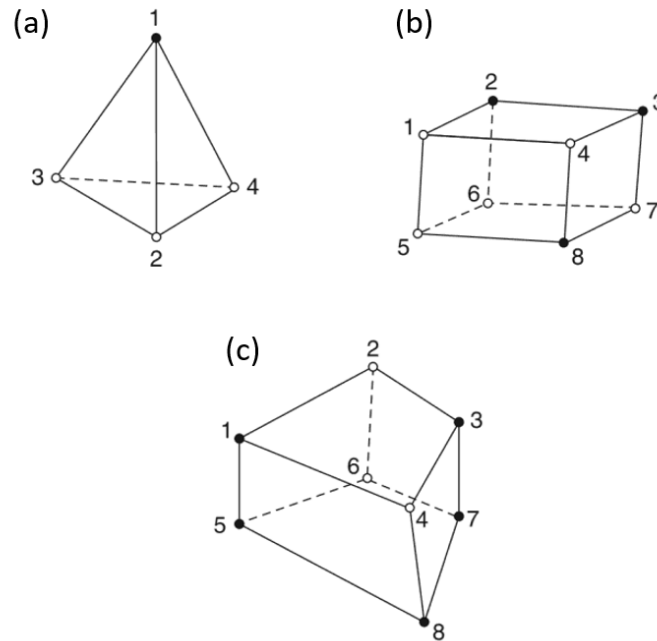


**Figure 3.20: Different finite element shapes (a) tetrahedron, (b) rectangular prism and (c) hexahedron (adapted from [141])**

The main benefits of this simulation technique are that it provides a solution over the entire model and that it can handle complex geometries with very different material properties (nonlinear, isotropic or anisotropic). However, there are significant challenges with this method. Mainly the need for high computational power to solve the complex set of equations, as well as the requirement for a large amount of random access memory (RAM) to store the calculated solutions. The use of a custom-built computer dedicated to *COMSOL* simulations was necessary to perform these tasks.

In this thesis, *COMSOL Multiphysics* has been used with two modules: the wave optics module and the heat transfer module. These modules can simulate electromagnetic wave interaction with plasmonic nanostructures and how the heat generated will propagate to the surrounding media.

### 3.4.2 Wave optics module

The Wave optics module specialises in solving problems requiring the simulation of electromagnetic waves at optical frequencies (nano- to micrometre range). It is commonly used for applications such as photonic waveguides and crystals, optical fibres and metamaterials. This module was used to solve Maxwell's equations for the electric and magnetic fields in various media in the frequency domain. It will therefore simulate stationary problems by giving complex-valued solutions, representing both the



amplitude and the phase of the field. This strategy is adapted for propagation and scattering problems but requires the mesh size to be small compared to the wavelength [142].

A set of equations is defined within ‘Electromagnetic Waves, Frequency Domain’ to solve Maxwell’s equations (see Section 2.1) using the FEM solver. The governing equation is written as follows [142]:

$$\nabla \times \frac{1}{\mu_r} (\nabla \times \mathbf{E}) - k_0^2 (\varepsilon_r - \frac{i\sigma}{\omega\varepsilon_0}) \mathbf{E} = 0 \quad (3.8)$$

$$\text{With } k_0 = \omega \sqrt{\varepsilon_0 \mu_0}. \quad (3.9)$$

Here,  $\mathbf{E}$  is the electric field and  $\omega$  is the frequency of the incident electromagnetic wave. The material properties are defined by  $\sigma$ , the electrical conductivity,  $\varepsilon_0$  and  $\varepsilon_r$ , the vacuum and relative permittivities and the permeabilities  $\mu_0$  and  $\mu_r$ .

For a closed system, the macroscopic response of a material to an electromagnetic field is described by the constitutive relations. In the case of a linear and isotropic medium, the electric field displacement  $\mathbf{D}$  and the magnetic field strength  $\mathbf{H}$  are defined by:

$$\mathbf{D} = \varepsilon_0 \varepsilon_r \mathbf{E} \quad (3.10)$$

$$\mathbf{H} = \mathbf{B} / \mu_0 \mu_r. \quad (3.11)$$

To model the effect of a chiral dielectric material on the optical properties of a system, these equations are modified as follows [143,144]:

$$\mathbf{D} = \varepsilon_0 \varepsilon_r \mathbf{E} + i \xi^T \mathbf{B} \quad (3.12)$$

$$\mathbf{H} = \mathbf{B} / \mu_0 \mu_r + i \xi^T \mathbf{E}. \quad (3.13)$$

The term  $i \xi^T$  introduces a cross-coupling between the electric and magnetic fields. Where  $\xi$  is the optical chirality parameter, sometimes referred to as the *Pasteur* coefficient, a second-order tensor that describes the chiral properties of the material, with a sign dependence on the handedness of the medium. When  $|\xi^T| > 0$ , right-circularly polarised light travels slower through the chiral medium, and when  $|\xi^T| < 0$ , left-circularly polarised light is slower [143].

In the case of a chiral isotropic environment, the diagonal components  $\xi_{xx}$ ,  $\xi_{yy}$  and  $\xi_{zz}$  are equal and non-null. This parameter can be expressed in its general form as [145]:

$$\xi^T = \beta_C \left( \frac{1}{\hbar\omega + \hbar\omega_0 + i\Gamma_{12}} + \frac{1}{\hbar\omega - \hbar\omega_0 + i\Gamma_{12}} \right). \quad (3.14)$$

This equation allows the calculation of the *Pasteur* coefficient at a certain wavelength or energy from an isolated molecular resonance at a frequency  $\omega_0$ . The values of all the parameters in this equation are generally derived from experimental data and are calibrated to fit the extinction and CD of the chiral molecule studied [97].  $\beta_C$  is a

coefficient intrinsic to the chiral material,  $\hbar$  is the reduced Plank's constant equal to  $\hbar = h/2\pi$ ,  $\omega_0$  is the absorption frequency and  $\Gamma_{12}$  is the width of the chiral molecular resonance. For chiral molecules, the optical chirality is weak and  $|\xi^T|$  typically has a small value ( $\sim 10^{-3}$ ).

The *Pasteur* parameter  $\xi$  is a complex frequency-dependent parameter, from which the ORD and CD spectra of a chiral molecule are proportional to  $Re[\xi(\omega)]$  and  $Im[\xi(\omega)]$ , respectively [146]. The CD signal is non null only in the vicinity of the molecular resonance ( $\omega_0$ ), which is often in the UV range, while the ORD intensity exists in the entire wavelength range, following the line shapes described by the Cotton effect discussed earlier in Section 2.4.3 [147]. For this reason, the interaction of a chiral dielectric medium with a plasmonic metamaterial is often modelled using only  $Re[\xi(\omega)]$  due to the wavelength range mismatch between the plasmonic resonance and the CD resonance [97].

### 3.4.3 Heat transfer module

This *COMSOL* module has been developed to simulate the three modes of heat transfer: conduction, convection, and radiation. Conduction is observed in any solid material and can be constant or dependent on the temperature. Convection describes the heat transfer due to the motion of fluids. Radiation is the propagation of heat through electromagnetic waves. A combination of these processes can be simulated in the software and tailored to specific problems, such as laser and joule heating, electronic cooling or chemical reaction heating [148].

As discussed in Section 2.6, heat conduction is governed by different mechanisms depending on the material studied. In solids, the primary mechanism behind temperature change is lattice vibrations (phonons), transferred by conduction through the direct contact between the particles. In metals specifically, heat is largely driven through the electron cloud, which can also interact with the lattice phonons. In fluids, heat conduction happens when the molecules vibrate and collide with their nearest neighbours. The modelling of heat transfers for all cases in *COMSOL* is based on Fourier's law of heat conduction [149]:

$$\mathbf{q} = -k\nabla T. \quad (3.15)$$

This equation states that the conductive heat flux  $\mathbf{q}$  (in  $W/m^2$ ) varies with the gradient of the temperature  $\nabla T$ . Where  $k$  is the thermal conductivity (in  $W/(m \cdot K)$ ), which is always a positive value since heat always flows from high temperature objects to low temperature ones.

In this PhD work, this module was used to simulate the heat generated in plasmonic nanostructures exposed to a laser pulse, and how it dissipates in the

surrounding media. This module was used along with the Wave optics module presented before through the Multiphysics feature of *COMSOL*. The Electromagnetic heating branch of Multiphysics was used to inform the software that the two physics modules are coupled. Two simulation study steps are then defined, the first one will solve the electromagnetic problem in the frequency domain and the second one will compute the heat transfer based on the solution of the first step in a time-dependent frame.

The heat transfer equation in different types of media is derived from the localised form of the heat balance equation, which is itself obtained from the principle of energy conservation (first law of thermodynamics). The time-dependent form of the energy conversion equation is expressed as [149–151]:

$$\rho C_p \frac{\partial T}{\partial t} + \nabla \cdot \mathbf{q} = Q . \quad (3.16)$$

Where  $\rho$  is the density of the material,  $C_p$  is the heat capacity,  $T$  is the temperature and  $t$  is the time. Here  $Q$  represents the heat source in the computation model (in  $W/m^3$ ).

When the heat source originates from an EM source, the Electromagnetic heating node of Multiphysics uses the solution of the Wave optics module to derive the value of  $Q$  from joule heating as  $Q = \mathbf{J} \cdot \mathbf{E}$  [152]. With  $\mathbf{J}$  the current density and  $\mathbf{E}$  the electric field strength. The temperature can then be plotted as a function of the wavelength of the incident light. The robustness of this coupled simulation was assessed by comparing the temperature obtained in the Heat transfer module to the electric field value integrated inside the plasmonic nanostructure in the Wave optics module.

### 3.4.4 3D Simulation model

The strategy employed to model 3D plasmonic metamaterials is to design a block containing one instance of the structure and assign Floquet periodic boundary conditions on the side surfaces to mimic an infinite repetition. The lateral dimensions of this block are thus set to the measured period of the array. The Floquet-Block theorem describes the behaviour of solutions to linear differential equations with periodic coefficients. It is frequently used to describe the behaviour of periodic structures, such as crystals [153].

The height of the domain above the nanostructure must be higher than  $\lambda_{max}/2$ , where  $\lambda_{max}$  is the maximum wavelength value of the incident light. This is to prevent the near field from extending all the way to the integration surface in the top of the model and giving an erroneous far field calculation. The ideal nanostructure shape can be modelled using any available CAD software or directly in *COMSOL*. In some cases, where the simulation needs to precisely fit the experimental conditions, an AFM micrograph file can be used to generate the nanostructure model. The resulting unit cell is split horizontally into many domains for which different mesh types (usually tetrahedrons)

and sizes can be assigned and the material properties defined. A schematic of a typical simulation model is shown in **Figure 3.21** (a). The top and bottom domains of the model are regions of infinite extent designed using the perfectly matched layer (PML) tool. This layer will absorb all the light reflected from the plasmonic nanostructure and will be numerically stretched towards infinity. For that reason, it is important to use a rectangular mesh for these domains, named Swept mesh, as the elements need to be parallel to the stretching direction. The mesh is automatically generated by the software based on all the constraints specified beforehand. Every domain has a mesh type applied to it, as well as a maximum element size. Generally, the nanostructure requires more elements to be precisely modelled, and the level of detail progressively falls farther away from it (see **Figure 3.21** (b)). This adaptative meshing allows our model to have a high level of detail in the near field, where most plasmonic interactions are happening, while keeping the total number of elements low enough to be handled by *COMSOL*. The maximum number of elements for the entire model was approximately 400,000, which was limited by the RAM memory of the computer and the computation time.

A wave excitation port is used to simulate an incident light beam that is positioned on the surface plane below the PML domain. Many parameters can be tuned at the port to fit the experimental conditions, such as the angles of incidence, the power and the polarisation of the light. The polarisation of the beam is defined through the  $x$ ,  $y$  and  $z$  components of the electric field vector. To model a linearly polarised light, the  $z$  component is set to zero and the direction of polarisation is defined in the plane  $xy$ . For a beam linearly polarised along the  $x$  axis, the  $x$  component of the electric field is set to 1 while  $y = 0$ . In the case of a circularly polarised light,  $y = 1$  and  $x = i$  or  $-i$  for RCP and LCP, respectively, with  $z$  kept equal to 0.

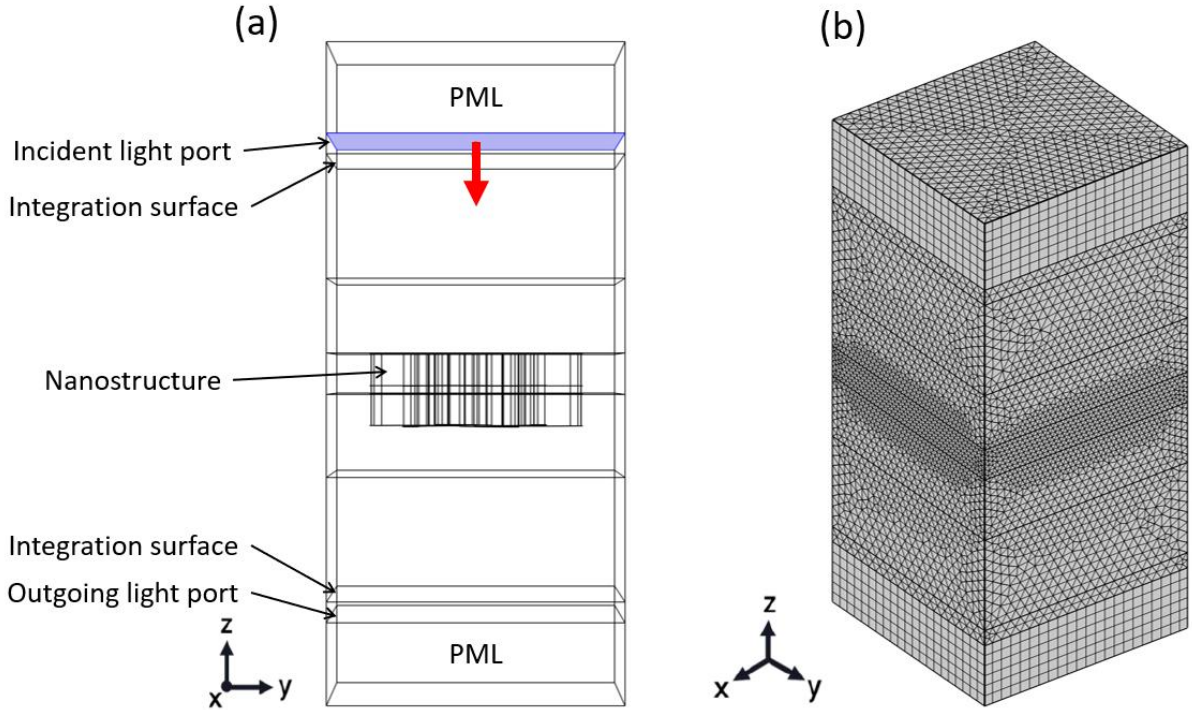


**Figure 3.21:** (a) block unit cell with the different domain separations, with in blue the port of the incident light, with the red arrow showing the direction of propagation. (b) The visual result of the autogenerated mesh on the entire model.

Two integration surfaces are defined just below the incident port and above the outgoing light port. These planes are useful to calculate the reflectivity and transmission of the plasmonic structure modelled and are obtained through the following expressions:

$$Reflectivity = 1 - \left| \frac{P_{av}}{P_0} \right| \quad (3.17)$$

$$Transmission = \left| \frac{P_{av}}{P_0} \right|. \quad (3.18)$$

Here,  $P_{av}$  is the average power passing through the integration surface and  $P_0$  is the power of the incident light generated at the input port. The reflectivity and transmission spectra can be obtained by setting the wavelength range and increment step using the 'parametric sweep' function in the study settings. The computed spectra can subsequently be compared to the experimental data to assess the robustness of the simulation model.

In this section, we have seen that *COMSOL Multiphysics* provides an intuitive interface for the modelling of a variety of scientific problems, automatically defining all the relevant equations and efficiently using the finite element method. But the general description of the simulation strategy provided here must be adapted and optimised for each study. As such, an in-depth examination of the models designed will be provided in all the subsequent chapters.

# Chapter 4

---

Selective Functionalisation  
of Metamaterials

## 4.1 Introduction

Incorporating molecular functionality into plasmonic nanostructures is key in many applications, such as in photovoltaic, biosensing, or biomedical fields [154]. The selective functionalisation of nanostructures is usually performed through expensive and time-consuming techniques like inkjet printing [155], dip-pen lithography [156] and laser-induced forward transfer [157]. These approaches have been studied thoroughly and are now showing limitations. Inkjet printing is a low-cost direct deposition technique, but it is mainly limited by a resolution in the micron range [158] and is not compatible with every material [159]. Dip-pen lithography is built on an AFM instrument, which has a high printing resolution (~50 nm) but is a time-consuming and labour-intensive process with a limited throughput and sample area [160]. Laser-induced forward transfer is a technique using a pulsed laser to project ink material or entire intact devices from a donor film to the sample [161]. Similar to dip-pen lithography, it has a high resolution but comes with low throughput and expensive equipment [159].

In this chapter, a high-throughput technique enabling the selective chemical functionalisation of a large area of nanostructures (>1 mm<sup>2</sup>) is presented. This method relies on a thermally responsive polymer that is chemically active but can become inert when subjected to a threshold temperature. The heat necessary to cause this change is locally generated directly by the plasmonic nanostructures exposed to a pulse laser through thermoplasmonic effects. This strategy was previously used to spatially functionalise the surface of complex plasmonic nanostructures by generating a heat gradient with a monochromatic pulsed laser [162]. Here, we go further by exploiting the thermal behaviour of metallic nanostructures exposed to a pulse laser at different wavelengths and polarisation orientations. This technique enables rapid selective functionalisation of a large array of nanostructures based on their optical properties. We demonstrate the validity of this strategy on gold nanorod arrays of two different aspect ratios, which have resonances at different wavelengths. These nanorods are functionalised with a SAM of a thermoresponsive polymer, attached through a gold-thiol bond. A biotin functional group is readily available at the end of the polymer chain, making the surface of the plasmonic sample chemically active and able to bind to streptavidin. When a laser irradiates the sample, heat will be generated through nonradiative decays of LSPR in the structures [163]. Heat causes the polymer to collapse, burying the biotin within the structure and effectively chemically passivating the surface of the nanostructures [164,165]. This is visually observed by using streptavidin conjugated QDs that will preferentially bond to unheated nanostructures compared to laser heated inert structures. Although the biotin-streptavidin system is used as an exemplar in this study, the reported strategy is generic, and the biotin end group can be changed depending on the specific application requirements.

## 4.2 Background

### 4.2.1 Pulse laser photothermal effects

When using plasmonic nanostructures to generate heat, the goal is often to deliver the heat locally around their surface. The typical time scale for thermal diffusion in nanoscale devices is  $\sim 10^{-12}$  s, which means that a constant wave laser would lead to a uniform temperature distribution. A femtosecond laser enables hot spots in the nanostructure, depending on the spatial location of the plasmonic electric field [166]. Alternatively, a nanosecond pulse laser can be used in various applications where a thermal gradient in the dielectric medium surrounding the plasmonic structure is required [167].

The heat generated by the plasmonic system will be transferred following the equation [168]:

$$C_s \rho \frac{\partial T}{\partial t} + \nabla \cdot (-k \nabla T) = Q. \quad (4.1)$$

Where  $C_s$ ,  $\rho$  and  $k$  are the specific heat capacity, density and thermal conductivity of the material (space dependent).  $T$  is the temperature of the nanostructure and  $Q$  is the heat source from the light dissipation in the volume, as defined in Section 3.4.3.

This equation is used mostly to describe macroscopic heat transfer, but it is still valid in nanoscale systems, provided that the thermal properties are modified to fit the size and shape of the nanostructure [169]. For a femto- or picosecond pulse laser, this equation is not applicable since, as discussed previously in Section 2.6, the heat dissipation to the surrounding area happens after 100 ps. Before that, the heat transfer can only be solved in a two-step radiation heating model where electrons have a different temperature compared to the lattice structure [170].

For a single spherical nanoparticle, this equation can be solved in the steady-state regime to obtain the temperature at a distance  $\mathbf{r}$  from the centre of the plasmonic structure [151]:

$$\Delta T(\mathbf{r}) = \frac{VQ}{4\pi k_0 \mathbf{r}}. \quad (4.2)$$

Here,  $V$  is the volume of the nanoparticle and  $k_0$  is the thermal conductivity of the surrounding medium.

A previous study in the Kadodwala group used these photothermal effects to achieve spatial chemical functionalisation of a complex chiral plasmonic shuriken sample (presented in Section 3.1.2) to enhance biosensing sensitivity [162]. This was possible



using a SAM of a high-molecular-weight (6 kDa) thermoresponsive polyethylene glycol (PEG) thiol to chemically passivate the gold plasmonic film. This polymer layer can be chemically deprotected through an irreversible, thermally driven molecular transformation of the PEG structure. By using an 8 ns pulse laser, it is possible to create a thermal gradient at the interface between the shuriken structure and the water medium (see **Figure 4.1** (a)). This gradient originates from the disparity in the thermal diffusion properties of gold and water and was not observed in the metal alone. The water in the arms of the nanostructure will heat up more rapidly than the centre due to a smaller volume of water present in the arms (see **Figure 4.1** (b) and (c)). This localised chemical deprotection allows another thiolated compound to bond to the gold surfaces inside the arms, where the EM field has a high asymmetry, leading to enhanced enantioselectivity of the biosensor.

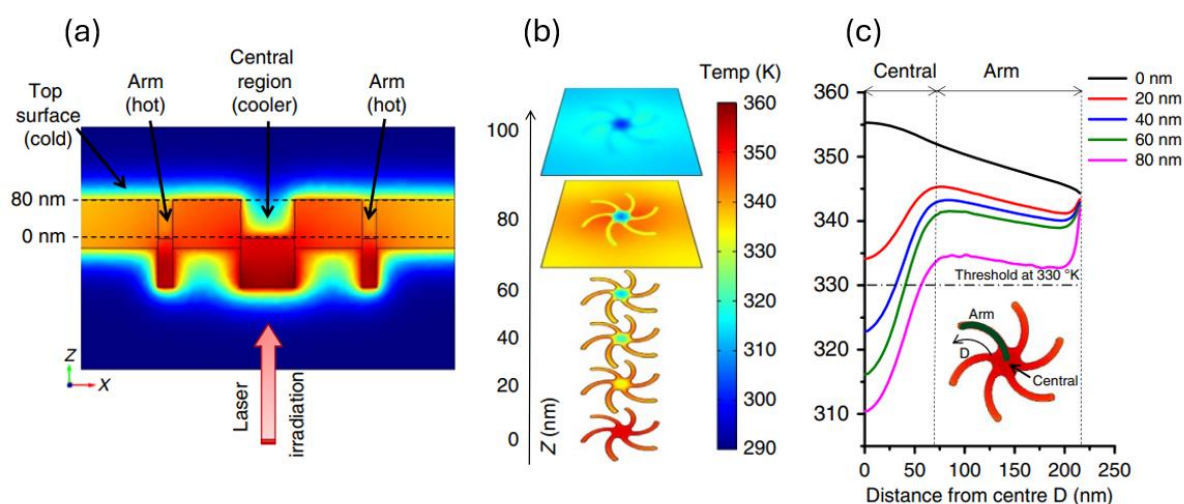


**Figure 4.1:** Thermal gradient after the 8 ns laser irradiation with (a) side view of the gold shuriken structure surrounded by water. (b) shuriken heat maps at an increasing height  $z$  and (c) temperature from the centre to the tip of the arm of the structure (as shown by the insert image), with the threshold of deprotection represented by the dashed line at 330 K (from [162]).

There are a variety of other thermoresponsive polymers, with different properties than those discussed here with PEG-thiol. The next section will extend on the chemistry of these polymers, switchable through a temperature change.

## 4.2.2 Thermoresponsive polymers

Thermoresponsive polymers are part of a larger 'stimuli-responsive' group of polymers, often referred to as 'smart' polymers. They have the ability to change their physicochemical properties in response to changes in their environment, among which

temperature is the most studied stimulus. These thermoresponsive polymers have recently seen a surge in applications in the field of smart materials [171]. They are divided into two types showing opposite behaviour to a change in temperature: lower critical solution temperature (LCST) and upper critical solution temperature (UCST). This threshold temperature marks a reversible phase transition between a hydrophilic and hydrophobic state of the polymer chains in water. In the hydrophilic form, the polymer chain is characterised by an extended molecular coil and in the hydrophobic case, the polymer is in a collapsed globular conformation. LCST polymers will undergo a coil to globular transition with an increase in temperature, and for the UCST polymers, a decrease in temperature will trigger this molecular change (see Figure 4.2).

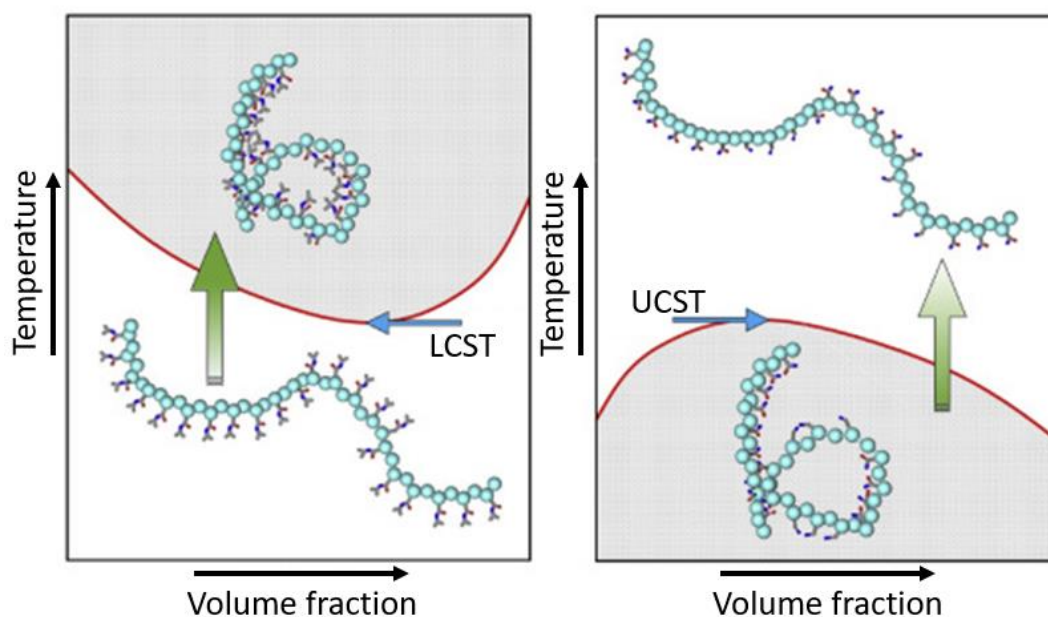


**Figure 4.2: Phase transition diagram in red of LCST and UCST thermoresponsive polymer types (adapted from [172]).**

The thermoresponsive polymer used in this study has LCST-type behaviour. At low temperatures, the polymer chains will share hydrogen bonds with the surrounding water molecules. When the temperature is increased above the LCST, these bonds are weakened, and intra-polymer hydrogen bonding will arise [173]. This will in turn lead to the dehydration of the chains and a reduction in the solubility, collapsing the polymer structure [174]. A decrease in the solvent-accessible surface area as well as a decrease in the torsional energy of the isopropyl groups has also been suggested by molecular dynamics computer simulations [175].

The progressive change in molecular conformation of thermoresponsive polymer chains will be accompanied by changes in their optical properties, notably, an increase in the refractive index in the high-density globular state. This reversible change in the refractive index as a function of temperature has been successfully monitored in several studies through the red shift in the resonance of plasmonic nanostructures [176,177].

## 4.3 Methods

### 4.3.1 Nanostructures and thermoresponsive polymer

To study the plasmonic heating of nanostructures, gold nanorods were fabricated by EBL and metal evaporation on a silicon wafer (as described in Section 3.1.1). The rod shape is simple and has been extensively studied in the field of thermoplasmonics [77,178–180]. It allows different plasmonic responses when using linearly polarised light along the short and long axes of the rods.

Two aspect ratios were manufactured in separate  $1 \times 1$  mm arrays. The longitudinal dimensions of the rods were measured by SEM to be  $\sim 750$  and  $\sim 850$  nm long for a common transversal dimension of  $\sim 140$  nm (see **Figure 4.3** (a) and (b)). In the rest of this chapter, the 750 nm structures will be called ‘short rods’ and the 850 nm size ‘long rods’ for simplification. The height of both rods’ lengths was measured by AFM to an averaged value of  $\sim 110$  nm (see **Figure 4.3** (c)).

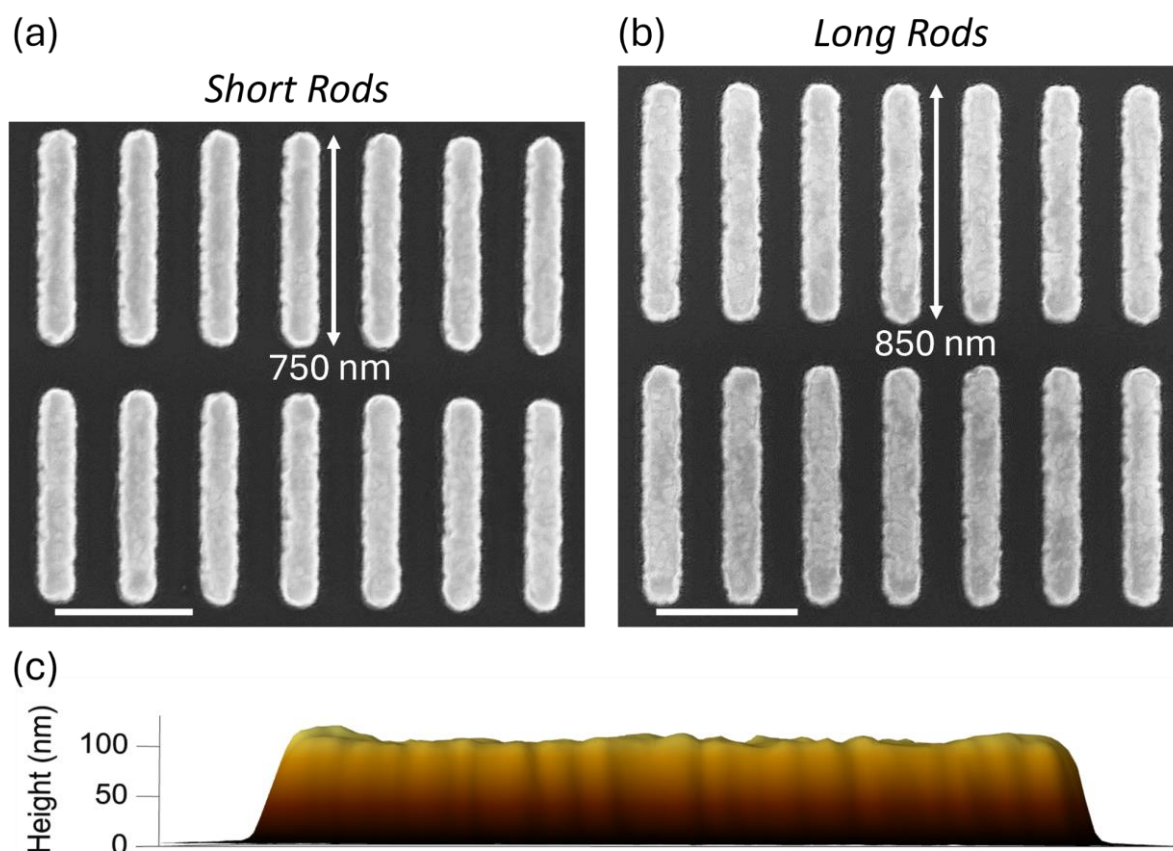


**Figure 4.3:** SEM images of (a) short and (b) long nanorod arrays with the scale bar representing 500 nm. (c) Side profile of a short rod taken by AFM.

A total of 24 arrays of 500 by 500  $\mu\text{m}$  are present on the sample for both rod's lengths, which were kept in an aqueous environment during the experiment using a rubber O-ring and a glass cover slide (see **Figure 4.4**).

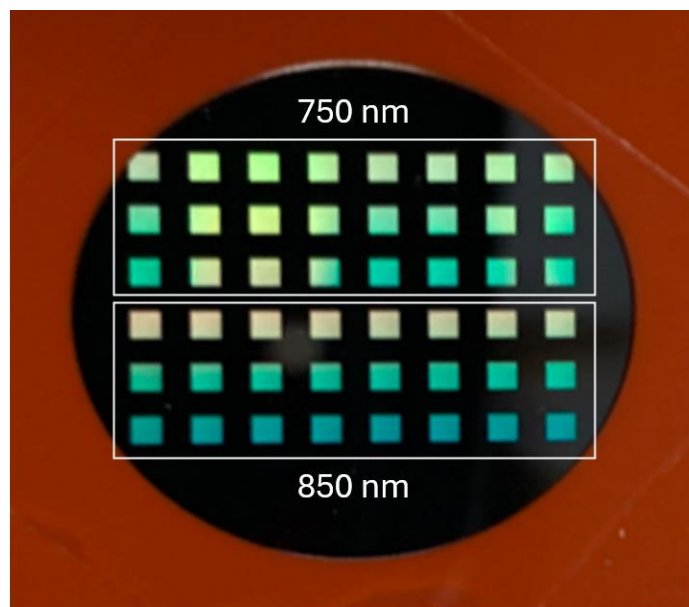


**Figure 4.4:** Photo of the silicon wafer sample with 24 arrays of each rod length kept under a liquid environment with a rubber ring and a glass cover slide.

The thermoresponsive polymer used in this study is a biotinylated thiol poly(*N*-isopropylacrylamide) (*p*-NIPAAm) with a molecular weight of  $\sim 10.4$  kDa (see **Figure 4.5**). It was synthesised by Michele Cariello as described elsewhere [181]. The investigated polymer consists of a biotin terminal group connected to a *p*-NIPAAm polymer segment through a tri-unit PEG linker. The *p*-NIPAAm segment contains 76 monomer units (MW = 129.20 g/mol each), yielding a total molecular weight of 10.4 kDa. When fully extended, the theoretical length of this polymer reaches approximately 30 nm, though in solution the molecule adopts a more compact, coiled conformation.

A SAM of *p*-NIPAAm was formed by chemically bonding a thiol group on one end of the polymer chain to the surface of the gold structures. For this, a 0.5 mg/mL solution of *p*-NIPAAm in phosphate-buffered saline (PBS) was left for 48 hours on the sample previously cleaned with an 80 W oxygen plasma treatment. The unbound molecules were rinsed with PBS, leaving only the SAM layer on the gold nanorods.

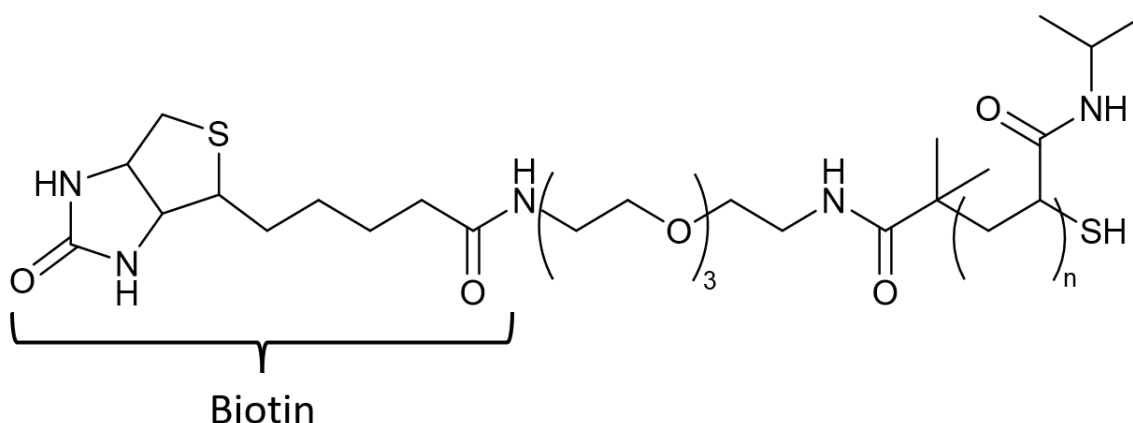


**Figure 4.5: Biotinylated thiol poly(N-isopropylacrylamide), or *p*-NIPAAM.**

This polymer has a LCST of  $\sim 316$  K or  $43$  °C in water solution, above which the conformation of the polymer chain will go from a helical structure to a globular state [182]. This temperature is determined by taking the midpoint of the transmittance curve (see **Figure 4.6** (a)).

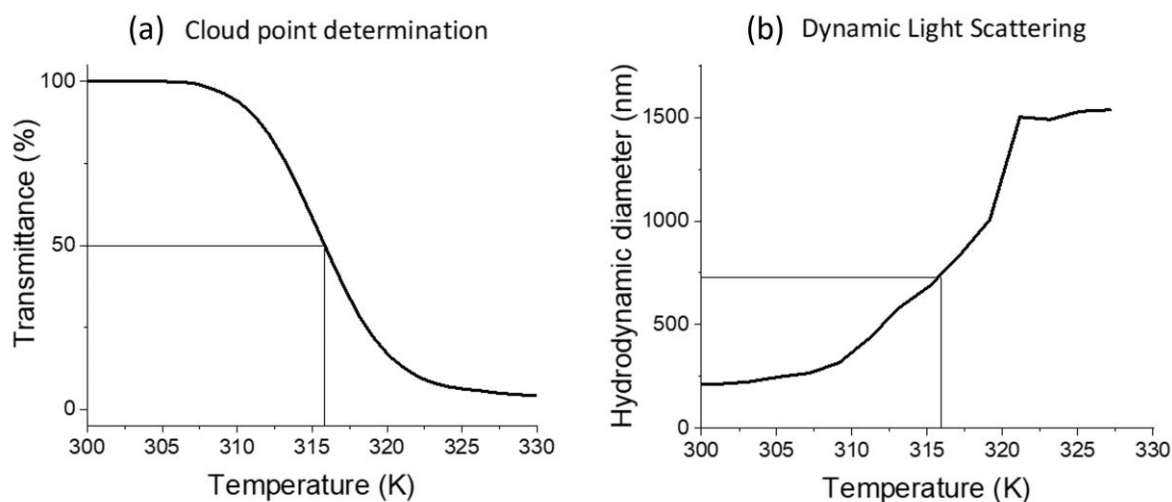


**Figure 4.6: Extrapolated curves from experimental data points of (a) transmittance of *p*-NIPAAM in water (0.2 mg/mL) at 500 nm varying with the temperature and (b) dynamic light scattering analysis as a function of the temperature. The LCST is highlighted on both plots (provided by Michele Cariello).**

The switch in molecular conformation that *p*-NIPAAM undergoes is reversible in solution, and researchers are routinely exploiting this property in biomedical applications [183]. In our study, the polymer chains are covalently bonded to the surface in a dense layer, rendering the transition irreversible through the entwining and weaving of the chains [162,184]. When *p*-NIPAAM is heated above its LCST, the biotin functional group at the end of the polymer chain will be hindered due to the collapse of the chain in

a high-density globular state. According to previous studies, the collapse of *p-NIPAAm*, also known as deswelling due to the water being expelled from the hydrogel, happens within 10 ns [184,185]. A 5 ns pulsed laser heating setup was employed to generate heat in the gold nanorods and initiate the switch in the *p-NIPAAm* monolayer. This setup is described in detail in the following section.

A solution of 15  $\mu\text{L}/\text{mL}$  of QDs 705 streptavidin conjugate (1  $\mu\text{M}$ ) from *Thermo Fischer* (see **Figure 4.7**) was diluted in PBS and left overnight at the surface of the sample after the laser heating phase. Streptavidin is a highly stable protein that exhibits high affinity with biotin, forming a strong non-covalent bond [186]. The  $\sim 15$  nm diameter semiconductor QDs (CdSe and ZnS) possess between 5 and 10 streptavidin at their surface, which will bind to the available biotin groups, and the unbound QDs will be subsequently rinsed using 1 mL of PBS. Adding the QDs after illumination (in dark conditions) prevents high EM field-trapping effects and ensures that they are guided only by the chemical availability of the biotin of the adsorbed polymer [187,188].

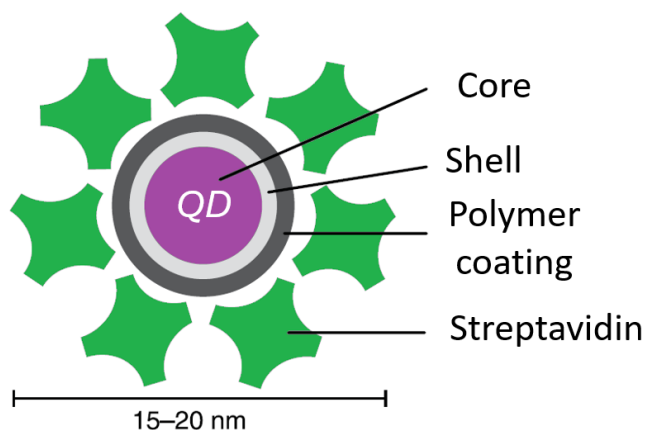


**Figure 4.7: Streptavidin conjugate QDs (adapted from thermofisher’s documentation).**

This QD functionalisation allows us to visualise the molecular state of the thermoresponsive polymer layer on each nanostructure. Through every step of this experiment, reflectance spectra of each nanorod array were measured using the polarisation microscope setup described in Section 3.3. The shift in the position of the plasmonic resonance allows us to monitor the change in refractive index caused by introducing new material on the sample (*p-NIPAAm* and QDs) [189].

Finally, an SEM examination of the sample after  $\text{N}_2$  drying is done to determine the average amount of QDs per rod. This provides a direct visualisation of the amount of free biotin available, and hence the amount of unaffected *p-NIPAAm*.



### 4.3.2 Pulsed laser heating setup

Unlike a continuous-wave laser, a nanosecond pulsed laser will give rise to a temperature gradient in the water surrounding the nanorods. This gradient is caused by the difference in thermal diffusivity between gold and water. For gold, this value is high with  $1.27 \times 10^{-4} \text{ m}^2/\text{s}$  at room temperature. After 5 ns illumination, the rods will reach a temperature nearly uniform within their volume. The heat accumulated by the rods will slowly be conveyed to the water medium, which has a much lower thermal diffusivity compared to gold ( $1.43 \times 10^{-7} \text{ m}^2/\text{s}$ ), generating a temperature gradient in the *p-NIPAAm* layer [162,190].

The pulsed laser source used here is a Radiant SE 532 LD from Oportek generating a 6.5 mm diameter linearly polarised beam with a 5 ns pulse duration (FWHM), at a tuneable wavelength between 650 and 2600 nm. It was used to illuminate the nanostructures at a 20-Hz repetition rate. Two experiments were conducted using this setup, with a different power for each one. The fluence of the laser beam was fixed at  $255 \text{ mJ cm}^{-2}$  (20 mW beam power) for one experiment and  $127 \text{ mJ cm}^{-2}$  (10 mW) for the other one. The wavelength of the laser beam was set prior to the heating step with a tolerance of  $\pm 1 \text{ nm}$ . Two different laser polarisation angles relative to the rods were tested by rotating the sample  $90^\circ$ .

The beam height is adjusted using a periscope Thorlabs RS99/M, it then passes through two Glan-Laser polarisers to control the power of the beam by rotating the first polariser. The laser is reflected down onto the sample at a normal incidence using a cage cube-mounted non-polarising beam splitter (Thorlabs) and an Olympus UPlanFLN  $10 \times / 0.3\text{na}$  objective to focus the beam in a 1 mm diameter spot for a duration of 2 min per array of nanorods. A Blackfly USB3 camera was used to focus the beam and aim the laser at the desired array. The setup schematic is shown in **Figure 4.8**.

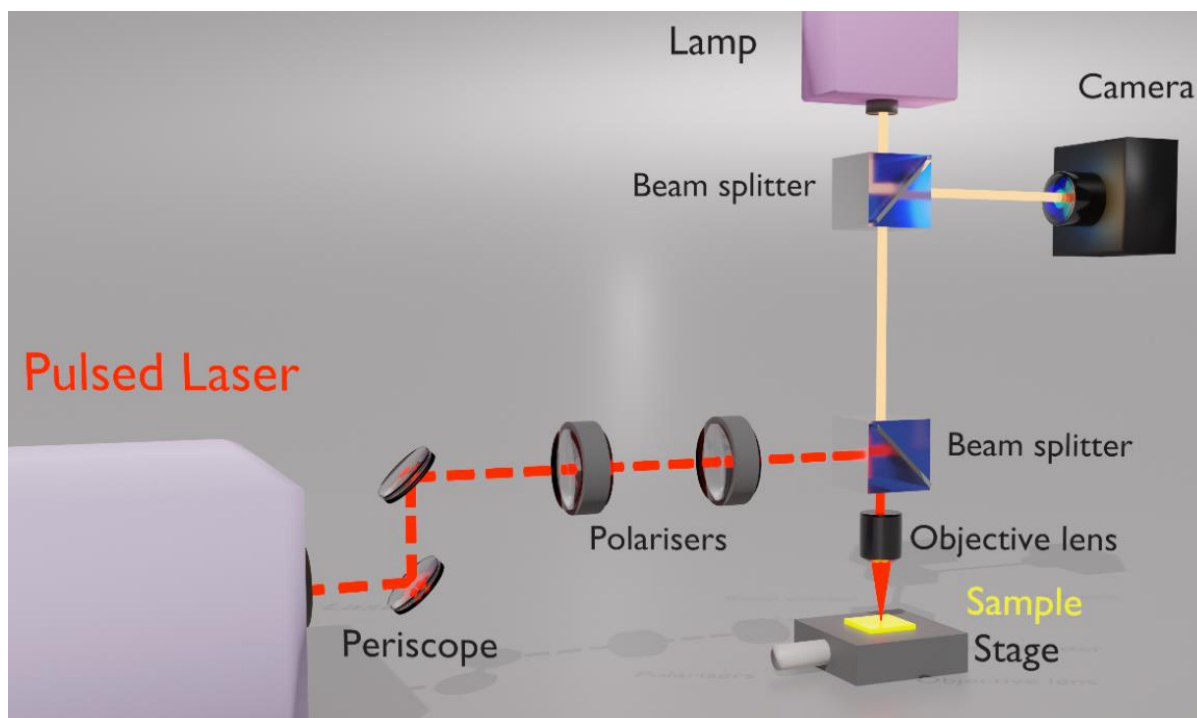


**Figure 4.8:** Schematic of the polarised pulsed laser heating setup, consisting of a 5 ns polarised pulsed laser and a camera system that enables the heating of one array of nanorod.

The Olympus objective has a high transmittance from 400 to 700 nm, which falls progressively above this range (see **Figure 4.9**). The power from the laser beam was measured at each wavelength used in the experiments at the sample position. This measurement could not be done with the objective lens due to a spot size too small for the power meter equipment. The thermal power sensor head S425C was used with a compact power meter console PM100D (Thorlabs) and an average of 100 measurements was collected.



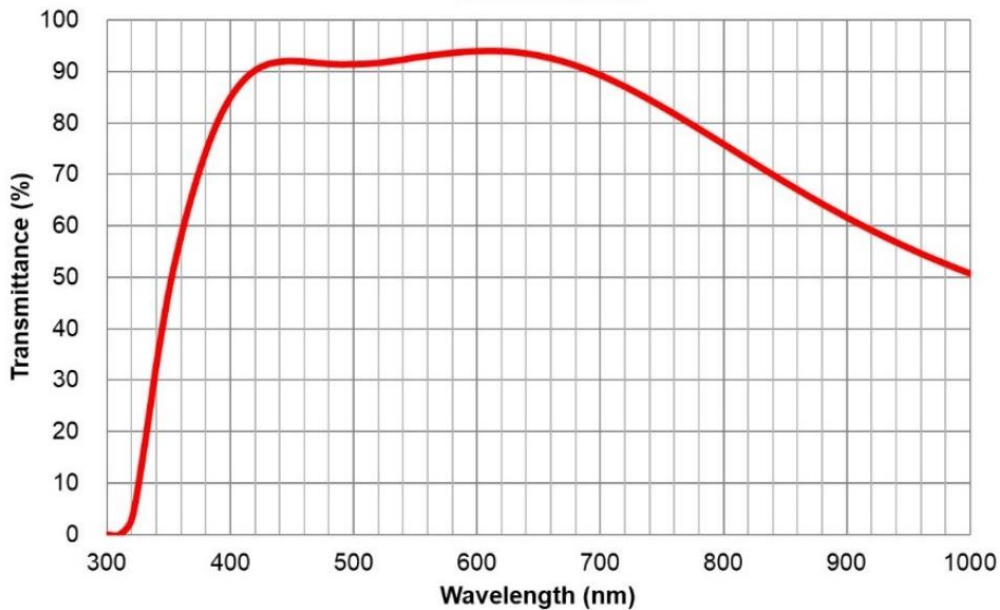


**Figure 4.9:** Transmittance of the Olympus UPLFLN10x2 objective as a function of the wavelength (from Olympus website).

### 4.3.3 Simulation model

A simulation model was constructed on *COMSOL V6.0* to better understand this experiment and replicate the results. This problem necessitated the use of the Wave optics module to solve Maxwell's equations and the Heat transfer module to understand the heat generation in the rods and how it is conveyed to the thermoresponsive polymer. These modules were paired using the *Multiphysics* node of *COMSOL* as described in Section 3.4.2 and 3.4.3.

This simulation model contains one nanorod, either short or long, obtained from an AFM file. This 3D structure was inserted in a block with lateral dimensions of  $900 \times 280$  nm and  $1000 \times 280$  nm for the short and long rods, respectively (see example in **Figure 4.10**). Periodic boundary conditions were applied on all sides to replicate the array of nanostructures. The height of the block was set to 2000 nm for both rod sizes and perfectly matched layers (PML) of 300 nm were defined on the top and bottom of the models. Materials properties were added to the model, with the refractive index values of the gold nanorod taken from Johnson and Christy [53]. The density, heat capacity and thermal conductivity values were set to the default properties provided by *COMSOL* in the water, gold and silicon domains.

The incident electromagnetic wave was defined in the port above the nanostructure, with a polarisation angle either longitudinal ( $x$  axis) or transversal ( $y$  axis) in respect to the rod's long axis (see **Figure 4.10**). The beam intensity profile was assumed

to have a perfect top-hat shape during the 5 ns pulse with a constant fluence of  $255 \text{ mJ} \cdot \text{cm}^{-2}$  or  $127 \text{ mJ} \cdot \text{cm}^{-2}$ . The loss of power in the water was neglected in the simulations.

The temperature was averaged in a 10 nm thick water domain at the surface of the gold nanostructure to replicate the adsorbed *p-NIPAAm* layer, which was assumed to have similar thermal properties as water. These simulations were conducted for each combination of rod length and laser polarisation in a wavelength range close to experimental conditions (625 to 915 nm) with an increment of 5 nm.

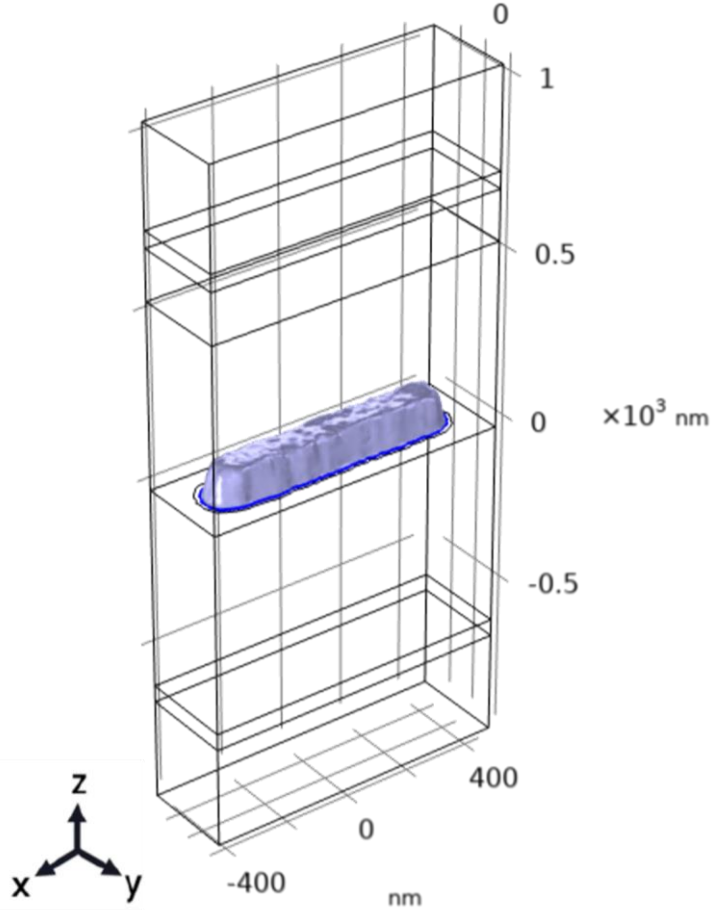


Figure 4.10: COMSOL model of a short rod from an AFM file (in blue).

The heat transfer equation solved by COMSOL in all the materials of the model is:

$$\rho C_p \frac{\partial T}{\partial t} - \nabla \cdot (\mathbf{k} \nabla T) = Q . \quad (4.3)$$

Where  $\rho$  the material density,  $C_p$  the heat capacity at constant pressure,  $\mathbf{k}$  is the thermal conductivity and  $Q$  is the heat source density, defined by:

$$Q = \mathbf{J} \cdot \mathbf{E} . \quad (4.4)$$

Here,  $\mathbf{J}$  is the current density and  $\mathbf{E}$  is the electric field. These values are obtained from solving Maxwell's equations using the Wave optics module in a simulation step in the frequency domain run before the heat transfer calculation, which is time dependent.

## 4.4 Results and discussion

To study the different thermoplasmonic properties of the two rod lengths, arrays of the nanostructures were subjected to 5 ns pulsed laser irradiation at different wavelengths and polarisation angles, while keeping the fluence of the laser constant. Two experiments were conducted on different samples at a power average of 20 mW and 10 mW.

### 4.4.1 Optical properties of the nanorod arrays

The reflectance spectra of all the arrays of nanostructures were measured relative to the silicon background using a broadband light source polarised linearly. The rods on the sample were orientated longitudinally with respect to the polarisation of the incident beam ( $0^\circ$ ), and the sample was rotated  $90^\circ$  to measure the transversal reflectance.

First, the reflectance spectra were taken on the clean sample in deionised water (DI) water, which served as references for the rest of the experiment. An example of spectra is presented in **Figure 4.11**, where the longitudinal and transversal reflectance spectra are shown for both rods' lengths.

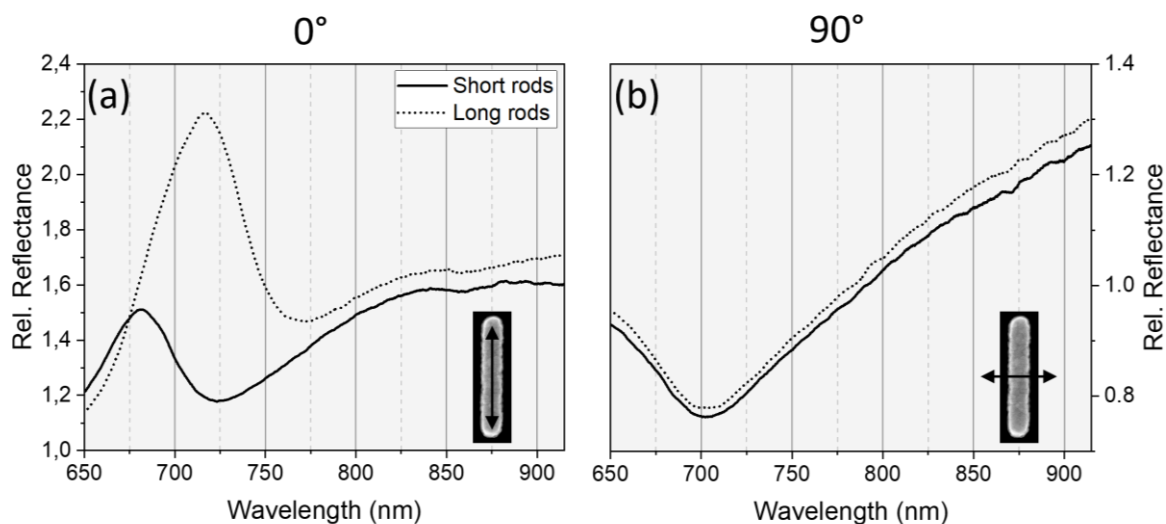


**Figure 4.11: Reflectance spectra of the arrays relative to the bare silicon background measured in water with a linear polarisation (a) along the rods' long axis ( $0^\circ$ ) and (b) across the short axis ( $90^\circ$ ) for a short and long nanorods in solid line and dashed line, respectively. A representation of the polarisation angle of the incident beam is represented by the black arrow in the insert image of a rod.**

When the rods are aligned with the polarisation of the incident light ( $0^\circ$ ), the plasmonic resonance of the short rods is located at  $\sim 680$  nm, while the resonance peak of the long rods is at  $\sim 720$  nm (see **Figure 4.11** (a)). This discrepancy is easily explained by the difference in the length of both rod shapes, generating LSPR at a higher wavelength for the longer rod assembly. For the transversal polarisation ( $90^\circ$ ), the reflectance spectra show the same profile shape, with a dip at 700 nm (see **Figure 4.11** (b)). As both rod aspect ratios have the same width and lateral periodicity, the transverse plasmonic modes will be identical.

The reflectance was measured on the *p-NIPAAAM* functionalised nanorods, then following the pulsed laser heating of the arrays, and finally, on the QD functionalised sample after rinsing it with PBS. These spectroscopic measurements are crucial to verifying the correct development of the experiment by monitoring the position of the plasmonic resonance  $\lambda$ , which correlates with the refractive index of the media surrounding the nanorods [189]. In the rest of this study, only the  $0^\circ$  reflectance spectra were considered for this purpose, due to a weak signal-to-noise ratio on the  $90^\circ$  spectra and a wide resonance shape.

An example of reflectance spectra measured at each stage of the experiment for both rod aspect ratios is presented in **Figure 4.12**.

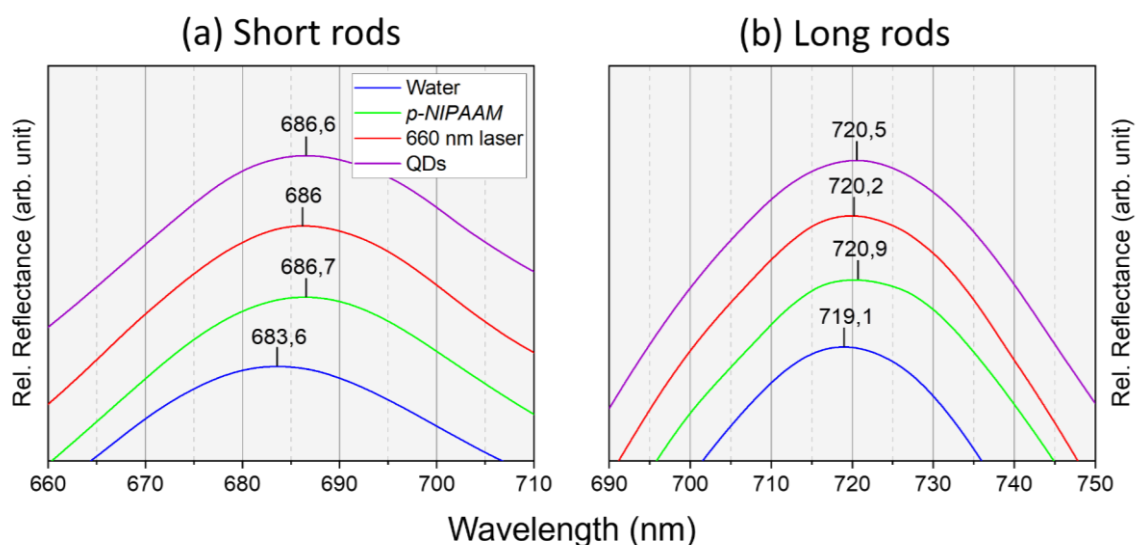


**Figure 4.12:** Reflectance spectra at  $0^\circ$  polarisation for (a) short rods and (b) long rods in water (blue), with the *p-NIPAAAM* SAM (green), after laser heating at 660 nm/ $0^\circ$  with 20 mW (red) and functionalised with QDs (purple). The wavelength  $\lambda$  of the plasmonic peaks is labelled for each curve (in nm).

When the *p-NIPAAAM* SAM is introduced, the local change in refractive index causes a red shift around 2 – 3 nm on both lengths (green spectra in **Figure 4.12**). After laser heating, the sample was left 15 min at room temperature before measuring the spectra, where a blue shift reaching a maximum value of  $\sim 0.7$  nm was observed (red spectra in

**Figure 4.12).** Following the QD functionalisation step, the reflectance peaks show a red shift varying from 0.3 to ~2 nm (purple spectra in **Figure 4.12**). This high degree of fluctuation in the shift after the QD functionalisation is correlated to the different amounts of QD present on the rods after being heated under different laser parameters.

The blue shift  $\Delta\lambda_{pNIPAAAM-Laser} = \lambda_{After\ Laser} - \lambda_{Before\ Laser}$  is crucial to understand the plasmonic heating of the rods and correlate it to the degree of QD functionalisation. Initially, the polymer chains are extended in a tightly packed SAM, where the intermolecular hydrogen bonds between the *p-NIPAAAM* chains and surrounding water molecules make the layer hydrophilic (see **Figure 4.13** (a)).

When the rods are heated by the laser, a temperature gradient close to the gold surface is generated locally. If the heat goes beyond the LCST, the polymer chains will collapse through intramolecular hydrogen bonding of the C = O and N – H groups, making the layer hydrophobic [191]. The refractive index has been shown to undergo a moderate increase in this high-density globular conformation ( $T > LCST$ ), while occupying a 40% smaller volume fraction (see **Figure 4.13** (b)) [192].

This transition is irreversible in our study, the *p-NIPAAAM* layer will not come back to its initial volume after the rods cool to room temperature. Unlike when the polymer chains are far away from each other (such as in a solution), here they are adsorbed in a high-density layer and interactions between the chains can happen. As observed in other studies [162,184], the entwining and weaving of the long polymer chains after repeated laser pulses can prevent the polymer from going back to its original molecular conformation (see **Figure 4.13** (c)).

This large change in the volume occupied by the polymer explains the blue shift observed after laser heating. Despite being accompanied by a small increase in refractive index of the polymer, the overall refractive index of the layer will decrease as the polymer chains occupy a smaller volume, and the rest is occupied by water, which has a lower refractive index. This irreversible reaction will cause a reduction of the refractive index experienced by the EM near field of the plasmonic nanorods, manifesting as a blue shift in the reflectance spectra [193].

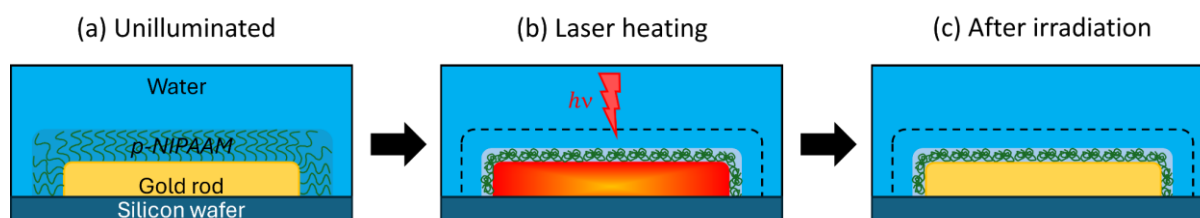


**Figure 4.13:** Schematic representation of the molecular changes in the *p-NIPAAAM* monolayer adsorbed on a gold nanorod (a) before illumination (b) heated above its LCST by a laser pulse and (c) cooled down at room temperature. The initial volume occupied by the *p-NIPAAAM* SAM is symbolised by the dashed line.

This change in the disposition of the polymer chains will result in the biotin groups being buried in the dense *p-NIPAAm* layer, making it unavailable to bond to streptavidin. Consequently, the number of streptavidin conjugated QDs on the rods will be reduced depending proportionally to the temperature reached during the pulsed laser heating phase.

The different laser wavelengths used in the following laser heating experiments were chosen based on the plasmonic resonances observed in the reflectance spectra (see **Figure 4.11**). The wavelengths at the resonance peak and on either side were studied to gain a better understanding of the thermoplasmonic properties of both nanorod sizes.

## 4.4.2 Experiment 20 mW

The laser power was set to an average of 20 mW in this experiment, which is the maximum power before concentric burn marks start to appear at the centre of the arrays. A set of short rod arrays was irradiated at a 0° polarisation for wavelengths of 660, 690, 725, 840 and 900 nm, each on different arrays. Another set of was exposed to the pulse laser at a 90° angle for 660, 700, 840, and 1000 nm. The long rods have been heated at a 0° polarisation with 660, 725, 790, 840 and 900 nm laser wavelengths. And at 90° with a laser at 660, 700, 840 and 1000 nm. A total of 15 arrays of each rod's aspect ratio were left unilluminated on the sample to use as a reference. The power of all the different wavelengths mentioned was measured separately before illuminating the nanostructure arrays, the values obtained are gathered in **Figure 4.14**. Here, the variation in the power was attributed to the instability of the laser system which depends on many factors such as the temperature, humidity, vibration and power supply stability.

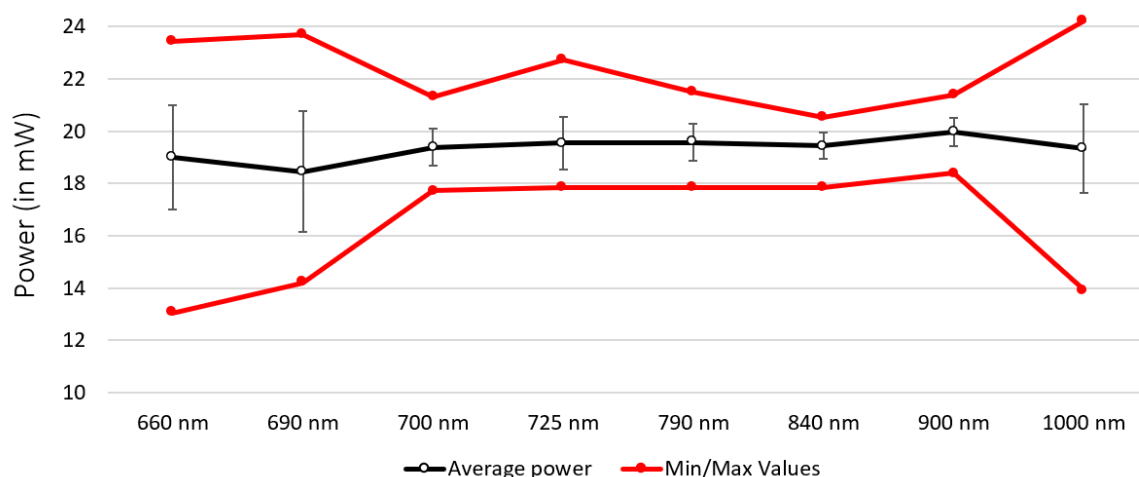


**Figure 4.14:** Pulse laser power measured in the 20 mW experiment at all the wavelengths studied, with the average of 100 measurements in black, the error bars representing the standard deviation and the minimum and maximum values in red.

The reflectance spectra were taken at each step of the experiment, and the shift  $\Delta\lambda_{pNIPAAM-Laser}$  was recorded and plotted for every laser wavelength and polarisation angle used. All the spectra with the positions of the plasmonic resonance labelled are available in **Appendix A**, with **Figure A.1** for the short rods and **Figure A.2** for the long rods.

After the laser heating step, the QD solution was deposited at the surface of the rods and left for 24 h. The sample was then rinsed with PBS to remove the unbound QDs, and the sample was dried with an N<sub>2</sub> gun to take SEM images of each array. Because the QDs are crystals of semiconductor materials, they are easy to visualise on the gold surface of the nanorods. In **Figure 4.15**, an example of a rod that has not been heated can be seen in (a) compared to a laser irradiated rod in (b).

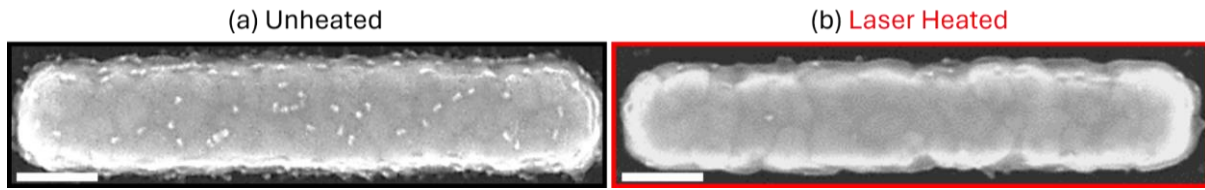


**Figure 4.15: SEM images of (a) an unilluminated short rod functionalised with QDs and (b) a short rod irradiated with a 660 nm pulse laser at 0° with a fluence of 255 mJ.cm<sup>-2</sup> (the scale bar represents 100 nm). These rods were present on the same silicon wafer, and were exposed to the same QDs solution.**

The pulse laser intensity profile doesn't have a perfect 'top hat' shape over the surface of the sample; thus, the middle of the array received a higher power than the edges. This was confirmed by increasing the power of the laser above 20 mW, which showed signs of damage at the centre of the array but not on the edge. The position where the SEM images were taken is therefore important, and only the structures at the centre of the arrays were considered in the rest of this study.

To compare the average number of QDs on the rods illuminated under different laser parameters (polarisation angles and wavelengths), the percentage of QD reduction  $R$  was defined:

$$R = \left[ 1 - \left( \frac{n_{laser}}{n_{ref}} \right) \right] \times 100 \text{ (\%)} . \quad (4.5)$$

Where  $n_{laser}$  is the average number of QDs per rod subjected to laser heating, and  $n_{ref}$  is the average number of QDs found per unilluminated rod.

To obtain these average numbers of QDs per rod, the QDs were counted on a total of 30 rods taken at 6 different locations on each different array. Tables summarising all the QD counts from the SEM images, along with the averages and standard deviation values are available in **Appendix B**.

If  $R = 100 \%$ , it means that there are no QD on the illuminated rods. In the case where  $R = 0 \%$ , there are as many QDs as with the unilluminated rods. In this experiment,



the average number of QDs per rod  $n_{ref}$  was found to be  $29 \pm 5$  QDs on the short unilluminated rods, and  $33 \pm 6$  QDs for the long unilluminated rods (from 30 rods on 6 different arrays).

The reflectance shifts  $\Delta\lambda_{pNIPAA\text{-}Laser}$  and the percentage of QD reduction ( $R$ ) are presented in **Figure 4.16** for both rod lengths with all the studied laser wavelengths and polarisation orientations ( $0^\circ$  and  $90^\circ$ ).



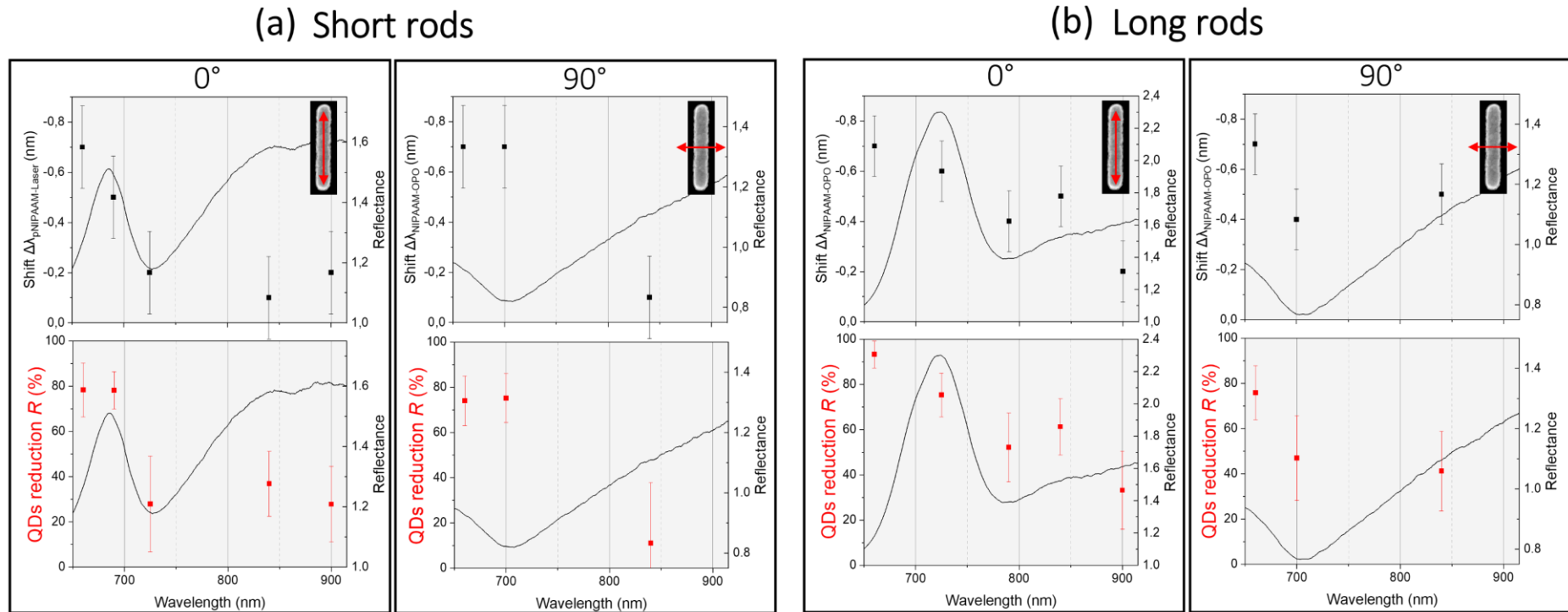


**Figure 4.16: 20 mW data of (a) short and (b) long rod with  $\Delta\lambda_{pNIPAAm-Laser}$  in black and QD reduction ( $R$ ) in red as a function of the wavelength of the laser for both  $0^\circ$  and  $90^\circ$  laser polarisation (shown by the red arrow relative to a rod on the insert image). The reflectance spectra corresponding to the laser polarisation are overlaid on each panel (black lines). The error bars are the standard deviation of 5 spectra for  $\Delta\lambda_{pNIPAAm-Laser}$  data and 30 different rods for  $R$ .**

The comparison between  $\Delta\lambda_{pNIPAAM-Laser}$  and  $R$  in **Figure 4.16** shows a good correlation, meaning that the shift in the plasmonic resonances can predict the number of QDs on the functionalised rods. Collecting the reflectance of millions of nanostructures is an effective tool to detect small molecular changes in the thermoresponsive layer. This structural collapse of *p-NIPAAM* is shown here to dictate the chemical activity of the nanostructures, which is verified by the number of QDs attached through biotin-streptavidin bonding. An important observation from **Figure 4.16** is that the QD reduction is higher at lower wavelength. This shows that the collapse of *p-NIPAAM* occurs over a wide range of temperatures. Therefore, the number of QDs observed on the structures can also give us information on the heat generated by the nanorod assemblies when irradiated by the pulse laser.

A significant decrease in QDs can be observed at the 660 nm laser wavelength, regardless of the polarisation of the beam and the size of the rods (see **Figure 4.16** (a) and (b)). For a laser wavelength of 1000 nm, no decrease in QDs number was observed due to a lack of transmission of the objective (see **Figure 4.9**) and the absorption of light in the water above the nanostructures at this wavelength [194]. This data point was therefore not included in the figures but can be found in **Appendix A** and **Appendix B**.

Interestingly, long rods illuminated at 725 nm/0° show a significant reduction in QDs ( $R = 76 \pm 10 \%$ ) while the short rods show little change compared to the unilluminated reference, with  $R = 28 \pm 20 \%$  (see **Figure 4.16**). The opposite behaviour is observed for 700 nm/90° laser settings. Here, a reduction factor  $R = 75 \pm 11 \%$  is obtained on the short rods compared to  $R = 47 \pm 19 \%$  on the long rods (see **Figure 4.16**). The opposite behaviour in both aspect ratios is again observed for laser parameters of 840 nm/90°, with  $R = 11 \pm 27 \%$  and  $R = 41 \pm 18 \%$  for the short and long rod sizes, respectively (see **Figure 4.16**).

SEM images of two rods per aspect ratio are shown in **Figure 4.17**, where all the laser settings discussed before are presented, along with the average number of QDs per rod. **Figure 4.17** shows that the QDs are randomly located on the rods and that they can almost completely be removed from the nanostructures using a pulse laser at 660 nm/0°. As observed before, the long rods show far fewer QDs than the short rods for the same laser parameters of 725 nm/0°. The opposite behaviour can be seen at 700 nm/90°. With a laser at 840 nm/90°, there is a slightly lower amount of QDs on the long rods compared to the short rods.

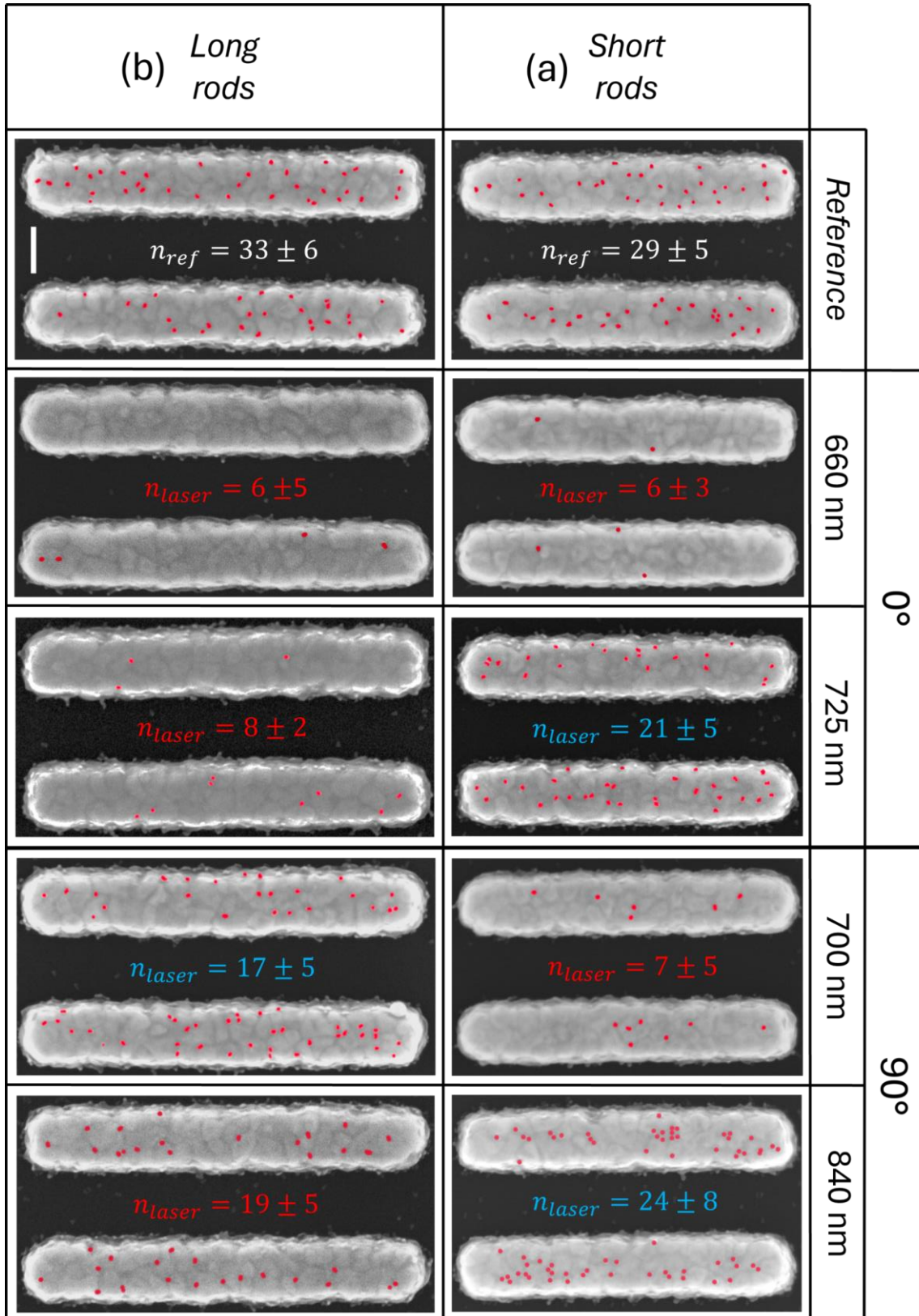
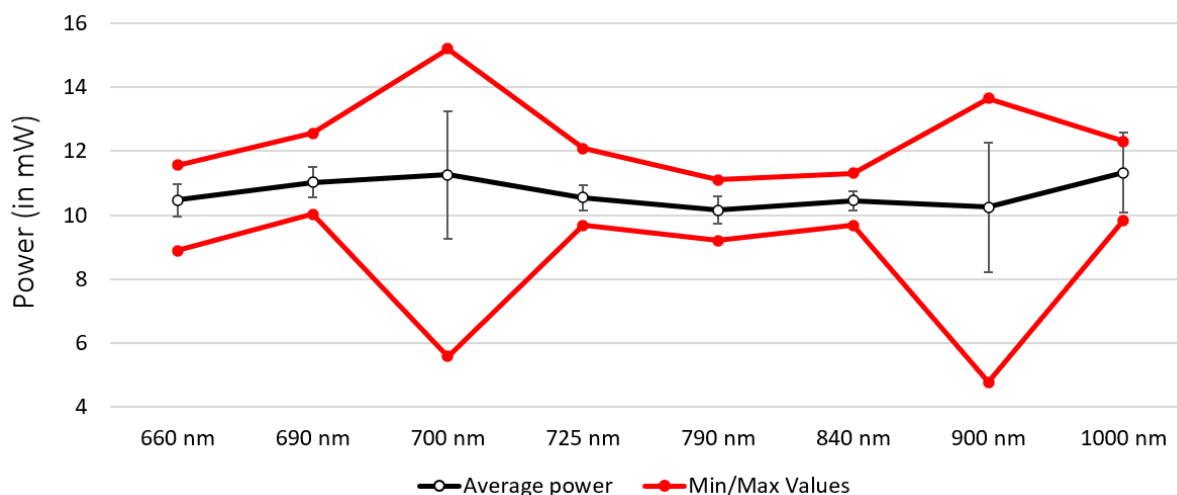


Figure 4.17: SEM images of (a) short and (b) long rods with the QDs in red. The unilluminated rods are compared to the rods irradiated by a 20 mW pulse laser. The average number of QDs per rod (30 rods) and the standard deviation are displayed in red for the lowest values and blue for the highest. The scale bar is 100 nm.

### 4.4.3 Experiment 10 mW

Here the experiment was repeated with half the power. This will provide additional information on the thermoplasmonic properties of both nanorod lengths. The power measured at each laser wavelength is plotted in **Figure 4.18**.



**Figure 4.18:** Pulse laser power measured in the 10 mW experiment at all the wavelengths studied, with the average of 100 measurements in black, the error bars representing the standard deviation and the minimum and maximum values in red.

For this experiment too, the reflectance spectra were measured at each step of this experiment and SEM images of the rods were taken at the end. The reflectance shifts  $\Delta\lambda_{pNIPAAM-Laser}$  and the QD reduction factor  $R$  were calculated for both rod aspect ratios at all the laser settings, and are presented in **Figure 4.19**. The reflectance spectra for all the laser wavelengths are available in **Appendix C**, with **Figure C.1** for the short aspect ratio and **Figure C.2** for the long one.

(a) Short rods

(b) Long rods

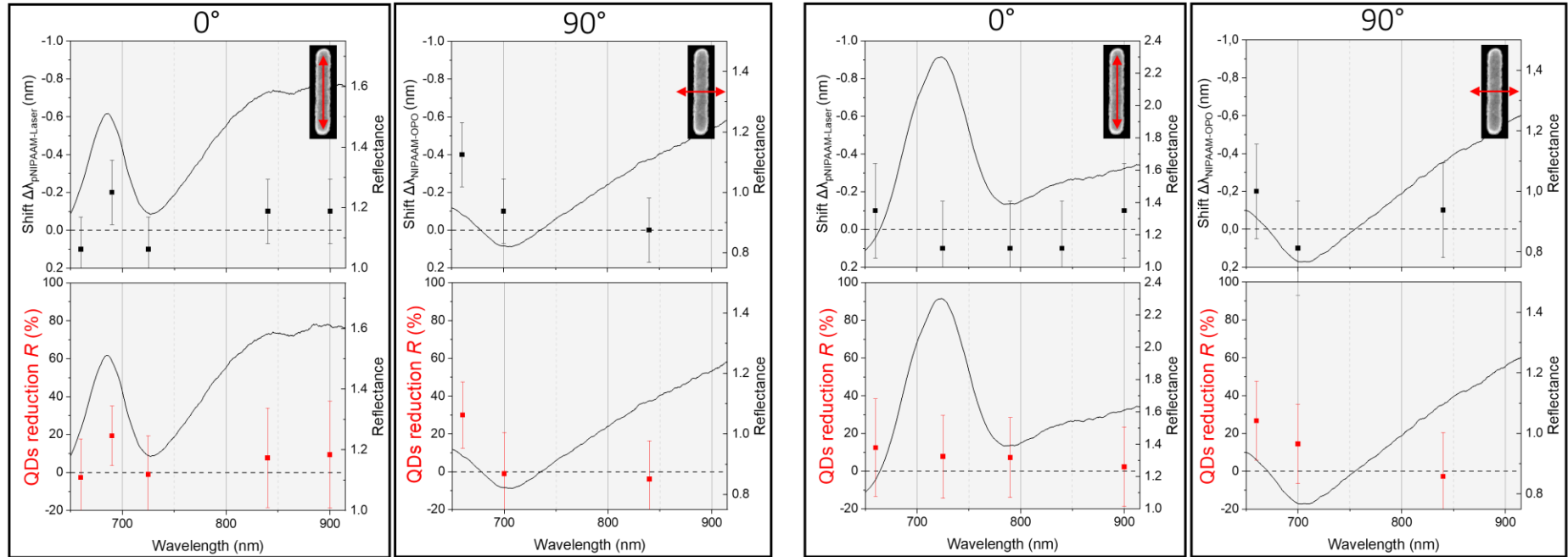
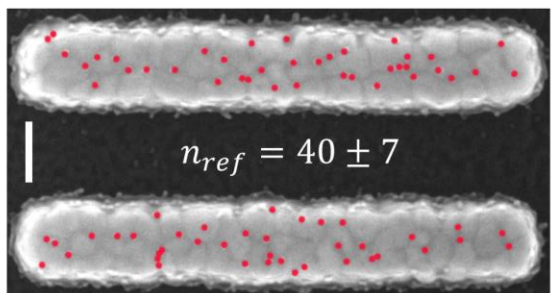
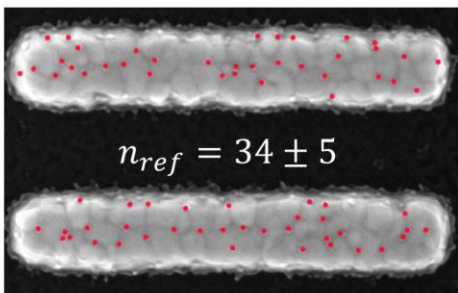
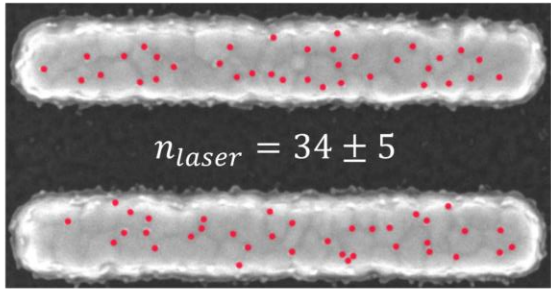
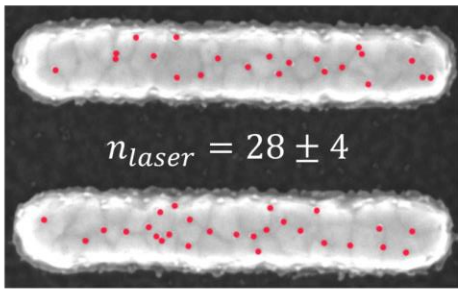
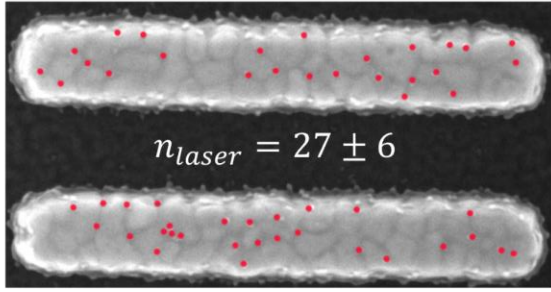
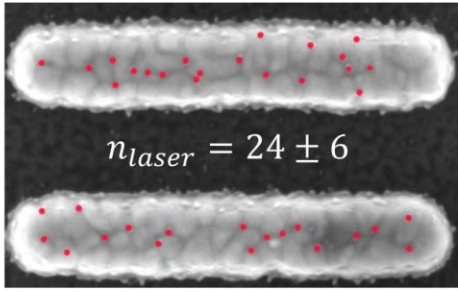


Figure 4.19: 10 mW data of (a) short and (b) long rods with  $\Delta\lambda_{pNIPAAM-Laser}$  in black and QD reduction factor ( $R$ ) in red as a function of the wavelength of the laser for both  $0^\circ$  and  $90^\circ$  laser polarisation (shown by the red arrow relative to a rod on the insert image). The reflectance spectra corresponding to the laser polarisation are overlaid on each panel (black lines). The error bars are the standard deviation of 5 spectra for  $\Delta\lambda_{pNIPAAM-Laser}$  data and 30 different rods for  $R$ .

Here, the laser heating causes a smaller blue shift  $\Delta\lambda_{pNIPAAAM-Laser}$  compared to the previous experiment carried out at a higher power. As expected, the QD reduction factor  $R$  mirrors this trend and only shows a slight change compared to the unilluminated rods (see **Figure 4.19**). The only laser wavelength and polarisation combinations showing any significant removal of QDs with respect to the reference unirradiated structures are 690 nm/ $0^\circ$  on the short rods, with  $R = 20 \pm 15 \%$ , and 660 nm/ $90^\circ$  for both short and long rods, with  $R = 30 \pm 17 \%$  and  $R = 26 \pm 20 \%$ , respectively.

The SEM images comparing the unilluminated rods to the rods irradiated at their plasmonic resonant wavelengths (690 nm for the short rods and 725 nm for the long rods) and at 660 nm/ $90^\circ$  are displayed on **Figure 4.20**.

| (b) Long rods   |  | (a) Short rods   |  |              |            |
|---|--|--|--|--------------|------------|
|   |  |   |  | Reference    |            |
|  |  |  |  | ON Resonance |            |
|  |  |  |  | 660 nm       | $90^\circ$ |

**Figure 4.20:** SEM images of (a) short and (b) long rods with the QDs in red. The unilluminated rods are compared to the rods irradiated by a 10 mW pulse laser. The average number of QDs per rod (30 rods) and the standard deviation are displayed at the centre of the images. The scale bar is 100 nm.



These results show that, as expected, the QD functionalisation is power dependent. Using a 10 mW pulse laser doesn't reduce significantly the QDs, which are still visually noticeable compared to the previous experiment. From these observations, we can conclude that the heat generated by the nanostructures was only able to reach values above the LCST of *p-NIPAAm* for 690 nm/0° on the short rods and 660 nm/90° for both rod sizes.

#### 4.4.4 Simulation results

Numerical simulations were performed to understand how the wavelength and polarisation dependency of plasmonic resonances impact the heat generated by nanorods and how this heat is transferred to the surrounding medium. A simulation model was defined for each rod length using an AFM file. This rod was set in the middle of the block between a silicon and water domain and periodic boundary conditions were set to mimic an array of rods (see **Figure 4.21**).

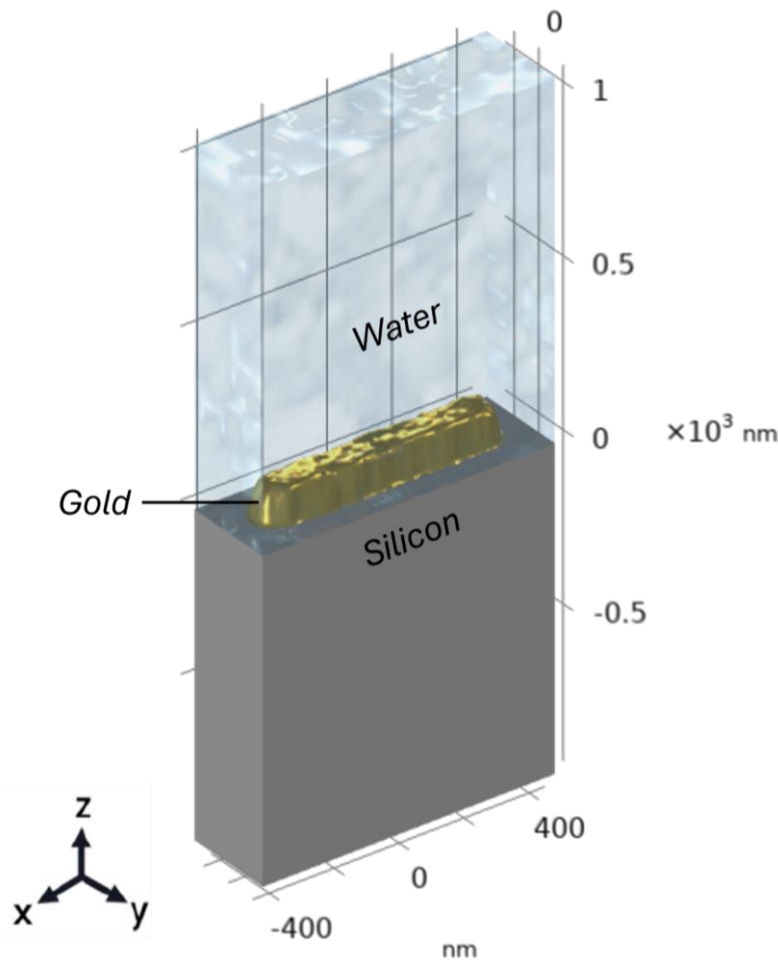


**Figure 4.21: COMSOL model of a short gold nanorod positioned in the middle of a 2000 nm high block, between the silicon and water media.**

Similar to other studies, the thermoresponsive polymer was assumed to have comparable optical and thermal properties as the solvent [162,185]. The temperature of the solvent close to the gold surface was thus considered to be the temperature reached by the polymer. This polymer domain was made by a 10 nm thick volume around the gold rod and the temperature was averaged inside.

To verify the fidelity of the models with the experimental data, the optical properties of the simulated rods were compared to the experimental data. First, the relative reflectance of the rods obtained in the simulation and the experiment was compared (see **Figure 4.22** (a) and (b)). For better clarity, the resonance peaks of the simulated plots were horizontally shifted to align with the wavelengths observed on experimental data ( $\sim 10$  nm red shifted). It is common to observe a red shift in the simulated spectra compared to the experiment. They are caused by the inherent simplification of the model compared to the real-world setup. In these simulations, the rods are made from AFM micrographs of the real rods. But the side wall of these AFM models is often distorted (as discussed in Section 3.2.1), leading to a difference in the resonance position.

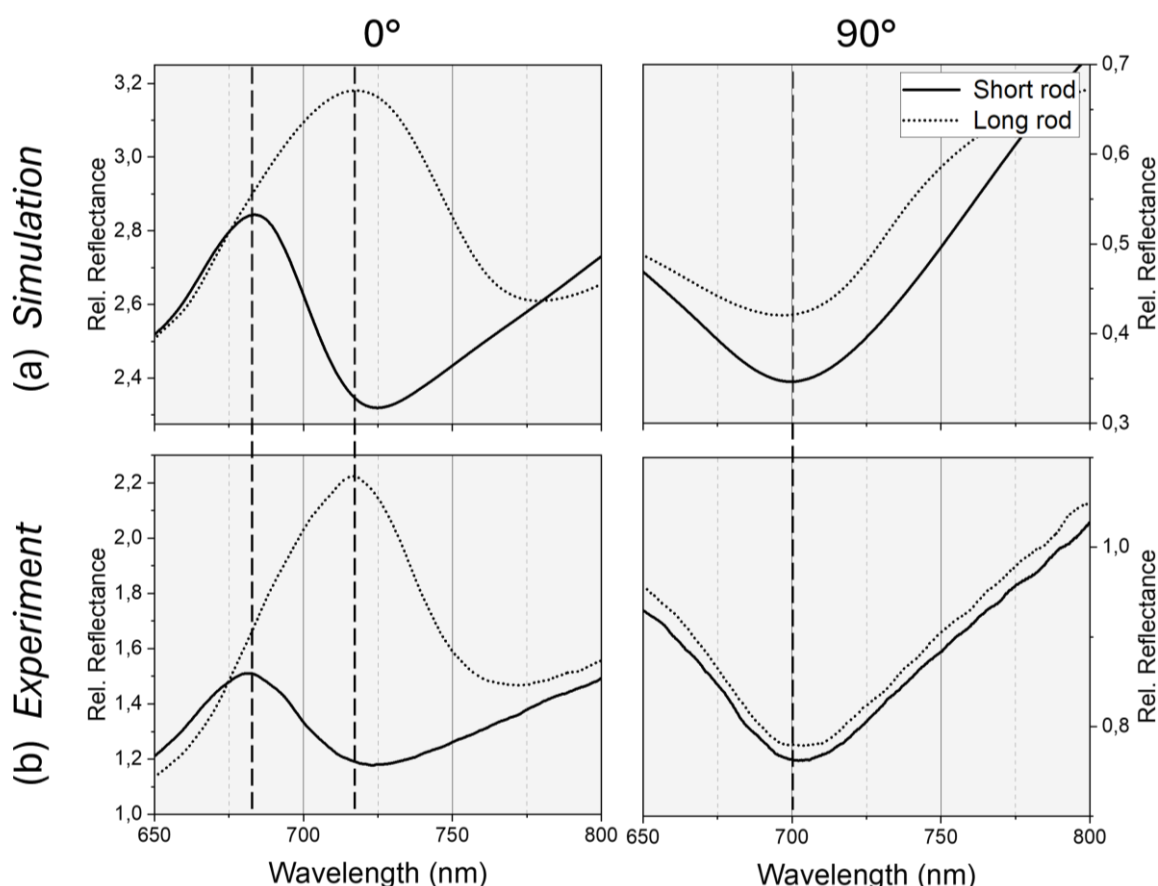


**Figure 4.22:** Reflectance spectra relative to the silicon background, with (a) simulated and (b) experimental spectra at  $0^\circ$  and  $90^\circ$  polarisation on the left and right columns, respectively. The short rod data is in the solid dark lines and the long rod data is in the dotted lines. The position of the resonance peaks is highlighted by dashed vertical lines.



On **Figure 4.22** (a) and (b), the plasmonic resonances on the reflectance spectra of the simulations qualitatively match the data obtained experimentally. With a resonance peak at 680 nm for the short rod and 720 nm for the long rod array at 0° polarisation. As for the 90° polarisation angle, a dip at 700 nm can be observed, matching the shape of the experimental spectra. The reflectance values in the simulation model are overestimated in the case of a 0° incident light but underestimated for 90° compared to the experimental data. This discrepancy will clearly mean a poorer quantitative agreement with the simulated temperature rises and the actual temperatures reached in the real system, since the amount of absorption will be under / overestimated.

As seen in equation (2.49), the absorption cross-section ( $\sigma_{abs}$ ) of the nanostructure plays a significant role in heat power generation. The absorption spectra will therefore be proportional to the temperature of the nanorods. The absorption (*Abs*) was calculated from the reflected light (*Ref*) and the transmitted light (*Trans*) in the simulation models, using the formula [195]:

$$Abs (\%) = 1 - Ref (\%) - Trans (\%) . \quad (4.6)$$

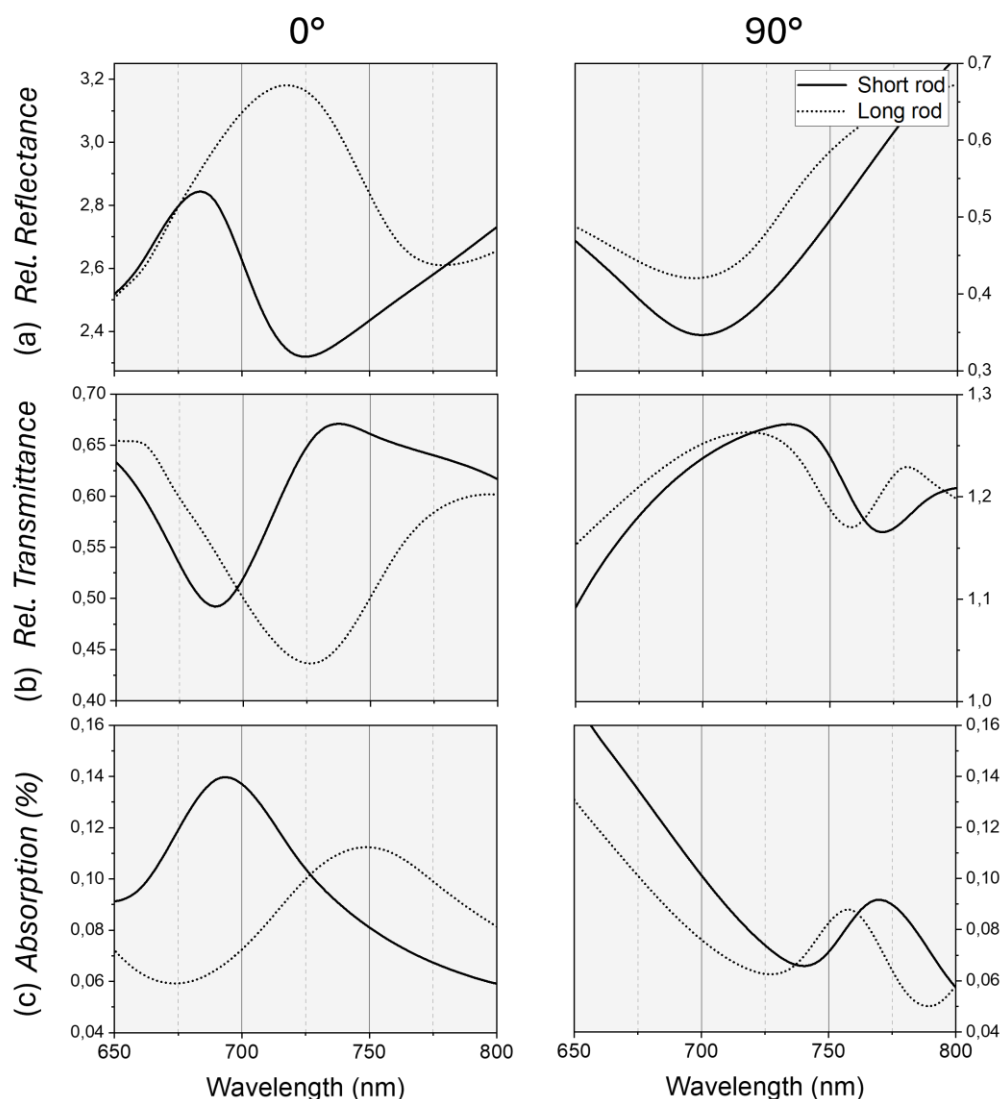


**Figure 4.23:** Simulation spectra of (a) the reflectance, (b) the transmittance and (c) the absorption for a polarisation of the incident beam at  $0^\circ$  and  $90^\circ$  on the left and right columns, respectively. With the short rod data in a solid line and the long rod data in a dotted line.

The absorption spectra shown in **Figure 4.23** (c) have different profiles compared to the relative reflectance (see **Figure 4.23** (a)). For a  $0^\circ$  polarisation angle, the absorption peaks are positioned at 695 and 750 nm for the short and long rods, respectively. With a  $90^\circ$  incident beam, a dip is observed at 728 nm for the short rod and 740 nm for the long rod. The position of the maximal absorption cross-section, and thus the temperature of the nanoparticle, have been shown to correlate with the position of the LSPR in the case of an isolated nanoparticle [196]. Here, we are studying a periodic assembly of nanorods, which will generate complex field coupling between the neighbouring plasmonic structures, resulting in different positions of the reflectance and absorption peaks. Some arrays of plasmonic nanostructures have been shown to produce an even larger mismatch between the scattering and absorption resonances [197].

Now that the optical properties of the model have been established, the temperature in the model can be studied. The average temperature in the gold rod and in the 10 nm water domain around it was plotted as a function of time (see **Figure 4.24**). A steep increase in the rod's temperature is noticeable during the laser pulse, closely followed by the surrounding water domain, where the *p-NIPAAM* SAM is subjected to a thermal gradient. It takes about 20 ns after the pulse for the heat to dissipate and cool down to room temperature. During this time, the thermoresponsive polymer can switch its molecular conformation if the temperature reaches values above the LCST, chemically passivating the rod. The collapse of the polymer chains has been shown to be faster with an increase in temperature [198]. This implies that, for the same pulse duration, the density of the polymer SAM, and therefore its chemical activity, will be proportional to the maximum temperature reached. The emphasis was thus placed on the temperature reached at the end of the laser pulse ( $t = 5\text{ ns}$ ).

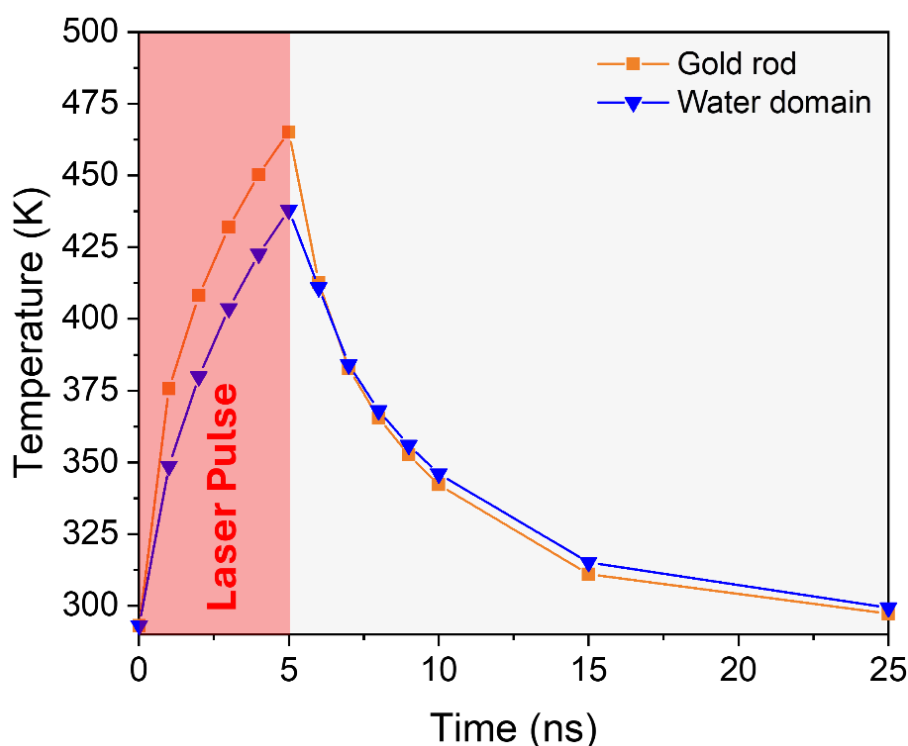


**Figure 4.24:** Average temperature of a short rod in the gold volume (orange) and in a 10 nm water domain around the plasmonic surface (blue) as a function of time. Obtained for a longitudinal polarisation of the pulsed laser relative to the rod at  $\lambda = 690\text{ nm}$  and fluence of  $255\text{ mJ} \cdot \text{cm}^{-2}$ .

To study the impact of the wavelength and polarisation of the laser on heat generation, the temperature in the models was computed just after the laser pulse ( $t = 5\text{ ns}$ ) and was averaged inside the 10 nm water domain close to the surface of the rod. The temperature obtained in both rods at the maximum power for the entire wavelength range and both polarisation angles are presented in **Figure 4.25**.

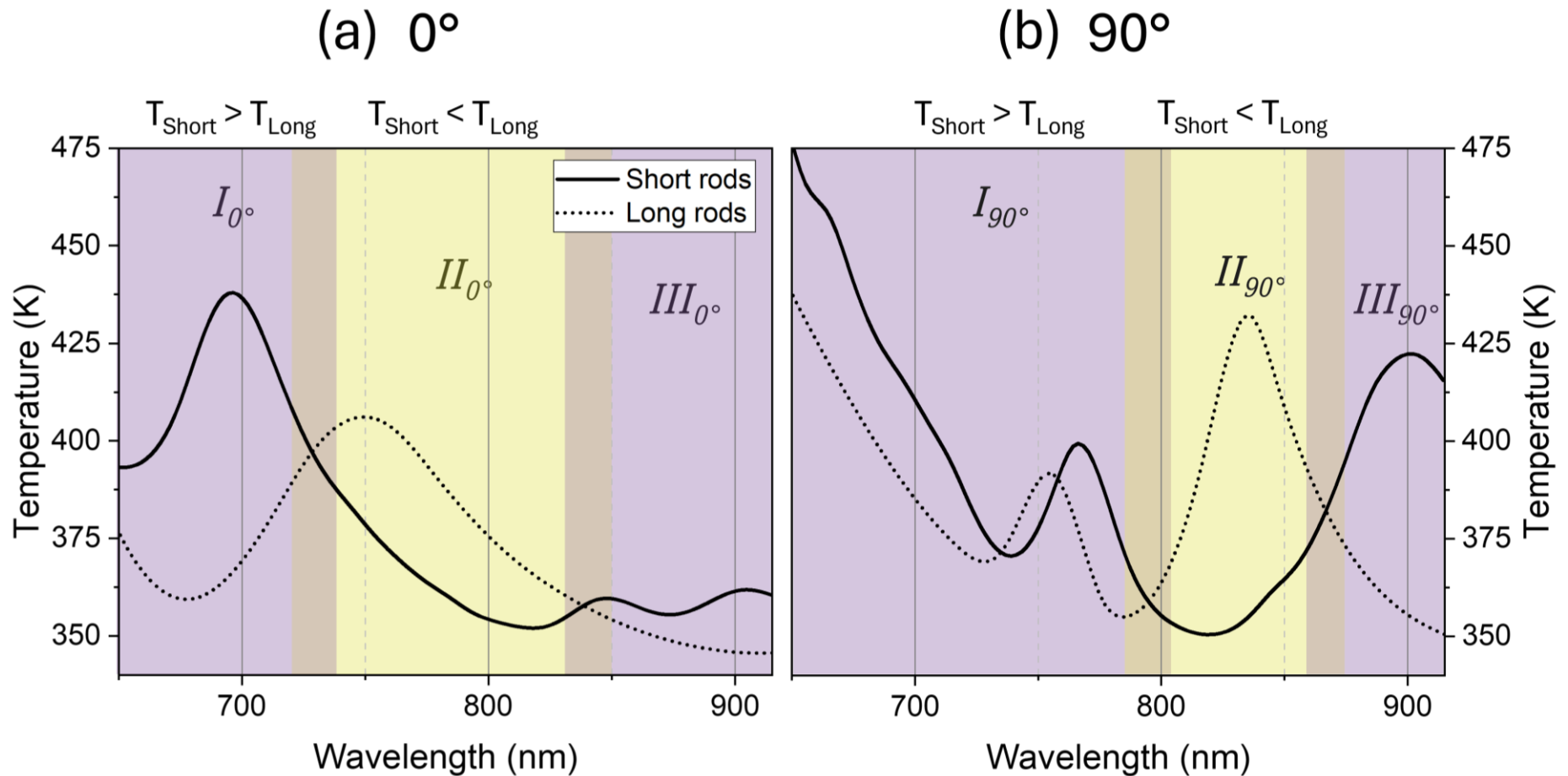


**Figure 4.25:** Average temperature around the gold rod as a function of the laser wavelength after a 5 ns laser pulse for (a)  $0^\circ$  and (b)  $90^\circ$  laser polarisation. A fluence of  $255 \text{ mJ} \cdot \text{cm}^{-2}$  was used. The short rod is represented by a solid line, and the long rod is represented by a dotted line. A purple zone indicates the wavelength range where the temperature for the short rod case is higher than for the long rod and the yellow zone represents the opposite scenario. The intersection of these zones shows the uncertainty of the model.

As expected, the temperature plots follow the light absorption spectra seen in **Figure 4.23** (c). For all the results of **Figure 4.25**, the temperature reached in the simulations has been shown to be above the LCST of *p-NIPAAm* (~316 K), but the simulation models have been assuming an ideal laser and neglecting the losses, which leads to an overestimation of the temperatures. The volume occupied by the *p-NIPAAm* shell is also unknown, thus the 10 nm large domain where the temperature has been averaged can also be a source of discrepancy with the experiments. Furthermore, as discussed before, the duration at which the polymer remained above the critical temperature also plays a key role.

Wavelength zones have been delineated in **Figure 4.25** to highlight ranges where one size reached a higher temperature than the other. When the short rods exhibit a higher temperature than the long ones, purple zones are defined at the relevant wavelength ranges. In the opposite case, the wavelength ranges were highlighted in yellow. The areas of mixed colours highlight regions of uncertainty.

When the laser is polarised in the long axis of the rods ( $0^\circ$ ), the temperature of the short rods is highest in the  $I_{0^\circ}$  region at ~695 nm. For the long rods, this temperature maximum is red shifted compared to the short rods and can be seen in the  $II_{0^\circ}$  zone at ~750 nm. This difference in the position of the temperature maximal is driven by the difference in plasmonic resonance of both rod lengths, impacting the position of their respective absorption cross-section  $\sigma_{abs}$  (see **Figure 4.25** (a)).

In the case of a laser polarised transversely ( $90^\circ$ ), the temperature profiles in the region  $I_{90^\circ}$  are mostly following the same trend. A difference of ~15 nm can be observed in the position of the first dip of both rod lengths. The rods are designed to have the same width; thus, one would expect identical temperature profiles. The shift observed here can be attributed to the inherent error and variation of the numerical simulation method, as well as different angles of the side wall in both AFM rods. In the  $I_{90^\circ}$  region, the small rod has a higher temperature mainly due to a difference in surface-to-volume ratios between both sizes, leading to faster heating in the short rods [199]. In the zone  $II_{90^\circ}$ , the long rods see a sharp increase in temperature at 835 nm, followed by the short rods at 900 nm. This can be rationalised by different plasmonic interactions with other neighbouring rods of the array.

For the half power simulation, the temperature plots were assumed to follow the same profiles as in **Figure 4.25**, only the maximum temperatures at  $0^\circ$  were simulated with 365 K ( $\lambda = 695$  nm) and 350 K ( $\lambda = 750$  nm) for the short and long rods, respectively. These values are still significantly higher than the LCST of approximately 316 K. However, the experimental observations seen in Section 4.4.3 don't show a substantial reduction in QD. This discrepancy highlights the comments made before on the approximation of the simulation model and show the importance of the duration spent above the critical temperature for the polymer's collapse.

## 4.5 Selective QD functionalisation

The experimental work demonstrates selective QD functionalisation of the rods depending on their aspect ratio. This is done through the chemical passivation of a thermoresponsive polymer using a monochromatic pulsed laser at different wavelengths and polarisations. This is achieved thanks to the distinct thermoplasmonic properties of each rod length, despite their similar shape and materials. The simulated temperature profiles of each size as a function of the laser wavelength and polarisation corroborate this statement. The different zones that were defined before show the wavelength ranges where the thermal behaviour of the nanostructures, and therefore their chemical activity, will vary significantly and show selective functionalisation (see **Figure 4.25**).

Experimentally, with a 20 mW laser, selective QD functionalisation was observed with pulse laser parameters of 725 nm/0° and 700 nm/90°. Indeed, a 725 nm/0° pulse laser could passivate significantly more the long rods compared to the short rods. This difference is clearly noticeable on the SEM images presented in **Figure 4.17**, where the average number of QDs per rod is  $21 \pm 5$  for the short rods and  $8 \pm 2$  for the long rods. Conversely, a pulse laser at 700 nm/90° achieved the opposite effect (see **Figure 4.17**), where the average number of QDs is  $7 \pm 5$  on the short rods and  $17 \pm 5$  on the long rods. Consequently, one can assume that the temperature difference between the short rod and the long rod,  $\Delta T = T_{Short} - T_{Long}$  is equal and opposite for both laser heating settings (725 nm/0° and 700 nm/90°).

In the simulated temperature profiles in **Figure 4.25**, 725 nm/0° is in the  $II_{0^\circ}$  zone (coloured in yellow) and 700 nm/90° is in  $I_{90^\circ}$  (coloured in purple), which is in qualitative agreement with the experimental observations. Although the simulation at 725 nm/0° doesn't show a significant temperature difference, extrapolation at 740 nm gives heating patterns consistent with the experimental results. The simulated temperature difference for 740 nm/0° is  $\Delta T = 383 - 405 = -22 \text{ K}$  and for 700 nm/90° it is  $\Delta T = 409 - 383 = 26 \text{ K}$ , yielding similar absolute values for  $\Delta T$  (see **Figure 4.25** (a) and (b)).

These two opposite cases of selective QD functionalisation are summarised in **Figure 4.26**, where simulated heat maps are associated with their corresponding experimental SEM images. For a 725 nm/0° laser, the heat maps (yellow  $II_{0^\circ}$  region) clearly show a higher temperature inside the long rod compared to the short rod, which translates into a large difference in the amount of QDs on the SEM of the rods (see **Figure 4.26** (a)). These rods, illuminated in their long axis, exhibit higher temperatures at their extremities due to strong plasmonic enhancement at both ends of the nanostructure [200]. This temperature gradient dissipates quickly after the laser pulse and no difference in the special distribution of the QDs on the rods is observed. In the second case, the opposite effect is obtained by using a 700 nm/90° laser (purple region  $I_{90^\circ}$ ), which

generates a higher temperature in the short rods compared to the long rods, preferentially functionalising the long rod with QDs (see Figure 4.26 (b)).

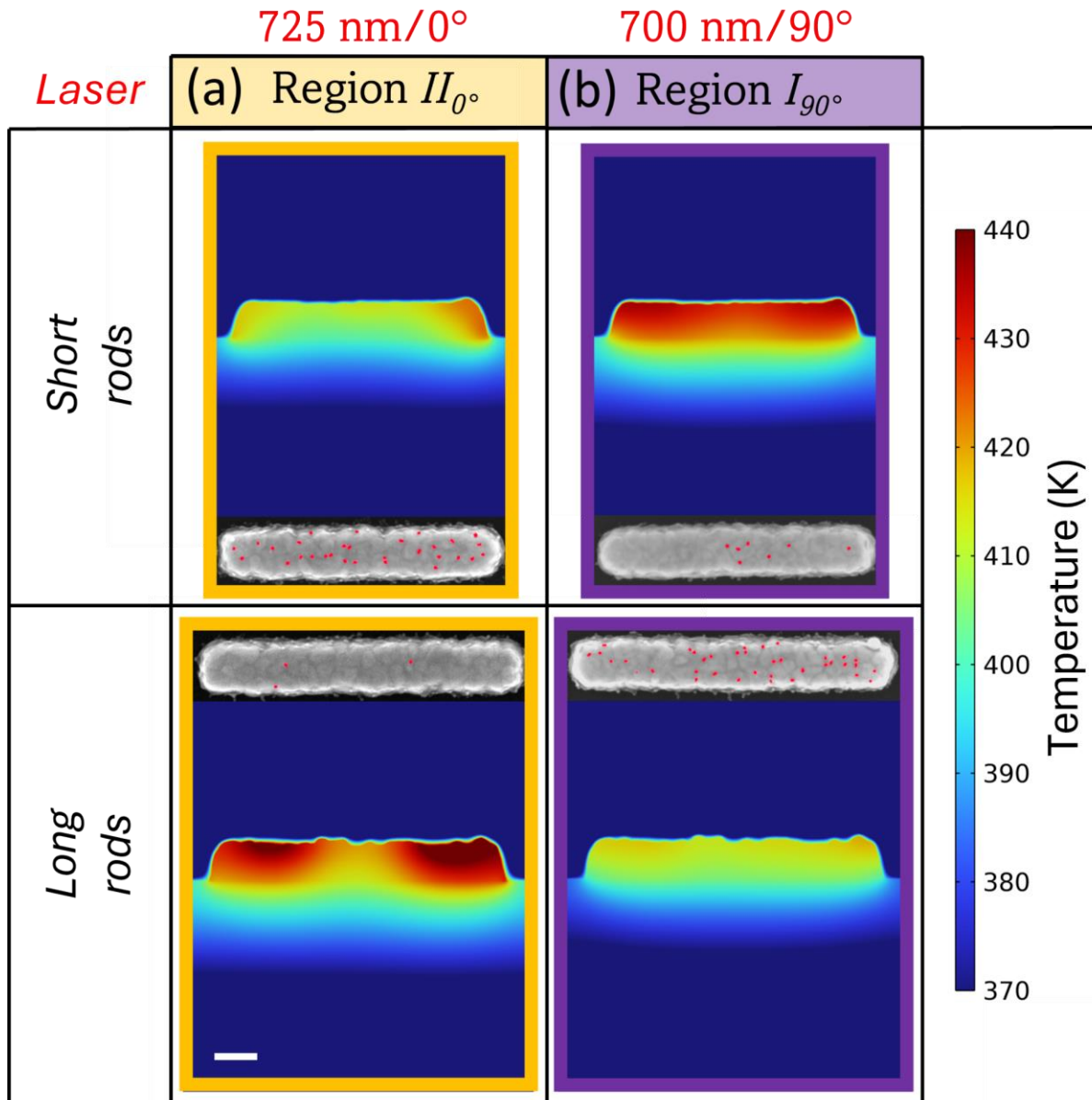


Figure 4.26: Simulated heat maps and SEM images with QDs in red of both rod lengths after 5 ns laser irradiation at different parameters with (a) 725 nm/0° (740 nm simulated) and (b) 700 nm/90°. The heat maps are taken from a slice *in the middle* of the rods. The scale bar represents 100 nm.

According to Figure 4.25, one would expect to observe more cases of selective QD functionalisation in the experimental results. Indeed, the temperature profiles between the short and long rod exhibit large temperature differences in the  $I_{0^\circ}$ ,  $I_{90^\circ}$  and  $II_{90^\circ}$  regions, which were tested experimentally at 660 nm/0°, 660 nm/90° and 840 nm/90°, respectively.

The laser irradiation at 660 nm in the 20 mW experiment resulted in the greatest amount of QD reduction for both polarisation angles, with no significant difference between both rod aspect ratios (see **Figure 4.16** and **Figure 4.17**). This is inconsistent with the simulated temperatures (see  $I_{0^\circ}$  and  $I_{90^\circ}$  in **Figure 4.25**). But it can be explained by the instability of the laser heating setup at this wavelength (see **Figure 4.14**). Where the maximum power at 660 nm reached values 20% higher than the mean, potentially heating the polymer far beyond its LCST, which explains why both rod lengths have a low amount of QDs. In the 10 mW experiment, the power measured at 660 nm is more stable and closer to the mean (see **Figure 4.18**). In this experiment, the only laser parameters showing a reduction in QD against the unilluminated rods ( $R > 0\%$ ) are 660 nm/ $90^\circ$  for both aspect ratios and 690 nm/ $0^\circ$  for the short rod size (see **Figure 4.19**). This is coherent with the simulation results, where these parameters are also shown to produce the highest temperatures in the simulation model (see **Figure 4.25** (a) and (b)). Although, no significant selective QD functionalisation is observed due to the temperature generated being too low at this power.

In the case of a laser heating at 840 nm/ $90^\circ$ , the long rods have a slightly lower average number of QD ( $n_{laser} = 19 \pm 5$ ) compared to the short rods ( $n_{laser} = 24 \pm 8$ ) (see **Figure 4.17**). The simulation agrees qualitatively with this observation, where 840 nm is in the  $II_{90^\circ}$  region, with a temperature difference of  $\Delta T \approx 64\text{ K}$  (see **Figure 4.25** (b)). This is too high to account for the small difference in QD number observed experimentally. This can be partially explained by the difference in transmittance of the objective used in the laser heating setup, with a value  $> 90\%$  for  $\lambda = 700\text{ nm}$ , decreasing to 70% for  $\lambda = 840\text{ nm}$  (see **Figure 4.9**). This will cause a decrease in the effective power, thus a lower temperature inside the rods. The other cause of discrepancy could be attributed to the simulation model itself. As discussed before, computation models are not perfect representations of reality and may give results that are not quantitatively coherent with the experiments.



## 4.6 Conclusion

To summarise, a novel approach was presented to achieve selective functionalisation of nanostructures using a monolayer of biotinylated thermoresponsive polymer, *p-NIPAAm*, which enables the controlled removal of streptavidin-conjugated QDs. By exploiting the heat generated through thermoplasmonic phenomena, tailored to each nanorod's specific size, we have reduced the chemical selectivity of the biotin end group of the polymer chains. The variation in plasmonic properties across different rod aspect ratios enables distinct outcomes with the same laser input. This technique offers significant tunability, achieved by adjusting the wavelength and polarisation of the pulsed laser, allowing for precise control over the functionalisation process. A key advantage of this approach is its high throughput and speed, enabling efficient functionalisation of large areas of plasmonic nanostructures. Furthermore, this method provides incremental control over QD quantities, unlike traditional approaches that operate in a more binary state (100% or 0%).

By combining thermoplasmonics with thermoresponsive polymers like *p-NIPAAm*, we have demonstrated a versatile route for producing advanced functional materials over macroscopic scales. The main challenges of this technique include the need for a complex optical setup and a deep understanding of the thermoplasmonic properties of the sample, which may require extensive testing and simulations.

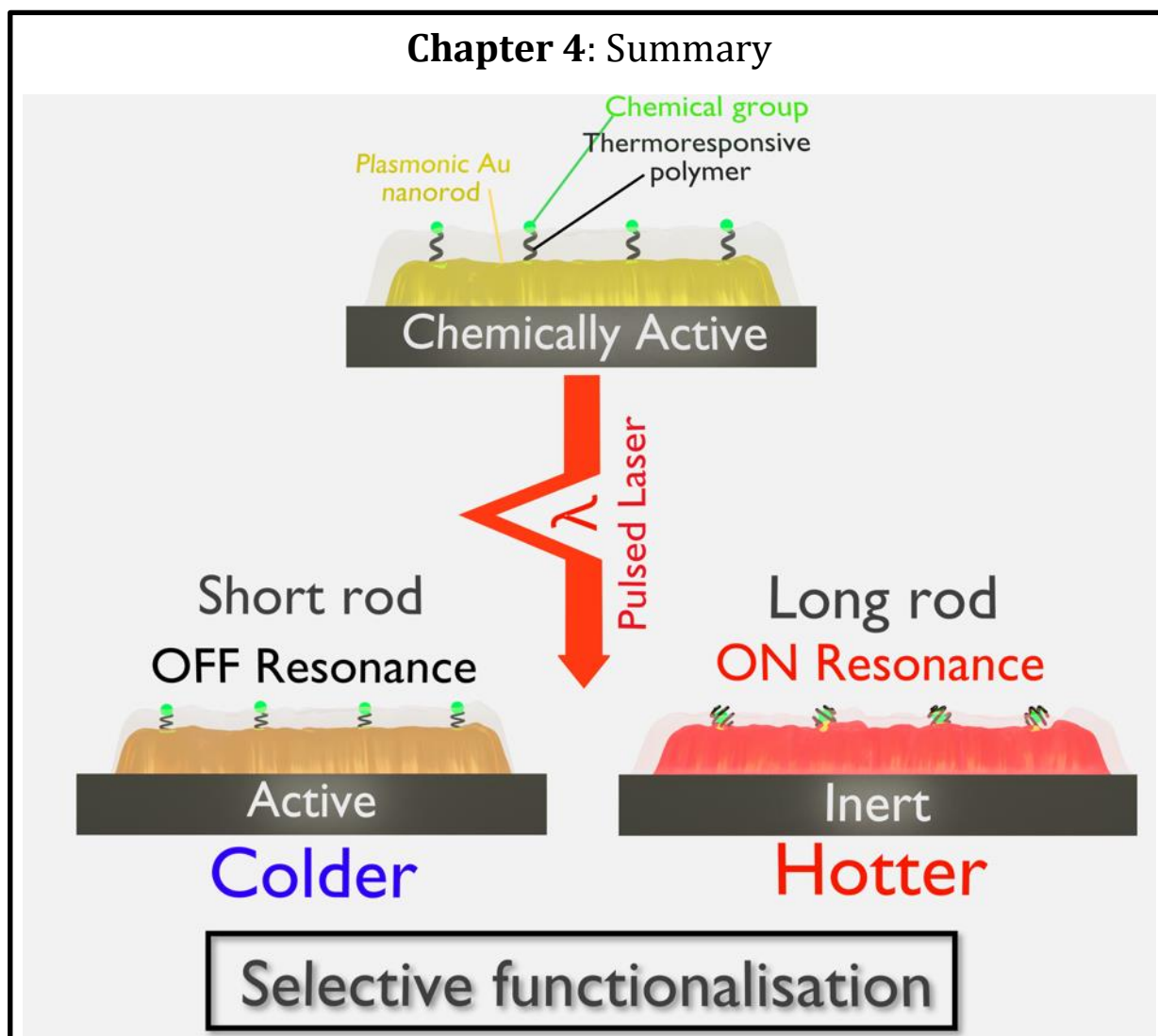


Figure 4.27: Chapter 4 concept illustration.

**Key Findings:**

- Successfully controlled the chemical selectivity of biotin at the surface of nanostructures through the intermediary of an adsorbed thermoresponsive polymer (*p-NIPAAM*), which was visually tested using streptavidin conjugated QDs bonding.
- A 5 ns pulsed laser was used to generate heat locally in large arrays of plasmonic nanorods, controlling the molecular conformation of *p-NIPAAM* (switch).
- Selective functionalisation was achieved by exploiting the different thermoplasmonic properties of the different nanorods for the same laser wavelength and polarisation.

# Chapter 5

---

Plasmonic Luminescence  
for Enhanced Bio-Detection

## 5.1 Introduction

The detection of biological molecules using plasmonic metamaterials has been extensively studied and offers a promising solution for various applications in the field of biomedical analysis [201]. These materials are able to manipulate light below the limit of diffraction [202], allowing for the detection of femtomole quantities of analytes. By using a pair of chiral plasmonic nanostructures, it is possible to generate an enhanced superchiral near field of opposite handedness that will interact differently with a chiral medium, allowing for the enantiomeric discrimination of chiral molecules. These changes in the EM fields at the surface of plasmonic samples are generally measured in the far field, using scattering spectroscopic techniques. The sensitivity of these techniques depends on the volume occupied by the molecules with respect to the extent of the near field at the surface of the nanostructures [189]. A single layer of molecules is often used, making these bio-detection techniques sensitive only to large molecules. Consequently, a technique sensitive to local changes in the optical chirality of the near field is required when investigating chiral molecules of small molecular weight.

In this chapter, a novel technique named plasmonic circularly polarised luminescence (PCPL) is used to probe the near field of plasmonic nanostructures. This technique has been successfully applied to the chiral detection of a monolayer of *de novo* peptide. To confirm the near field sensitivity of PCPL, the performance of this strategy has been benchmarked against the traditional far field light-scattering measurements. Additional work using numerical simulation is also presented in this chapter, giving further insight into the local field properties and validation of the experimental observations.

## 5.2 Background

### 5.2.1 Plasmonic enhanced photoluminescence

Photoluminescence (PL) is the process by which light is emitted from a material after absorbing photons. This phenomenon occurs when absorbed photons elevate electrons to higher energy states, and as the electrons return to a lower energy state, they release the excess energy as light. PL is divided into two different phenomena, fluorescence and phosphorescence. Fluorescence is characterised by the fast relaxation time of the excited electron, generally in the pico to nanosecond range. This is due to the spin allowed in the transition between states of the same multiplicity, and the nature of

the transition. Phosphorescence, which is a spin-forbidden process due to transitions between states of different multiplicities, happens on a much longer timescale, typically seconds [203].

PL from gold was first observed in 1969, when a sample was illuminated by UV light, which resulted in the emission of visible to near-IR photons [204]. Photon excitation creates holes in the d-band of the metal, which are recombined with electrons near the Fermi level, releasing photons of a characteristic energy.

It has been observed that plasmonic excitation can enhance the amount of luminescence of metals through the roughness of the metal surface [205]. In plasmonic nanostructures, PL enhancement is linked to the increase of the spontaneous emission rate in the vicinity of plasmonic nanostructures, where the near field is strongly enhanced [206]. Since this discovery, a lot of research has been dedicated to the study of NP of various shapes, including nanospheres, nanorods, and nanowires, among others [207–209]. The applications of the plasmonic enhanced PL phenomenon encompass surface-enhanced spectroscopy, bioimaging, solar energy and display technology [210].

Fermi's golden rule states that the spontaneous emission rate of an excited emitter is directly linked to the local density of optical states (LDOS) at its position and transition frequency. The LDOS refers to the number of optical modes available per unit of volume at a set location and frequency, determining the efficiency of light emission at that point [54]. In a homogeneous and isotropic medium, the LDOS  $\rho(r_0, \omega)$  at a position  $r_0$  and frequency  $\omega$  is given by [211]:

$$\rho(r_0, \omega) = \frac{2\omega n^2}{\pi c^2} \text{Tr}[\text{Im}[\mathbf{G}(r_0, r_0, \omega)]] . \quad (5.1)$$

With  $n$ , the refractive index of the medium,  $c$ , the speed of light in vacuum and  $\mathbf{G}(\mathbf{r}, \mathbf{r}', \omega)$ , the electromagnetic dyadic *Green* function, which is a  $3 \times 3$  tensor that represents the response of an EM field located at  $\mathbf{r}$  to a point source positioned at  $\mathbf{r}'$  [212]. When an emitter is placed in the vicinity of a plasmonic nanostructure, the localised surface plasmon resonances will influence the LDOS experienced by this emitter compared to the case in free space. The LDOS can be enhanced or quenched depending on the distance separating them, and the overlap in their respective resonances [213].

The Purcell effect is another phenomenon that can lead to an enhancement of the spontaneous emission rate of an emitter when it is placed in a resonant optical cavity [214]. This phenomenon is linked to Fermi's golden rule and is proportional to the change in the LDOS at the emitter position in a cavity relative to free space. The enhancement in emission rate is referred to as the Purcell factor ( $F_p$ ) [215]:

$$F_p = \frac{\gamma}{\gamma_0} = \frac{3}{4\pi^2} \left(\frac{\lambda_0}{n}\right)^3 \left(\frac{Q}{V_p}\right) . \quad (5.2)$$

With  $\gamma$  and  $\gamma_0$ , the decay rates of the emitter in proximity to a resonator and in free space, respectively.  $\lambda_0$  is the resonance wavelength in vacuum and  $n$  is the refractive index of the resonator's material.  $Q$  is the quality factor, proportional to the power stored over the power dissipated and the cavity photon lifetime.  $V_p$  is the effective mode volume, which can be understood as the electric field strength per photon, and is equal to [181]:

$$V_p = \frac{U}{2u_{E,max}}. \quad (5.3)$$

Here  $U$  is the total energy and  $u_{E,max}$  is the energy density. The values of  $Q$  and  $1/V_p$  represent the spectral and spatial energy density of the resonant mode.

The Purcell effect can also be understood as an interference phenomenon. Indeed, when the emitter radiates a wave, it can be reflected from the cavity and excite the emitter either in or out of phase. In the case of a constructive interference with the emitter's field, the LDOS, and thus the emission rate, is increased and the Purcell factor  $F_p$  is superior to 1. The opposite is observed when the wave is out of phase, and  $F_p < 1$  [216,217].

Metallic nanostructures can have the same effect as an optical cavity thanks to the enhanced LDOS in their vicinity, resulting in a large  $Q/V_p$  value and an enhancement of the emission [218].

Besides the enhancement of the radiative decay rate through the increase of the LDOS in the near field of plasmonic nanostructures, the PL intensity also depends on the excitation rate of the emitter. This excitation rate is proportional to the absorption cross-section of the system. In the case of a monochromatic light and in the dipole approximation, the absorption cross-section is defined as the ratio of the absorbed power to the intensity of the incident light [219]:

$$\sigma = \frac{P_{abs}}{I_{inc}} = \frac{1/2 \int_V \omega(\epsilon''[\mathbf{E}]^2 + \mu''[\mathbf{H}]^2)dV}{I_{inc}} = c\mu_0 Im(\alpha) \frac{|\hat{n}_d \cdot \mathbf{E}(r_0)|^2}{|\mathbf{E}_0|^2}. \quad (5.4)$$

With  $E_0$  and  $E(r_0)$ , the amplitude of the electric field of the incident light and external electric field at the position of the ion, respectively.  $\epsilon''$  and  $\mu''$  are the imaginary parts of permittivity and permeability, respectively, with  $\mu'' = 0$  for frequencies in the optical range; therefore, we only consider the electric contribution.  $\hat{n}_d$  is the unit vector in the induced dipole moment direction and  $\alpha$  is the polarisability. From this equation, we can deduce that the plasmon resonance enhances the absorption cross-section of the system as  $|E/E_0|^2$ .

## 5.2.2 Photoluminescence chiroptical spectroscopic measurements

When applied to chiroptical spectroscopic techniques, PL is usually employed in two distinct strategies. The first one monitors the total yield of PL in CD measurements to determine the level of asymmetric absorption of fluorescent biomolecules. The second strategy uses circularly polarised luminescence to directly measure the differential emission of left and right circularly polarised radiation of luminescent molecules [220]. These techniques are limited by the necessity of having a fluorescent analyte, and by the very small asymmetry observed ( $< 0.1\%$ ) [221].

As discussed earlier, the PL signal of an emitter is enhanced in the near field of plasmonic nanostructures, which is proportional to the LDOS, making it an efficient probe of the near field environment of plasmonic nanostructures. Earlier work demonstrated that PL enhancement is dependent on the electromagnetic coupling of the emitter dipoles with the plasmon modes instead of an enhancement of the excitation rate [222]. In another study [223], it was shown that the polarisation property of PL is linked to the chiral asymmetry of the electromagnetic near fields close to the plasmonic surface. By using an achiral dye molecule near chiral plasmonic nanostructures, the degree of circular polarisation of the PL signal was shown to vary as a function of the level of chiral asymmetry of the near field. The chiral asymmetry of the near field surrounding plasmonic nanostructures is defined by the optical chirality density  $C$  parameter [3], which is a conserved quantity [224] defined previously in Section 2.4.4.

The electromagnetic chirality  $C$  of the near field was shown to be interacting with the emitters in the form of a preferential circular polarisation of the PL enhancement, measured in the far field. The conclusion of this study determined that the nanostructures act as antennas that direct LCP and RCP light in opposite directions depending on their emission pattern [223]. This does not change the emission probabilities of the fluorescent dye molecules for each handedness of circular polarisation. Therefore, the parameter  $C$  describes the coupling between the emitter and the nanoantenna. Specifically, how the chirality of the near field dictates which chiral modes of the nanoantenna the emitter will couple its emission to.

Later work [225,226] also used these properties to enhance the PL of achiral and chiral emitters in the near field of plasmonic nanostructures.

## 5.3 Methods

### 5.3.1 Sample and analyte

The plasmonic sample used during this study is the gold shuriken metafilm TPS, the fabrication of which has been described in Section 3.1.2. This sample is made of several shapes of different sizes and with both the left and right handedness (LH & RH). For this study, the 500 nm large shuriken shape was selected (see **Figure 5.1** (a)). The pitch of the shuriken arrays is set at 720 nm, with the structures being arranged in a square lattice and reaching a depth of ~80 nm (see **Figure 5.1** (b) and (c)). The shuriken indentations are gathered in 400  $\mu\text{m}$  large square arrays, containing either LH or RH structures. The optical properties of these plasmonic nanostructures are well understood and have been extensively studied in the Kadodwala group, especially their optical chirality in the near field [126,227–234].

The chiral molecule that will be studied here is a peptide manufactured by *Research Assoc.* Rebecca Clarke, under the supervision of *Prof.* Andrew Sutherland at the University of Glasgow. This *de novo* peptide is a  $\alpha$ -helical coiled coils heptamer (*cc-Hept*) weighing around 3.3 kDa (see **Figure 5.1** (d) and (e)) [235]. These helical structures within the peptide are chiral since they are folded clockwise (dextrogyre). The secondary structure of this molecule, describing the folding of the proteins it is made of, can be detected by conducting CD spectroscopy in a solution. The CD spectra of this peptide show a characteristic  $\alpha$ -Helix signal as expected (see **Figure 5.1** (f)) [236]. This peptide has a thiol polyethylene glycol linker group at one end of its chain. The thiol group allows it to form a strong gold–sulphur bond and is often used to create self-assembled monolayers (SAMs) [229,230].



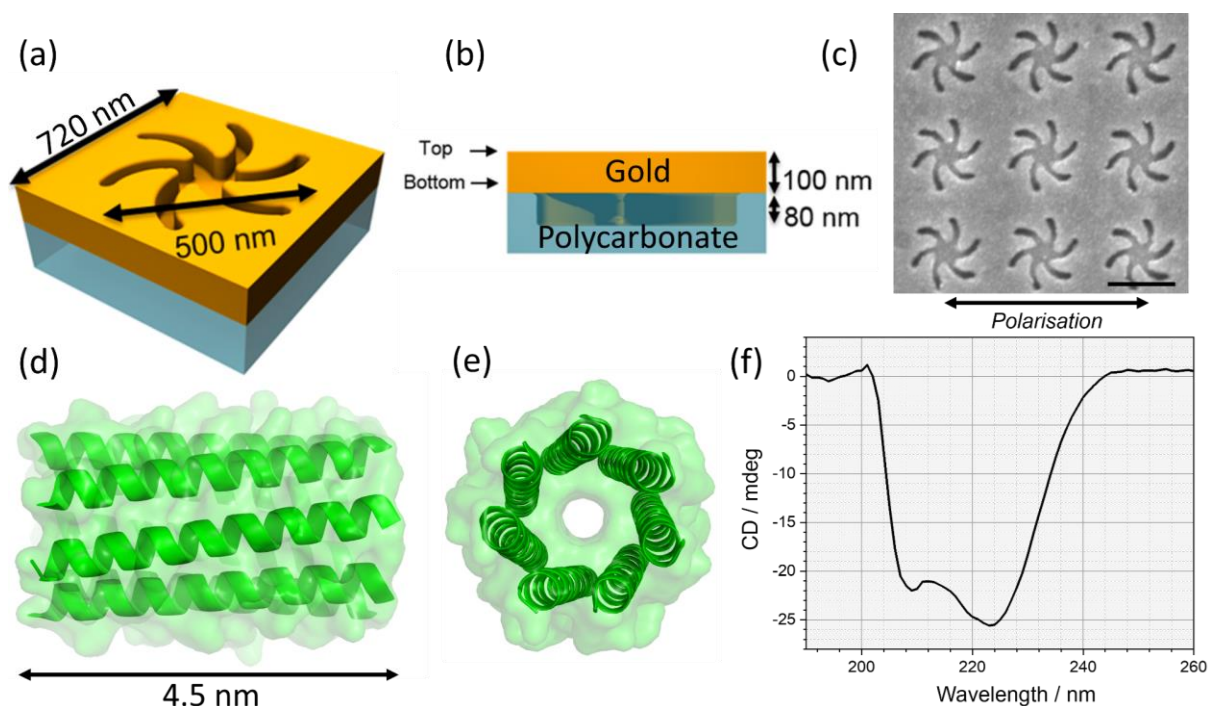


**Figure 5.1:** Schematic of the (a) orthographic and (b) side view of the (LH) TPS metafilm. (c) Scanning electron microscopy (SEM) image of a LH TPS with the scale bar showing 500 nm. (d) Side view of the structure of the *cc*-Hept peptide and (e) top view (adapted from [235]). (f) CD spectrum of 50 mM *cc*-Hept in HEPES buffer (figure from [139]).

The *cc*-Hept SAM was deposited on the TPS slides after a cleaning protocol involving an IPA bath followed by N<sub>2</sub> gun drying and a 1 min oxygen plasma treatment at 80 W. The sample was then left 24 h in a solution of the peptides at a concentration of 0.1 mM diluted in 4-(2-hydroxyethyl)-1-piperazineethanesulfonic acid (HEPES) buffer (10 mM HEPES and 150 mM NaCl in water at pH 7.2). It was subsequently rinsed with 1 mL of HEPES Buffered Saline (HBS) to leave only the molecules adsorbed at the surface of the gold.

The thickness of the SAM layer was measured using a spectroscopic ellipsometer M-2000XI from J.A. Woolam Co. and by fitting the data afterwards on *CompleteEASE* software (see methods in Section 3.2.3). The peptide layer was modelled using Cauchy equations on top of flat gold. The value of the thickness obtained was plotted against the mean square error (MSE) of the Cauchy fitting (see **Figure 5.2**). The value of the thickness corresponds to the lowest MSE value reached. The thickness of this SAM was measured in PBS to be equal to  $3.44 \pm 0.01$  nm. The theoretical length of the peptide is close to 4.5 nm, suggesting that the individual peptides are slightly tilted relative to the surface normal.

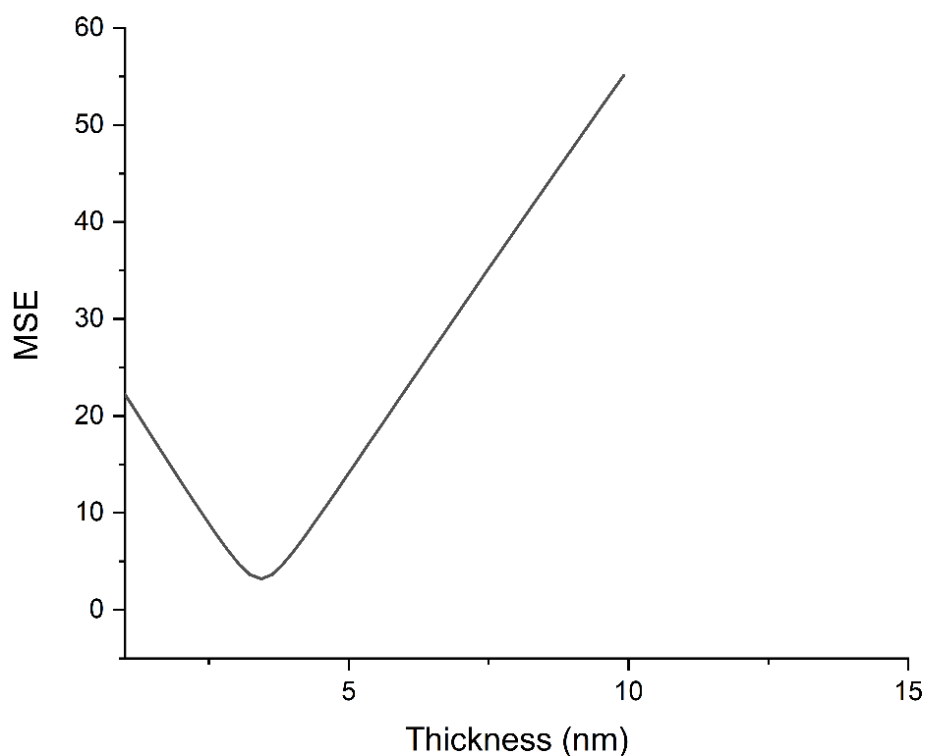


**Figure 5.2:** Plot of the peptide layer thickness corresponding to the mean square error (MSE) of the fitting model.

To verify the uniformity of the peptide layer on the gold surface, the root-mean-square roughness of the gold surface was measured by AFM with the *cc-Hept* SAM, giving  $1.4 \pm 0.1$  nm (see **Figure 5.3**). This value is similar to the roughness of unfunctionalised gold film obtained in a prior study [237], suggesting a uniform coverage of the *cc-Hept* SAM.

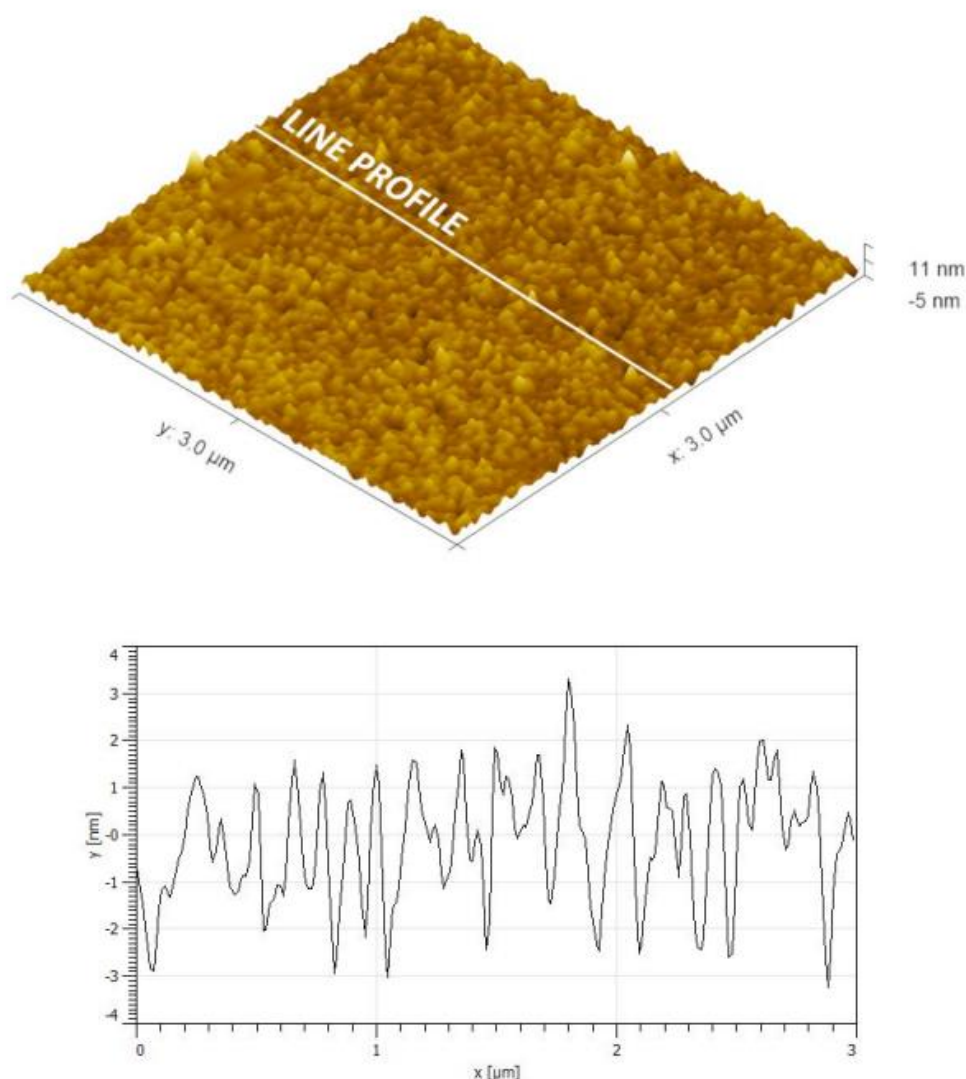


**Figure 5.3:** (Top) 3D AFM image of the *cc-Hept* functionalised gold surface and (bottom) height profile taken along the white line represented above (from [139]).

### 5.3.2 Measurement setups

As discussed in Section 2.4.3, linearly polarised light, which is the sum of both handedness of CPL, will experience optical rotation and circular dichroism when passing through an optically active medium. These two effects can be measured by the rotation angle  $\theta$  and the ellipticity angle  $\phi$  (see **Figure 5.4**). These angles are related through the Cotton effect, and it is possible to use the *Kramers-Kronig* (KK) mathematical relations to calculate one angle from the other. A *MatLab* code has been developed by *Postdoc* Rahul Kumar to convert ORD to ellipticity and vice-versa.

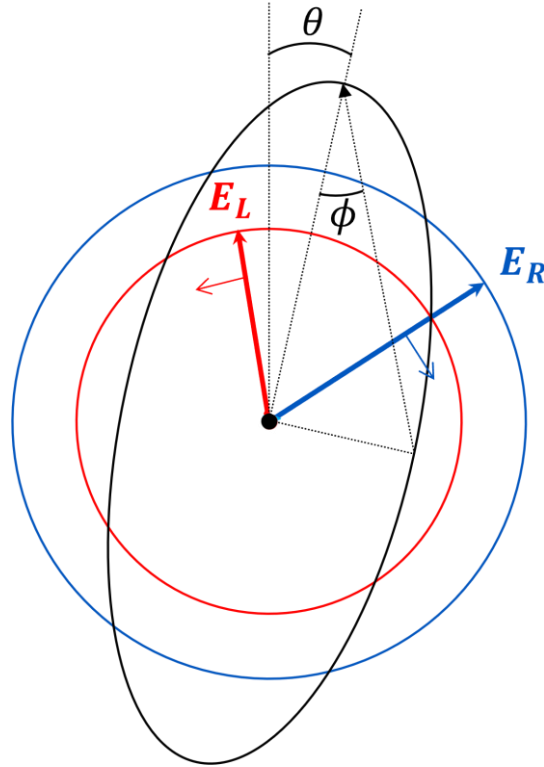


**Figure 5.4:** Linearly polarised light after traversing a chiral medium, with both electric field vectors  $E_L$  and  $E_R$ , and the rotation angle  $\theta$  and the ellipticity angle  $\phi$ .

The far-field measurements were obtained using a polarisation microscope described in Section 3.3. This setup uses a linearly polarised broadband light to excite the plasmonic nanostructures and measure the reflectance spectra and the angle  $\theta$  using optical rotatory dispersion (ORD) for both handedness of the shuriken arrays. The ellipticity angle  $\phi$  could not be directly measured with this setup; it was therefore calculated with the KK relations.

The near-field photoluminescence measurements were collected using a custom-built microscope from Thorlabs (ESI) depicted in **Figure 5.5**. The excitation source is a 404 nm laser diode, with a 180-mA fixed current and maximum optical power output of  $\sim 17$  mW. The input power and the polarisation were adjusted by using two linear polarisers at the input after the laser diode. The first polariser was used to modify the input power, and the second polariser was fixed to set the input polarisation. A  $10\times$  (NA=0.3) objective was used to focus the beam and the photoluminescence signal was collected with the same objective by reflection through a longpass filter, blocking light below 500 nm. An optical camera was mounted to position the sample and align the laser on the shuriken arrays. The orientation of the beam polarisation was at the same angle as for the far field measurements, shown in **Figure 5.1** (c). A charged-coupled device was mounted on the top of the configuration to capture the signals. This setup can monitor

both the ORD angle ( $\theta$ ) and ellipticity angle ( $\phi$ ), unlike the polarisation microscope. This is thanks to the addition of a quarter wave plate (QWP), which is used to introduce a  $90^\circ$  phase shift between two orthogonal polarisation components of light, converting linearly polarised light into CPL or vice versa.

The angle  $\theta$  is obtained in the same manner as for the polarisation microscope setup, shown in Section 3.3. Regarding  $\phi$ , it is calculated by rotating the analyser to  $45^\circ$  and  $315^\circ$  and applying this equation:

$$\phi = 2 \times \frac{(I_{45} - I_{315})}{(I_{45} + I_{315})}. \quad (5.5)$$

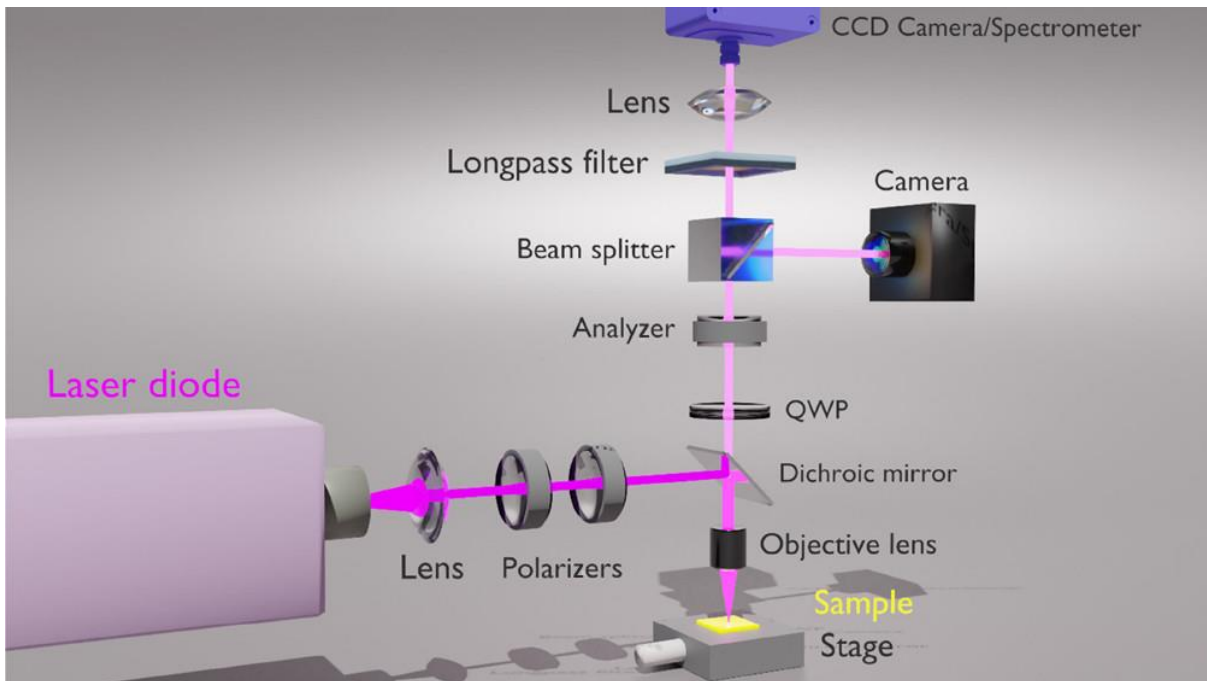


**Figure 5.5: Photoluminescence setup measuring the near-field ORD and ellipticity using a linearly polarised 404 nm laser source (from [139]).**

### 5.3.3 Simulation model

Simulation data was obtained from the software *COMSOL V5.6 Multiphysics* with the Wave Optics module described in Section 3.4.2. The simulation model used an idealised shuriken shape in a 1600 nm high square block of 720 by 720 nm with vertical periodic boundary conditions to mimic an array of nanostructures (see **Figure 5.6**). The shuriken shape is 500 nm large from arm-to-arm, with 38 nm arm width and the thickness of the gold metafilm was set to 100 nm with a depth of the structure of 80 nm. Perfectly matched layers were added on the top and bottom of the model cell to avoid

unwanted reflection from the input and output ports. The optical properties of gold were taken from Johnson and Christy [53], and the default values provided by *COMSOL* software were used for water and polycarbonate materials. A 10 nm continuous domain at the surface of the gold nanostructure was defined to simulate the response of an achiral dielectric and an isotropic chiral layer of *cc-Hept*. The discrepancy between the thickness of the domain and the measured size of the peptide layer is due to the lack of memory and computational power of the computer used for the simulation, which only allows for a limited amount of mesh elements. The mesh type used for the perfectly matched layers was set to square elements (swept), and the rest of the model used tetrahedral elements. The maximum element size was set to 30 nm in the water and polycarbonate domains, 18 nm in the gold layer and 10 nm in the dielectric domain at the surface of the gold that was used to simulate the adsorbed chiral *cc-Hept* molecules. The incident light was linearly polarised along the y axis.

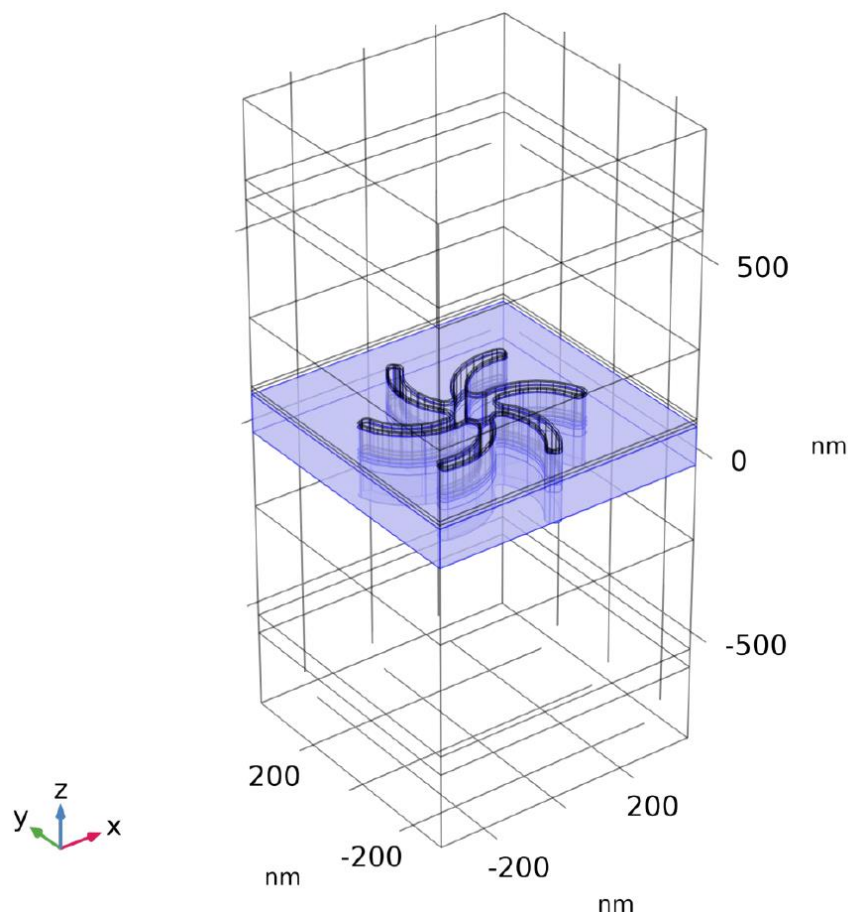


**Figure 5.6: *COMSOL* simulation model used to reproduce experimental spectra, with the gold layer highlighted in blue (from [139]).**

Simulating the response of a chiral medium requires solving a modified version of Maxwell's equations described by the equations (3.12) and (3.13) discussed in detail in Section 3.4.2.  $\xi^T$  is a second rank tensor that defines the chiral property of a medium. In the case of an achiral material  $\xi = 0$ , and for an isotropic chiral layer the diagonal



components are non-null ( $\xi_{xx} = \xi_{yy} = \xi_{zz} \neq 0$ ) [227,230]. The value selected to simulate the chiral *cc-Hept* peptide layer was  $\xi_{xx} = \xi_{yy} = \xi_{zz} = 1.7 \times 10^{-4}$ , which has been used in a previous study focussing on protein layers [230].

The main hypothesis of this work is that the PCPL technique studied here is sensitive to a smaller volume above the surface than the light-scattering strategy. To verify this using EM simulation, we calculated the volume integral of the optical chirality flux  $F_z$  in a small and large volumes above the gold nanostructure. The small “near-field” volume corresponds to the 10 nm thick chiral dielectric layer, and the larger “far-field” volume is made of the peptide layer plus the entire water domain above (see **Figure 5.7**).

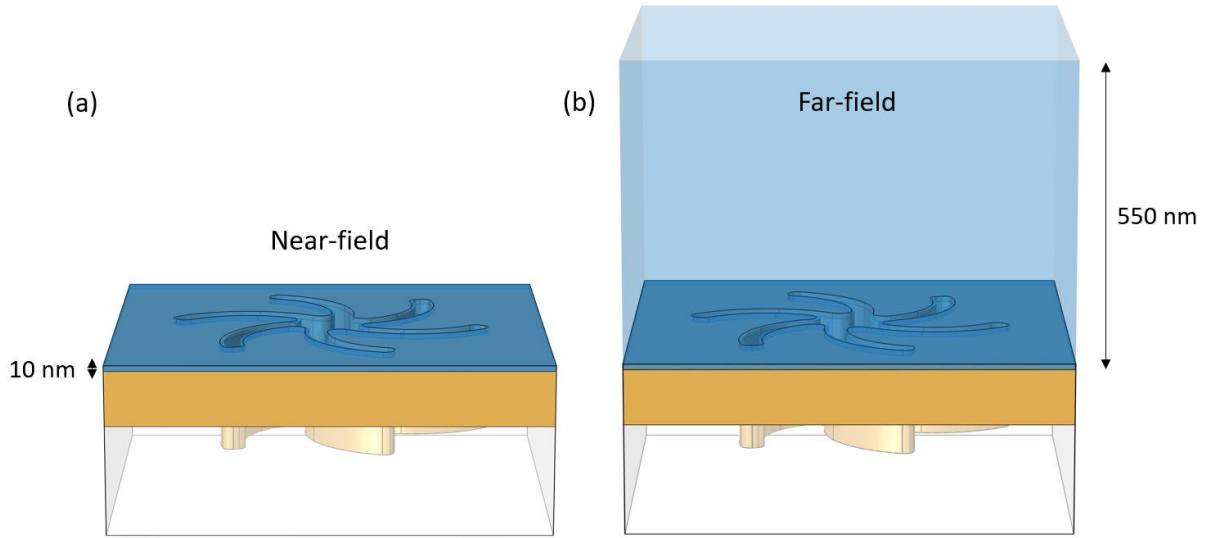


**Figure 5.7:** *COMSOL* model with (a) the near-field volume made of the same continuous 10 nm domain used to model the adsorbed dielectric medium and (b) the far-field volume extending 550 nm above the gold surface (from [139]).

The optical chirality flux along the axis of the propagation of the light  $F_z$  was derived from the work of Poulikakos et al. [238]:

$$F_z = \frac{1}{4} \left[ \left( E_x \left( \frac{\partial H_x}{\partial z} - \frac{\partial H_z}{\partial x} \right) - E_y \left( \frac{\partial H_z}{\partial y} - \frac{\partial H_y}{\partial z} \right) \right) - \left( H_x \left( \frac{\partial E_x}{\partial z} - \frac{\partial E_z}{\partial x} \right) - H_y \left( \frac{\partial E_z}{\partial y} - \frac{\partial E_y}{\partial z} \right) \right) \right]. \quad (5.6)$$

The values of  $F_z$  obtained were normalised with respect to left CPL to give the degree of circular polarisation of the light in both volumes, which was converted into an ellipticity spectra ( $\phi$ ). The  $\theta$  corresponding spectra were here too obtained by applying the KK transforms.

## 5.4 Results and discussion

### 5.4.1 Far field measurements

First, the optical response of both shuriken handedness was recorded using the polarisation microscope setup, serving as a reference to benchmark the PCPL technique. The reflectance and ORD ( $\theta$ ) response were recorded simultaneously on the clean sample in PBS (pH of 7.4) and repeated after the *cc-Hept* peptide functionalisation. Measurements in an achiral salt reference (0.1 M NaCl) were also performed as a reference to assess the margin of error coming from inherent defects in the fabrication process, as well as the spectroscopic setup.

Light reflected off the plasmonic arrays can be influenced by a chiral medium present close to the surface, where the superchiral near field is strongly enhanced, resulting in an asymmetry in the LH and RH spectra [227]. This difference can be quantified using the parameter  $\Delta\Delta S$ , which represents the difference between the distances  $\Delta S$  separating the spectral dips for the analyte and the clean buffer reference for the LH and RH arrays (see **Figure 5.8** (a)):

$$\Delta S^{RH/LH} = S_{Mat}^{RH/LH} - S_{Ref}^{RH/LH} \quad (5.7)$$

$$\Delta\Delta S = \Delta S_{LH} - \Delta S_{RH} . \quad (5.8)$$



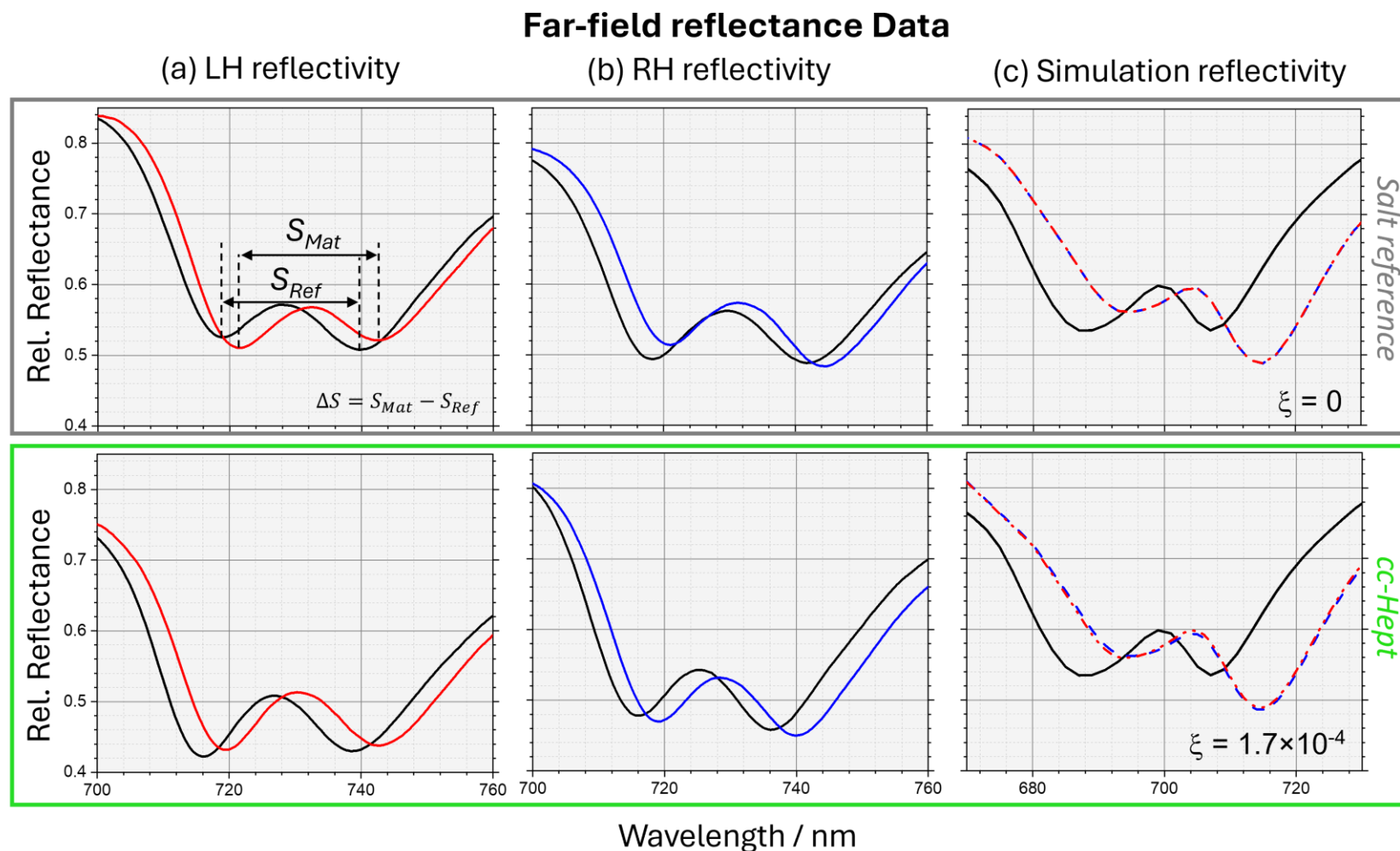


Figure 5.8: Displayed in upper and lower panels are far field reflectance data for the achiral salt reference and *cc-Hept* functionalised TPS, respectively, in comparison to buffer (in black), with columns (a), (b) and (c) containing reflectance for the left-handed (red), right-handed (blue) structures and the simulated reflectance spectra obtained for  $\xi$  of 0 and  $1.7 \times 10^{-4}$  for both handedness. In the upper panels (a) the asymmetry parameter  $\Delta S$  is illustrated ([139]).

The parameter  $\Delta\Delta S$  is equal to zero for an achiral material, and  $\Delta\Delta S \neq 0$  if a chiral dielectric interacts strongly enough with the EM field generated by the plasmonic structures. The values measured for  $\Delta\Delta S$  on the achiral salt reference and the *cc-Hept* chiral peptide monolayer are displayed in **Table 5-1**:

| $\Delta\Delta S$ (Asymmetry parameter) | Achiral Salt   | Chiral <i>cc-Hept</i> |
|--|----------------|-----------------------|
| Experimental (in nm)                   | $-0.2 \pm 0.3$ | $-0 \pm 0.5$          |
| Simulation (in nm)                     | 0              | 1                     |

**Table 5-1: Far-field asymmetry parameter  $\Delta\Delta S$  values obtained for the achiral salt solution and the *cc-Hept* monolayer measured experimentally (average of 4 data sets) and through EM simulation.**

The values calculated experimentally for  $\Delta\Delta S$  are not showing any asymmetry on the chiral peptide measurements. The simulation results predict a value of  $\Delta\Delta S = 1$ , which is due to the use of a thicker layer of chiral material in the simulation model compared to the real thickness and because the simulated results are not suffering from any noise or setup defects.

ORD spectra of the achiral salt and *cc-Hept* peptide layer are gathered in **Figure 5.9** (a), they were converted to ellipticity ( $\phi$ ) spectra through the (KK) transforms (see **Figure 5.9** (b)).

An asymmetry factor  $A$  was created to characterise the asymmetric response in the spectra. This parameter represents the relative peak-to-peak height change of the spectral resonances on both handedness for the  $\phi$  and  $\theta$  spectra, and is defined as follows:

$$A = \frac{H_{Ref}^{RH} \times H_{Mat}^{LH}}{H_{Ref}^{LH} \times H_{Mat}^{RH}}. \quad (5.9)$$

With  $H_{Ref}^{RH/LH}$  the peak-to-peak amplitude between the minima and maxima of the buffer spectral plots for both handedness (dashed lines in **Figure 5.9**). The wavelengths at which these positions are derived are  $\sim 720$  and  $745$  nm for  $\theta$ , and  $710$  and  $730$  nm for  $\phi$  spectra.  $H_{Mat}^{RH/LH}$  corresponds to the amplitude of these same peaks, at positions slightly red shifted (as shown by  $\Delta\lambda$  in **Figure 5.9** (a)), for the achiral salt and *cc-Hept* (solid lines in **Figure 5.9**). If  $A = 1$ , there is no asymmetric response between LH and RH shuriken arrays. Otherwise, if  $A \neq 1$ , there is a difference in the spectra measured on both mirror structures.

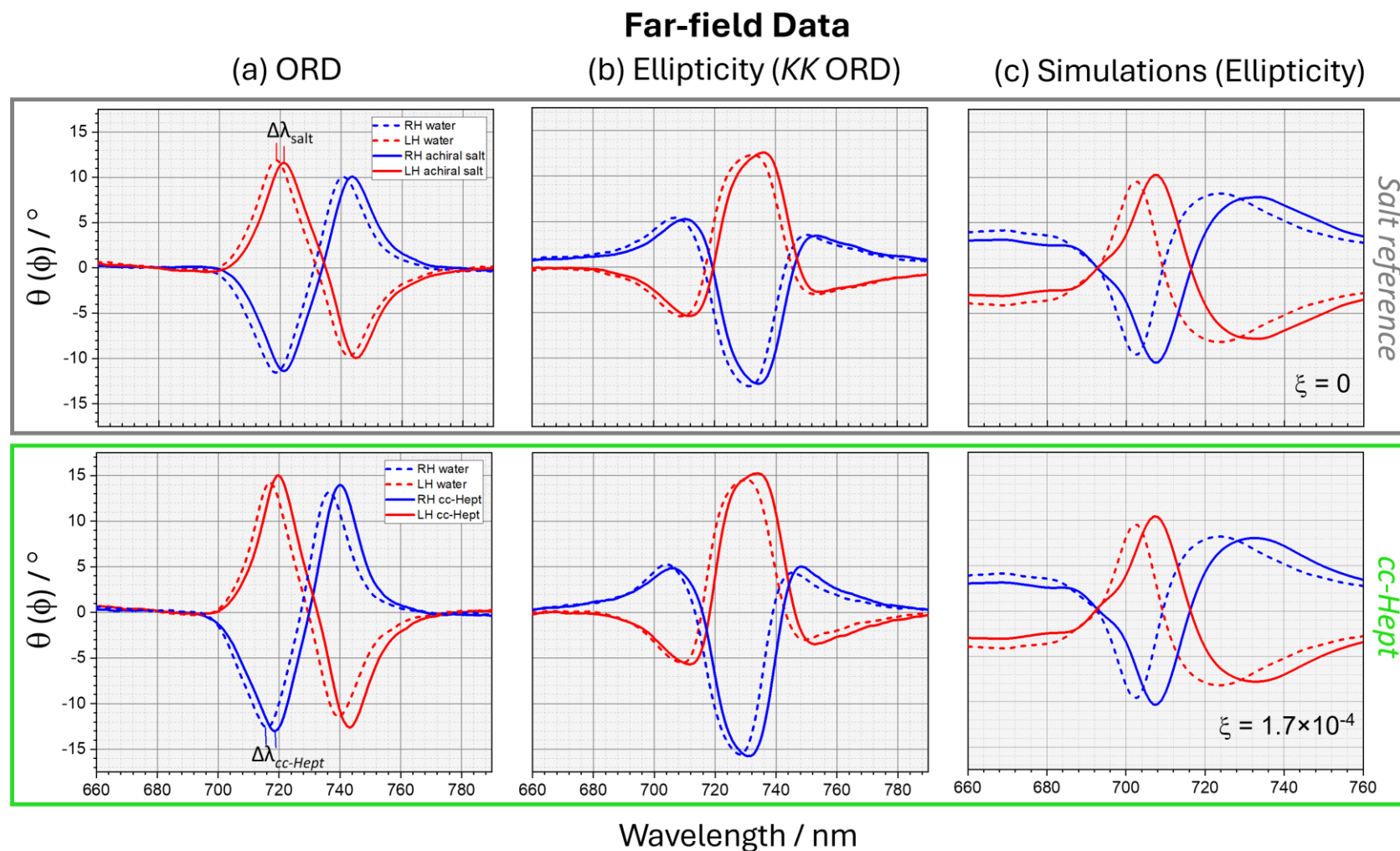


**Figure 5.9:** Far field spectra and of LH (red) and RH (blue) shuriken arrays, derived from the light scattering measurements averaged of 4 separate arrays, for the achiral salt reference in the upper panels and *cc-Hept* functionalised TPS in the lower panels, respectively represented by a solid line and compared to spectra obtained in buffer (dotted line), with columns (a-c) containing ORD, ellipticity (*kk*-ORD), and simulated ellipticity spectra obtained for  $\xi$  of 0 and  $1.7 \times 10^{-4}$  (from [139]).

The values of  $A$  are displayed in **Table 5-2**, where they are shown to be close to 1 for the achiral analyte and the chiral peptide, and therefore don't display any asymmetric response:

| <b><math>A</math> (asymmetry parameter)</b> | <b>Achiral Salt</b> | <b>Chiral <i>cc-Hept</i></b> |
|---|---------------------|------------------------------|
| <b>Experimental ORD</b>                     | $1.00 \pm 0.05$     | $1.03 \pm 0.05$              |
| <b>Simulated ORD</b>                        | 1                   | 1                            |

**Table 5-2: Far-field asymmetry parameter  $A$  obtained for the achiral salt solution and the *cc-Hept* monolayer measured experimentally (average of 4 data sets) and through EM simulation.**

We have seen that this light-scattering far-field technique is not sensitive enough to the changes in the near field introduced by a small chiral molecule, which occupies a small volume of the superchiral near field. Much larger chiral molecules have been successfully detected with this technique using the same shuriken TPS, such as 5-enolpyruvylshikimate 3-phosphate synthase from *Escherichia coli* with a molecular weight of 46 kDa or Shikimate kinase from *Erwinia chrysanthemii* (19 kDa) [234]. To obtain a chiroptical response on the *cc-Hept* peptide SAM, a more sensitive technique able to probe the near field of the plasmonic structures is needed. In the next part, we will review and analyse the results of a photoluminescence-based technique employed on the same enantiomeric structures.

## 5.4.2 Near Field measurements

The photoluminescence setup used to obtain the  $\phi$  and  $\theta$  spectra was described earlier in Section 5.3.2. This setup can measure the intensity of left and right CPL emitted from the sample using a combination of a QWP and a linear polariser (LP). A combination of spectra using the following parameters was taken to derive  $\phi$  and  $\theta$  angles:  $0^\circ$  QWP/ $0^\circ$  LP,  $0^\circ$  QWP/ $45^\circ$  LP,  $0^\circ$  QWP/ $90^\circ$  LP,  $0^\circ$  QWP/ $315^\circ$  LP,  $45^\circ$  QWP/ $45^\circ$  LP,  $315^\circ$  QWP/ $315^\circ$  LP. Here too, the measurements were performed on 4 arrays of each shuriken handedness and averaged out. The photoluminescence spectra obtained measure the photon counts as a function of their respective wavelengths (see **Figure 5.10**). The dark current baseline present at wavelengths lower than 500 nm was removed before using the data.

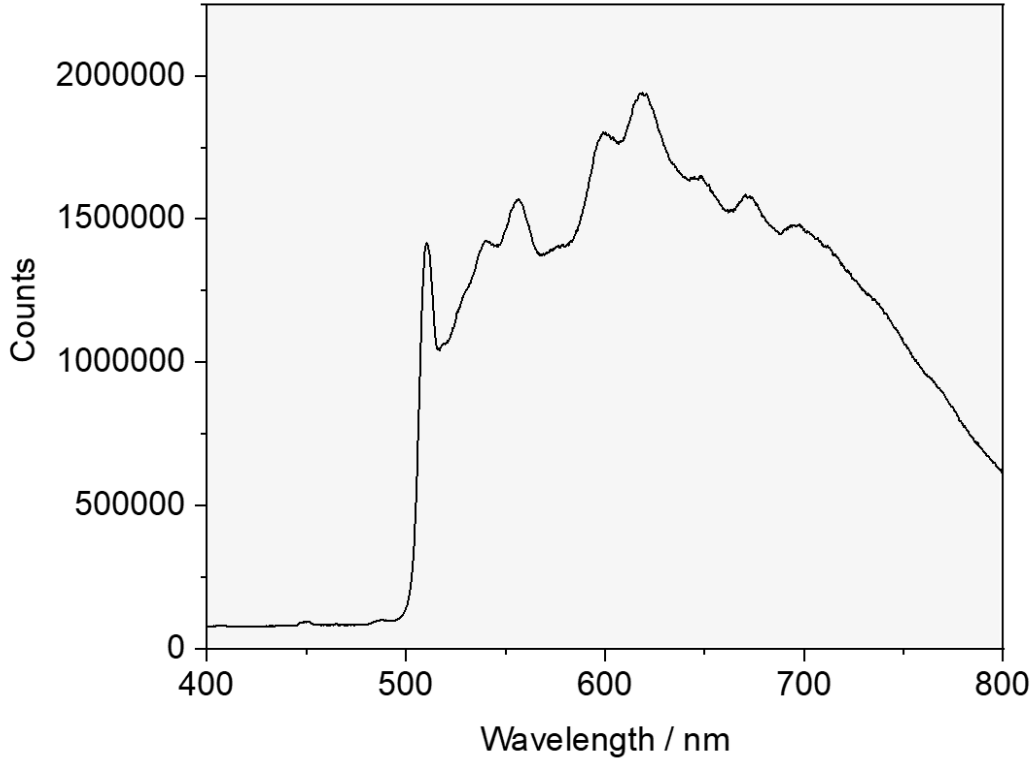


**Figure 5.10: Photoluminescence spectra of the flat gold background with the QWP and LP set at  $0^\circ$  (from [139]).**

The formulas employed to calculate both angles from the photoluminescence intensity  $I_{QWP/LP}$  are expressed as:

$$\phi = \frac{\sqrt{I_{0^\circ/45^\circ}} - \sqrt{I_{0^\circ/315^\circ}}}{\sqrt{I_{0^\circ/45^\circ}} + \sqrt{I_{0^\circ/315^\circ}}} \quad (5.10)$$

$$\theta = \frac{180}{2\pi} \times \tan^{-1} \left( \frac{I_{45^\circ/45^\circ} - I_{315^\circ/315^\circ}}{I_{0^\circ/0^\circ} - I_{0^\circ/90^\circ}} \right). \quad (5.11)$$

The peptide monolayer was exposed to the 404 nm laser for an extended period, it was therefore necessary to confirm that it was not degrading under near-UV exposure. Two spectra have been collected on both handedness of the sample at the same spots after 12 min of illumination and showed no change, indicating that there is no radiation-induced damage on *cc-Hept* for the duration of the experiment (see **Figure 5.11**).

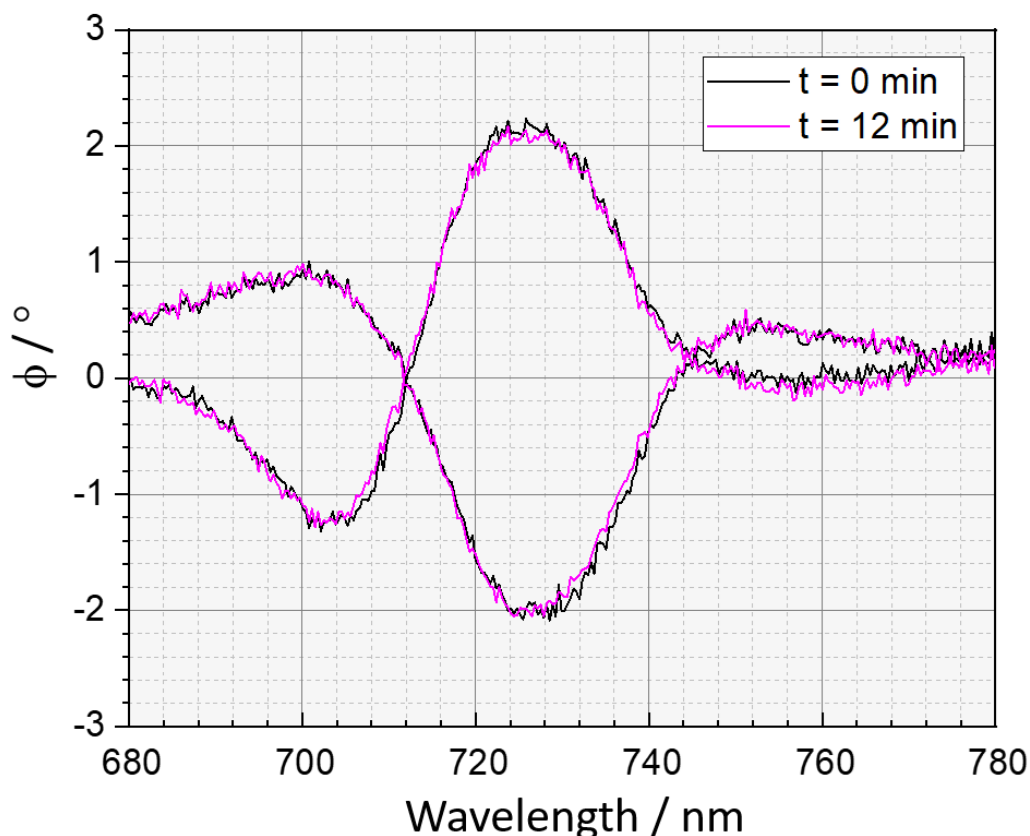


**Figure 5.11:** Raw ellipticity spectra of the same LH and RH arrays functionalised with the *cc-Hept* peptide SAM at 0 min (black) and after 12 min (purple) of exposure to the 404 nm laser (from [139]).

The spectra of  $\phi$  and  $\theta$  for the achiral salt reference solution and the *cc-Hept* monolayer are displayed on the column (a) of **Figure 5.12** and **Figure 5.13**. These spectra were compared to the calculated KK data from the other dataset (see column (b)), and show a good correspondence, giving a high level of confidence in the experimental measurements. As expected, the spectra obtained with the achiral analyte give a symmetrical response. In the case of the chiral *cc-Hept* peptide, the spectra show a clear asymmetric response between the LH and RH shuriken shapes.

## Near-field Ellipticity Data

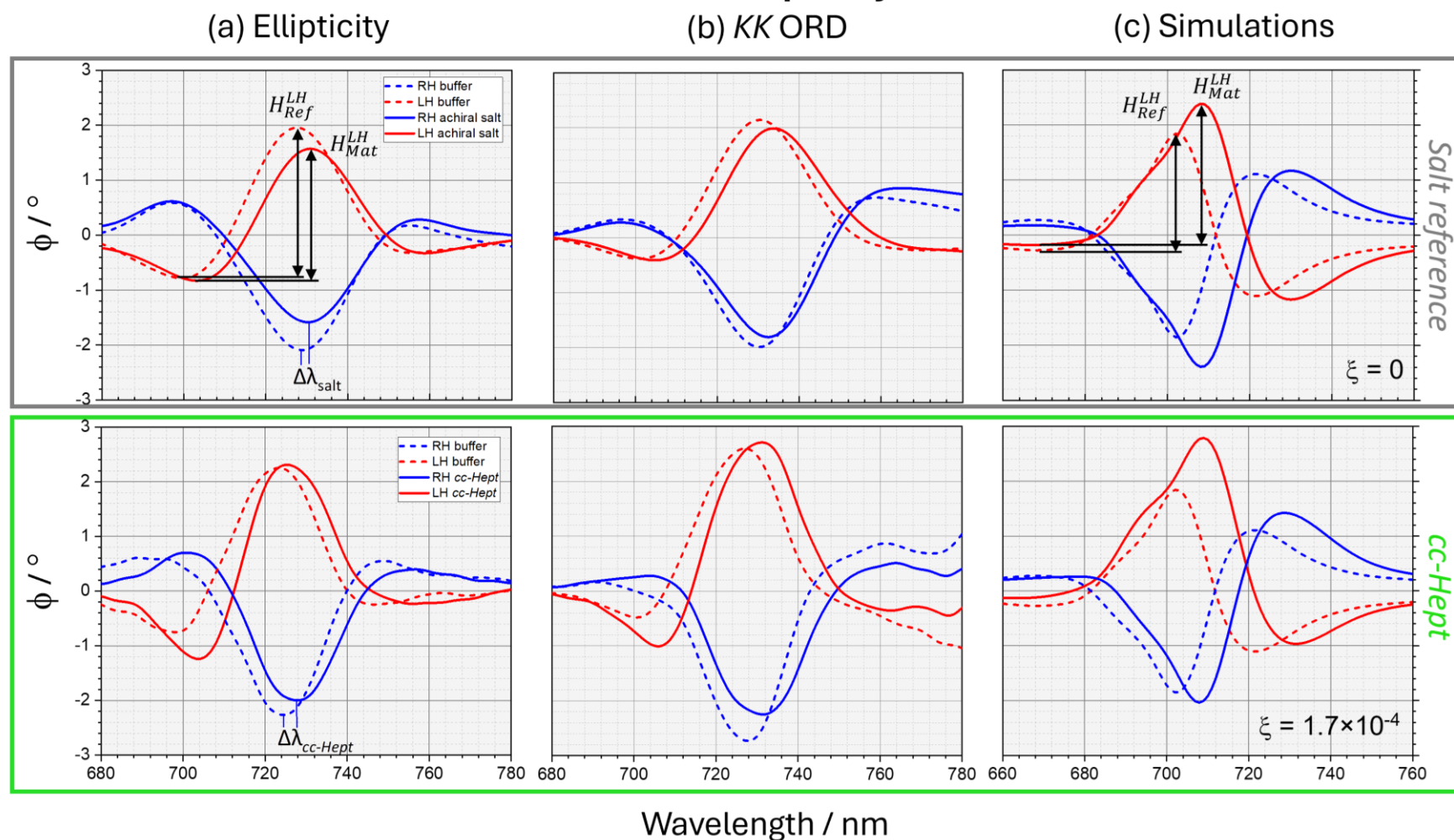


Figure 5.12: Near-field ellipticity data of LH (red) and RH (blue) shuriken, for the achiral salt on the top panel and *cc-Hept* on the bottom panel (solid line), compared to buffer (dotted line), (a-c) containing experimental, *kk*-ORD derived and simulated ellipticity. In the upper panels (a,c), heights used for the asymmetry parameter  $A$  are illustrated (from [139]).



## Near-field Optical Rotation Data

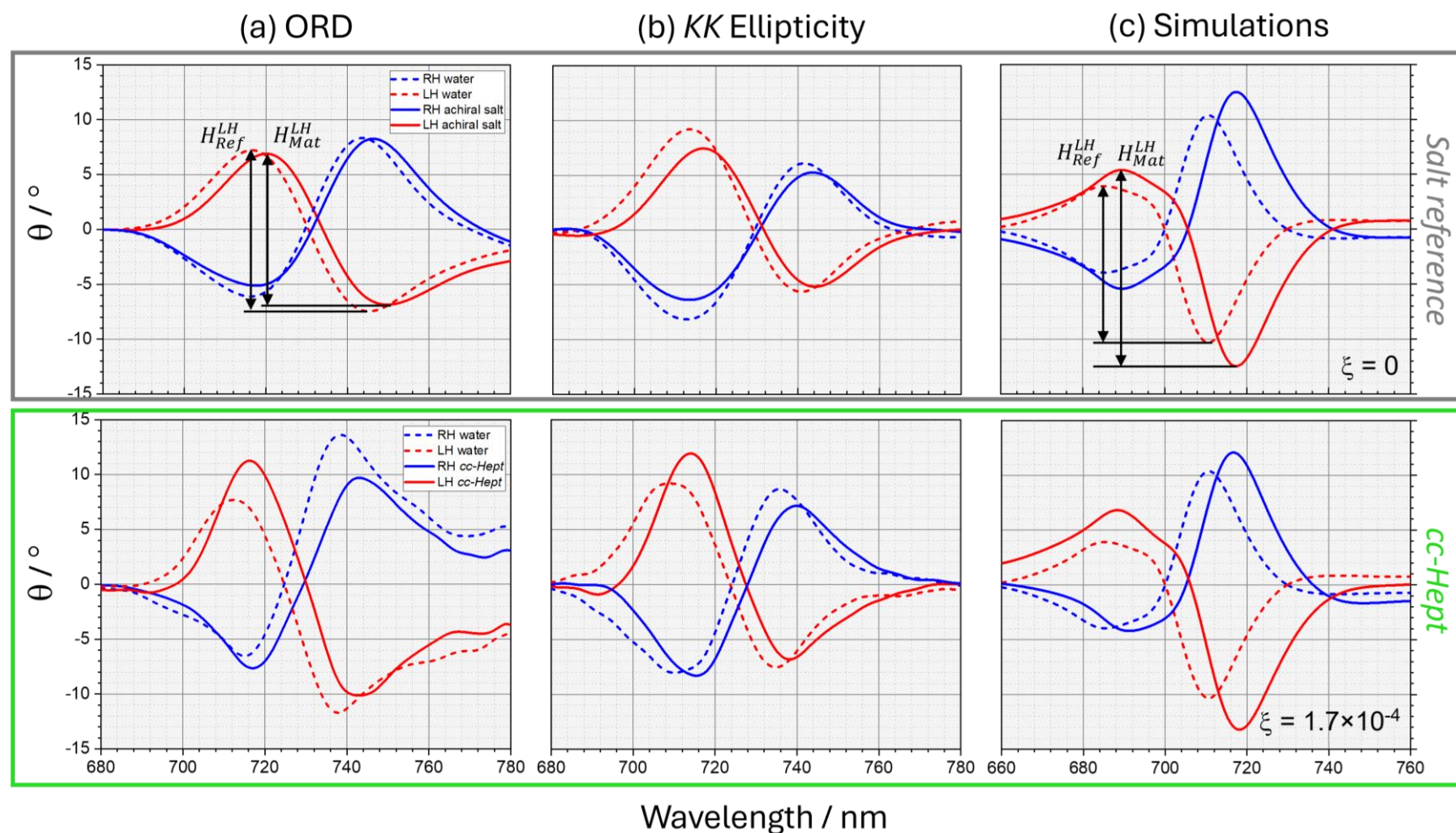


Figure 5.13: Near-field ORD data of LH (red) and RH (blue) shuriken, for the achiral salt on the top panel and *cc*-Hept on the bottom panel (solid line), compared to buffer (dotted line), (a-c) containing experimental,  $kk$ -Ellipticity derived and simulated ORD. In the upper panels (a,c), heights used for the asymmetry parameter  $A$  are illustrated (from [139]).



The asymmetry parameters  $A$  obtained for all the near-field data are presented in **Table 5-3**:

| $A$ (asymmetry parameter) | Achiral Salt    | Chiral <i>cc-Hept</i> |
|---------------------------|-----------------|-----------------------|
| Experimental ellipticity  | $0.98 \pm 0.07$ | $1.25 \pm 0.07$       |
| Simulated ellipticity     | 1.00            | 1.25                  |
| Experimental ORD          | $1.00 \pm 0.07$ | $1.25 \pm 0.07$       |
| Simulated ORD             | 1.00            | 1.25                  |

**Table 5-3: Near-field asymmetry parameter  $A$  obtained for the achiral salt solution and the *cc-Hept* monolayer measured experimentally (average of 4 data sets) and through EM simulation.**

As observed visually on the spectra, the achiral salt solution is not showing any asymmetry with a parameter  $A$  equal to 1, unlike for the chiral *cc-Hept* molecule, which returns a consistent value of 1.25 across the experimental and simulated spectra. The simulated spectra, displayed in the column (c) of **Figure 5.9**, **5.12** and **5.13** are in good agreement with the experimental data, showing similar shapes and asymmetry parameters  $A$  (see **Table 5-3**).

The parameter  $A$  has been used in a previous study, which linked this value to the net charge distribution and the chirality of the analyte [232]. For  $A < 1$ , the biomolecule has a net negative charge, if  $A > 1$ , the net charge is positive, and if  $A = 1$ , there is no net charge. The net charge of a biomolecule analyte is obtained through its isoelectric point (IP) and with the value of the solution's pH. For an IP value below the pH of the surrounding buffer, a net negative charge is observed. If IP is above the pH, the net charge is positive. In our case, the IP of *cc-Hept* has been calculated to be 10, and the pH of the buffer is equal to 7.2, giving the biomolecule a net positive charge. Proteins with a net positive charge studied in previous work on the same TPS sample gave a positive value for  $A$  between 1.15 and 1.25 [232], which is coherent with the values observed in this study.

To further our understanding of the interaction between the chiral layer and the superchiral near-field in the vicinity of the nanostructures, several parameters were studied using numerical simulation. The spatial distribution of the electric field norm as well as the optical chirality factor  $C$ , and the optical chirality flux  $F_z$  obtained were plotted in a 2D slice 10 nm above the gold surface for an incident beam at a wavelength of 699 nm (see **Figure 5.14**). This wavelength was selected to be in the middle of the simulated reflectance spectra (see **Figure 5.8 (c)**).

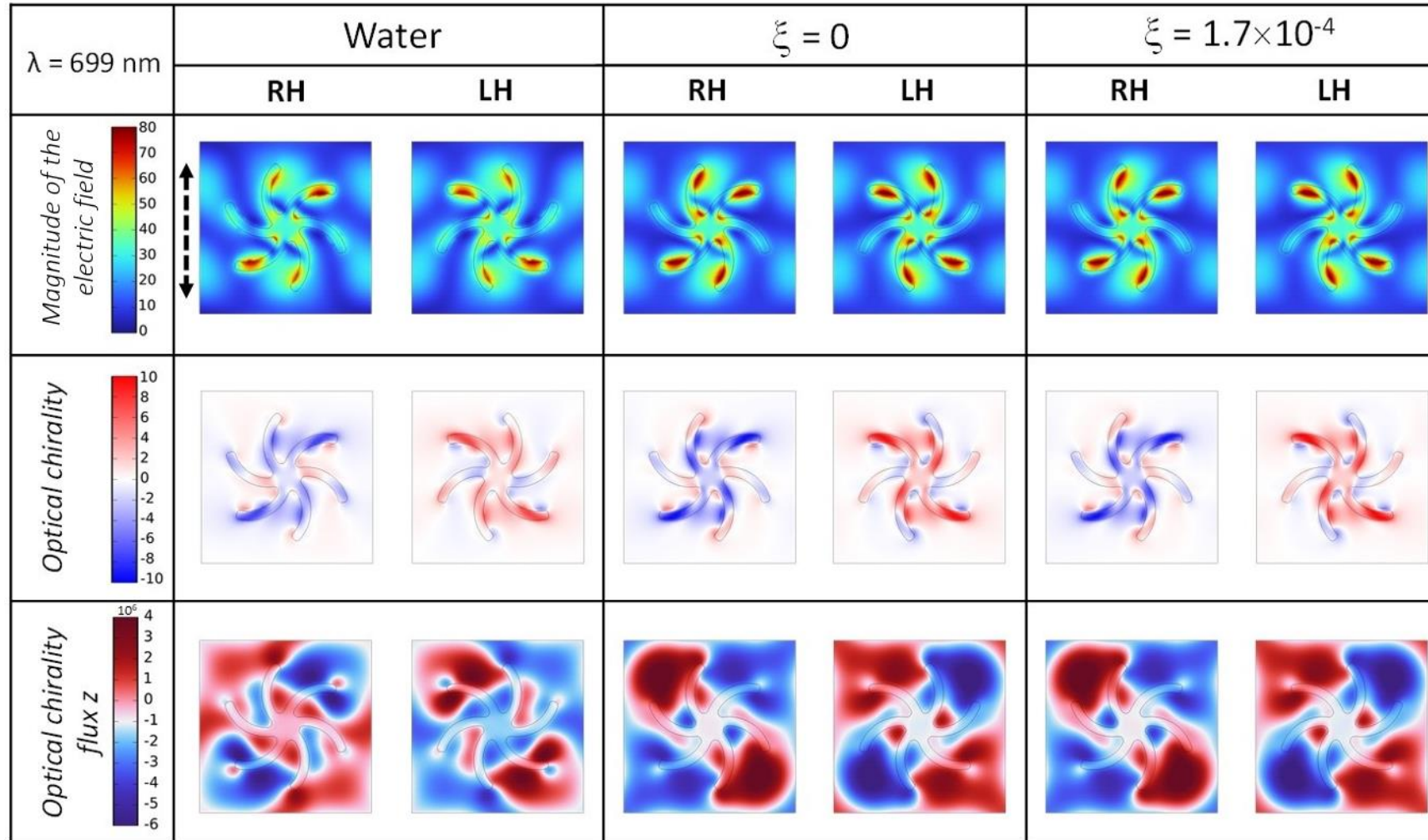


Figure 5.14: 2D maps for both shuriken handedness of the magnitude of the electric field ( $|E|$ ), the optical chirality factor  $C$ , and the optical chirality flux along the  $z$  axis  $F_z$  in water, with an achiral layer ( $\xi = 0$ ) and a chiral layer ( $\xi = 1.7 \times 10^{-4}$ ) with both having the same refractive index of 1.44. The slices were taken 10 nm above the gold film surface with an incident beam of 699 nm polarised as indicated by the dashed arrow on the top left panel (from [139]).

Each parameter shows a symmetric distribution if comparing the water and the achiral dielectric ( $\xi = 0$ ), but when the dielectric layer is chiral, the distribution becomes asymmetrical ( $\xi = 1.7 \times 10^{-4}$ ). This effect is only located in close proximity to the plasmonic surface, where the fields are strongly enhanced. To verify this, the average values of the electric field  $|E|$ ,  $C$  and  $F_z$  have been computed in the small 10 nm near-field volume and the larger far-field volume of the model and are presented in **Table 5-4**:

| Volume average | Shuriken handedness | Water |       |       | $\xi = 0$ |       |       | $\xi = 1.7 \times 10^{-4}$ |       |       |
|----------------|---------------------|-------|-------|-------|-----------|-------|-------|----------------------------|-------|-------|
|                |                     | $ E $ | $C$   | $F_z$ | $ E $     | $C$   | $F_z$ | $ E $                      | $C$   | $F_z$ |
| Far field      | <b>RH</b>           | 12.53 | -0.16 | -0.08 | 12.41     | -0.22 | -0.03 | 12.44                      | -0.21 | -0.04 |
|                | <b>LH</b>           | 12.53 | 0.16  | 0.08  | 12.41     | 0.22  | 0.03  | 12.39                      | 0.23  | 0.03  |
| Near field     | <b>RH</b>           | 24.23 | -0.42 | -0.16 | 22.26     | -0.39 | -0.12 | 22.32                      | -0.30 | -0.15 |
|                | <b>LH</b>           | 24.23 | 0.42  | 0.16  | 22.26     | 0.39  | 0.12  | 22.18                      | 0.49  | 0.08  |

**Table 5-4: Comparison of the volume averaged values of the magnitude of the electric field ( $|E|$ ), the optical chirality factor  $C$ , and the optical chirality flux along the z axis  $F_z$  of both handedness in the far-field and near-field volume with a water, achiral and chiral layer.**

As expected, the water and achiral dielectric have equal absolute values between both handedness of the shuriken, and the intensity of each parameter is higher in the near-field volume than in the larger volume. This good agreement between the LH and RH models in absence of a chiral medium shows that the mesh is reliable. With a chiral layer, we can observe an asymmetry in the response between both enantiomorphous shuriken shapes. This asymmetric response is amplified in the near field volume, with  $F_z$  values of  $-0.04$  and  $0.03$  in the far-field volume compared to  $-0.15$  and  $0.08$ . These simulation results agree with experimental observations and show that using a chiral sensing technique based on photoluminescence is a more sensitive probe of the near field than its light-scattering counterparts.

## 5.5 Conclusion

To conclude this study, we have demonstrated that chiroptical sensors based on photoluminescence have a higher sensitivity than light-scattering techniques. The *de novo* peptide monolayer has successfully generated a chiral response using the PCPL strategy while showing no measurable effect between the opposite handedness of the nanostructure using the traditional setup. The observed enhancement in the photoluminescence technique is attributed to its inherent sensitivity to the LDOS of the EM field near the surface, unlike light scattering measurements, which are effective over a much larger far-field volume. The simulation work reinforces this hypothesis by reproducing the experimental results and showing that a bigger chiroptical signal is obtained in a volume closer to the surface.

This study represents an improvement when compared to previous work that has been conducted on much larger molecules such as proteins and viruses that have a mass  $> 10 \times$  higher than *cc-Hept* [126,239]. Their impact on the EM fields generated by plasmonic nanostructures being important, a large redshift ( $> 5$  nm) can be observed and an asymmetry between both handedness can be detected, whereas the peptide studied here only causes a  $\sim 2$  nm shift relative to buffer. This novel technique based on plasmonic enhanced photoluminescence could bring innovation to the field of nanometrology and point-of-care diagnostics by efficiently probing the changes in the near-field optical chirality caused by femtomoles of chiral analyte.

## Chapter 5: Summary

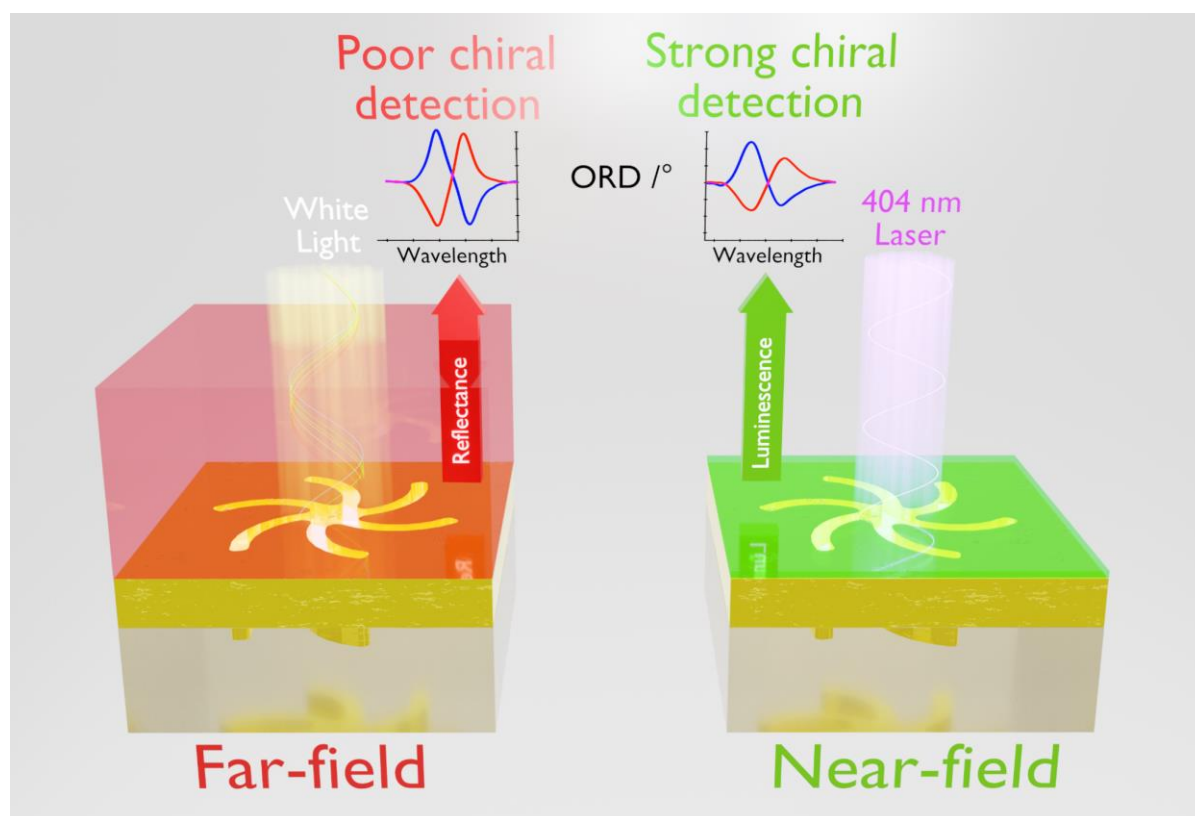


Figure 5.15: Chapter 5 concept illustration (from [139]).

### Key Findings:

- Successfully detected chiral *de novo* designed peptide using photoluminescence from plasmonic enantiomorph shuriken arrays.
- Photoluminescence probes a much smaller volume of the near field compared to far field light scattering measurements, which can't detect the small peptide.
- The simulation work supports this hypothesis and replicates the experimental observations.

# Chapter 6

---

Enantiomeric  
Discrimination of Helicoid  
Nanoparticles

## 6.1 Introduction

Raman spectroscopy is a powerful technique used in chemical analysis to measure and identify the vibrational modes of molecular structures. The Raman effect was discovered in 1928 by the Indian physicist who gave it his name [240]. It relies on the inelastic scattering of photons from monochromatic light when interacting with the sample. Due to the weakness of this effect compared to elastic scattering, this spectroscopic technique initially faced limitations from its weak signal intensity. However, significant technological advances have given rise to a plethora of applications across multiple scientific sectors [241].

Surface enhanced Raman spectroscopy (SERS) was first observed in 1974 by Fleischmann *et al.* from pyridine molecules adsorbed on a roughened silver electrode [242]. In 1977, SERS was independently verified by Jeanmaire *et al.* [243] and the enhancement was later rationalised as an electromagnetic effect originating from the high EM field of the excited plasmonic surface [244,245]. Another theory postulated that the formation of chemical charge-transfer complexes was the source of the observed enhanced Raman spectra [246]. In the 1990s, the considerable development of nanotechnology and photonics led to the fabrication and study of new SERS substrates applied to molecular sensing in a wide range of analytes [247].

The discovery of a small difference in the Raman scattering intensity of chiral molecules exposed to left- and right-circularly polarised light led to the development of Raman optical activity (ROA) [248]. This technique suffers from its inherent signal weakness, which is 3 to 5 orders of magnitude smaller than the Raman intensity itself. The development of SERS techniques using the plasmonic resonance of nanofabricated samples led to surface enhanced Raman optical activity (SEROA), which has significant potential as a chiroptical molecular probe [249].

In this chapter, SERS is used to probe large signal asymmetries in the near field of chiral plasmonic indentations in a gold metafilm. These differences in the EM environment are generated by chiral helicoid nanoparticles deposited at the surface of the metafilm. This novel technique uses an achiral molecule as a Raman signal reporter, which is also employed to bind the chiral nanoparticles to the metafilm.

## 6.2 Background

### 6.2.1 Basic principle of vibrational spectroscopy

There are three main techniques focused on the study of molecular vibration modes, namely near-infrared (NIR), mid-infrared (MIR) and Raman spectroscopy. Amongst these, MIR is the most well-established technique in the industrial and academic fields. NIR and Raman spectroscopy have recently gained traction with new technological advances but are still limited in their industrial applications [250]. These three different techniques are complementary and have advantages and disadvantages depending on the application considered.

Although these three techniques rely on different working principles, they have the same physical origin: their absorption bands are caused by molecular vibrations. In the case of a simple diatomic oscillator with an atom of mass  $M$  and the other one  $m$ , the harmonic oscillator approximation gives the vibrational wavenumber  $\bar{\nu}$  ( $\text{cm}^{-1}$ ) following Hooke's law [250]:

$$\bar{\nu} = \frac{1}{2\pi c} \sqrt{\frac{k}{\mu}}. \quad (6.1)$$

Where  $c$  is the speed of light,  $k$  is the force constant reflecting the strength of the bond between the diatomic molecule and  $\mu$  is the reduced mass, given by:

$$\mu = \frac{mM}{m + M}. \quad (6.2)$$

The vibrational frequencies are thus sensitive to the molecular structure of the analyte, making these techniques very useful in the identification and characterization of chemical compounds, as well as in studying molecular interactions and dynamics.

In its gaseous form, a molecule has three degrees of kinetic freedom per constituent atom, or  $3N$  for an  $N$ -atom molecule. For a linear molecule, there are two degrees of freedom as rotations and three as translations, therefore, there will be  $3N - 5$  vibration modes. In a nonlinear species, there are three rotations possible, hence, there are  $3N - 6$  vibrations [251].



## 6.2.2 Theory of Raman spectroscopy

When photons interact with matter, they can be either elastically or inelastically scattered. In the case of elastic scattering, called *Rayleigh* scattering, the kinetic energy of the photon is conserved. Inelastic scattering, on the other hand, arises from the excitation of the molecular analyte by the incident photon, raising its energy to a virtual energy state. The scattered photon can either possess a lower energy than the original one, referred to as *Stokes* Raman scattering, or a higher energy, called *anti-Stokes* Raman scattering. When a monochromatic laser interacts with a sample, in which most molecules are at the lowest energy vibrational level, the majority of the incident photons will be elastically scattered through the *Rayleigh* process. But approximately one in every  $\sim 10^6 - 10^8$  scattered photons will be Raman scattered. This Raman process will result in energy absorption by the molecule, bringing its vibrational energy from a ground state  $m$  to an excited state  $n$  in the case of *Stokes* scattering. Some molecules are already present in an excited state  $n$  due to thermal energy, thus, the interaction with photons can deexcite them to the ground state  $m$  through *anti-Stokes* scattering (see **Figure 6.1**) [252].

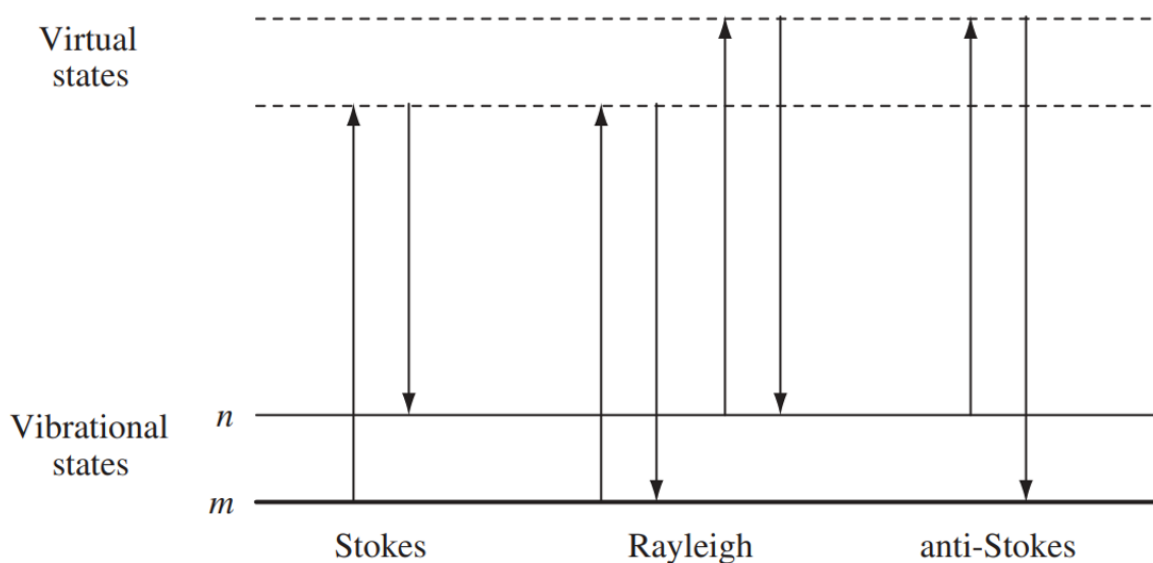


**Figure 6.1:** Energy diagram of the Rayleigh and Raman scattering. The lowest vibrational state is  $m$ , whereas  $n$  has higher energy [252].

As most molecules in the sample are present at rest before the laser interaction, the Raman signal will come mostly from *Stokes* photon scattering. The ratio between *Stokes* and *anti-Stokes* scattering will depend on the number of molecules in the ground state  $m$  ( $N_m$ ) and excited state  $n$  ( $N_n$ ). It is calculated from the Boltzmann formula [253]:

$$\frac{N_n}{N_m} = \frac{g_n}{g_m} \exp\left[\frac{-(E_n - E_m)}{kT}\right]. \quad (6.3)$$

Where  $g_m$  and  $g_n$  are the degeneracy of the  $m$  and  $n$  levels, respectively. Here,  $E_n - E_m$  is the difference between the two vibrational energy levels.  $T$  is the temperature in  $K$  and  $k$  is the Boltzmann constant ( $1.3807 \times 10^{-23} \text{ JK}^{-1}$ ).

Every molecule possesses several electronic states that have a certain number of vibrational states. These levels can be described by the *Morse* potential model, as shown in **Figure 6.2**. The energy of the system is expressed as a function of the internuclear distance  $r$ . When the atoms are far away from each other, they are considered free. As this distance decreases, electromagnetic interactions between the electrons and nuclei of the atoms lead to a net attractive force, resulting in the formation of a chemical bond. If this distance decreases further, the energy will rise, and the atoms will repel each other due to the electrostatic repulsion between the positively charged nuclei and the Pauli exclusion principle between electrons. Since Raman scattering is faster than nuclear movement, there is no change along the  $x$ -axis of **Figure 6.2** (nuclear separation). As said before, most of the molecules occupy the ground vibrational level ( $\nu = 0$ ), which corresponds to the bond length. When the molecule is excited through the Raman effect, it can rise to the first quantised excited state ( $\nu = 1$ ), referred to as the fundamental vibration. Higher states of vibration can occur and are called overtones. The probability of a transition to a level  $\nu > 1$  is very low, thus, only the first transition is considered in Raman spectroscopy [252].

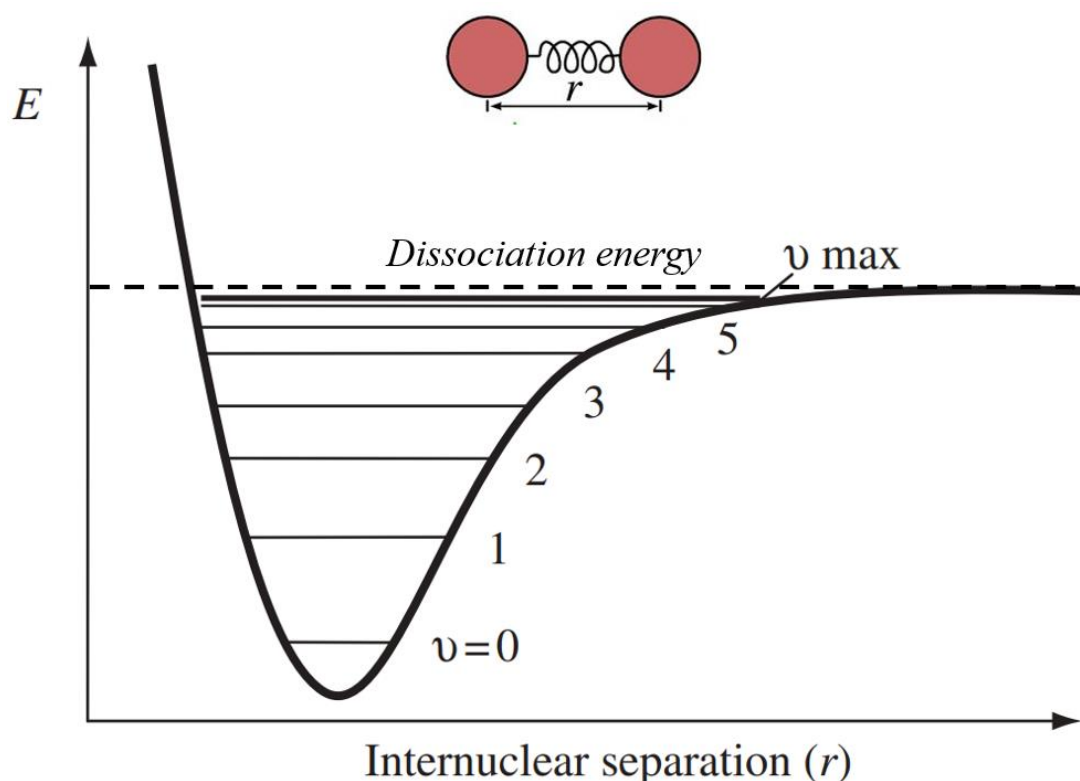


**Figure 6.2:** Morse potential curve of an electronic state with the vibrational levels represented as horizontal lines (adapted from [252]).

The Raman effect can be understood within the classical laws of electrodynamics and in a model of a quantum harmonic oscillator [254]. When a molecule interacts with an EM wave, an electric dipole moment  $P$  will be induced. The strength of this dipole moment will depend on the intrinsic polarisability of the material  $\alpha$  and the strength of the electric field  $E$  as [255]:

$$P = \alpha E . \quad (6.4)$$

The polarisability of the molecule defines its ability to form an electric dipole under an external electric field. It is a property called electric susceptibility  $\chi_e$  for the bulk material.

The time-dependent expression of the induced dipole moment in a vibrating molecule under an EM wave of frequency  $\nu_0 = c/\lambda$  can be expressed as [256]:

$$P = \alpha E_0 \cos(2\pi \nu_0 t). \quad (6.5)$$

As the displacement of the atoms is small, the molecular polarisability tensor can be expressed as a Taylor series expansion, which can be simplified by the double harmonic approximation. This gives a linear dependence of the polarisability to each vibration coordinate:

$$\alpha_k = \alpha_0 + \left( \frac{\partial \alpha}{\partial Q_k} \right) Q_k . \quad (6.6)$$

Where  $Q_k$  describes the physical displacement of the atom as a harmonic oscillation associated with the  $k^{th}$  vibration mode of wavenumber  $\nu_k$ , and amplitude  $Q_{k0}$ .  $Q_k$  can be expressed as:

$$Q_k = Q_{k0} \cos 2\pi \nu_k t . \quad (6.7)$$

Combining these expressions gives a simplified form of  $P$  at the mode  $k$  following:

$$P_k = P_k(\nu_k) + P_k(\nu_0 - \nu_k) + P_k(\nu_0 + \nu_k). \quad (6.8)$$

This equation consists of three different parts, so the induced dipole will oscillate at three different frequencies simultaneously, with the Rayleigh scattering term for an excitation frequency  $\nu_0$  being:

$$P_k(\nu_k) = \alpha_0 E_0 \cos(2\pi \nu_0 t) . \quad (6.9)$$

The other two terms describe the *Stokes* and *anti-Stokes* Raman scattering at  $\nu_0 - \nu_k$  and  $\nu_0 + \nu_k$  wavenumber, respectively. They are expressed as follows:

$$P_k(\nu_0 \pm \nu_k) = \frac{1}{2} Q_{k0} E_0 \frac{\partial \alpha}{\partial Q_k} \cos[2\pi c(\nu_0 \pm \nu_k)t] . \quad (6.10)$$

This classical approach successfully described the scattering of light through the Raman effect. The elastically scattered signal is at the same frequency as the incident radiation ( $\nu_0$ ) and the inelastically scattered frequencies are shifted lower or higher for

$(\nu_0 - \nu_k)$  and  $(\nu_0 + \nu_k)$ , respectively. An important observation is that for Raman scattering to occur, the term  $\partial\alpha/\partial Q_k$  must be non-null, meaning that a Raman-active molecular vibration must induce a change in polarisability of the molecule. This is called the Raman selection rule, dictating that symmetric vibrations will give the most intense Raman signal. Unlike infrared (IR) spectroscopy, which relies on a dipole change in the molecule, only asymmetric vibrations will be active [252]. This property makes Raman and IR spectroscopy two complementary molecular analysis techniques.

Equation (6.10) also demonstrates that the wavenumber of the Raman shift doesn't depend on the wavelength used for the excitation laser. Nonetheless, the Raman intensity  $I$  of the signal will vary depending on the characteristics of the laser, as follows [252]:

$$I = Kl\omega^4\alpha^2. \quad (6.11)$$

Where  $K$  encompasses different constants such as the speed of light,  $l$  and  $\omega$  is the laser power and frequency, and  $\alpha$  is the polarisability of the molecular analyte. From this equation, it can be noted that the laser used in the Raman setup has a major impact on the amount of Raman photons and thus the quality of the spectra.

### 6.2.3 Surface enhanced Raman spectroscopy (SERS)

As discussed in the introduction 6.1, SERS is a technique that can enhance the Raman signal, which is a naturally very rare effect. Two models of understanding were developed to explain this observed enhancement, namely the chemical complexation and the electromagnetic models.

The chemical complexation mechanism involves charge transfer between the adsorbed molecule and the metallic surface. This will create new electronic states, altering the polarisability of the molecule. The EM model is explained through the LSPR process. The contribution of the EM model to SERS has been associated with the majority of the observed enhancement and will therefore be the focal point of this part [257].

When an incoming EM wave at a frequency close to the LSPR frequency reaches the metallic surface, an oscillation of the electronic cloud will lead to a plasmon-induced enhancement of the local electric field near the metal surface. This increase in the local field intensity will, in turn, cause an increase in the intensity of the incident light experienced by the adsorbed molecules. Some of the Raman scattered light will also participate in the excitation of the LSPR of the plasmonic structure [258].

The SERS intensity will thus depend on the incident light frequency  $\nu_{inc}$  and the outgoing Raman signal at a shifted frequency  $\nu_R = \nu_{inc} - \nu_{vib}$ , as [258]:

$$I_{SERS} = |E_{inc}(\nu_{inc})|^2 \cdot |E(\nu_R)|^2. \quad (6.12)$$

This equation indicates that the maximum SERS enhancement is observed when the incident light frequency ( $\nu_{inc}$ ) and the Raman scattered light frequency ( $\nu_R$ ) both match the resonance frequency of the metal's plasmonic mode (LSPR).

The SERS enhancement factor (EF) can be expressed in terms of the material properties of the metal and the distance of the molecular analyte ( $d$ ) from the surface. In the simplified case where the plasmonic nanostructure is a sphere of radius  $r$ , far smaller than the wavelength of the incident light, we obtain [258]:

$$EF(\nu_R) \cong \left| \frac{\varepsilon(\nu_{inc}) - \varepsilon_0}{\varepsilon(\nu_{inc}) + 2\varepsilon_0} \right|^2 \left| \frac{\varepsilon(\nu_R) - \varepsilon_0}{\varepsilon(\nu_R) + 2\varepsilon_0} \right|^2 \left( \frac{r}{r+d} \right)^{12}. \quad (6.13)$$

Here,  $\varepsilon(\nu)$  is the complex frequency-dependent dielectric function of the plasmonic material and  $\varepsilon_0$  is the dielectric constant in the bulk. The SERS enhancement is therefore maximised when the real part of  $\varepsilon(\nu)$  is equal to  $-2\varepsilon_0$  and the imaginary part is close to zero. This strong dependence of the SERS signal on the material properties makes the choice of the plasmonic metal a key factor in SERS. Noble metals, like gold and silver, are the most widely used materials with an excitation wavelength in the visible to near-IR range. The EF is also proportional to the distance of the molecular analyte with the plasmonic structure as  $(1/d)^{12}$ , with an effective distance  $d \leq 5$  to 10 nm [259].

## 6.2.4 Raman optical activity (ROA)

Raman optical activity (ROA) or surface enhanced Raman optical activity (SEROA) are chirally sensitive techniques derived from the Raman scattering effect. Similar to CD, they rely on the measurement of a small difference in the Raman intensities coming from an incident LH and RH circularly polarised light.

The relative strength of the (SE)ROA signal is characterised by the circular intensity difference (CID), which is calculated from the intensities  $I_{LH}$  and  $I_{RH}$  of the inelastically scattered light as [249]:

$$\Delta = \frac{(I_{RH} - I_{LH})}{(I_{RH} + I_{LH})}. \quad (6.14)$$

Ever since the pioneering work of L. Barron [30,260], ROA and its derivatives are recognised as promising chiral spectroscopic techniques with the potential to bring new applications to this field. Despite technological advances, the ROA signal is still weak, with a CID lower than  $10^{-3}$ , and a signal intensity 3 to 5 orders of magnitude smaller than traditional Raman scattering. In addition, the background noise hinders the selectivity and sensitivity of this chiral spectroscopic technique. Although SEROA can be used to

moderately enhance the signal and reach a CID  $\geq 10^{-3}$ , this technique has been faced with several challenges.

Indeed, SEROA suffers from a lack of reproducibility that originates from the fabrication of the SEROA nanopatterned platforms. Its relatively weak enhancement of the ROA signal also makes it time-consuming to acquire quality spectra. Furthermore, the anisotropic distribution and orientation of the Raman-active analytes or chiral nanostructures also limit this technique by adding an angular dependency to the signal [261].

One alternative to SEROA in the detection of chiral analytes is chirally dependent SERS, which is the focal point of this chapter. Instead of using circularly polarised excitation light, this technique relies on the asymmetric change in the local EM environment near chiral plasmonic platforms. This technique benefits from the strong enhancement of SERS (up to  $10^8$ ), which suggests it can achieve single-molecule chiral detection [262,263].

## 6.3 Method

The experimental work summarised here was executed by Martin Kartau and Anastasia Skvortsova at the University of Glasgow and at the University of Chemistry and Technology in Prague. My contribution to this study was on the simulation part, which supports the experimental results. Further details on the experimental work are available in the paper published in the *Advanced Optical Materials* journal [264].

### 6.3.1 Sample and analyte

The plasmonic sample used in this study is the gold metafilm TPS shuriken array. The nanofabrication process and the dimensions of the metamaterials have already been described in Section 3.1.2. This sample contains arrays of left-handed (LH) and right-handed (RH) shuriken-shaped cavities (see Figure 6.3 (a) and (b)).

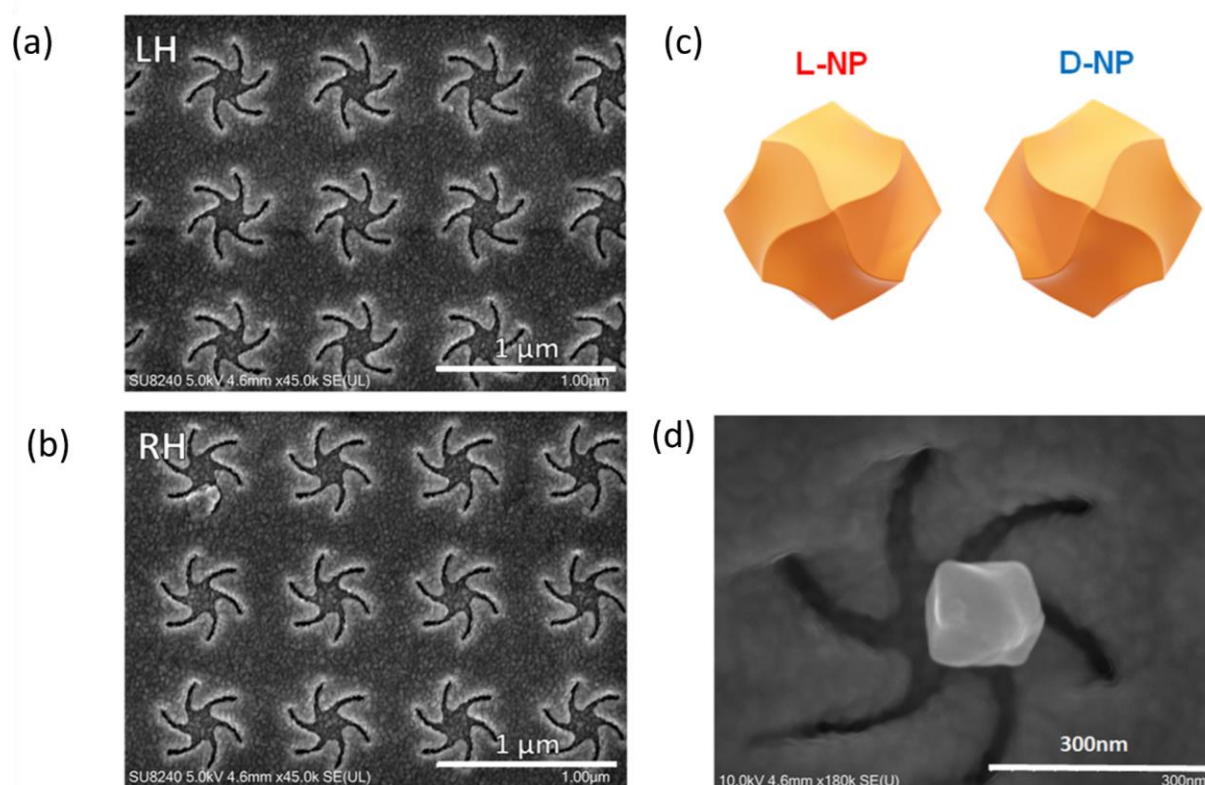


**Figure 6.3:** SEM images of (a) the LH array and (b) the RH array. (c) Ideal representation of the L and D gold HNPs (from [265,266]). (d) SEM image of a RH shuriken functionalised with a L-HNP (from [264]).

The chiral nanoparticles used in combination with the TPS sample are ~260 nm large gold helicoidal nanoparticles (HNP) with a rhombic dodecahedral shape (see Figure

6.3 (c) and (d)). These HNP were designed to have optical activity in the same region as the TPS plasmonic metafilm. They were synthesised by a seed-mediated colloidal growth strategy [265,266], with cysteine, a chiral amino acid, used to control the handedness of the final shape. This technique allowed the fabrication of enantiomorphous HNP, the orientation obtained using L-cysteine was called L-HNP (left-handed), and D-HNP (right-handed) when D-cysteine was used as an additive.

To functionalise the TPS metafilm with the HNP, a SAM of achiral biphenyl-4,4'-dithiol (BPDT) (see **Figure 6.4**) was deposited on the metafilm surface through thiol bonding, the other thiol group being used to anchor the HNP. This SAM was obtained after cleaning the TPS with methanol and O<sub>2</sub> plasma treatment at 100 W for 5 min. Then, a 3 mM solution of BPDT (95%) (Sigma-Aldrich) in methanol was left for 24 h at the gold surface of the nanostructures. After rinsing with methanol, a solution of 30 mg/mL of HNP in DI water was then left on the sample for 24 h. Unbound HNP were rinsed with DI water and subsequently dried with N<sub>2</sub>.

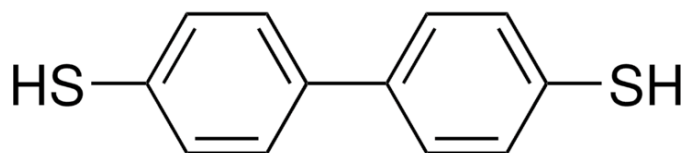


**Figure 6.4: biphenyl-4,4'-dithiol (BPDT) molecule.**

This molecular SAM was used as a Raman reporter to provide a SERS signal and compare the enhancements of the different combinations of shuriken and HNPs. The Raman measurements were obtained using a NT-MDT NTEGRA commercial Raman microscope with a 633 nm laser excitation (35 mW). The Raman scattered signal was taken using a 20× objective with a 100 μm spot size and 10 s of accumulation time.

### 6.3.2 Simulation modelling

The EM simulations were conducted on *COMSOL V6.0 Multiphysics* using the Wave Optics module described in Section 3.4.2. An ideal shuriken shape was defined at the centre of a 1600 nm height block in a 100 nm thick gold domain. The properties of the domains above and below the metafilm were set to air and polycarbonate, respectively. A ~260 nm large HNP from end-to-end, of either L or D handedness, was placed at the centre of the shuriken and close to one of the arms in another simulation model. This is the average size of the particles, found from measuring and counting the particles on SEM images of the sample. Due to computation limits, this HNP could not be positioned 1 nm away from the gold surface as in the experiment. Instead, the HNP was placed around 15 nm from the shuriken. Periodic boundary conditions were applied to the vertical surfaces of the block to mimic an array of shuriken nanostructures. Perfectly matched layers were



defined on the top and bottom domains to avoid light reflection back in the model. The mesh size was adapted depending on the medium, with a 30 nm maximum mesh size in the polycarbonate, 23 nm in the air medium, and a finer mesh of 13 nm in the gold domains.

## 6.4 Results and discussion

### 6.4.1 Sample optical properties

The plasmonic properties of both shuriken handedness have been measured in air by reflectance and ORD spectroscopy and are displayed in **Figure 6.5** (a). A broad resonance in the reflectance spectra is visible between 500 and 650 nm, and sharper peaks are located in the 700 to 770 nm region, displaying Fano coupling between multiple modes [181,232]. The gold HNP are plasmonic materials as well as the TPS shuriken substrate, and their strongest resonance region is in a similar range, between 500 and 650 nm (see **Figure 6.5** (b)). The different combinations of chiral shuriken nanostructures and HNPs can be considered as diastereomers, where these two objects are non-mirror images and non-identical stereoisomers. The 4 possible combinations are named LL, LR, RL, and RR, with the first letter corresponding to the shuriken handedness and the second one to the HNP's. All the combinations have been studied, with the HNPs distributed over the surface randomly, as seen in **Figure 6.6** (a).

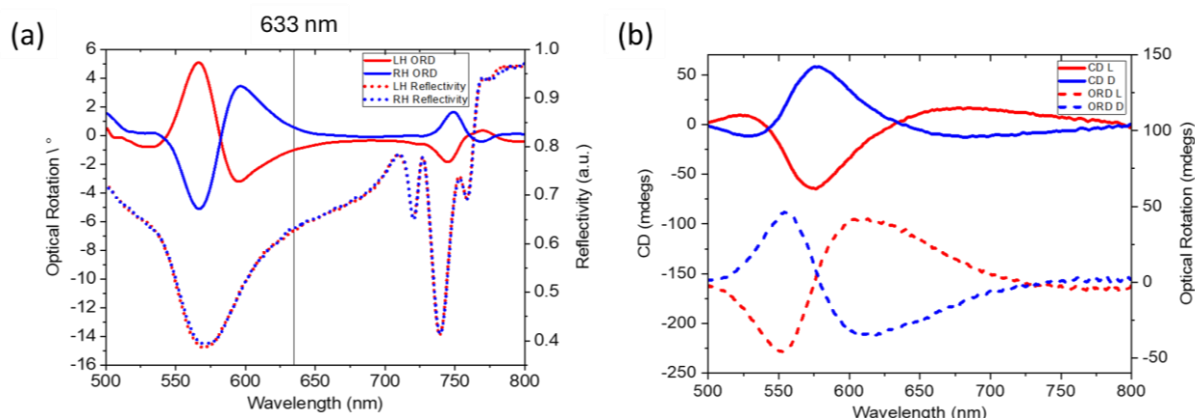


**Figure 6.5:** (a) ORD and reflectance of LH (red) and RH (blue) plasmonic shuriken with the position of the Raman excitation wavelength in the vertical black line, and (b) measured CD and calculated ORD spectra (Kramers-Kronig transform) of L- and D-HNPs in aqueous solution in red and blue, respectively (from [264]).

The ORD spectra of all the combinations have been measured using the setup described in Section 3.3 and are shown in **Figure 6.6** (b). The BPDT SAM adsorbed on the gold shuriken film causes a red shift of  $\sim 2.2$  nm between the enantiomorphs, indicating a uniform SAM across the sample [264]. The HNP functionalised samples displayed a red shift in the ORD spectra of  $\sim 1.6$  nm for all the combinations, thus, no measurable asymmetric response in the far field was observed. This also demonstrates a similar HNP coverage between all the combinations.

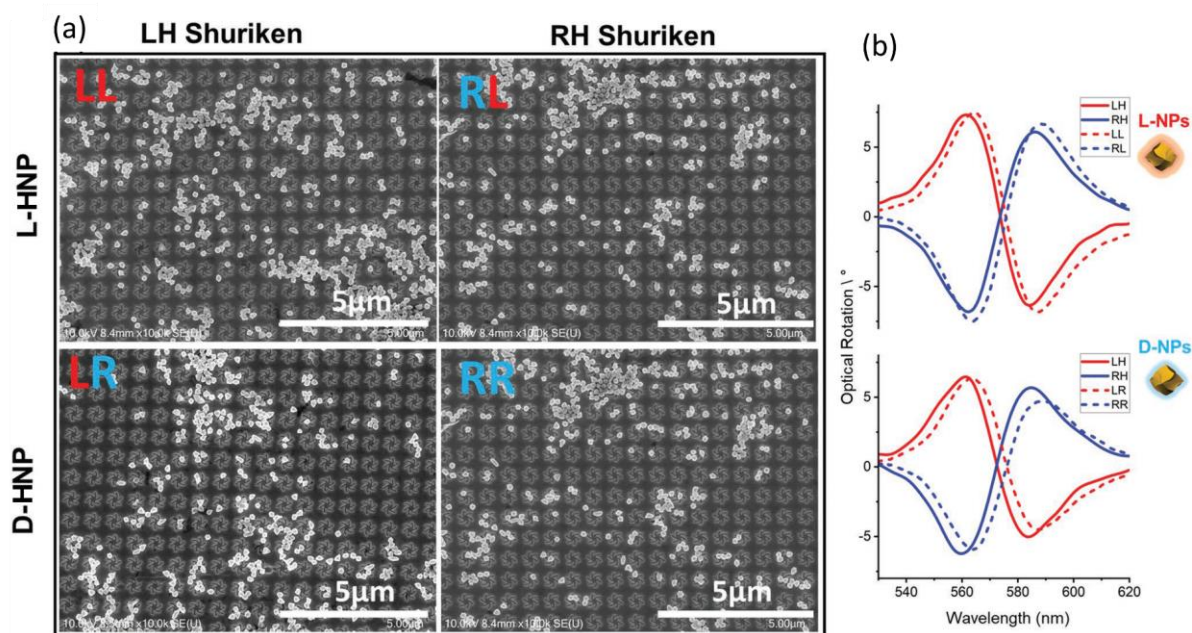


**Figure 6.6:** (a) SEM images of all the combinations of LH and RH shuriken arrays functionalised with BPDT and L- and D-HNPs. (b) ORD spectra of clean (solid lines) and HNP's functionalised LH (in dotted red lines) and RH (in dotted blue lines) shuriken arrays (from [264]).

## 6.4.2 SERS measurements

The SERS signal obtained is derived solely from the vibration bands of the achiral BPDT molecular SAM, which acts as a Raman reporter. The main Raman peaks are located at 1589, 1285, 1200 and 1084  $\text{cm}^{-1}$ , with 1589  $\text{cm}^{-1}$  being the strongest (see **Figure 6.7** (e)). These SERS peaks are coherent with the vibration modes observed in other studies [267].

In a first step, SERS of the BPDT SAM was recorded without the HNP on the flat gold and on both handedness of shuriken arrays (see **Figure 6.7** (a)). As expected, the spectra showed no enhancement on flat gold and an identical response from both handedness of the plasmonic nanostructures. The Raman signal from both L- and D-HNP was measured on flat gold, and the intensity of the two spectra was found to be identical within the standard error (see **Figure 6.7** (b)).

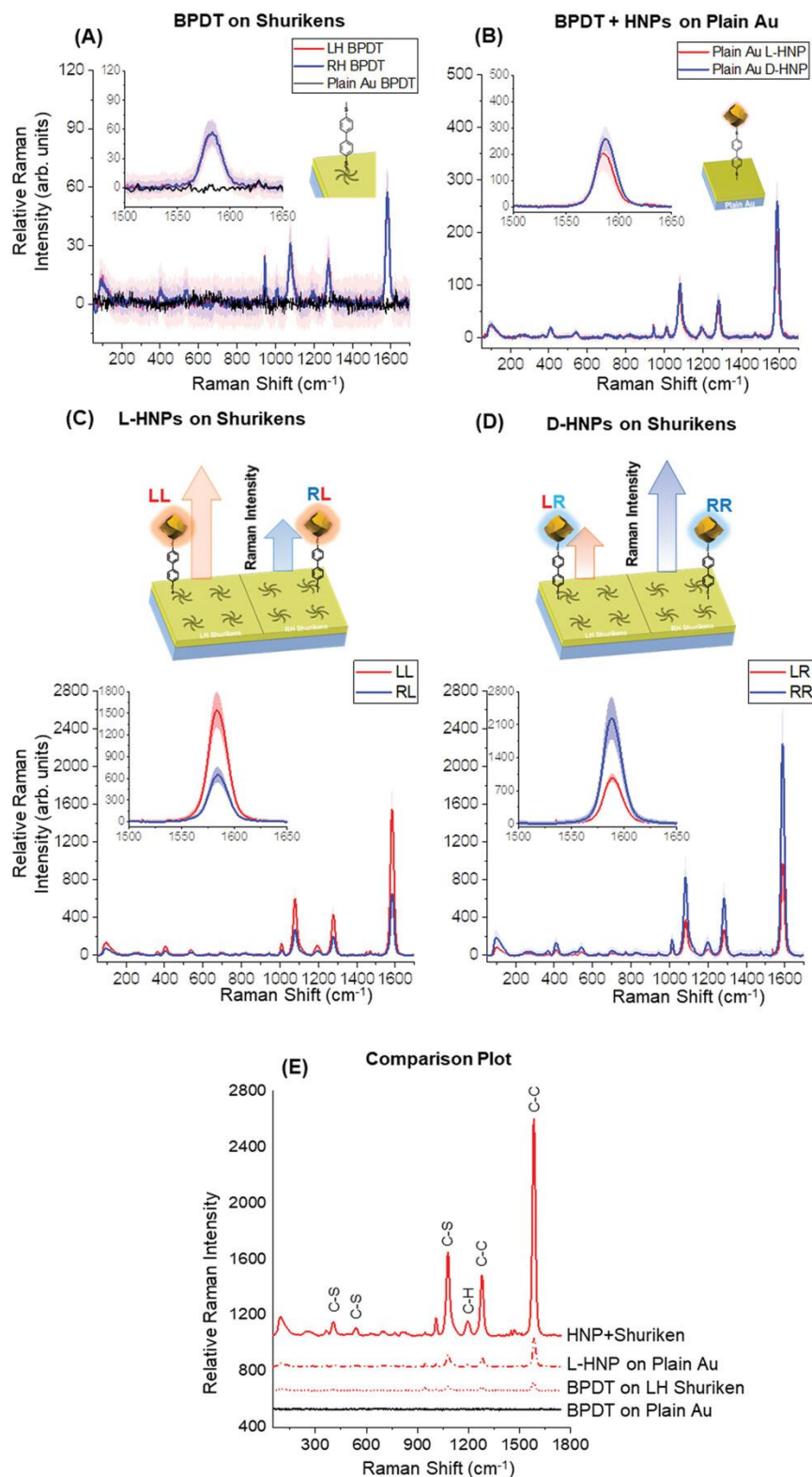


Figure 6.7: SERS spectra of (a) LH (red) and RH (blue) shuriken with BPDT only, (b) L (red) and D-HNP (blue) on flat gold (c) L-HNPs and (d) D-HNPs functionalised LH and RH shuriken arrays. The solid lines are the average of 9 data sets and the shaded area is the standard error. The inset plots are zoomed-in views of the most intense peak. (e) SERS intensities from BPDT on plain gold and on LH array, L-HNPs on flat gold and finally HNPs on shuriken nanostructures with the assignment of the chemical groups (from [264]).

When the plasmonic shuriken structures are combined with the chiral HNPs, the resulting Raman signals show a strong dependence on the diastereomer combination. As seen on **Figure 6.7** (c) and (d), when the handednesses are matching (LL and RR), the SERS signal is significantly enhanced compared to the mismatched combinations (LR and RL). The average ratios of these combinations were found to be  $0.50 \pm 0.02$  and  $0.47 \pm 0.02$  for LR/RR and RL/LL, respectively. The amplitude of the SERS signal from the HNP-functionalised shuriken arrays has been shown to be significantly increased compared to the signal coming solely from the HNPs on a flat gold surface ( $\sim 7.5$  times). The SERS intensity of the HNPs on gold was also  $\sim 4.5$  times stronger than the signal from the BPDT functionalised shuriken film alone (see **Figure 6.7** (e)). This is because the SERS signal is proportionnal to the EM hotspot (see Section 6.2.3), which is govern mainly by the width in the arms of the shuriken (without HNPs), or the gap between the HNPs and either the flat gold or shuriken nanostructure. The width of the arms being much larger than the length of the BPDT molecule that separates the HNPs from the surface, the SERS signal will therefore be higher in the latter case.

These experimental results show a dependency between the Raman signal enhancement and the symmetry of the diastereomeric pair. To ensure this asymmetry between the SERS signals was not due to an uneven coverage of the HNPs, the measurements have been reproduced by taking the SERS signal at 10 different spots on the chiral arrays, showing the same trend (see [264]). This observation can be understood by the difference in the EM environment created between the matching and mismatching pairs. In the next part, the experimental results will be rationalised through EM simulation of all the combinations of shuriken and HNP.

### 6.4.3 Simulation results

Firstly, the reflectivity of both handedness of the shuriken metafilm was simulated in air without any HNP and compared to the experimental measurements. As seen in **Figure 6.8**, the simulation model qualitatively agrees with the experimental spectra, showing an identical response for both shuriken handedness. A dip is present at 573 nm in the experimental data (see **Figure 6.8** (b)), while this plasmonic mode is red shifted by around 10 nm at 584 nm in the simulations (see **Figure 6.8** (a)). This slight shift in the position of this spectral feature is insignificant in our study, since the laser wavelength used by the SERS equipment is far outside this reflectance resonance (633 nm).

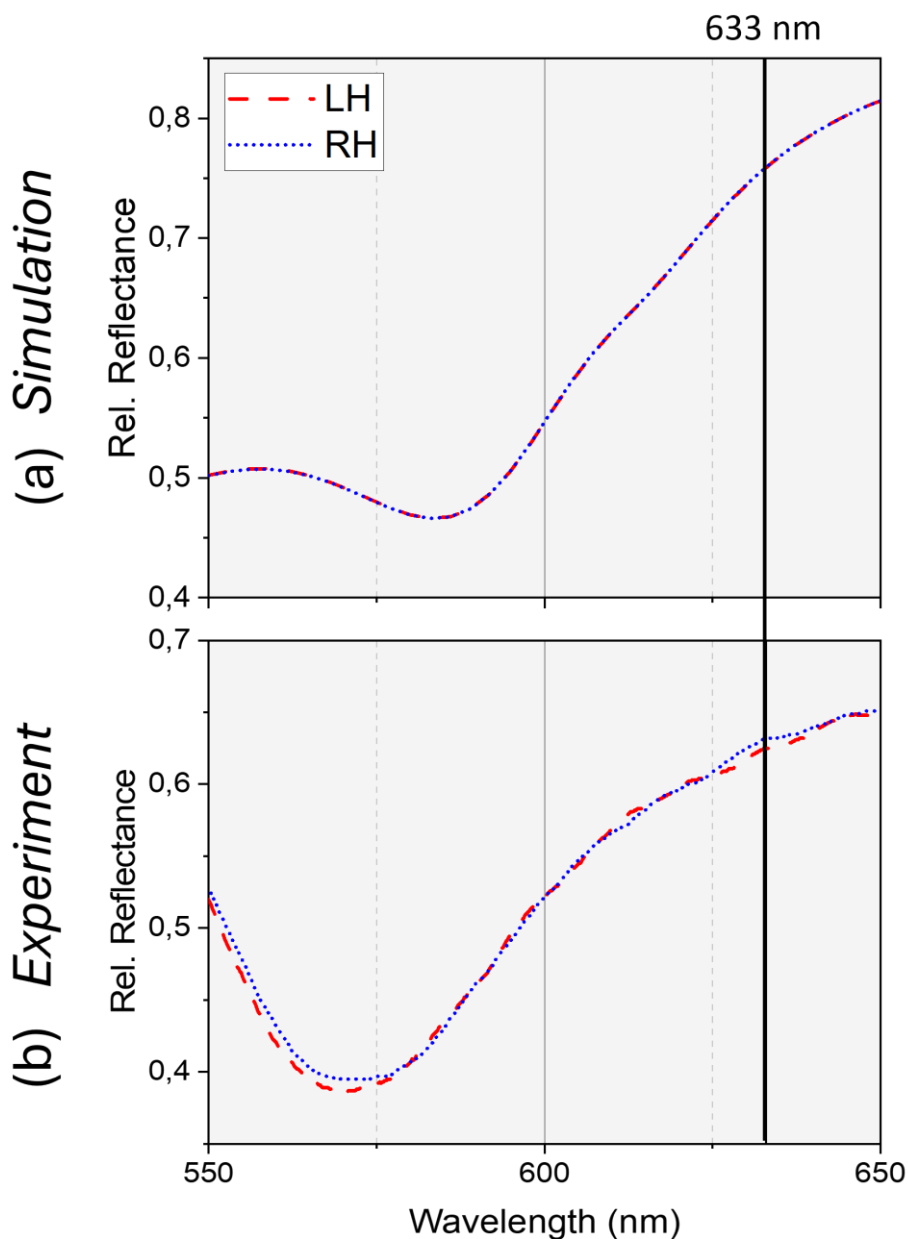


**Figure 6.8:** Reflectance spectra relative to the gold background for the LH (red) and RH (blue) shuriken arrays with (a) the simulated data and (b) the experimental data. The laser wavelength of the SERS setup is represented by a solid black line at 633 nm.

In a second step, the CD response of both handedness of the HNP was studied, isolated from the chiral plasmonic metafilm (see **Figure 6.9** (a)). The difference in the transmission between LH and RH CPL was used to obtain the CD spectra of both HNP handedness in water and in air (see **Figure 6.9** (b) and (c)).

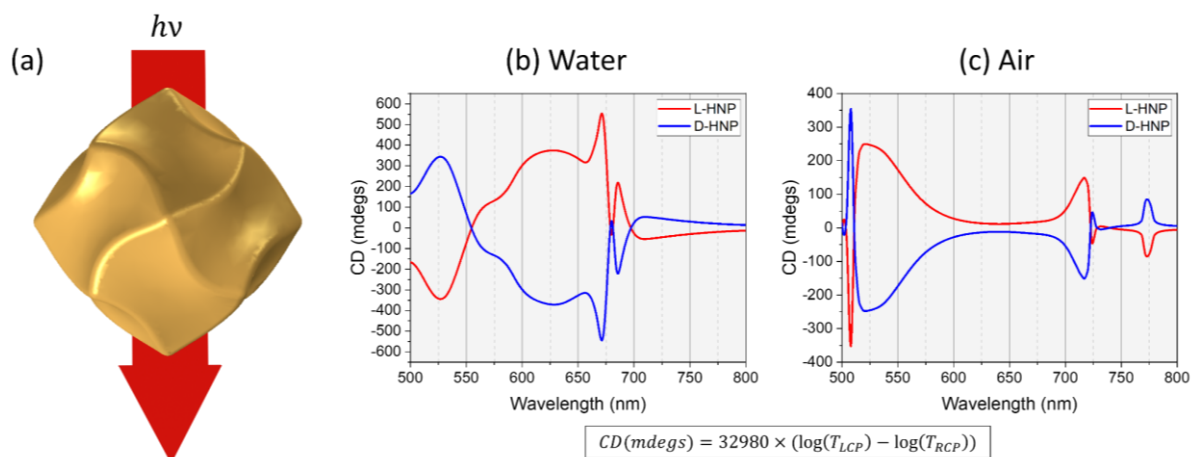


**Figure 6.9:** (a) Orientation of the HNP relative to the propagation direction of the incident CPL in the model. CD spectra of the L-HNP (red) and D-HNP (blue) calculated from the transmitted light ( $T_{LCP/RCP}$ ) in (b) water and (c) air.

As expected, the CD response obtained is equal and opposite between both handedness of HNP in water and in air. The simulated spectra in water have a peak at 525 nm, which is blue shifted compared to the experimental CD presented in **Figure 6.5** (b) where the main resonance is at 575 nm, but they are qualitatively matching, with a positive CD for the D-HNP and negative CD for L-HNP. This discrepancy originates from the simplification of the simulation model, in which a single HNP is used (see **Figure 6.9** (a)). This model does not account for the variation in particle orientation and size, as well as plasmonic interactions with neighbouring HNPs in the solution. In air, a sharp peak is located at 510 nm, blue shifted from the water data due to a lower refractive index.

The HNP can now be associated with the shuriken metafilm to study the far field optical response and the near field EM environment of all the combinations. Due to limited computational resources, a single HNP of 260 nm end-to-end dimension was used. In order to replicate the experimental conditions and account for different HNP orientation and location relative to the shuriken cavity, three models were designed. The first model contains the HNP of either L- or D-orientation placed in the middle of a LH or RH shuriken, 250 nm above the bottom of the cavity (see **Figure 6.10** (a)). In the second model, the HNP is rotated  $45^\circ$  relative to the first model (see **Figure 6.10** (b)). The third model was designed with the HNP in proximity to one of the arms of the shuriken structure, where the bottom of the HNP was at the same height as the top surface of the gold film (see **Figure 6.10** (c)).



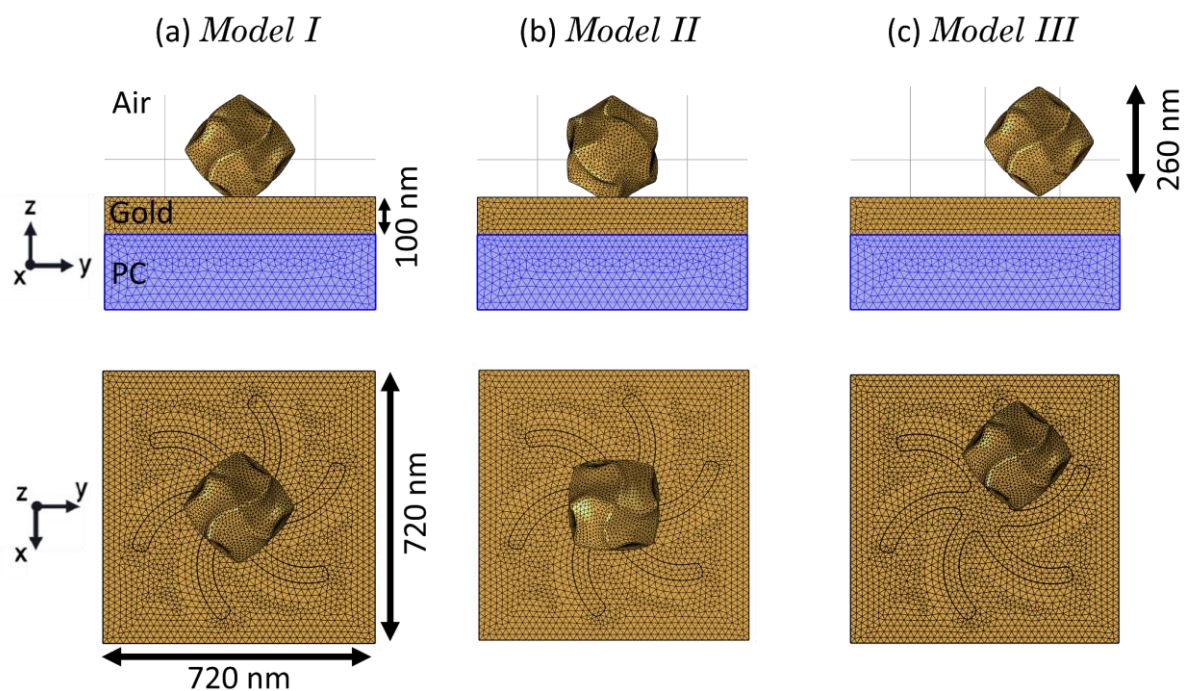


Figure 6.10: Side and top views of the three simulation models, with a LH Shuriken combined to an L-HNP placed (a) in the middle of the cavity, (b) rotated  $45^\circ$  from the first model and (c) in the middle of an arm of the shuriken.

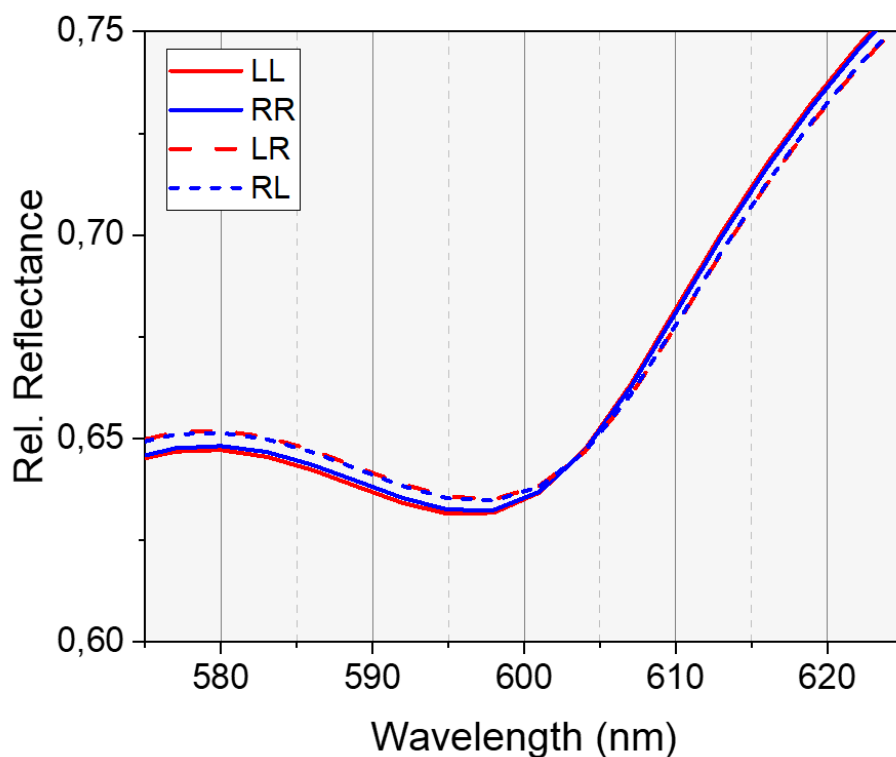


Figure 6.11: Reflectance spectra of Model I for all the combinations of HNP and shuriken handedness in air, with the matching handedness in the solid lines and the mismatching pairs in the dashed lines.



For *Model I*, the reflectance spectra of all four combinations were plotted in **Figure 6.11**. The introduction of the HNP causes a reflectance shift of ~12 nm, which is higher than the ~2 nm red shift observed experimentally (see **Figure 6.6 (b)**). This discrepancy can be caused by the simplification of the simulation model, where the HNP is perfectly centred, and all the shapes are idealised. A small shift, of less than 1 nm, can be seen here between the matching (LL and RR) and mismatching (LR and RL) pairs (see **Figure 6.11**). This relative shift is small compared to the absolute shift caused by the HNP, and as concluded from the experimental data of the ORD spectra, a far-field measurement is unable to detect any change in combination. This lack of sensitivity justifies the use of another technique, more sensitive to the near-field EM environment between the shuriken cavity and the particle.

As discussed in the background, Section 6.2.3, it is known that Raman scattering enhancement is the result of the EM field enhancement in the plasmonic nanostructure and the increase in radiative decay rate at the Stokes frequency [218,268]. The SERS enhancement factor (EF) represents the relative intensity of the Raman signal compared to the Raman signal obtained conventionally. When the frequency of the scattered light is close to the excitation beam, EF can be expressed as [269]:

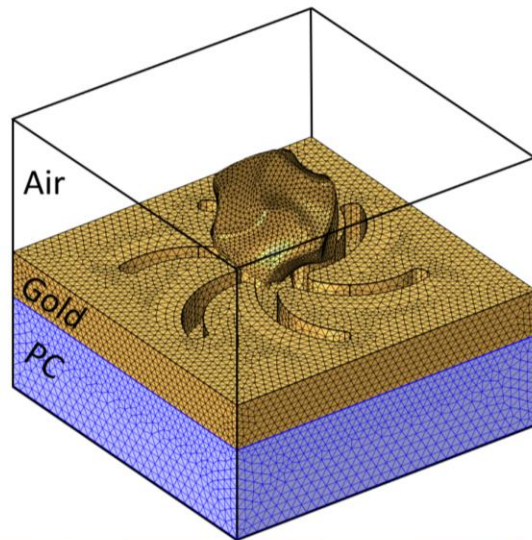
$$EF \approx \left| \frac{E_{loc}}{E_0} \right|^4. \quad (6.15)$$

With the local electric field amplitude  $E_{loc}$  at the Raman active site and  $E_0$  the electric field amplitude of the incident excitation beam. The intensity of the ‘hotspots’ in the matching combinations (LL and RR) is consequently postulated to be greater than in the mismatching pairs (LR and RL), such as:

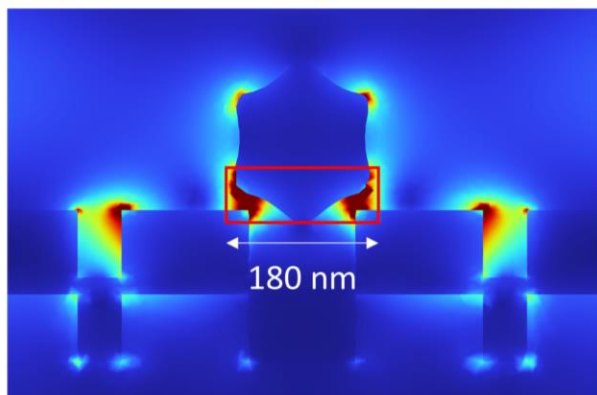
$$\left| \frac{E_{loc}}{E_0} \right|_{LL,RR} > \left| \frac{E_{loc}}{E_0} \right|_{LR,RL}. \quad (6.16)$$

To verify this hypothesis, a 633 nm incident beam polarised linearly was used in the models of all the diastereomeric combinations. The EM environment in the narrow gap between the Shuriken and the HNP was studied in all three models (see **Figure 6.12, 6.13 and 6.14 (a)**), where the amplitude of the electric field was plotted in vertical slices, and the values of  $E_{loc}/E_0$  were averaged in all the hotspot regions (see red box in **Figure 6.12, 6.13 and 6.14 (b)**). The result of this work is presented in **Figure 6.12, 6.13 and 6.14 (c)**, where a top view shows the position where the vertical slice was taken, and a side view of the hotspots for each diastereomeric combination.

(a) Model I



(b)



(c)

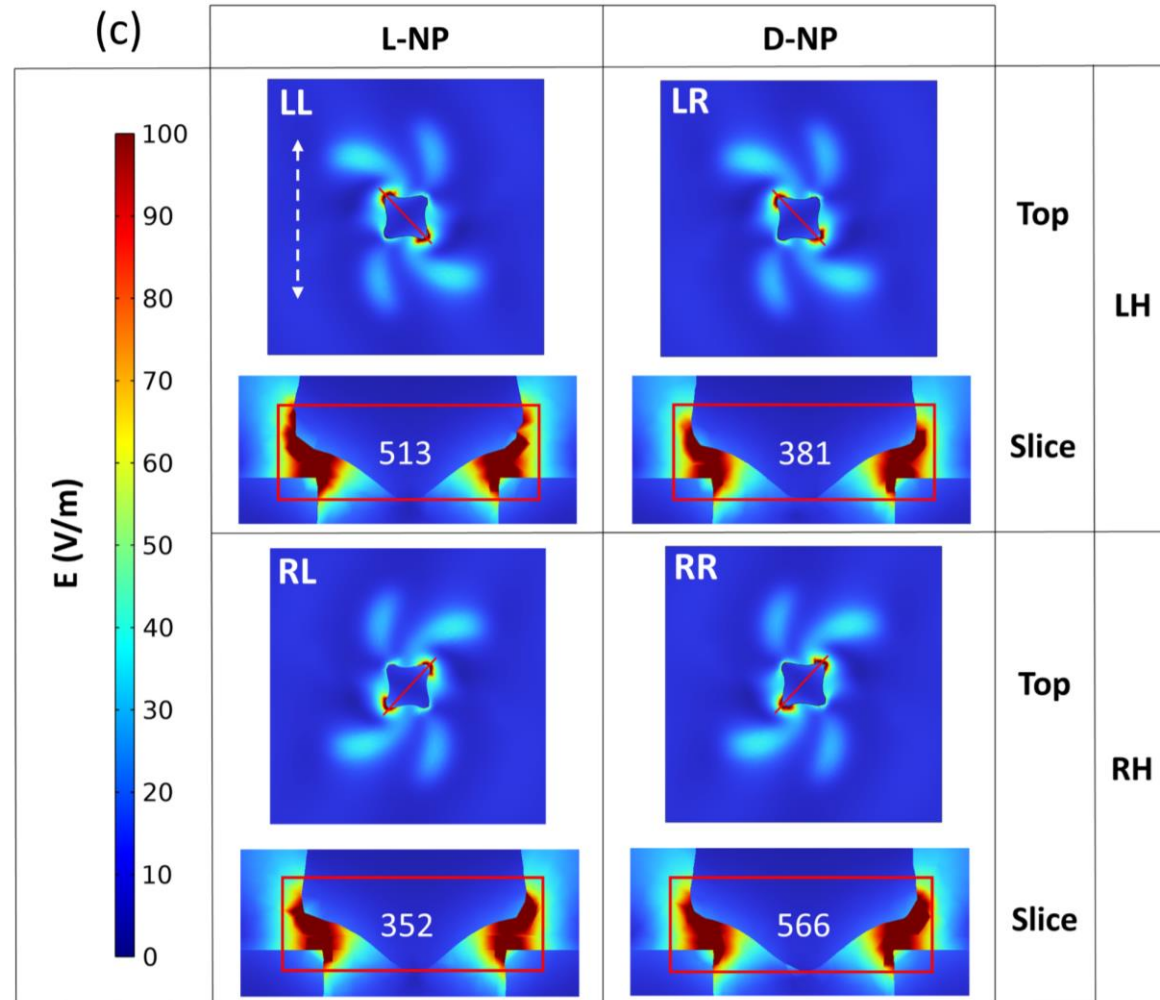


Figure 6.12: Simulation model of an HNP at the centre of the shuriken nanostructure with (a) orthogonal view of the LL diastereomer, (b) sliced view of the simulated  $|E|$  showing the hotspot zone in the red box of  $55 \times 180$  nm. (c) Simulation maps of  $|E|$  for all the combinations with a top view above a sliced view with the average of  $|E_{loc}/E_0|^4$  in the middle of the box. The polarisation angle of the incident light is represented by a dashed white arrow in the top left panel [264].

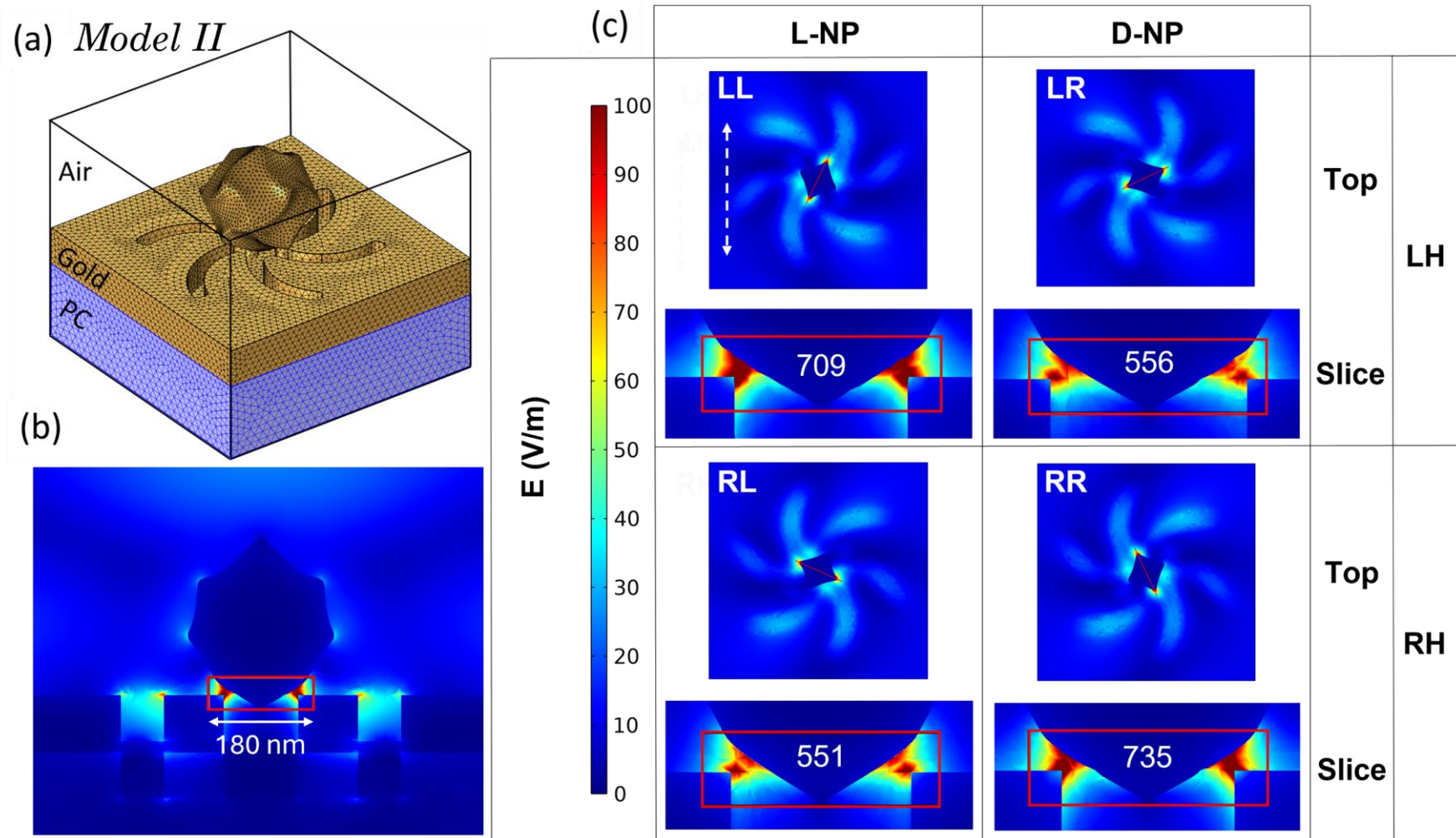
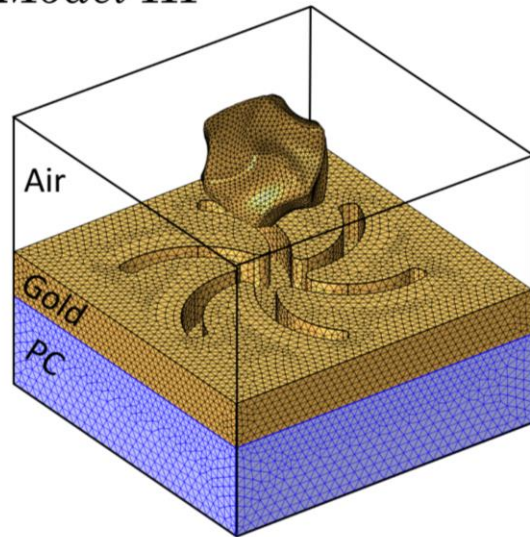
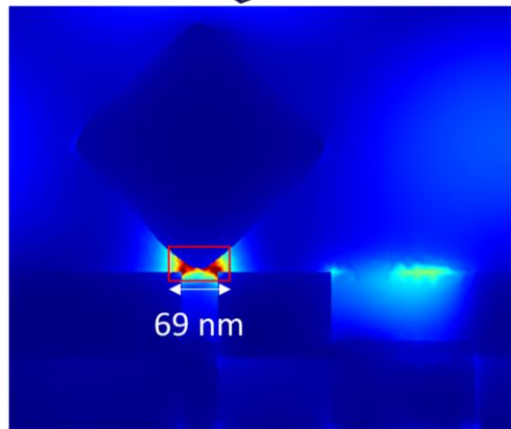


Figure 6.13: Simulation model of an HNP at the centre of the shuriken rotated by  $45^\circ$  with (a) orthogonal view of the LL diastereomer, (b) sliced view of the simulated  $|E|$  showing the hotspot zone in the red box of  $45 \times 180$  nm. (c) Simulation maps of  $|E|$  for all the combinations with a top view above a sliced view with the average of  $|E_{loc}/E_0|^4$  in the middle of the box. The polarisation angle of the incident light is represented by a dashed white arrow in the top left panel [264].

(a) Model III



(b)



(c)

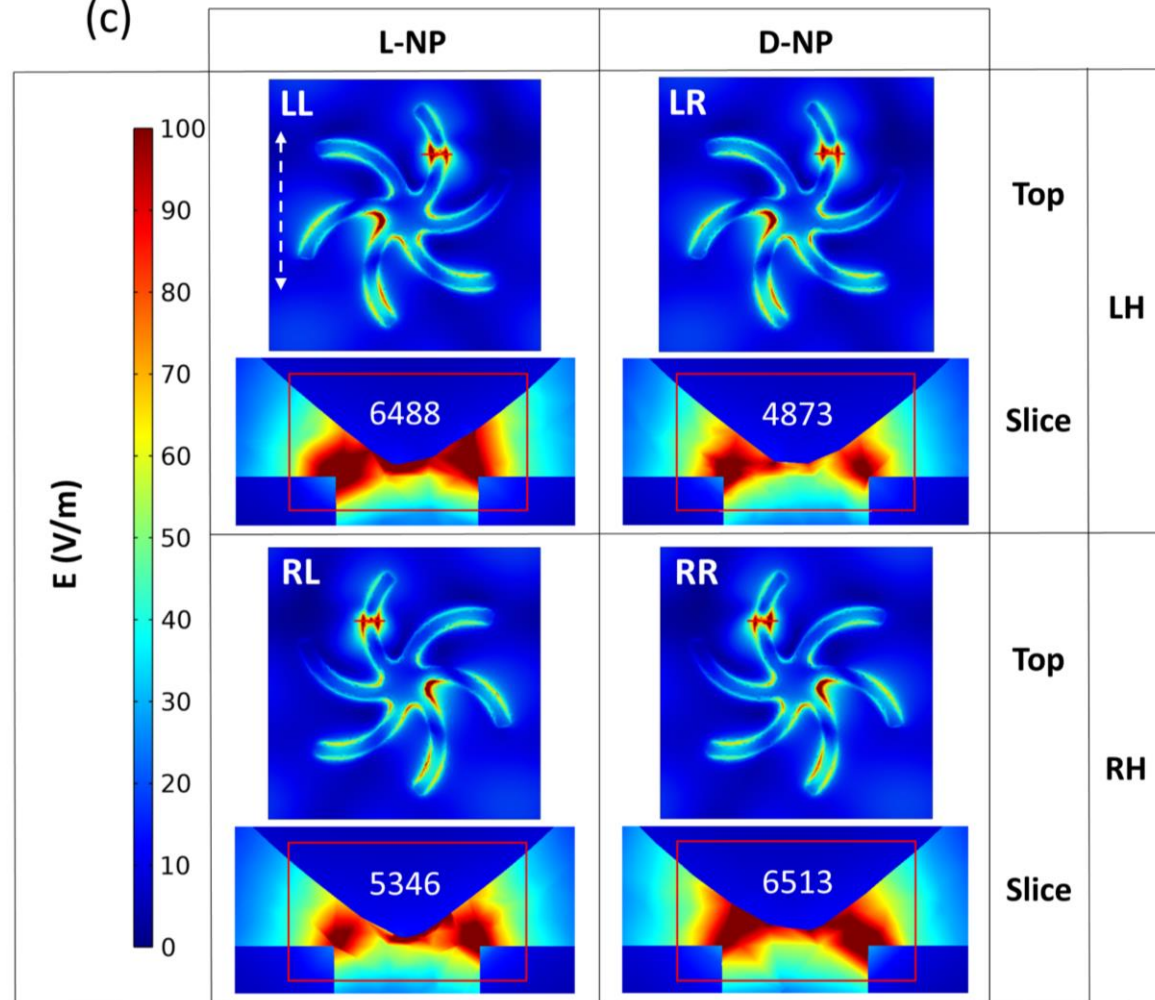


Figure 6.14: Simulation model of an HNP at the centre of a shuriken arm with (a) orthogonal view of the LL diastereomer, (b) sliced view of the simulated  $|E|$  showing the hotspot zone in the red box of  $35 \times 69$  nm. (c) Simulation maps of  $|E|$  for all the combinations with a top view above a sliced view with the average of  $|E_{loc}/E_0|^4$  in the middle of the box. The polarisation angle of the incident light is represented by a dashed white arrow in the top left panel [264].



The averaged values of  $|E_{loc}/E_0|^4$  obtained in all the models for all the combinations are presented in **Table 6-1**. The key observation from these simulation results is that, as expected, the matching combinations (LL and RR) have the most intense hotspots compared to the mismatched pairs (LR and RL). This hotspot intensity is translated in the experiment as a Raman signal enhancement. The small variations between the averaged values obtained here on diastereomers of the same symmetry can be attributed to the difference in the meshing process.



| $ E_{loc}/E_i ^4$   | <b>LR</b>          | <b>RR</b>   | <b>RL</b>          | <b>LL</b>   |
|---------------------|--------------------|-------------|--------------------|-------------|
| <b>Model I</b>      | 381                | <b>566</b>  | 352                | <b>513</b>  |
| <i>Ratios</i>       | <i>0.67</i>        |             | <i>0.69</i>        |             |
| <b>Model II</b>     | 556                | <b>735</b>  | 551                | <b>709</b>  |
| <i>Ratios</i>       | <i>0.76</i>        |             | <i>0.78</i>        |             |
| <b>Model III</b>    | 4873               | <b>6513</b> | 5346               | <b>6488</b> |
| <i>Ratios</i>       | <i>0.75</i>        |             | <i>0.82</i>        |             |
| <b>Av. Models</b>   | <i>0.73</i>        |             | <i>0.76</i>        |             |
| <i>Ratios</i>       | <i>0.73</i>        |             | <i>0.76</i>        |             |
| <b>Experimental</b> | <i>0.50 ± 0.02</i> |             | <i>0.47 ± 0.02</i> |             |
| <i>Ratios</i>       | <i>0.50 ± 0.02</i> |             | <i>0.47 ± 0.02</i> |             |

**Table 6-1: Summary table of the three models compared to the experimental data, with the averaged values of  $|E_{loc}/E_0|^4$  and the ratios of LR/RR and RL/LL.**

The ratios of the average values of  $|E_{loc}/E_0|^4$  between LR/RR and RL/LL were calculated for all three simulation models and are available in **Table 6-1**. The average of all the ratios obtained from the different simulation models is 0.73 and 0.76 for LR/RR and RL/LL, respectively. These values are in qualitative agreement with the experimental observations, calculated at 0.43 and 0.46. The discrepancy between these ratios can originate from the fact that the areas where  $|E_{loc}/E_0|^4$  is averaged contain a large surface within the metal volumes, where the electric field is insignificant (see **Figure 6.12, 6.13 and 6.14 (c)**).

The distance between the HNP and the shuriken cavity has a major impact on the enhancement of the electric field; it is thus important to take it into account. In *Model I*, the HNP is ~18 nm away from the edge of the shuriken cavity in all the combinations (see **Figure 6.12** (a)). *Model II* is different, the 45° rotation of the HNP causes an asymmetry in the separation of the HNP and the shuriken depending on the symmetry of the diastereomeric pair. Where the distance of the gap for pairs of same symmetry is ~13 nm and for pairs of opposite symmetry it increases to ~17 nm (see **Figure 6.13** (a)). One would imagine that this bias in the separation would lead to a higher electric field enhancement in the matched pairs relative to the mismatched ones. However, the ratios calculated for *Model II* are higher than those of *Model I* (see **Table 6-1**). In *Model III*, the HNP is ~12 nm close to the arm of the shuriken. The values of  $|E_{loc}/E_0|^4$  in this model are one order of magnitude greater than for the previous two. This is because the enhancement of the electric field is higher in the arms of the shuriken relative to the centre of the cavity.

These simulations support the hypothesis that the EM near field is strongly dependent on the symmetry of the diastereomeric pair. The combinations with the strongest near field enhancement were found to be the ones with matching handedness (LL and RR), with almost identical values, while the mismatched pairs had a significantly lower field enhancement. This enhancement in the near field translates into an enhancement of the Raman signal of the BPDT reporter molecule.

## 6.5 Conclusion

This work provides an enantiospecific detection method for chiral HNPs using the SERS technique. This was achieved through the association of the HNPs with a chiral plasmonic template, enabling chiral EM field coupling. The measurements were conducted through the intensity of the SERS signal of an achiral molecular reporter (BPDT), which gave a double increase for the pairs of matching symmetry compared to the mismatching ones. The control experiments confirmed that only the combination of the shuriken metafilm with the HNPs gives an asymmetric SERS response while also having the highest signal enhancement.

The interaction between the diastereomeric pair will generate “hotter” and “cooler” hotspots depending on whether they are of matching or mismatching handedness, respectively. Far-field ORD and reflectance measurements were unable to achieve any chiral detection, while SERS, being directly proportional to the intensity of the EM near-field environment, successfully completed this task. This experiment is supported by the numerical simulations of three different models, where an HNP was placed in the centre and in an arm of the plasmonic shuriken cavity. The simulation work confirmed that in all three HNP positions, the intensity of the EM fields was higher for the pairs of same symmetry compared to the pairs of opposite symmetry.

This study gives an innovative approach compared to previous work that used metamaterials to enhance SEROA measurements [270], while the SERS signal here is not intrinsically optically active. The main advantage of this “metamaterial-diastereomers” technique is that the SERS signal is significantly amplified compared to SEROA, by as much as two orders of magnitude. The plasmonic HNPs used here could be replaced by another analyte, such as a chiral molecule, making use of this SERS-based technique in the fields of drug development and biosensing.

## Chapter 6: Summary

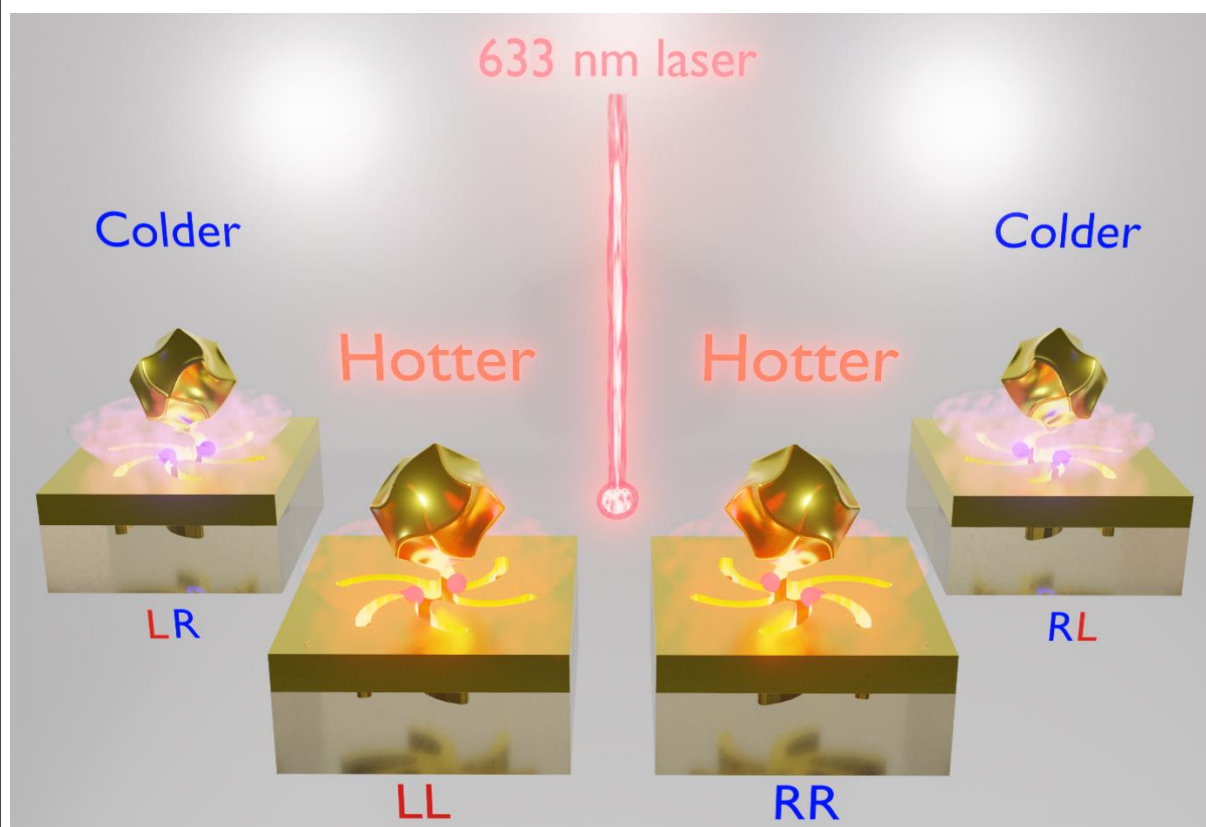


**Figure 6.15: Chapter 6 concept illustration.**

### **Key Findings:**

- SERS mediated by a reporter molecule can achieve enantiospecific recognition through “cooler” and “hotter” hotspots in the near field of diastereomers.
- SERS is a more sensitive probe of the near-field EM environment than reflectance, which measures a much larger volume.
- SERS is not an optically active technique, but the method presented here shows an increase in the asymmetry of the signal by two orders of magnitude compared to SEROA.



# Chapter 7

---

Plasmonics for Enhanced  
Vibrational Bio-Detection

## 7.1 Introduction

The detection of molecular vibrational modes in the infrared (IR) region, typically spanning from 400 to 4000  $\text{cm}^{-1}$ , is frequently used to provide insights into the chemical substances and functional groups in solid, liquid, or gaseous samples [271]. IR-based techniques give greater details on the molecular bonds than their UV/visible counterparts. These other techniques are mostly used to characterise the electronic transitions and quantify the concentration of the analytes through the Beer-Lambert law [272].

In the study of chiral analytes, vibrational optically active (VOA) techniques are required to discriminate between enantiomers. Traditionally, the absolute stereochemistry of molecules is established using X-ray crystallography. But this technique suffers from drawbacks such as the need for a quality single crystal of the sample, obtained through a complex and time consuming stereocontrolled synthesis that may not reflect the bulk properties [273]. Recent progress in VOA techniques is leading to more adoption in the pharmaceutical industry, enabling the assessment of the absolute stereochemistry of both crystalline and non-crystalline samples [274]. The main chirally sensitive VOA methods are vibrational circular dichroism (VCD) and Raman optical activity (ROA). ROA measures the difference in intensity of Raman scattering between left and right circularly polarised light [275]. And VCD is derived from the dichroic absorption of circularly polarised light (CPL) in the infrared [276]. Both techniques are extensively used in pharmaceutical research, with VCD being accepted by regulatory agencies in the determination of the absolute configuration of single-enantiomer drugs [277].

In 1997, Biotools introduced the first commercial Fourier transform VCD spectrometer to the market, after its invention in 1979 [278]. Before that, researchers used dispersive VCD instruments that were limited to a smaller wavenumber range and a low signal-to-noise ratio (S/N), but they are still relevant today for some specific applications [279]. Despite technical advancements in VCD spectroscopy, considerable limitations are still preventing this technique from reaching its full potential. Namely the lack of sensitivity, which requires a large quantity of analytes (50 to 100  $\text{mg/mL}$ ) dissolved in heavy water ( $\text{D}_2\text{O}$ ) to prevent IR absorption of background water, which overlaps with the signal from the chiral molecules. This technique can also be time-consuming depending on the concentration of analyte, ranging from several minutes to hours [280]. Here we explore the use of chiral nanophotonic platforms applied to the detection of biomolecular vibrations to discriminate between amino acid enantiomers.

## 7.2 Background

In the previous chapter, the basic principle of vibrational spectroscopy was introduced. The focus was put on the Raman effect, which is one of the main techniques used to characterise compounds based on the vibration modes of their chemical bonds. Here, the concept and theory specifically surrounding IR spectroscopy will be discussed.

### 7.2.1 IR spectroscopy theory

In IR spectroscopy, the light beam will transfer energy to the molecular species, resulting in changes in vibrational energy levels. Several atomic motions can arise through this interaction with light, namely stretching ( $\nu$ ), scissoring ( $\delta$ ), twisting ( $\tau$ ), rocking ( $\rho$ ) and wagging ( $\omega$ ). These vibration modes will happen at different frequencies depending on the structure of the molecule and its local environment. Unlike with Raman spectroscopy, where a monochromatic light is inelastically scattered, here, the vibrational modes will manifest as absorption bands on the IR spectrum. These IR bands can then be assigned to specific vibrational modes to identify the chemical species [281].

In practice, IR spectra are obtained using a Fourier transform infrared (FTIR) spectrometer. This equipment uses a polychromatic light source passing through an interferometer to separate the different wavelengths during the spectra acquisition. This light is then passed through the sample, and the intensity of the transmitted light is analysed by the detector.

As discussed in the background of the previous Chapter, in Section 6.2.2, the selection rule dictates which molecular vibration will be Raman active or IR-active. The Raman active modes cause a change in the polarisability  $\alpha$ , while the IR active modes originate from changes of the dipole moment  $\mu$ , defined by [282]:

$$\mu = \delta r \text{ and } I_k \propto (\partial\mu/\partial Q_k)^2 . \quad (7.1)$$

Where  $\delta$  is the magnitude of the charge and  $r$  is the distance between the charges. The intensity of the IR absorption peak  $I_k$  will be proportional to the square of the change in the dipole moment, with  $Q_k$  being the normal coordinate of the  $k^{th}$  vibration mode.

The mutual exclusion rule states that if a molecule has a centre of symmetry, then the Raman active vibrations will be IR inactive and vice versa (e.g., CO<sub>2</sub>). In the case where the molecule has no centre of symmetry, then some vibrations can be both Raman and IR active (e.g., H<sub>2</sub>O) [283].

## 7.2.2 Surface-enhanced infrared absorption

The main limitation of mid-IR spectroscopy is its inherently high wavelength range, which is three – four orders of magnitude larger than the size of the molecule probed. This large mismatch leads to low absorption cross-sections of molecules ( $\sigma_{abs} \approx 10^{-20} \text{cm}^2$ ) and thus a low sensitivity, restricting the scope of applications in fields requiring trace chemical detection such as biosensing [284].

In 1980, for the first time, an enhancement of the IR absorption of a monolayer quantity of molecule was observed using thin films of gold and silver [285]. This phenomenon is known as surface-enhanced infrared absorption (SEIRA). It has been shown to increase the detection sensitivity by enhancing the light-matter interaction using the SPPs at the surface of the plasmonic sample [286]. In the past decade, researchers have ventured away from thin films to explore more complex plasmonic designs and materials [287].

As discussed in Section 7.2.1, the intensity of the vibrational absorption band is proportional to the square of the electric-dipole transition moment of the molecule. For the  $k^{\text{th}}$  mode, it can be noted as  $E_{g1,g0}(k)$ , which describes the transition from the ground electronic (g) and ground vibrational state (0) to the ground electronic (g) and vibrationally excited state (1), described as follows [288]:

$$E_{g1,g0}^2(k) = |\langle \Psi_{g0} | \mu_{el} | \Psi_{g1} \rangle|^2. \quad (7.2)$$

Where  $\Psi_{g0}$  and  $\Psi_{g1}$  are the wave functions describing the ground vibrational state and the vibrationally excited state, respectively. Here,  $\mu_{el}$  is the electric dipole moment operator.

The fundamental principle of SEIRA is based on the plasmon excitations of the sample in the IR range, increasing the level of optical absorption of the molecules placed in these plasmonic hotspots. The molecular vibrations can then be observed in the change in absorption or reflectance of the plasmonic sample. This technique can be compared to SERS, described in the previous chapter. In SEIRA, the probability of a photon to be inelastically absorbed is proportional to the intensity of the incident light multiplied by the enhancement at the plasmonic hotspot where the molecule is adsorbed. This echoes with the EM model responsible for most of the SERS effect. The chemical complexation mechanism, or chemical enhancement, can also play a role in SEIRA, where it is responsible for changes in the dipole strength of the analyte through charge transfer and electronic hybridisation with the surface [289]. Despite their similarities, SEIRA is still weaker than SERS, scaling as  $\propto E^2$ , compared to  $\propto E^4$  for SERS (see equation (6.12)). Nonetheless, ultrasensitive detection is still achievable by placing the analyte molecules in the EM hotspot, with theoretical values close to regular SERS [290].

The enhancement factor of SEIRA has been defined by the following equation [291]:

$$EF = \frac{I_{SEIRA}}{I_0} \frac{A_0}{A_{SEIRA}}. \quad (7.3)$$

Where  $I_{SEIRA}$  is the enhanced signal through SEIRA and  $I_0$  is the unenhanced signal intensity. Here,  $A_{SEIRA}$  and  $A_0$  refer to the areas (or volume) containing the molecules in the SEIRA and reference measurements, respectively.

Gold is the most common metal used in metal-based SEIRA thanks to its biocompatibility and stability. The size of the plasmonic nanostructures used in SEIRA is usually large ( $\sim 1 \mu\text{m}$ ), causing significant radiative losses and thus plasmon damping, limiting the enhancement of SEIRA [287]. For this reason, researchers are experimenting with other materials, such as graphene or doped Si, which show higher light confinement in the IR region [292,293].

### 7.2.3 Surface enhanced vibrational circular dichroism

As previously stated, VCD is the extension of CD spectroscopy in the IR range. It provides identification of vibrational modes for chiral molecules, giving spectra of the opposite sign between the two enantiomeric forms. VCD is routinely used for chiral discrimination, particularly in the identification of protein secondary structures through the asymmetric response to CPL and the IR fingerprints of the molecule [294]. It is often used to probe the amide I region ( $1700\text{-}1600 \text{ cm}^{-1}$ ), which is the most commonly used vibrational band to determine the conformation of proteins [295]. This has many applications in the field of medical diagnosis, where the misfolding and aggregation in the secondary structures of proteins have been shown to be linked to Alzheimer's disease and Parkinson's disease [296]. VCD suffers from the same limitations as IR spectroscopy, with a relatively weak signal, usually three orders of magnitude smaller than UV-visible CD [297].

The intensity of the VCD band at the  $k^{\text{th}}$  mode is given by the rotatory strength  $R_{g1,g0}(k)$ . It is defined by the imaginary part of the scalar product of the electric-dipole transition moment and the magnetic-dipole transition moment as follows [298]:

$$R_{g1,g0}(k) = \text{Im}[E_{g1,g0}(k) \cdot M_{g1,g0}(k)^*]. \quad (7.4)$$

Where  $E_{g1,g0}(k)$  and  $M_{g1,g0}(k)$  are the electric and magnetic transition dipole vectors, respectively. Here  $M_{g1,g0}(k) = \langle \Psi_{g0} | \mu_{mag} | \Psi_{g1} \rangle$ , where  $\mu_{mag}$  is the magnetic dipole moment operator.

Unlike with a regular IR spectrum, where the vibration band at a given mode is always positive ( $E_{g1,g0}^2(k) > 0$ ), the VCD intensity can be either positive or negative. From

the equation (7.4), one can determine that the sign of  $R_{g1,g0}(k)$  is ruled by the cosine of the angle between the electric and magnetic transition dipole vectors,  $E_{g1,g0}(k)$  and  $M_{g1,g0}(k)$ . When this angle is below  $90^\circ$ , the VCD intensity is positive, and when it is above  $90^\circ$ , the VCD band is negative. In the case of an achiral molecule, these two vectors are orthogonal, resulting in  $R(k) = 0$ .

Nanophotonic platforms in the MIR have recently been used to enhance the VCD signal in a similar way as for regular CD [299]. This technique is often referred to as SEVCD, which has been exploited in both chiral [300–302] and achiral [299,303] substrates. In this study, a chiral platform will be used to probe the vibrational bands of a chiral analyte.

## 7.3 Methods

### 7.3.1 Sample and analyte

The plasmonic samples studied here are arrays of chiral ‘shuriken’ structures made of gold on a silicon wafer. The manufacturing process employs EBL and metal evaporation as described in Section 3.1.1. Two different sizes were manufactured in separate arrays, with 1000 nm and 1500 nm large shuriken of a single structure’s handedness per array. The pitch of the periodic arrays was set to  $1.5\times$  the size of the plasmonic structure, thus the distance from centre-to-centre was 1500 nm and 2250 nm for the 1000 nm and 1500 nm large shuriken, respectively (see Figure 7.1). The height of these structures was probed using AFM, averaging  $\sim 110$  nm (see Figure 7.2).

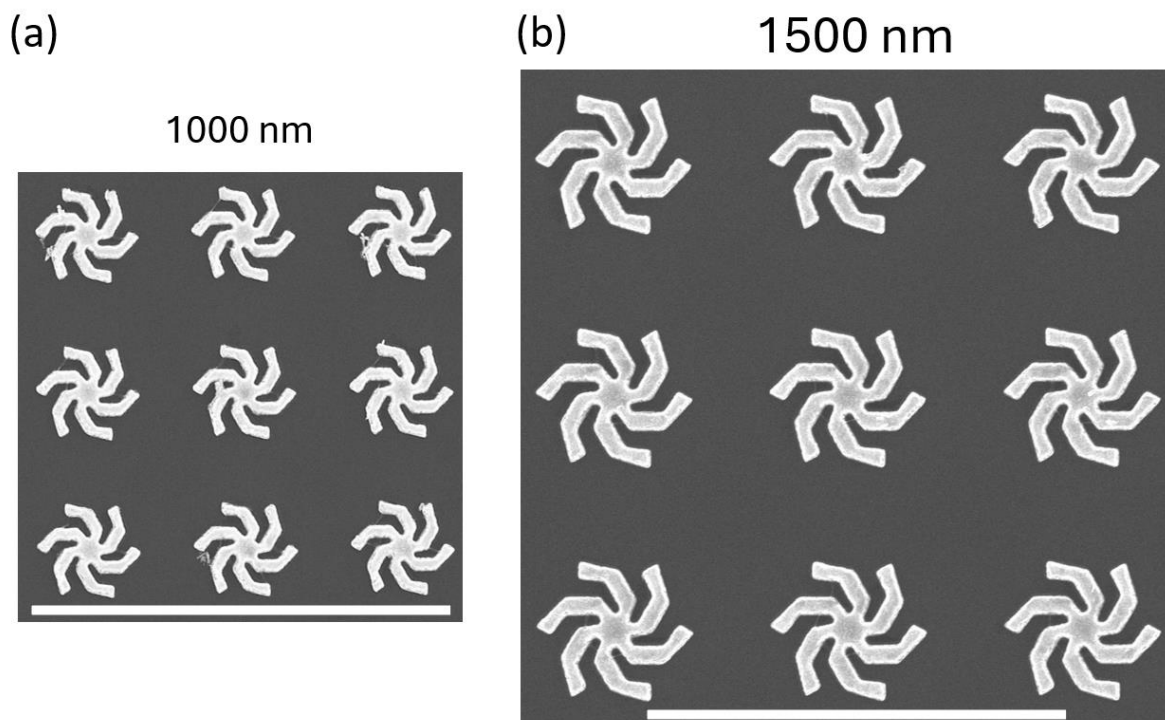


Figure 7.1: SEM images of a) 1000 nm large gold LH shuriken array and b) 1500 nm LH shuriken array (the scale bar represents  $4\ \mu\text{m}$ ).

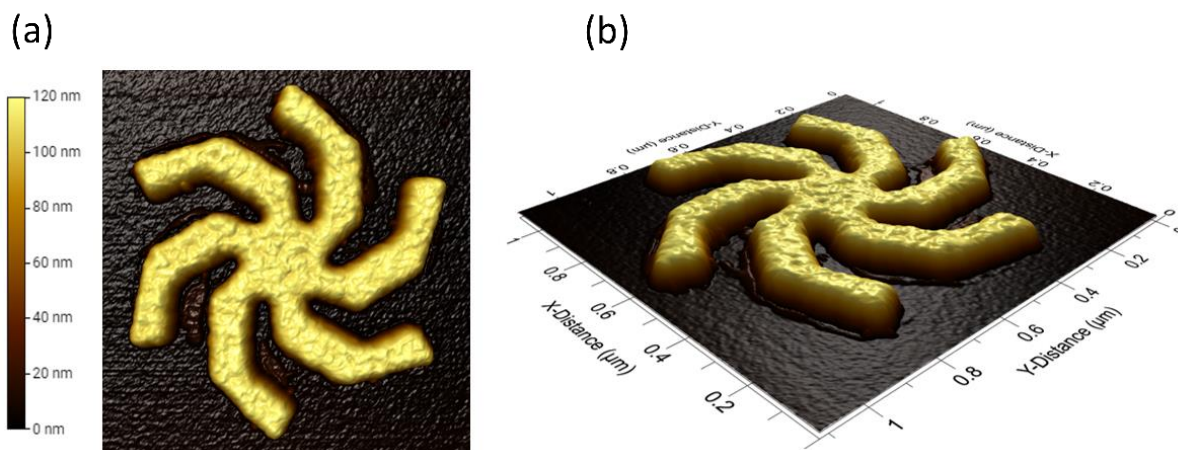


Figure 7.2: a) Top view and b) 3D orthogonal view of an AFM micrograph of a 1000 nm large LH shuriken structure.

These two sizes were designed to exhibit broad plasmonic resonances at different wavenumbers, specifically at  $1650\text{ cm}^{-1}$  for the 1000 nm shuriken and  $1050\text{ cm}^{-1}$  for the 1500 nm shuriken arrays. The 1000 nm large shuriken resonate within the amide I region ( $1700\text{-}1600\text{ cm}^{-1}$ ), which is of significant importance in the vibrational spectroscopy of proteins (see Section 7.2.3). In contrast, the 1500 nm shuriken was selected to have a plasmonic resonance in a wavenumber range with minimal IR activity to our analyte, serving as a point of comparison.

The analyte chosen for this study was the cysteine amino acid (see Figure 7.3), which has a thiol group, enabling a SAM deposition directly on the gold shuriken structures. This relatively small molecule (121 Da) is chiral and has L- and D-enantiomeric forms that will be studied here.

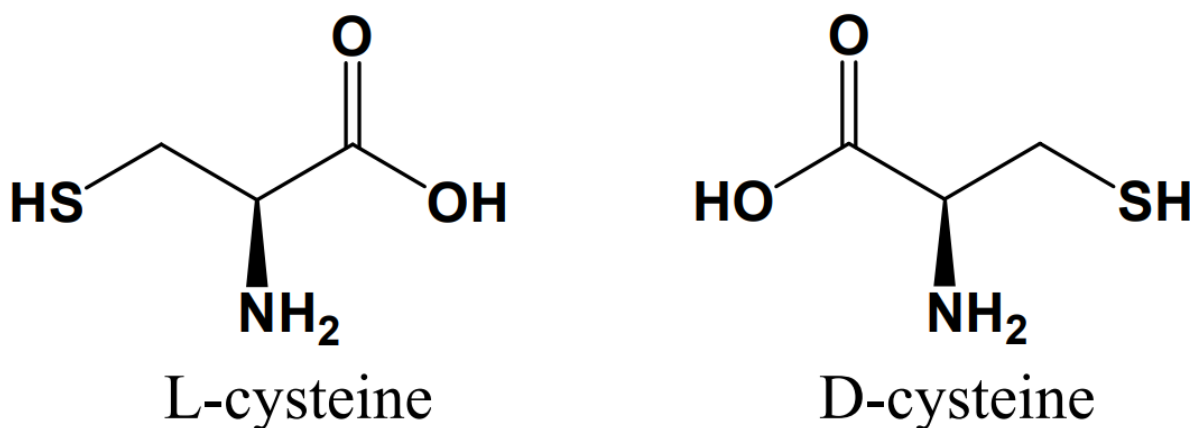


Figure 7.3: L- and D-cysteine amino acids.



In addition to the thiol group, cysteine possesses a carboxylic acid functional group (R-COOH) and an amino group (R-NH<sub>2</sub>). The pH of the cysteine solution used to make the SAM will dictate the form of the adsorbed amino acid. Cysteine can be in a cationic (fully protonated), zwitterionic and anionic (fully deprotonated) form for a pH  $\ll$  p*H*<sub>iso</sub>, pH = p*H*<sub>iso</sub> and pH  $\gg$  p*H*<sub>iso</sub>, respectively [304]. Where the isoelectric point p*H*<sub>iso</sub> of L-cysteine is equal to 5.04. In this study, a solution of 10 mM of cysteine in DI water was used for each enantiomer. The pH of this solution was measured at 5.4 using a pH meter PH828+ by smart sensor. It has been shown that cysteine from a solution of similar pH adsorbs on the gold surface mostly as a zwitterionic species, which is obtained by transferring a proton from the carboxyl group to the amino group [305].

In this chapter, two separate instruments have been used to study all the combinations of plasmonic shuriken and cysteine enantiomers, namely an FTIR and a VCD setup, for which different methodologies were used.

For the FTIR measurements, a monolayer of cysteine was formed at the surface of the gold shuriken through a thiol bond in a SAM. First, the samples were cleaned in a sonic bath of acetone for 5 min and then IPA for the same duration. Next, they were dried with a N<sub>2</sub> gun and plasma treated with O<sub>2</sub> at 80 W. The IR spectra were then taken on the clean samples to provide a reference before the cysteine SAM functionalisation. After these measurements, the plasmonic samples were left overnight in a solution of 10 mM of either L-, D- or DL-cysteine dissolved in DI water. The silicon slides were then rinsed with DI and dried using a N<sub>2</sub> gun. This protocol insures a complete adsorption of the amino acid in a single molecular layer on the gold structures. The samples were then placed in the FTIR instruments to measure the spectra with a monolayer quantity of analyte. These steps were repeated for all the shuriken sizes and handedness and for all the chiral analytes as well as for an achiral PEG-thiol SAM, deposited in the same fashion (10 mM) and serving as a reference with no vibrational bands at the position of the plasmonic resonances [306].

The VCD measurements were taken on multilayers of cysteine to generate enough VCD signal, this was achieved by drop-casting and drying the solution on the samples. the clean shuriken arrays first. Then, 100  $\mu$ L of 10 mM cysteine solution in DI water was drop-casted on the slides and evaporated in an oven at 40 °C. In between the measurements, the slides were cleaned in a sonic bath of acetone and then IPA followed by O<sub>2</sub> plasma treatment. Here, only the 1000 nm shuriken size was studied.

### 7.3.2 FTIR transmission spectroscopy setup

FTIR transmission spectroscopy measurements have been taken using a Bruker Vertex 70 machine. The sample was mounted using blue tack on a sliding sample holder, aligning the array in the middle of the IR beam thanks to a red pointer laser included in

the setup (see **Figure 7.4**). This tool measures the transmitted IR radiation after the unpolarised incident light has passed perpendicularly through the sample. A first spectra of the background is taken on bare silicon, which is then used to normalise the sample measurements by dividing the sample spectra by the previously acquired background spectra. To have better confidence in the data, an average of four spectra was obtained by rotating the sample 90° in-between the measurements.



**Figure 7.4:** Vertex 70 FTIR machine by Bruker and sample holder (from Bruker brochure).

The wavenumber range of the beam was set from 350 to 5000  $\text{cm}^{-1}$ , with a 1  $\text{cm}^{-1}$  resolution. The beam aperture size was selected at 3 mm beam diameter. The background scan time on the silicon wafer was 1 min and the sample scan time was 2 min. This setup is equipped with a  $\text{N}_2$  purging system that allows the  $\text{H}_2\text{O}$  and  $\text{CO}_2$  peaks from the atmosphere to be removed, but it was found that the resulting spectra in air were as good as the purged ones. This is because the atmospheric peaks are subtracted from the background spectra. For more efficient time management, the  $\text{N}_2$  purging was not used.

### 7.3.3 Vibrational circular dichroism setup

The VCD measurements presented in this work are the result of a one-month long collaboration with *Professor Ewan Blanch* research team at the Royal Melbourne Institute of Technology (RMIT). During this month, I was trained on a *ChiralIR-2X<sup>TM</sup>* instrument by *Postdoc Jeremy Landry*, who generously took complementary measurements after my

departure. In this short timeframe, only the 1000 nm shuriken size has been studied. The *ChiralIR-2X* equipment is widely used in the pharmaceutical industry and regulatory agencies to measure both IR and VCD spectra simultaneously.

In this setup too, the plasmonic silicon samples were fixed on a sliding sample holder using blue tack, and the measurements were obtained in transmission (see **Figure 7.5**). The position and orientation of the slides were kept identical between the measurements using two straight pieces of plastic glued onto the plane of the sample holder. Each sample was placed in a chamber under N<sub>2</sub> purging while the spectra were acquired.



**Figure 7.5: ChiralIR-2X VCD setup from Biotools with a zoomed in view on the sample holder.**

The setup, presented in **Figure 7.6**, uses a source and interferometer over a wide spectral range going from 4000 to 850 cm<sup>-1</sup> without the need for additional filters. This instrument uses a dual photo-elastic modulator (PEM) for all the data acquisition. This piece of equipment is required to modulate the polarisation of the light between left and right-handed circularly polarised light at a high frequency. The two PEM placed on both sides of the sample allow a significant improvement in the baseline position, as well as a reduction in spectral artifacts. The spectra were recorded by a mercury cadmium telluride (MCT) photovoltaic detector at a 4 cm<sup>-1</sup> resolution and were obtained from the average of 6 blocks of 1000 scans each, for a total duration close to 2 hours. The Blackmann-Harris apodization function was used before performing the Fourier transform to improve the overall shape of the spectral peaks and suppress sidelobes [307].

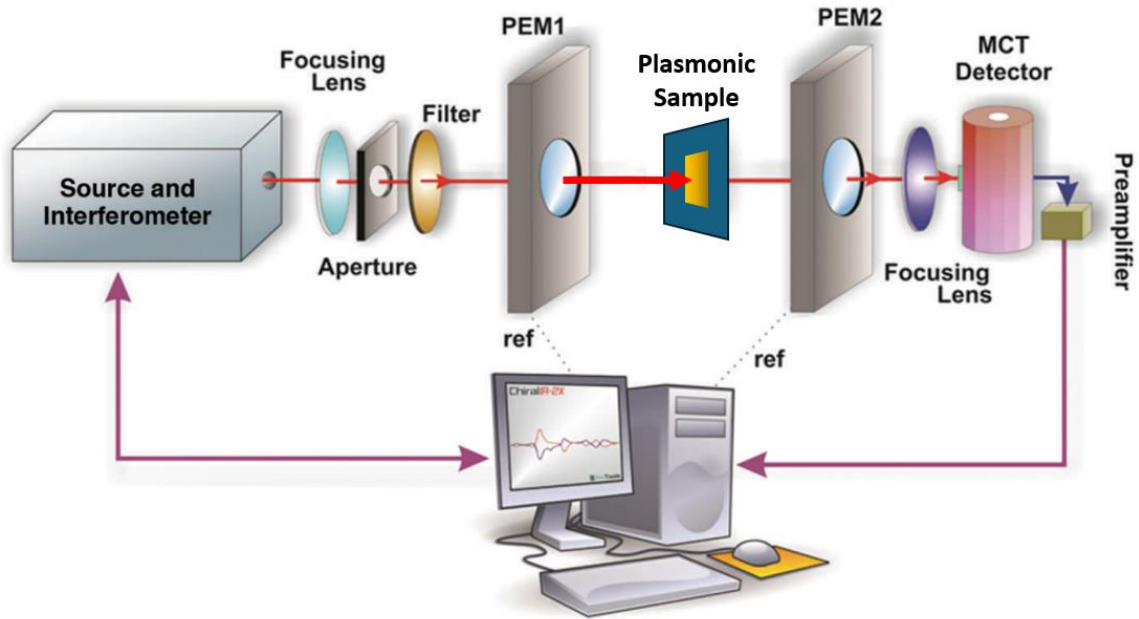


Figure 7.6: Schematics of a ChiralIR-2X VCD instrument from Biotools (adapted from [308]).

The spectra were recorded on the clean plasmonic slides of both sizes and handedness and following the cysteine functionalisation. The 6 block spectra were then averaged to be analysed. In this setup, the background spectrum of bare silicon is not useful for the VCD data, since the silicon wafer is achiral.

This setup calculates the VCD spectra from the difference in absorbance ( $A$ ) at a wavenumber  $\nu$  between LCP and RCP light, as [309]:

$$\Delta A(\nu) = A_{LCP}(\nu) - A_{RCP}(\nu). \quad (7.5)$$

Where the absorbance of each polarisation handedness is derived from the intensity of the light measured at the detector with and without the sample  $I(\nu)$  and  $I_0(\nu)$ , respectively [309]:

$$A(\nu) = -\log_{10}[I(\nu)/I_0(\nu)]. \quad (7.6)$$

### 7.3.4 Simulation model

A *COMSOL Multiphysics* model was created to better understand the experimental data. Only the 1000 nm large shuriken was tested here, using an ideal shape of the structure. The position of the resonance was adjusted to fit the experimental observation ( $\sim 1650 \text{ cm}^{-1}$ ) by tuning the size of the shuriken ( $\sim 930 \text{ nm}$  large and  $100 \text{ nm}$  high). This plasmonic structure was placed at the centre of a  $6000 \text{ nm}$  high square block with  $1400 \text{ nm}$  lateral dimensions. A small  $10 \text{ nm}$  layer was defined around the gold shuriken

structure to mimic an adsorbed dielectric medium (see **Figure 7.7 (a)**). The incident IR light was polarised linearly along the y axis to replicate the FTIR spectra (see **Figure 7.7 (b)**).

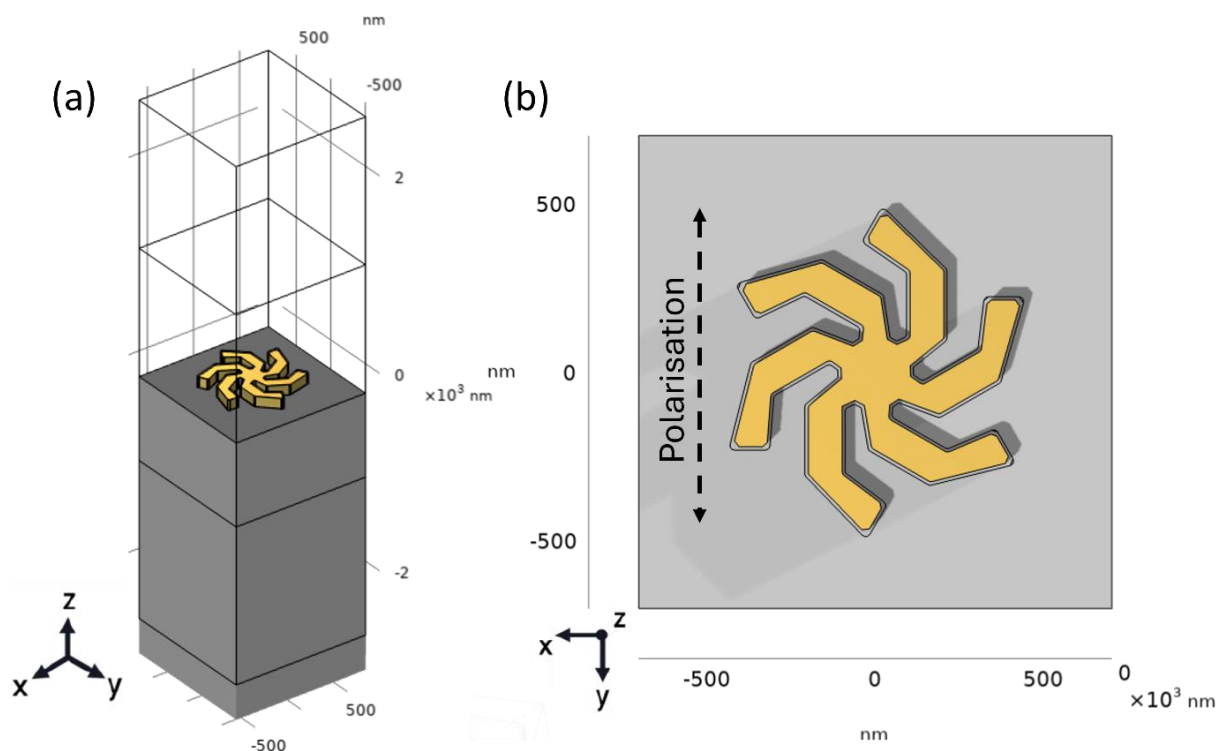


**Figure 7.7: COMSOL simulation model of a RH 1000 nm large gold shuriken structure in blue with (a) orthogonal view and (b) top view with the polarisation angle indicated by a dashed double arrow.**

The VCD data was obtained by changing the incident light to a circularly polarised beam for both handedness. The percentage of transmitted light was then converted to the absorbance in the same way as equation (7.6). Then, the CD signal was derived from the difference between LCP and RCP as in equation (2.16).

## 7.4 Results and discussion

### 7.4.1 Cysteine on bare silicon

The IR spectrum of L-cysteine on bare silicon was measured to identify the position of the vibrational bands that will be studied here. The IR transmittance spectra of the 1000 and 1500 nm shuriken arrays were also acquired to locate the position of their plasmonic resonance and estimate the effective range by taking the full width at half maximum (FWHM) of the peak.

The spectrum of L-cysteine deposited on a silicon wafer is presented in **Figure 7.8**, where the position of the FWHM of both shuriken sizes is overlaid. Four vibrational modes fall within the plasmonic peaks of the shuriken structures, located at 1609, 1582, 1553 and 1065  $\text{cm}^{-1}$ . These vibronic modes can be assigned to the asymmetric deformation  $\delta_{as}(\text{NH}_3^+)$ , the asymmetric stretching  $\nu_{as}(\text{CO}_2^-)$ , the symmetric scissoring  $\delta_s(\text{NH}_3^+)$  and finally the rocking mode  $\rho(\text{NH}_3^+)$ . They will be referred to as modes I, II, III and IV, respectively (see **Table 7-1**). This assignment is supported by other studies on the solid form of the zwitterionic cysteine, where the positions reported here are within  $\sim 10$   $\text{cm}^{-1}$  from these previous studies [310,311].

Modes I, II and III are inside the plasmonic resonance of the 1000 nm shuriken, while mode IV is in the plasmonic resonance of the larger 1500 nm shuriken. It is important to note that the intensity of these absorption bands varies significantly, with mode I being nearly  $10\times$  more intense than mode IV (see **Figure 7.8**).

| Mode | Position ( $\text{cm}^{-1}$ ) | Assignment                   |
|------|-------------------------------|------------------------------|
| I    | 1609                          | $\delta_{as}(\text{NH}_3^+)$ |
| II   | 1582                          | $\nu_{as}(\text{CO}_2^-)$    |
| III  | 1553                          | $\delta_s(\text{NH}_3^+)$    |
| IV   | 1065                          | $\rho(\text{NH}_3^+)$        |

**Table 7-1: L-cysteine vibrational mode assignment.**

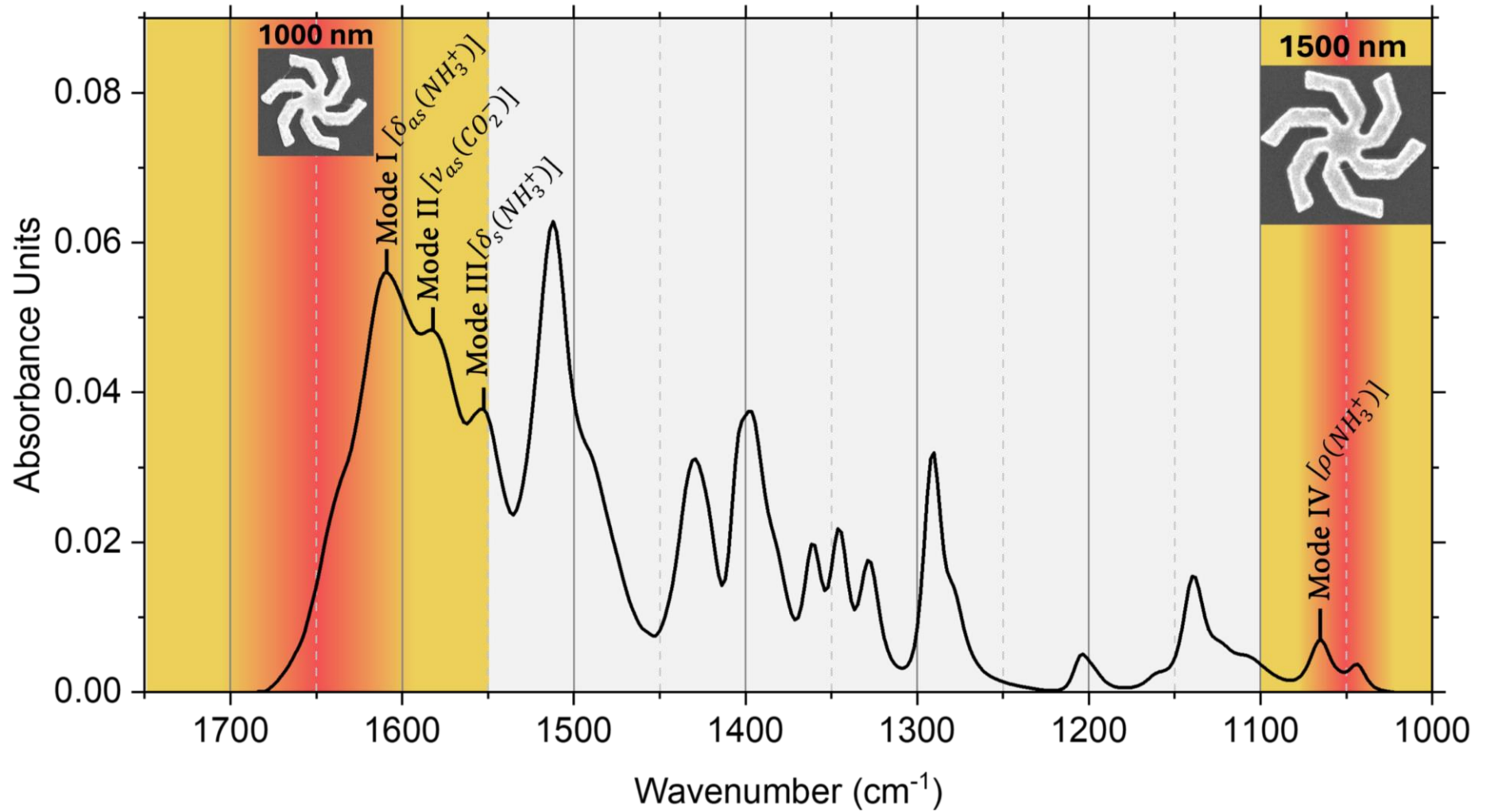


Figure 7.8: FTIR spectrum of dried L-cysteine on a bare silicon wafer (10 mM of 100  $\mu$ L), the position of the full width at half maximum range of the transmittance spectra of the 1000 and 1500 nm large plasmonic shuriken are overlaid in the yellow and red bands. The modes within the bands are labelled and numbered.



## 7.4.2 IR plasmonic detection of cysteine monolayer

The IR transmittance spectra of the 1000 and 1500 nm large shuriken sizes were taken on the clean slides, followed by the SAM measurements of the L- and D-cysteine enantiomers as well as the racemic mixture (DL-cysteine). The spectral acquisition was repeated on a SAM of achiral PEG-thiol reference, which doesn't have any vibrational activity within the position of the plasmonic resonances for both the 1000 and 1500 nm large shuriken structures [306].

The 2<sup>nd</sup> order derivatives of all the spectra were calculated following the Savitzky-Golay (SG) polynomial derivative technique, smoothing the spectra prior to calculating the derivatives in order to decrease the noise. This method is widely used in IR spectroscopy owing to the capability of derivatives to get rid of both additive and multiplicative effects in the spectra. The 1<sup>st</sup> order derivative is often used to remove only the spectral baseline, whereas the 2<sup>nd</sup> order derivative can suppress both baseline and linear trend [312]. In our case, the resolution of the spectral curves was improved using the 2<sup>nd</sup> order derivative, which allows the detection of features originating from molecular vibrations that are hidden within the plasmonic peak [313,314].

The IR transmittance spectra of both shuriken sizes, along with their respective 2<sup>nd</sup> order derivatives, were plotted to characterise the shape of the IR transmittance curves and determine the biosensing ability of this technique (see **Figure 7.9** and **Figure 7.10**). For the clean 1500 nm shuriken transmittance spectra have a broad peak shape with a position located around  $\sim 1060\text{ cm}^{-1}$ , while the 1000 nm size is narrower at  $\sim 1650\text{ cm}^{-1}$ . The transmittance spectra show a red-shift of  $\sim 3\text{ cm}^{-1}$  with the adsorbed PEG-thiol on the 1500 nm structures, and  $\sim 6\text{ cm}^{-1}$  for the smaller 1000 nm shuriken structure. The spectra obtained with the SAM of different cysteine enantiomers show a smaller red-shift in the position of the resonance peak ( $\sim 1\text{ cm}^{-1}$ ). Interestingly, a broadening of the transmittance peak can be noticed on all the 1000 nm shuriken adsorbed with cysteine (see **Figure 7.10 (a)**), while the 1500 nm shuriken spectra don't show a noticeable change in shape (see **Figure 7.9 (a)**). The 2<sup>nd</sup> order derivative of these spectral curves gives a clearer view of the plasmonic broadening caused by the cysteine monolayer. A double peak shape can be seen for both plasmonic size and both handedness on the clean and functionalised samples (see **Figure 7.9 (b)** and **Figure 7.10 (b)**). The 1500 nm size shows very little change throughout the measurements, while a significant peak splitting is noticeable in the case of the smaller 1000 nm shuriken.



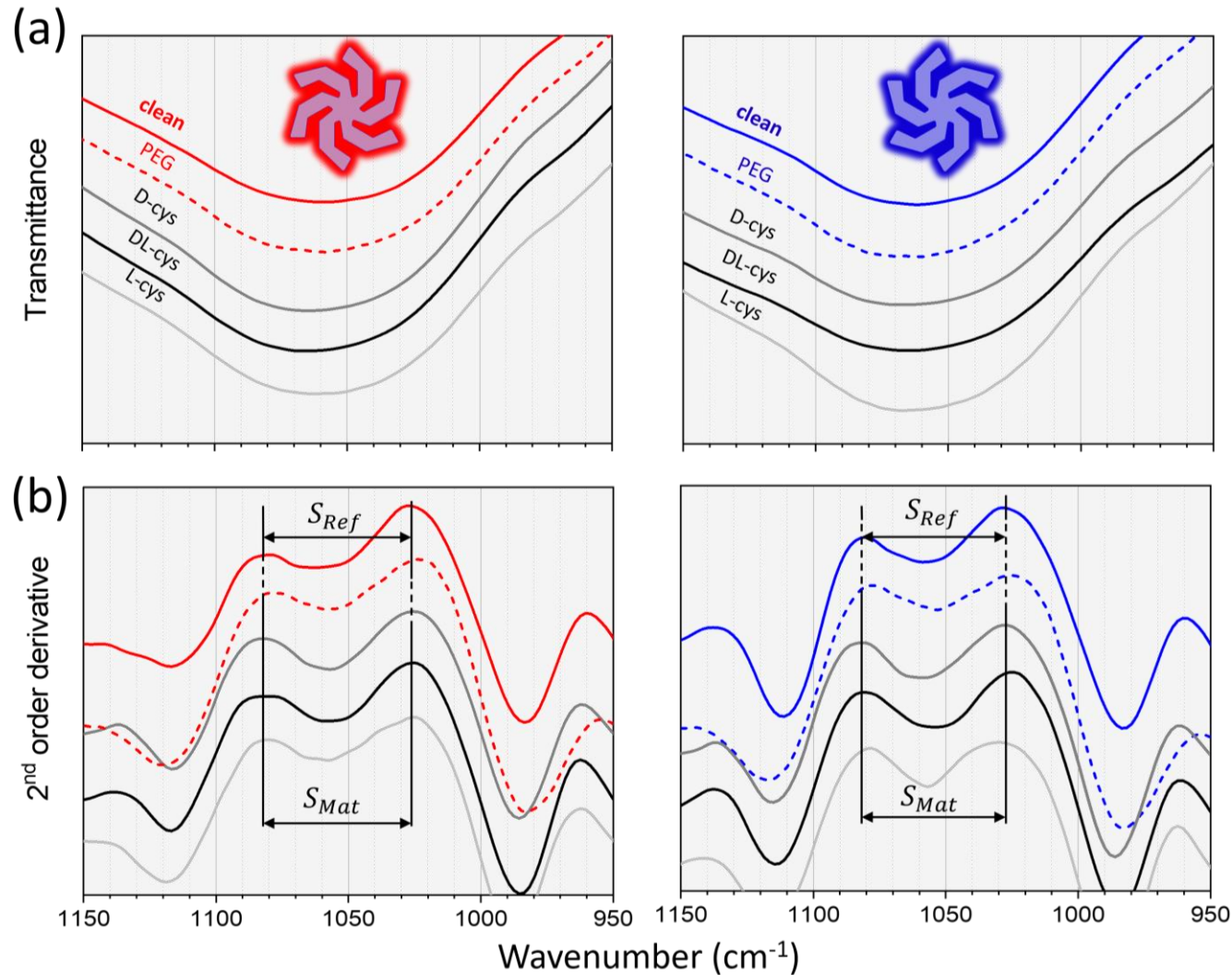


Figure 7.9: 1500 nm LH (red) and RH (blue) shuriken arrays with (a) transmittance spectra and (b) their respective 2nd order derivatives. The clean reference spectra are in dashed lines, the achiral PEG reference is shown with a red (LH) or blue (RH) solid line and the different enantiomers of cysteine along with the racemic mixture are shown in different shades of grey.

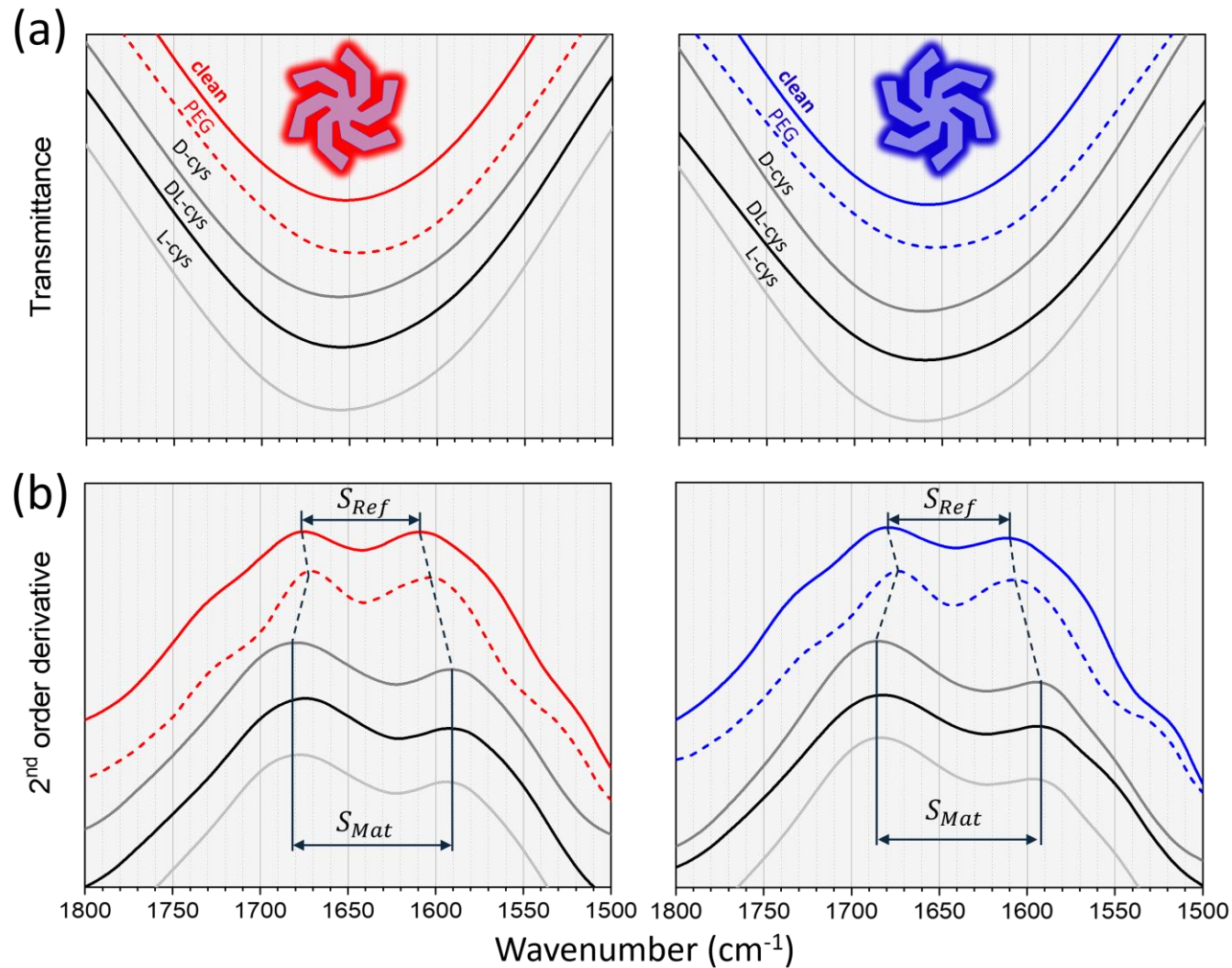
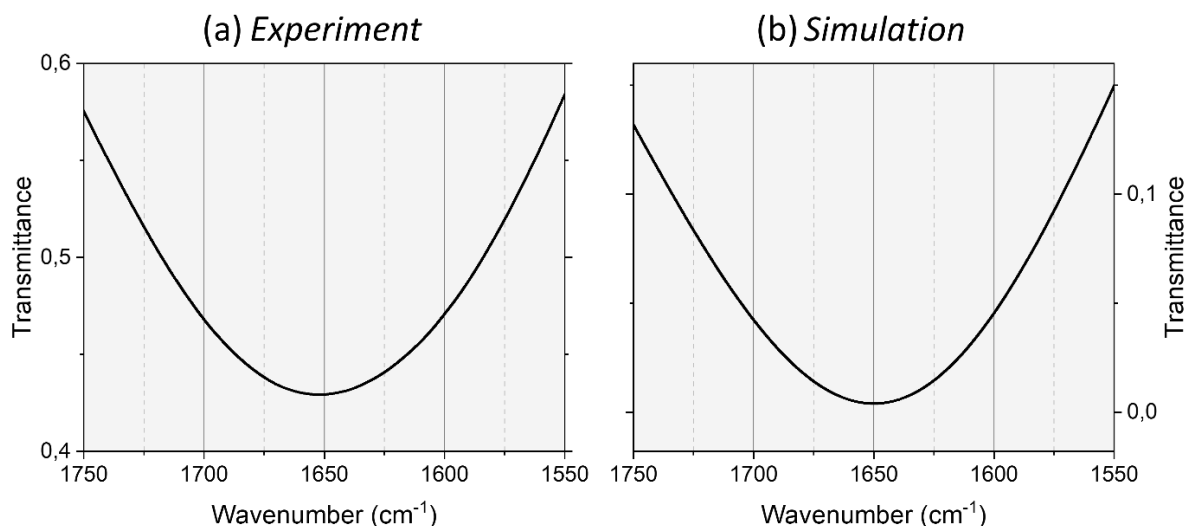


Figure 7.10: 1000 nm LH (red) and RH (blue) shuriken arrays with (a) transmittance spectra and (b) their respective 2<sup>nd</sup> order derivatives. The clean reference spectra are in dashed lines, an achiral PEG reference is shown with a red (LH) or blue (RH) solid line and the different enantiomers of cysteine along with the racemic mixture are shown in different shades of grey.

Numerical simulations were performed on a 1000 nm shuriken to explain the experimental observations. First, the optical properties of the model were compared to the experimental measurements via the transmittance spectra, presented in **Figure 7.11**.



**Figure 7.11: Transmittance spectra of a pristine 1000 nm large LH shuriken obtained (a) experimentally and (b) using numerical simulation.**

The simulated spectrum can reproduce the experimental measurements, displaying an identical shape and position of the plasmonic resonance. During the experimental measurements, the sample was exposed to ambient air containing water vapour. It is known that the H<sub>2</sub>O molecule has strong IR absorbance in the same region as the resonance peak of the 1000 nm shuriken size [315]. Consequently, water was added in a 10 nm domain around the gold shuriken to recreate the experimental conditions. The index of refraction  $n(\lambda)$  and extinction coefficient  $k(\lambda)$  of water were both interpolated on the wavenumber range from the data of Hale and Querry [316]. The resulting simulated transmittance spectra and 2<sup>nd</sup> order derivatives were then plotted in **Figure 7.12**.

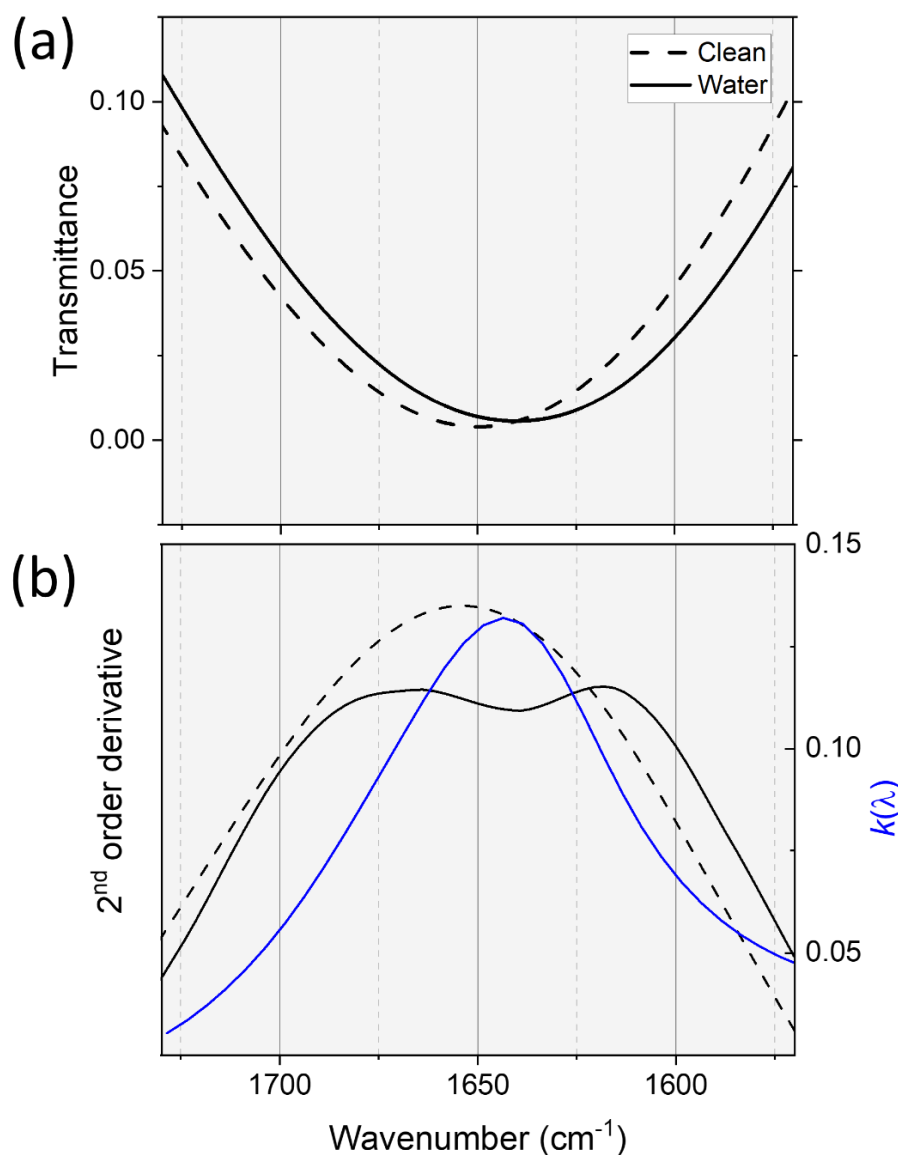


**Figure 7.12:** (a) Simulated transmittance spectra of a clean LH shuriken in air (dashed line) and with a 10 nm water layer around it (solid line) and (b) the corresponding 2<sup>nd</sup> order derivatives with the extinction coefficient of water overlapped in blue.

As expected, the transmittance spectrum computed with the dielectric layer is red-shifted compared to the spectra obtained only in air. A slight broadening of the peak can also be noticed (see **Figure 7.12** (a)). The 2<sup>nd</sup> order derivative of these simulated transmittance spectra was plotted in along with the extinction coefficient of water (see **Figure 7.12** (b)). For the clean shuriken only exposed to pure air, the 2<sup>nd</sup> order derivative has a gaussian shape, which is not what was observed in the experimental results. When the water layer is introduced, the double peak shape seen experimentally in **Figure 7.10** (b) is reproduced. The valley between these two peaks coincides precisely with the position of the extinction coefficient maxima (see blue curve in **Figure 7.12** (b)). This absorption peak is attributed to the main IR active mode of water located at 1647  $\text{cm}^{-1}$  and assigned to the  $\nu_2$  bending mode of H-O-H [317].

This observation can be applied to the 1500 nm data, where the double peak shape can be attributed to the thin silicon oxide layer at the surface of the wafer, with the Si-O stretching band located around 1065 cm<sup>-1</sup>. The absorbance of this band has been correlated to the oxide layer thickness in previous studies [318,319].

To determine the impact of the cysteine SAM adsorbed on the shuriken structures, the distance separating the two peaks on the 2<sup>nd</sup> order derivative plots was measured for both shuriken handedness on the clean samples and with the SAM layer, named  $S_{Ref}$  and  $S_{Mat}$ , respectively (see **Figure 7.9** and **Figure 7.10 (b)**). The broadening parameter  $\Delta S$  was then calculated to compare the response of the samples for each analyte to the clean condition for the LH and RH arrays, defined as:

$$\Delta S^{RH/LH} = S_{Mat}^{RH/LH} - S_{Ref}^{RH/LH} . \quad (7.7)$$

These results are displayed in **Table 7-2** and **Table 7-3** for the 1500 and 1000 nm large shuriken, respectively:

| 1500 nm     | $\Delta S_{LH}$ (cm <sup>-1</sup> ) | $\Delta S_{RH}$ (cm <sup>-1</sup> ) |
|-------------|-------------------------------------|-------------------------------------|
| PEG-thiol   | 1                                   | 0                                   |
| D-cysteine  | 2                                   | 3                                   |
| DL-cysteine | 2                                   | 2                                   |
| L-cysteine  | 2                                   | 1                                   |

**Table 7-2: 1500 nm shuriken broadening parameter  $\Delta S_{LH/RH}$  obtained for the PEG-thiol SAM reference (in red) and the different cysteine enantiomer SAM.**

| 1000 nm     | $\Delta S_{LH}$ (cm <sup>-1</sup> ) | $\Delta S_{RH}$ (cm <sup>-1</sup> ) |
|-------------|-------------------------------------|-------------------------------------|
| PEG-thiol   | 0                                   | -1                                  |
| D-cysteine  | 23                                  | 22                                  |
| DL-cysteine | 17                                  | 21                                  |
| L-cysteine  | 17                                  | 19                                  |

**Table 7-3: 1000 nm shuriken broadening parameter  $\Delta S_{LH/RH}$  obtained for the PEG-thiol SAM reference (in red) and the different cysteine enantiomer SAM.**

The adsorbed PEG-thiol SAM doesn't result in any broadening of the plasmonic resonance, with values of  $\Delta S$  in both shuriken sizes showing no change from the clean spectra (see **Table 7-2** and **Table 7-3**). This is to be expected, since PEG-thiol adsorbed on gold is IR active outside of the plasmonic resonance of both shuriken sizes, with no vibrational band around 1650 cm<sup>-1</sup> (see **Figure D.1** in **Appendix D**), and a narrow one at 1116 cm<sup>-1</sup> assigned to  $\nu_s(C-O-C)$  (see **Figure D.2** in **Appendix D**) [306]. On the other

hand, the cysteine SAM causes a small broadening of  $\sim 2 \text{ cm}^{-1}$  for the 1500 nm shuriken size, and a much larger one of  $\sim 20 \text{ cm}^{-1}$  in the case of the 1000 nm shuriken (see **Table 7-2** and **Table 7-3**). We can thus postulate that the broadening of the plasmonic resonances is caused by the vibration modes of the cysteine molecule in these regions.

As discussed earlier in Section 7.4.1, the IR spectra of cysteine deposited on silicon exhibit several vibration bands that overlap with the plasmonic resonances associated with both dimensions of the shuriken structures, labelled mode I, II, III and IV (see **Figure 7.8**). Mode I has the most intense absorbance, located at  $1609 \text{ cm}^{-1}$ , which is close to the bottom of the valley formed by the two peaks in the 2<sup>nd</sup> order derivative of the 1000 nm shuriken, at  $1620 \text{ cm}^{-1}$  (see **Figure 7.10 (b)**). In the case of mode IV, which is situated at  $1065 \text{ cm}^{-1}$ , it coincides with the valley observed in the 2<sup>nd</sup> order derivative of the 1500 nm shuriken at  $\sim 1060 \text{ cm}^{-1}$  (see **Figure 7.9 (b)**). It was noted earlier that the absorbance intensity in mode I is about one order of magnitude higher than for mode IV, which is coherent with the experimental values of  $\Delta S_{LH/RH}$  presented in **Table 7-2** and **Table 7-3**.

The slight mismatch in the position of the mode I of cysteine compared to the plasmonic response obtained experimentally in the 1000 nm shuriken can be explained by the presence of the plasmonic structures and by the different arrangement of cysteine adsorbed in a monolayer. In another study, where cysteine was adsorbed from a solution at a pH of 5.7 on metallic surfaces, the main feature of the L-cysteine spectra on gold was assigned to the  $NH_3^+$  degenerate deformation mode at  $1647 \text{ cm}^{-1}$  [320]. In yet another study, where cysteine was adsorbed on Cu(110) at a pH of 5.4, which is the pH of the solution employed here, the most intense IR peak was located at  $\sim 1620 \text{ cm}^{-1}$  [321]. This peak was ascribed to the combination of the  $\delta_{as}(NH_3^+)$  and  $\nu_{as}(COO^-)$  modes, located at  $1630$  and  $1610 \text{ cm}^{-1}$ , respectively. The position of this main IR absorbance peak coincides precisely with the valley of the 2<sup>nd</sup> order derivative of the 1000 nm shuriken adsorbed with cysteine (see **Figure 7.10 (b)**). The assignments made in these studies correspond to modes I and II observed on the bare silicon spectra.

The experimental results described here are unlike the SEIRA effect, where Fano-like resonances are observed in the plasmonic extinction peak at the absorption bands of the chemical analyte [291,322,323]. As discussed earlier in Section 7.2.2, SEIRA scales to  $\propto E^2$ , numerical simulation was therefore performed on the 1000 nm shuriken model to study the electric field enhancement ( $|E/E_0|$ ). The electric field strength was averaged in the small 10 nm domain around the plasmonic shuriken for an incident beam at the plasmonic resonance and outside of the resonance (see **Figure 7.13 (a)**). As expected, the enhancement outside of the resonance ( $2100 \text{ cm}^{-1}$ ) is very small, with  $|E/E_0|^2 = 1.1$  (see **Figure 7.13 (b)**). At the plasmonic resonance ( $1650 \text{ cm}^{-1}$ ), the enhancement of the electric field is increased, with  $|E/E_0|^2 = 8.1$ . This electric field enhancement is too small to observe SEIRA from a single molecular layer. Indeed,



in a study mentioned before [320], a monolayer of L-cysteine adsorbed on gold was studied using IR reflection-absorption spectroscopy, where the absorbance measured was only in the order of 0.1%.

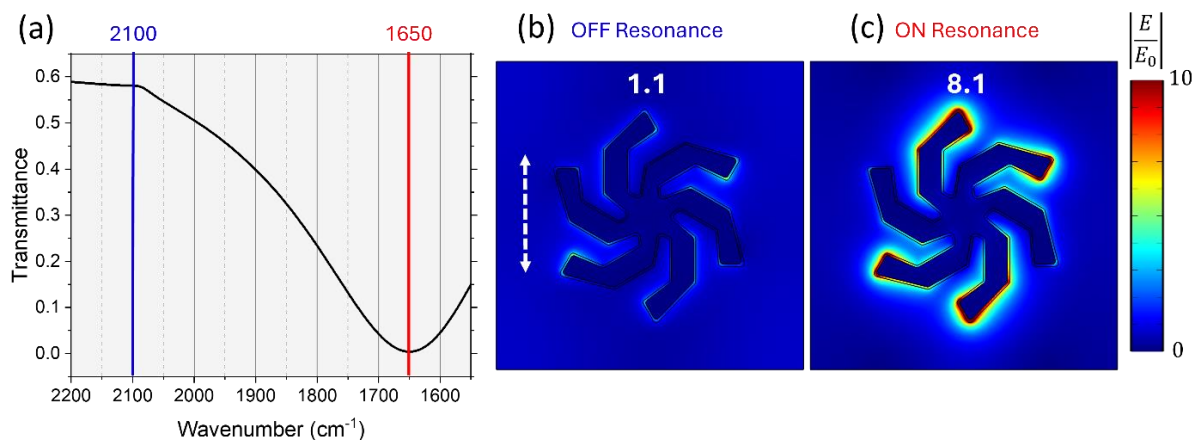


**Figure 7.13:** (a) Simulated transmittance spectra of a 1000 nm RH shuriken, (b) and (c) are maps of the time-averaged electric field strength at the wavenumbers marked in (a), with the average value of  $|E/E_0|^2$  in the 10 nm domain. All the fields are calculated at the substrate interface and normalised by the incident field ( $E_0$ ) polarised in the direction represented by the white dashed arrow.

Instead of SEIRA, the broadening of the plasmonic peaks observed experimentally can be attributed to vibrational damping or vibrational-plasmonic coupling. When the molecular vibration mode coincides with the plasmonic oscillation, they can couple, leading to an exchange of energy. This energy transferred from the plasmon excitation in the metallic nanostructures to the lossy adsorbed molecules leads to a shorter plasmon lifetime and can be observed by a broadening of the spectral resonance [324]. This effect is highly specific to the vibration mode of the analyte, unlike other plasmonic damping effects such as chemical interface damping, which is sensible to the electronic structure of the adsorbate [325].

Despite the successful detection of vibrational bands, coming from a single molecular layer of cysteine, the values of  $\Delta S_{LH/RH}$  obtained don't show any asymmetric response between L- and D-cysteine enantiomers (see **Table 7-2** and **Table 7-3**). This vibrational damping effect is therefore not sensitive enough with the methodology adopted here to discriminate the cysteine enantiomers; another technique is therefore required to achieve enantioselectivity.

### 7.4.3 VCD of thick cysteine layer

In this section, the measurements of the drop-casted cysteine solution taken on the *ChiralIR-2X* instrument will be presented and discussed. The IR transmittance and VCD spectra were measured at the same time for consistency. The relative IR transmittance spectra taken on both handedness of the 1000 nm shuriken with a deposited layer of L- and D-cysteine are presented in **Figure 7.14**.

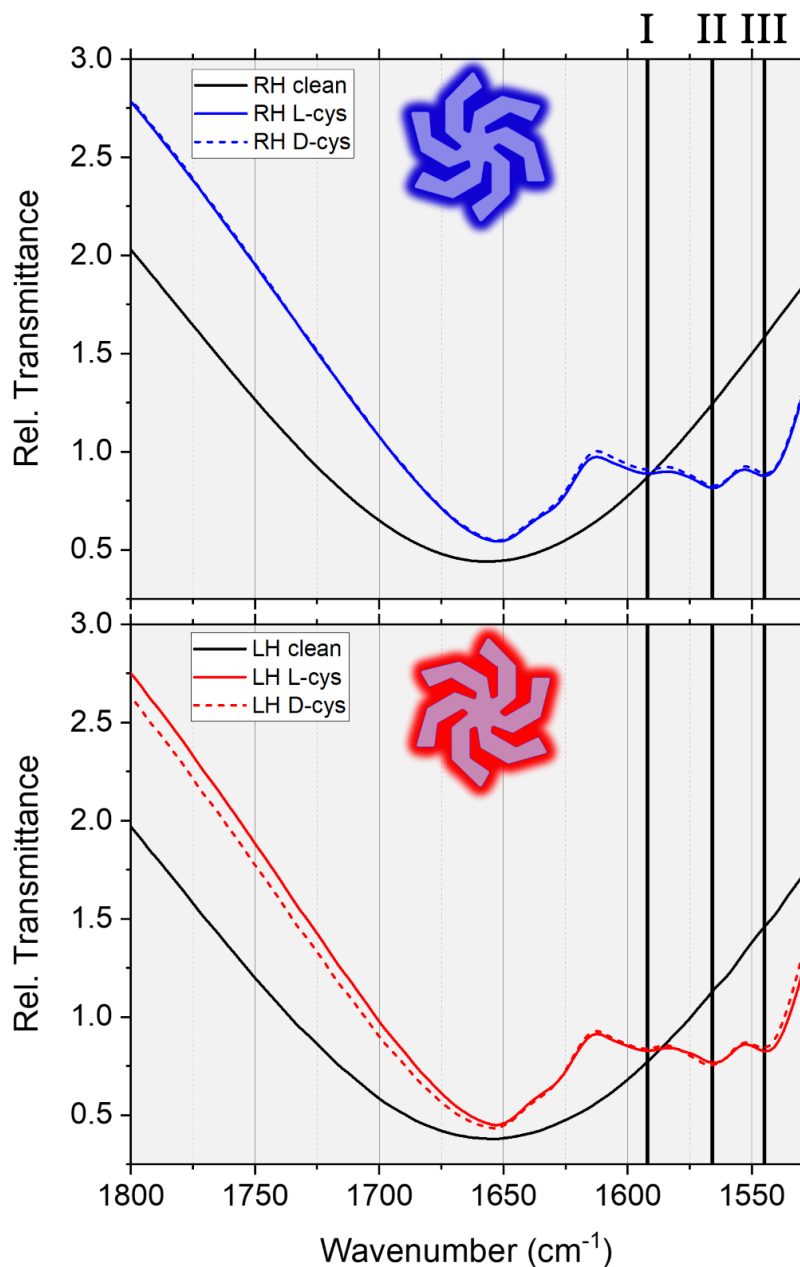


**Figure 7.14:** IR relative transmittance spectra obtained on the clean arrays (solid black curves), and after drying 100  $\mu\text{L}$  of 10 mM solution of L- (solid) and D-cysteine (dashed) in blue and red for the RH and LH shuriken handedness, respectively. With the vibrational modes highlighted by vertical lines.



The clean IR spectra for the LH and RH shuriken follow the same shape as the spectra obtained with the *Vertex 70* instrument presented in the previous section (7.4.2), with a plasmonic peak located at  $\sim 1650\text{ cm}^{-1}$  (compare **Figure 7.10** and **Figure 7.14**). After depositing the cysteine layer on top of the arrays of plasmonic shuriken, the IR spectra change drastically, and 3 IR vibrational modes appear (see **Figure 7.14**). These peaks correspond to modes I, II and III presented earlier in **Figure 7.8**. The position of these cysteine vibrational modes is slightly red-shifted compared to the measurements conducted on bare silicon. Here, modes I, II and III are situated at 1592, 1566 and 1545  $\text{cm}^{-1}$ , respectively. Because IR spectroscopy is blind to chirality, the IR spectra of the deposited L- and D-cysteine layers are almost perfectly overlapping each other, showing no enantioselectivity. This also shows that the amount of analyte covering the arrays is nearly identical between both enantiomers.

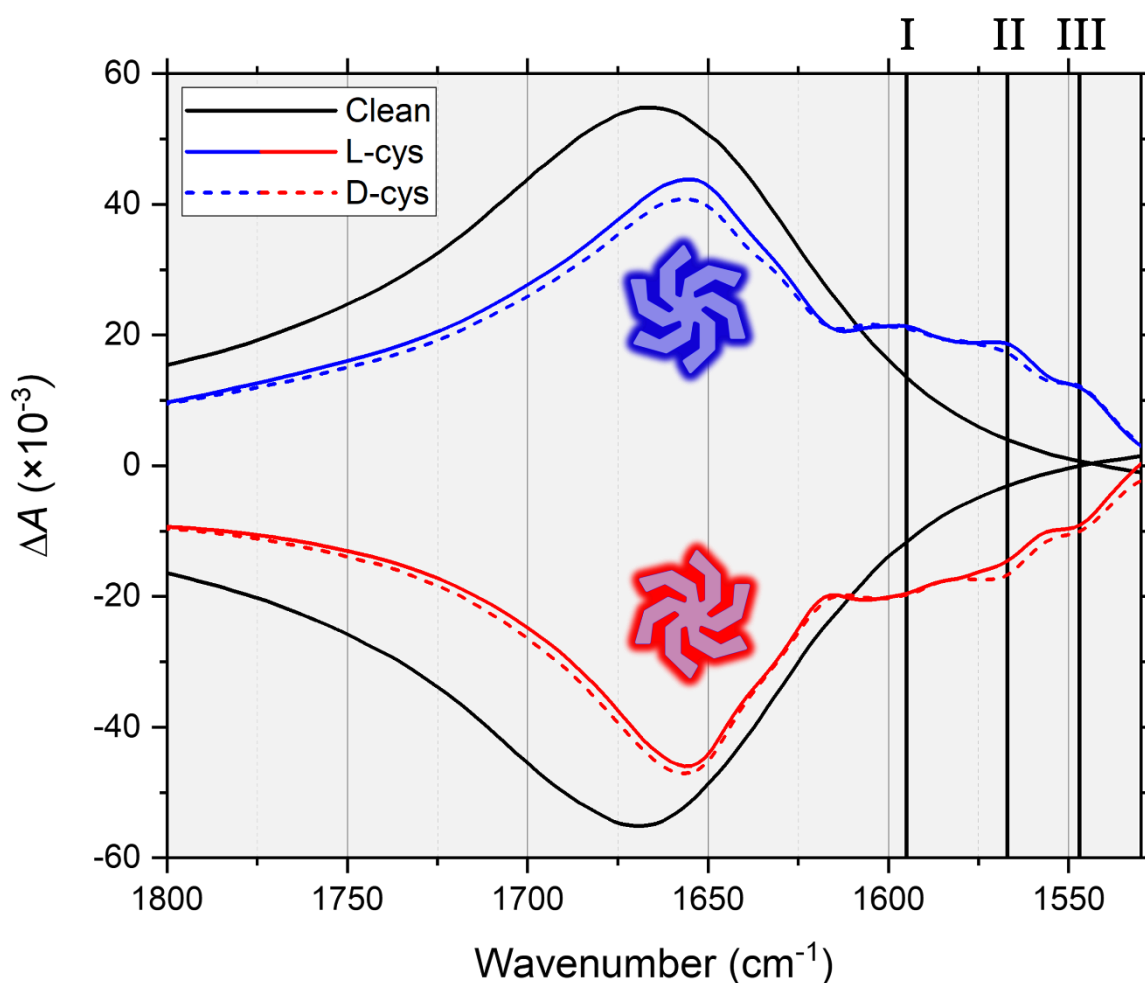


**Figure 7.15:** VCD spectra obtained on the clean arrays (solid black curves), and after drying 100  $\mu\text{L}$  of 10 mM solution of L- (solid) and D-cysteine (dashed) in blue and red for the RH and LH shuriken handedness, respectively.

The VCD spectra were then plotted in **Figure 7.15**. As expected, the spectra show opposite values of  $\Delta A$  depending on the handedness of the plasmonic shuriken. The introduction of the cysteine layer is causing a  $13\text{ cm}^{-1}$  red-shift of the main

plasmonic peak, and the 3 vibrational modes are visible at the same positions as in the IR spectra. Interestingly, the main plasmonic peak has a different intensity depending on the cysteine enantiomer deposited. Furthermore, the behaviour observed between the LH and RH arrays is opposite, suggesting enantiosensitivity.

To investigate this experimental observation, numerical simulations were performed in *COMSOL* Multiphysics. The 1000 nm shuriken model presented in **Figure 7.7** was used, with all the domains above the gold nanostructure defined as a chiral dielectric material. The shuriken was exposed to LCP and RCP incident light normal to the surface, and the interaction of the EM fields with the chiral dielectric was modelled using the constitutive equations, discussed in detail in the Section 3.4.2. The *Pasteur* coefficient  $\xi^T$  was used to define the property of the chiral dielectric medium, with a sign that depends on the handedness of the molecules, and which is null for an achiral media. In this study, the chiral layer was defined as an isotropic medium, with the diagonal components of the *Pasteur* coefficient fixed in all the wavelength range at  $\xi_{xx} = \xi_{yy} = \xi_{zz} = \pm 1.7 \times 10^{-5}$ . This value is coherent with a previous study [326]. Here, L-cysteine was given a positive value for  $\xi$  and D-cysteine was negative.

The simulated CD spectra, obtained from the difference of absorption between LCP and RCP, are compared to the experimental measurements in **Figure 7.16**.

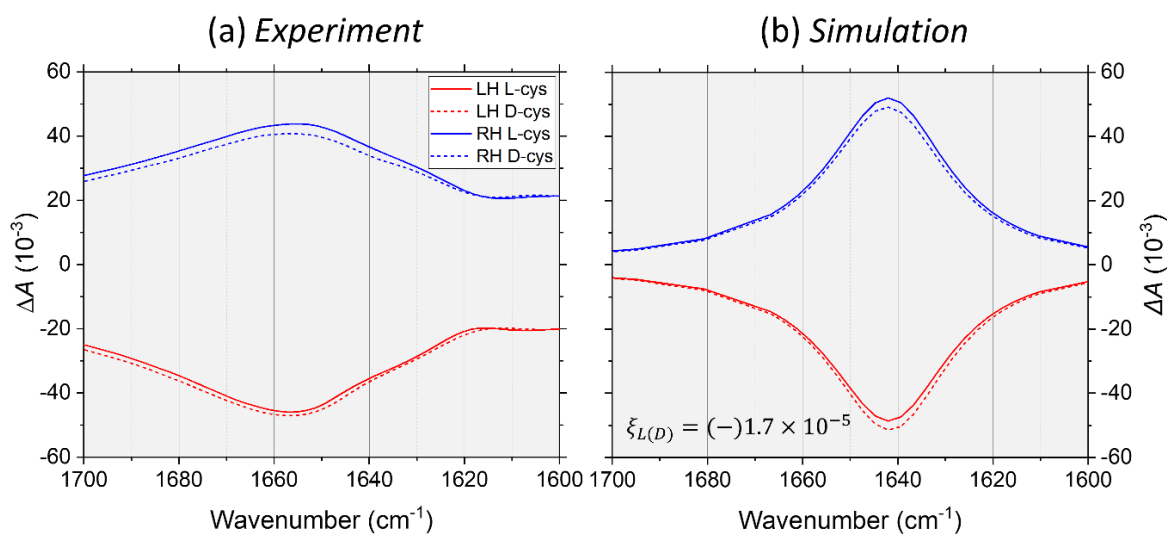


**Figure 7.16:** (a) Experimental and (b) simulated CD spectra of the LH (red) and RH (blue) 1000 nm large shuriken covered with the layer of either L- or D-cysteine in the solid and dashed lines, respectively.

These simulated CD spectra are qualitatively matching the experimental observations, replicating the enantio-dependent behaviour. The simulation model is also able to provide values of  $\Delta A$  very close to the experimental measurements.

The asymmetry observed here was characterised using the height ratio parameter  $H = \Delta A_{L-cys} / \Delta A_{D-cys}$ , which is taken at the apex position of each

spectrum. This parameter was calculated for the experimental and simulated spectra, for both LH and RH shuriken. The values of  $H$  are displayed in **Table 7-4**:

| $H$                 | LH   | RH   |
|---------------------|------|------|
| <b>Experimental</b> | 0.97 | 1.08 |
| <b>Simulation</b>   | 0.94 | 1.06 |

**Table 7-4: Experimental and simulated H height asymmetry ratios observed for both shuriken handedness.**

The values of the height ratio  $H$  obtained in the simulation agree with the experimental measurements, giving additional support to the observed enantio-dependent behaviour of this technique. This change is due to the asymmetric interaction of the chiral molecules with the chiral EM near field generated at the surface of the plasmonic metamaterials.

Another key observation can be made at the position of the vibrational modes I, II and III, described previously in the IR transmittance spectra in **Figure 7.14**. As seen in **Figure 7.15**, the VCD spectra are greatly impacted by the addition of the cysteine layer, with a clear broadening of the spectra compared to the clean reference. A zoomed-in view of these modes can be seen in **Figure 7.17**.

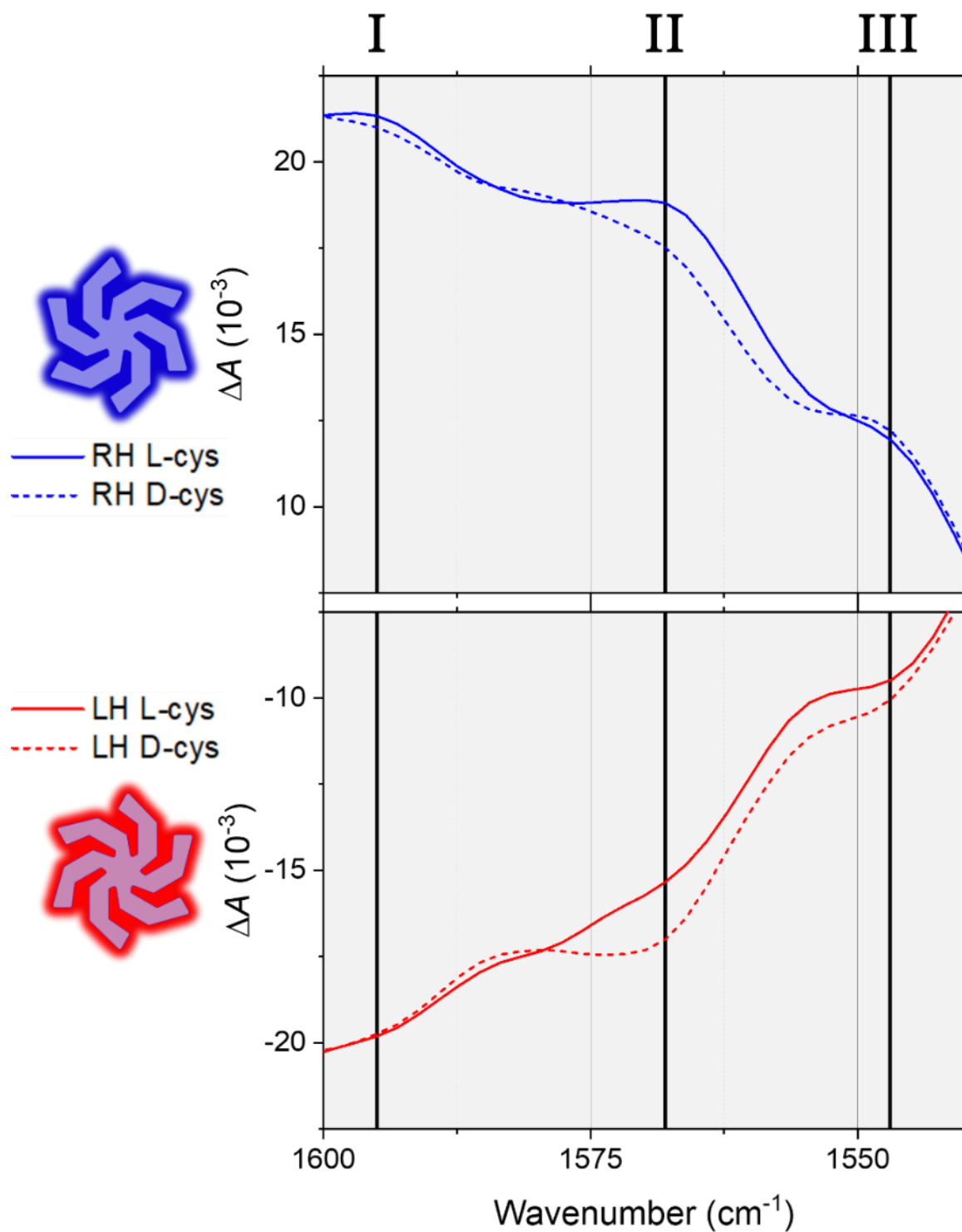
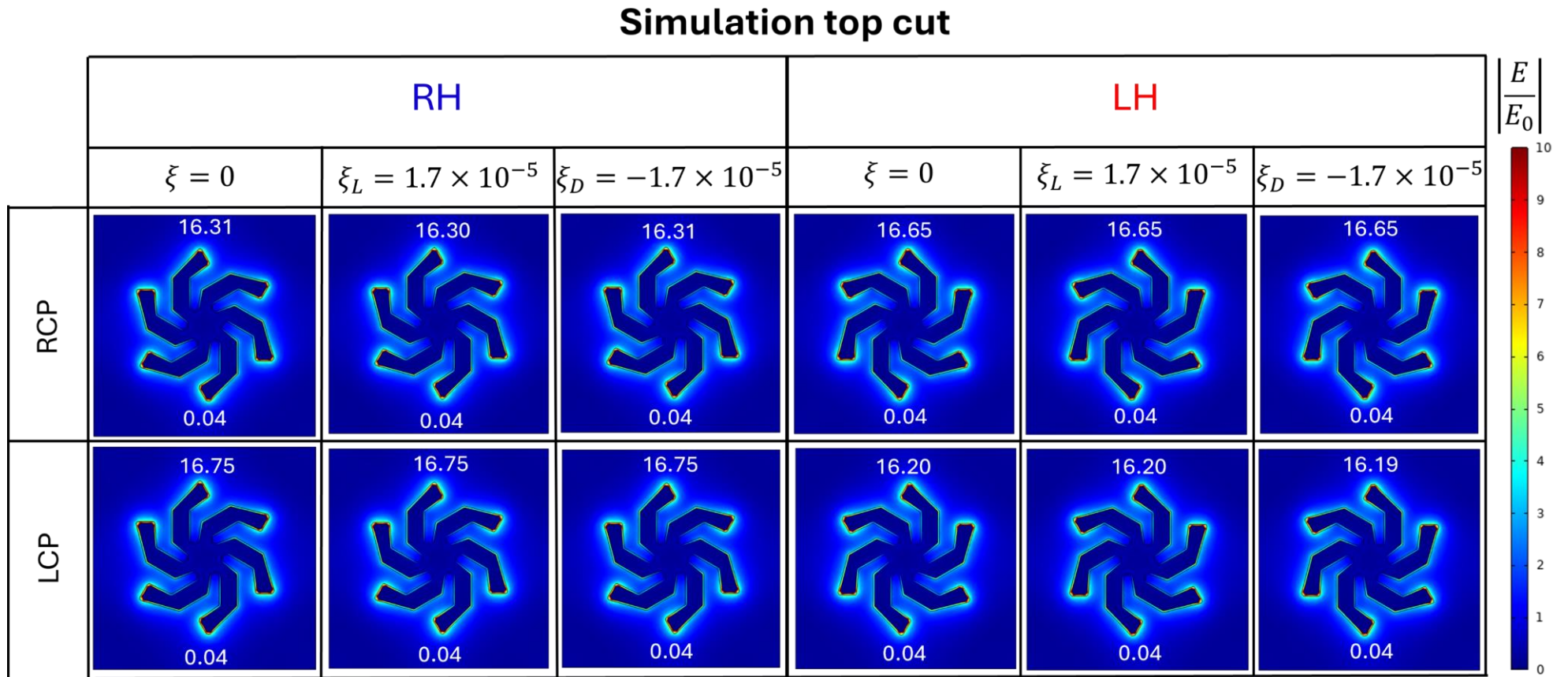


Figure 7.17: Zoomed-in VCD spectra of the RH (top) and LH (bottom) shuriken arrays with either L- (solid) or D-cysteine (dashed lines) drop casted at the surface, and the 3 vibration modes highlighted.

Here, mode II shows a clear enantio-dependent behaviour, while mode I and III have overlapping VCD signals for the two enantiomers, with no visible difference between the shuriken handedness. In other studies, the strongest VCD band of cysteine was found to be the asymmetric stretching  $\nu_{as}(CO_2^-)$ , which is coherent with the assignment made earlier on mode II [327–329]. Modes I and III can be called “pseudo VCD”, since the differences in absorption between LCP and RCP originate from a plasmonic effect and are not linked to a VCD response from the molecule itself. This effect has been reported in another study [300], where atmospheric CO<sub>2</sub> bands were detected in a VCD spectra of a chiral plasmonic template, which was rationalised by the strong differences in the near field enhancement between both nanostructure handedness exposed to CPL. In the case of mode II, it can be referred to as “true VCD” because of the enantio-dependent behaviour of the signal coming directly from the molecular VCD response (see **Figure 7.17**).

To understand these “pseudo VCD” and “true VCD” modes, numerical simulation was performed at 1628 cm<sup>-1</sup>, where the simulated values of  $\Delta A$  are similar to the experimental measurements observed at mode I (see **Figure 7.16** (a) and (b)). For modes I and III, the cysteine layer was assigned the same *Pasteur* coefficient ( $\xi_{L(D)} = (-) 1.7 \times 10^{-5}$ ) as in the previous simulation, presented in **Figure 7.16** (b), where the experimental observations at the plasmonic peak were replicated. The chiral parameter  $\xi$  is a complex frequency-dependent function defined previously in equation (3.14), where its real part describes the ORD signal and its imaginary part the CD spectra of a given chiral dielectric [97]. Here, the cysteine ORD and CD spectra are unknown, we therefore simplify the simulation model by taking a real value of  $|\xi|$ . To replicate mode II, where cysteine is assumed to be VCD active, the value of  $|\xi|$  was set higher than for modes I and III, with  $\xi_{L(D)} = (-)5.7 \times 10^{-5}$ .

The simulation model of both shuriken handedness was exposed to RCP and LCP light, where a chiral dielectric domain was defined on top of the gold structure with  $\xi_{L(D)} = (-)1.7 \times 10^{-5}$  and  $\xi_{L(D)} = (-)5.7 \times 10^{-5}$  successively, and compared to an achiral reference ( $\xi = 0$ ). Maps of the electric field enhancement ( $|E/E_0|$ ) were taken at the top surface of the shuriken nanostructure for all the combinations. The chiral asymmetry of the near field was also parametrised by the optical chirality parameter  $C$ , defined in Section 2.4.4, and normalised to the helicity of RCP light in air. These results are displayed in the following pages, with **Figure 7.18** to **Figure 7.21**. Similar figures taken at the middle and bottom of the plasmonic nanostructure are presented in **Appendix E**, with **Figure E.1** to **E.4** and **E.5** to **E.8** for the middle and bottom cut, respectively.



**Figure 7.18:** Simulated maps of the electric field enhancement  $|E/E_0|$  obtained for a circularly polarised incident light (RCP and LCP) at  $1628 \text{ cm}^{-1}$ , at the top surface of the RH and LH shuriken structures. An achiral dielectric medium ( $\xi = 0$ ) is compared to a small *Pasteur* coefficient of  $\xi_{L(D)} = (-)1.7 \times 10^{-5}$ . The maximum and minimum values obtained in each cut map are displayed on the top and bottom, respectively.



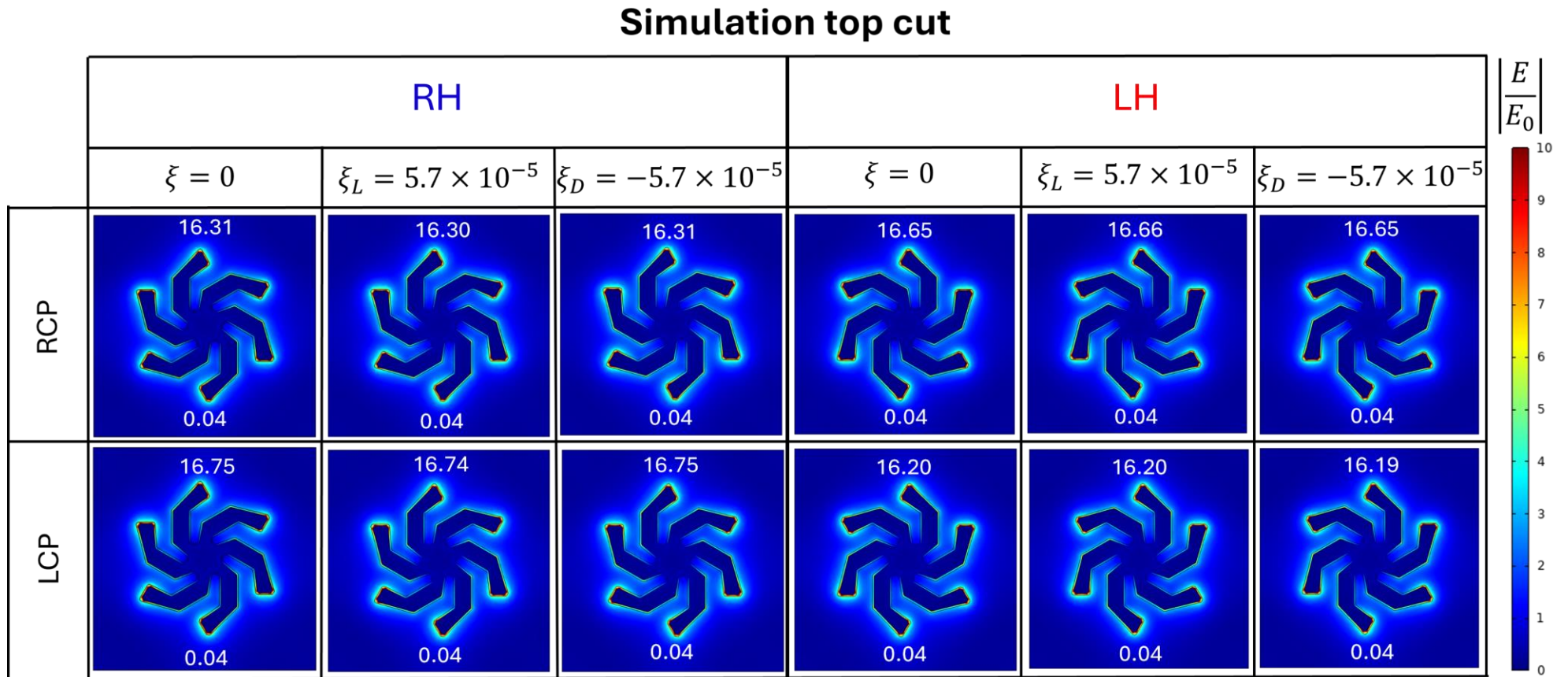


**Figure 7.19:** Simulated maps of the electric field enhancement  $|E/E_0|$  obtained for a circularly polarised incident light (RCP and LCP) at  $1628 \text{ cm}^{-1}$ , at the top surface of the RH and LH shuriken structures. An achiral dielectric medium ( $\xi = 0$ ) is compared to a higher *Pasteur* coefficient of  $\xi_{L(D)} = (-)5.7 \times 10^{-5}$ . The maximum and minimum values obtained in each cut map are displayed on the top and bottom, respectively.

Simulation top cut

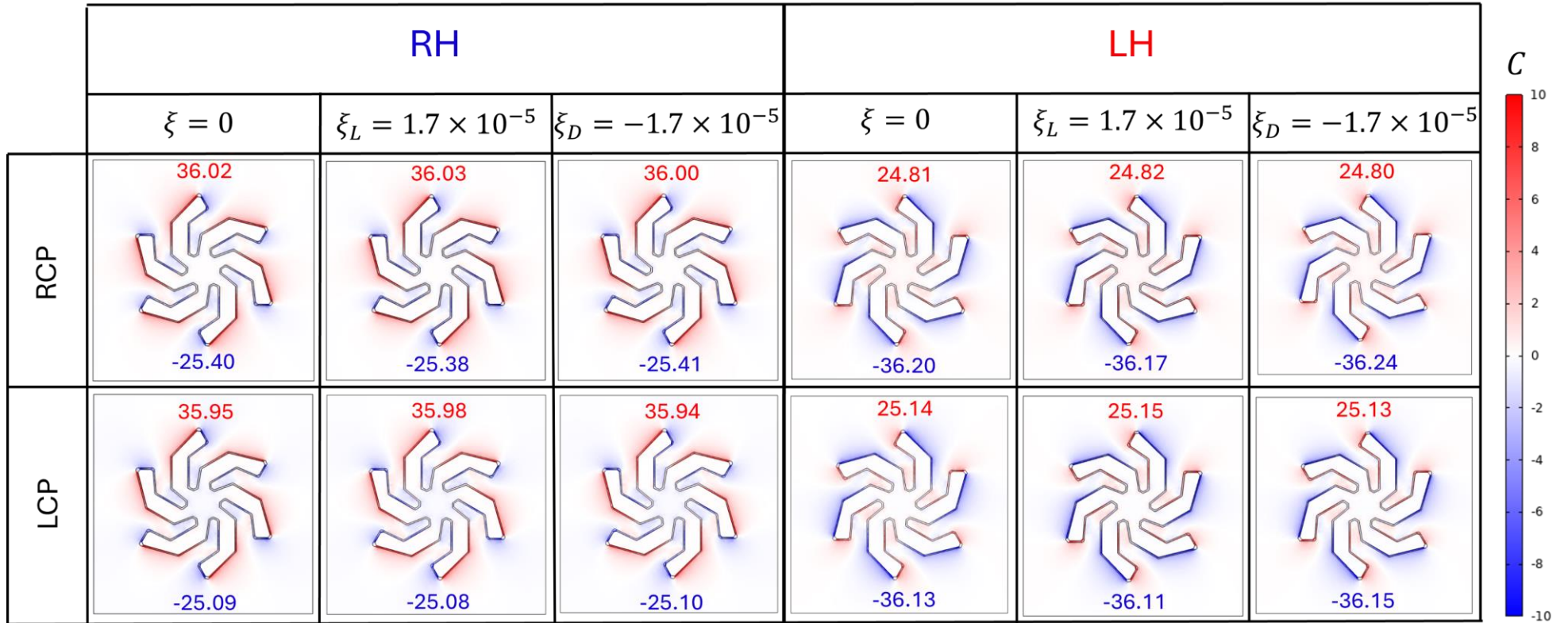


Figure 7.20: Simulated maps of the optical chirality  $C$  obtained for a circularly polarised incident light (RCP and LCP) at  $1628 \text{ cm}^{-1}$ , at the top surface of the RH and LH shuriken structures. An achiral dielectric medium ( $\xi = 0$ ) is compared to a small *Pasteur* coefficient of  $\xi_{L(D)} = (-)1.7 \times 10^{-5}$ . The maximum and minimum values obtained in each cut map are displayed on the top and bottom, respectively.



### Simulation top cut

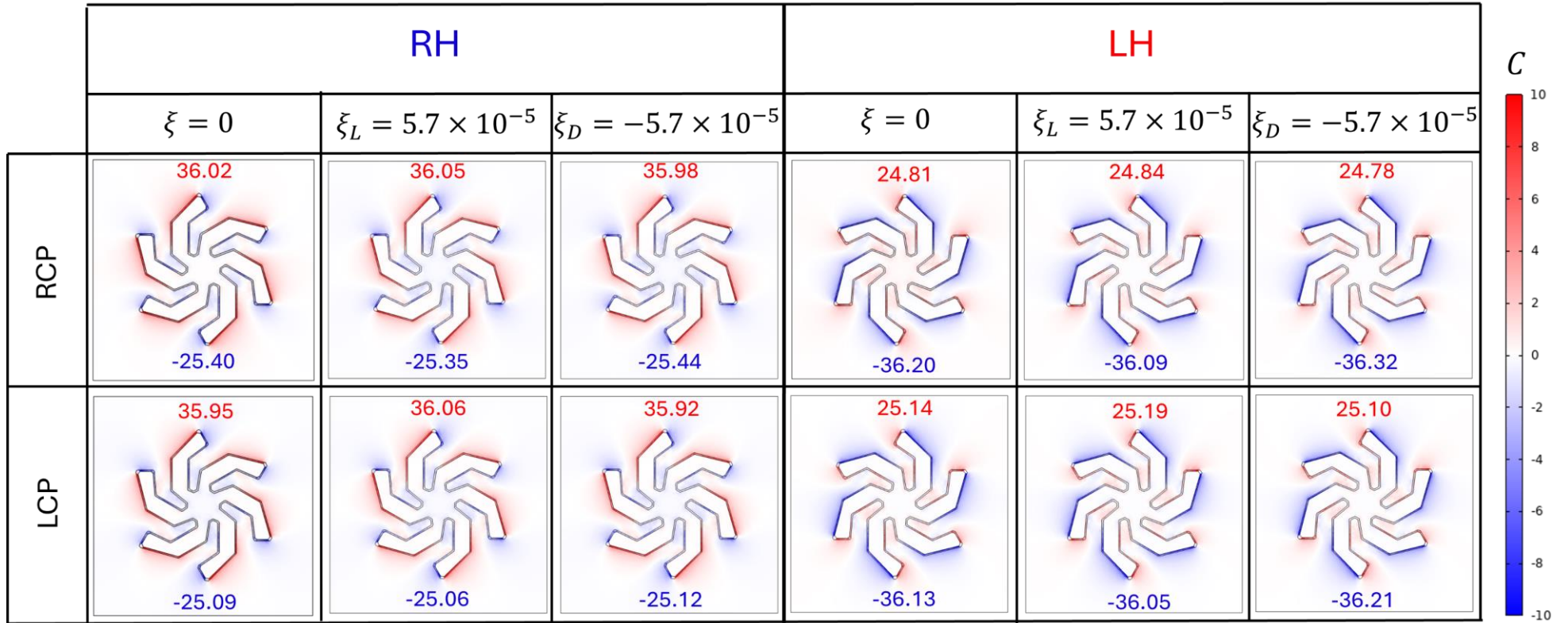
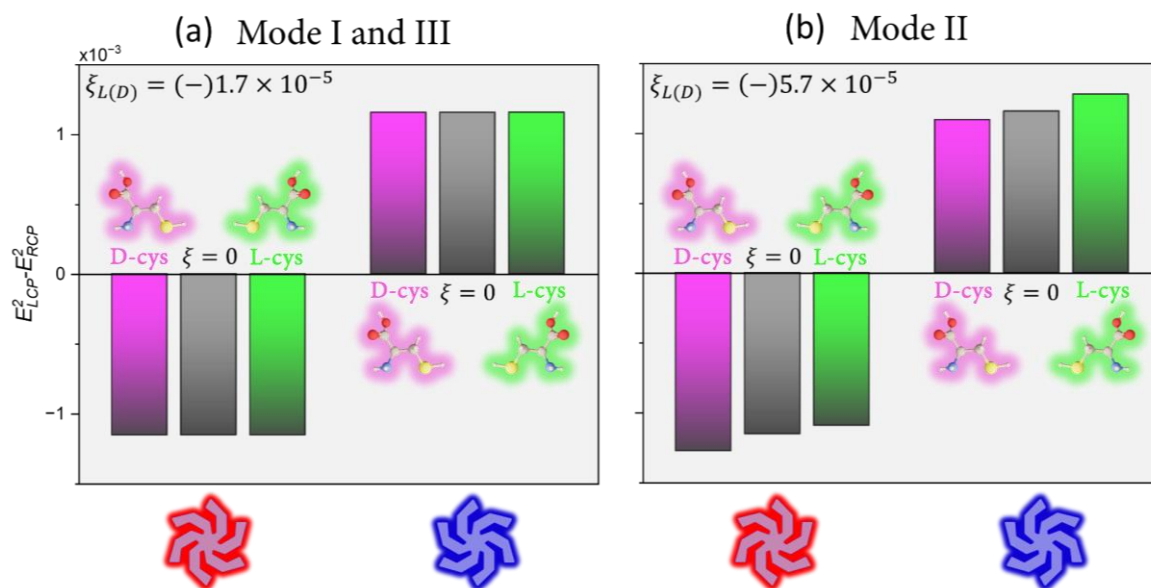


Figure 7.21: Simulated maps of the optical chirality  $C$  obtained for a circularly polarised incident light (RCP and LCP) at  $1628 \text{ cm}^{-1}$ , at the top surface of the RH and LH shuriken structures. An achiral dielectric medium ( $\xi = 0$ ) is compared to a higher *Pasteur* coefficient of  $\xi_{L(D)} = (-)5.7 \times 10^{-5}$ . The maximum and minimum values obtained in each cut map are displayed on the top and bottom, respectively.

The electric field maps show that the highest enhancement is reached at the end of the shuriken's arms (see **Figure 7.18** and **Figure 7.19**). The chiral asymmetry of the near field, parametrised by the optical chirality parameter  $C$ , also shows superchiral fields at the vicinity of the gold shuriken's arms (see **Figure 7.20** and **Figure 7.21**). These optical chirality maps have an opposite response between enantiomorphic structures, with a small variation in the maximum and minimum values reached depending on the handedness of the incident circularly polarised light. When  $\xi_{L(D)} = (-)1.7 \times 10^{-5}$ , there is a variation of only  $\leq 0.1\%$  in the minimum and maximum values of  $C$  compared to the reference ( $\xi = 0$ ) (see **Figure 7.20**). In the case of  $\xi_{L(D)} = (-)5.7 \times 10^{-5}$ , the variation increases to  $\leq 0.3\%$  (see **Figure 7.21**). For the electric field maps, the maximum simulated values show an asymmetry depending on the handedness of the incident light, with a higher electric field maximum when RH shuriken is exposed to LCP, and RCP for the case of the LH shuriken (see **Figure 7.18** and **Figure 7.19**). This is coherent with the sign of the measured VCD spectra, obtained experimentally from  $\Delta A = A_{LCP} - A_{RCP}$ , where RH is positive and LH negative (see **Figure 7.15**).

It is known that the enhancement of the CD response of chiral plasmonic metamaterial is proportional to the enhancement of the electric field, following  $\Delta A \propto E_{LCP}^2 - E_{RCP}^2$  [330,331]. Therefore, to replicate the experimental results, the electric field strength obtained with both LCP and RCP incident light was averaged in the entire cystine volume above the chiral plasmonic nanostructure and normalised to the incident light (same volume in air). The difference in the average electric field between LCP and RCP ( $E_{LCP}^2 - E_{RCP}^2$ ) was calculated for both shuriken handedness covered by a chiral layer with opposite values of  $\xi$  for L- and D-cysteine, and  $\xi = 0$  for DL-cysteine. The results are displayed in **Figure 7.22**.



**Figure 7.22:** Simulated values of  $E_{LCP}^2 - E_{RCP}^2$  for all the combinations of shuriken handedness and with (a) a small chiral parameter of  $\xi_{L(D)} = (-)1.7 \times 10^{-5}$  for the cysteine layer and (b) a higher value of  $\xi_{L(D)} = (-)5.7 \times 10^{-5}$ .

Here again, the sign of the VCD spectra is reproduced in the values of  $E_{LCP}^2 - E_{RCP}^2$ , with negative values for LH shuriken and positive values for RH. When the *Pasteur* coefficient is low ( $\xi_{L(D)} = (-)1.7 \times 10^{-5}$ ), the simulated results show identical values of  $E_{LCP}^2 - E_{RCP}^2$  between both cysteine enantiomers, comparable to an achiral medium ( $\xi = 0$ ) (see **Figure 7.22 (a)**). This agrees with the experimental observations of “pseudo VCD” made in the VCD spectra at modes I and III, where the signals for L- and D-cysteine overlap (see **Figure 7.17**). When the *Pasteur* coefficient is higher ( $\xi_{L(D)} = (-)5.7 \times 10^{-5}$ ), an asymmetric response arises between LH and RH shuriken (see **Figure 7.22 (b)**). The LH shuriken handedness has a bigger absolute response with D-cysteine compared to the other enantiomer, and the opposite behaviour is observed for the RH shuriken, where L-cysteine gives a higher  $E_{LCP}^2 - E_{RCP}^2$  value, reproducing the experimental measurements of “true VCD” at mode II.

To highlight the enantioselective behaviour observed in the experimental VCD spectra at the position of mode II and compare it to mode I and II, the parameter  $\Delta\Delta A_{cys} = \Delta A_{RH} + \Delta A_{LH}$  was calculated for L-, D- and DL-cysteine, respectively. The same was done for the simulations, with  $\Delta(E_{LCP}^2 - E_{RCP}^2)$ , which is the sum of the values obtained on LH and RH structures for each cysteine enantiomer. The resulting  $\Delta\Delta A_{cys}$  spectra and  $\Delta(E_{LCP}^2 - E_{RCP}^2)$  values for different  $\xi$  parameters are plotted in **Figure 7.23**.

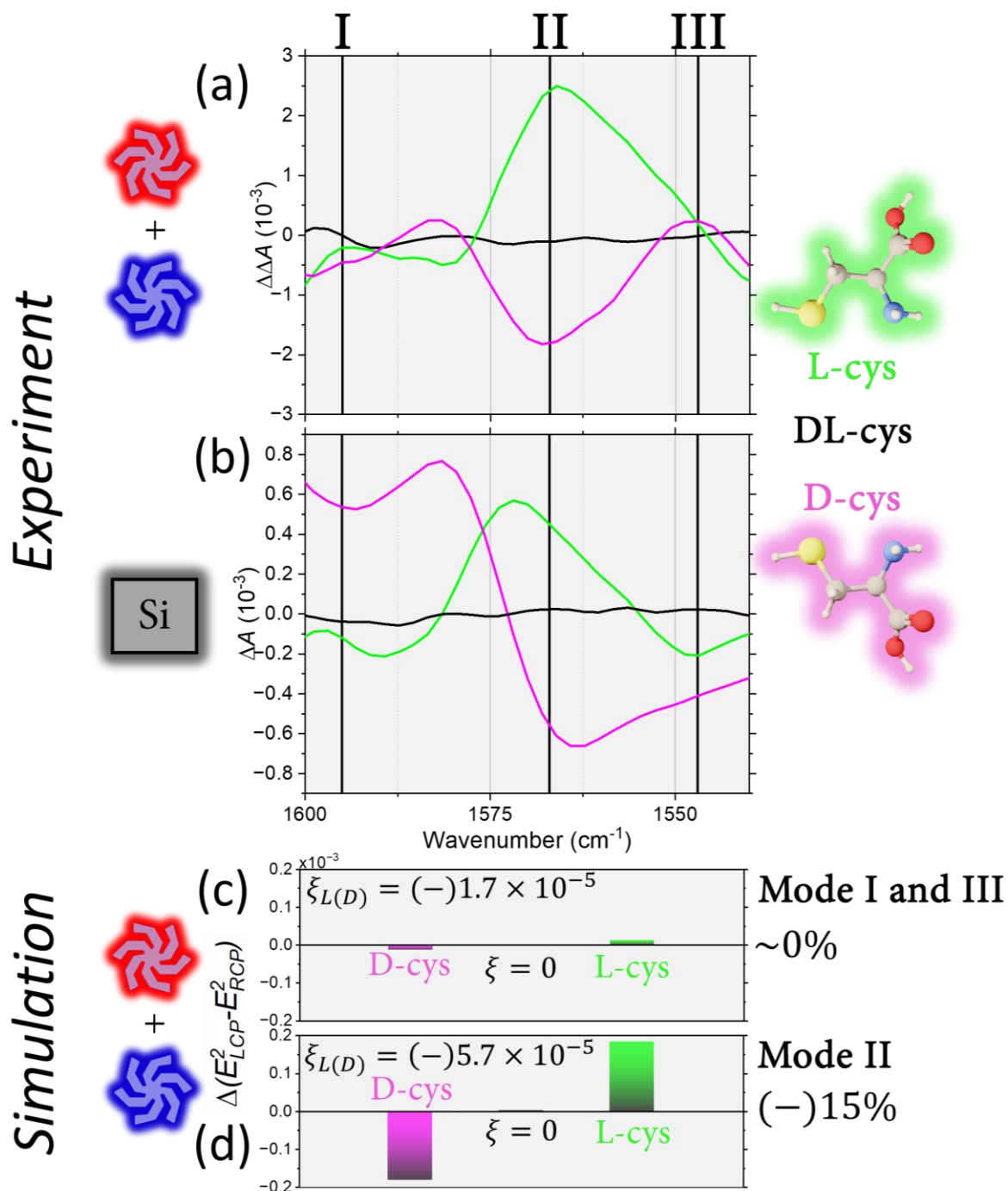


**Figure 7.23:** (a) Sum of the normalised VCD spectra ( $\Delta\Delta A_{cys}$ ) measured on the RH and LH shuriken arrays and (b) VCD spectra of L-, D- and DL-cysteine (100  $\mu$ L at 30 mM) deposited on bare silicon. The lower panel presents the sum of the simulated values of  $E_{LCP}^2 - E_{RCP}^2$  obtained for both shuriken handedness with (c) a low  $\xi$  of  $1.7 \times 10^{-5}$  and (d) a higher value of  $5.7 \times 10^{-5}$ .

As expected, the spectra of  $\Delta\Delta A_{cys}$  show no difference between the different cysteine enantiomers and the racemate mixture at modes I and III, whereas a clear enantio-specific behaviour is visible at the position of mode II (see **Figure 7.23** (a)). The VCD measurements of the deposited cysteine on bare silicon agree with these

results, where there is a clear opposite VCD response around the position of mode II, but no significant response at modes I and III (see **Figure 7.23** (b)). One can observe that the spectra obtained on the plasmonic arrays yield a moderate enhancement of the signal, while the amount of material was 3 folds higher on bare silicon. A better mirror response between both cysteine enantiomers can also be noted.

The results for modes I and III are reproduced by the simulated values of  $\Delta(E_{LCP}^2 - E_{RCP}^2)$ , which is negligible for a small value of  $\xi$  (see **Figure 7.23** (c)). When the value of  $\xi$  increases, an asymmetry appears, mirroring the experimental results at mode II (see **Figure 7.23** (d)). This asymmetry is equal to 15% in the simulations, which is close to the experimental observations presented in **Figure 7.23** (a). The simulation work supports the experimental hypothesis, where the VCD response from a specific vibrational band of the molecular analyte was directly measured using chiral nanophotonic templates.

## 7.5 Conclusion

To summarise, chiral plasmonic metamaterials have been successfully employed for the detection of molecular vibrational modes of a single molecular layer of the cysteine amino acid using an FTIR spectrometer. This is observed by a broadening of the plasmonic resonance, which can be rationalised by a plasmonic damping effect mediated by the vibration of the adsorbed molecular layer, leading to a shorter plasmon lifetime. Despite its ultrasensitive capability, this technique was unable to discriminate between the cysteine enantiomers.

A thicker layer of the amino acid was then tested on the same plasmonic metamaterials using VCD spectrometry, which is an optically active technique. Here, an enantio-selective response was obtained through two phenomena. The first one is seen in the amplitude of the plasmonic peak in the VCD spectra, outside of any molecular vibrational modes. This effect manifests by an asymmetry in the coupling of the bright and dark modes mediated by chiral molecular vibrations, leading to a dichroic absorption between both handedness of the plasmonic shuriken depending on cysteine enantiomeric form. The second phenomenon is a direct measurement of the VCD band originating from the molecular layer itself, where the VCD signal has an opposite behaviour depending on the handedness of the shuriken metamaterial.

Using chiral nanophotonic platforms has several advantages compared to traditional techniques. It has far superior sensitivity, with the ability to detect vibrational modes from a monolayer amount of analyte (picomole). These platforms also don't necessitate an aqueous environment, for which a complex background subtraction of water IR peaks must be conducted or D<sub>2</sub>O must be used instead. The time of the measurement is also drastically reduced, from as much as 48 hours to a few minutes. This technique opens a new avenue for the detection and characterisation of chiral molecules based on their molecular vibrational modes.

## Chapter 7: Summary

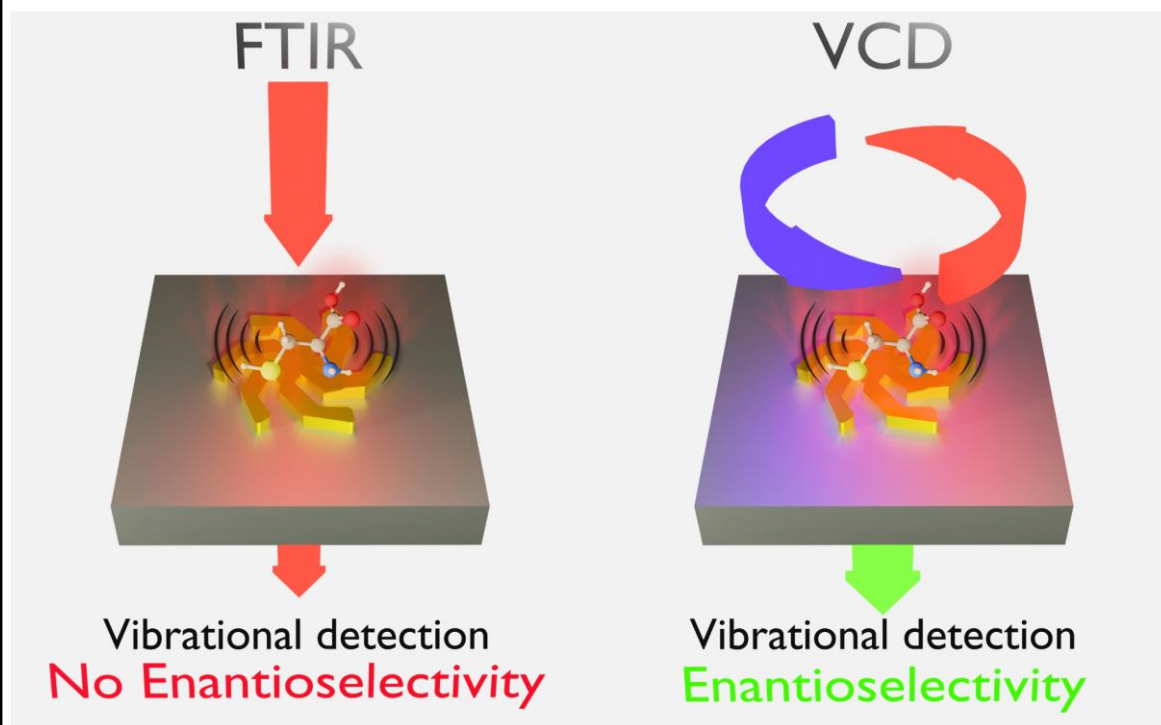


Figure 7.24: Chapter 7 concept illustration.

### **Key Findings:**

- Successful detection of the vibrational modes of a monolayer of adsorbed cysteine using a conventional FTIR instrument, but enantiomeric discrimination was not achieved.
- Enantio-sensitive detection of a multilayer of cysteine using VCD through two different plasmonic phenomena: 1) the change in intensity of the main plasmonic VCD peak and 2) the direct enhancement of the “true VCD” signal of the chiral molecule through the enhancement of the plasmonic near field.
- The experimental observations made for these two techniques have been reproduced/supported by numerical simulation work.

# Chapter 8

---

Summary and outlook



This thesis encapsulates most of the scientific research conducted over four years as a PhD student at the University of Glasgow. The work presented here spans four different yet interconnected projects, each participating in the advancement of metamaterials in addressing real-world challenges. A new functionalisation technique and several applications of metamaterials in the field of biosensing have been presented in detail and discussed. In this chapter, a brief summary of the results obtained during this PhD will be provided, along with a short outlook on the future prospects of these technological innovations.

The different methods presented in **Chapter 3** detail the fabrication protocols adapted to the fabrication of the metamaterials that have been studied during this PhD. These complex samples, made of periodic arrays of nanoscale structures, require the use of a cleanroom facility, where they are manufactured and characterised by state-of-the-art instruments. Two types of plasmonic metamaterials have been fabricated in this work: gold nanostructures on silicon wafer and the shuriken metafilm.

Both samples require EBL and metal evaporation, which are complex and expensive manufacturing techniques. However, the shuriken metafilm offers distinct advantages over the gold-on-silicon samples, primarily its low cost and high reproducibility. This is achieved using injection moulding, which has the potential to produce thousands of polycarbonate slides from a single master shim. This inexpensive and high-throughput technique holds promise for commercial biosensing applications, while the gold-on-silicon protocol is more adapted to prototyping and research usage.

In **Chapter 4**, a novel functionalisation technique is discussed, where the chemical activity of plasmonic nanorods is controlled *via* thermoplasmonic effects combined with a thermoresponsive polymer anchored to the gold plasmonic surface. Heat generation was once considered an unwanted byproduct of plasmonic phenomena; it is now recognised as a powerful tool for localised heating in numerous applications. One such field is cancer therapy, where the heat generated by plasmonic NPs is used to destroy cancer cells in a more selective manner as compared to traditional therapies. This technique has already been exploited in the Kadodwala group to specially functionalise only specific parts of the shuriken metafilm cavities with a monochromatic pulsed laser. In this chapter, the thermoplasmonic response at different wavelengths and for different polarisation angles was investigated, enabling more control over the chemical activity of metamaterials.

The thermoresponsive polymer was designed with a functional group at its extremity (biotin), making the surface of the sample chemically active. By employing a pulsed laser, a heat gradient in the solvent around the plasmonic nanostructures, will cause the thermoresponsive polymer to collapse above a threshold temperature (LCST). This irreversible change in the molecular conformation of the polymer chains will hinder the functional group by effectively burying it in the polymer layer. This new

technique proved to be highly effective at gradually controlling the chemical activity of the samples, which is a significant advantage compared to traditional binary techniques.

The study investigates nanorods of two different lengths, possessing slightly different plasmonic properties that have been predicted by simulation work. By tuning the laser's wavelength and polarisation, selective functionalisation was achieved using streptavidin conjugate QDs. Notably, the heat generated by one length was significantly higher than that of the other under specific laser parameters.

This technique is a significant innovation over other techniques such as dip-pen lithography, which are expensive, have a low throughput and are limited to micron-scale surface area. This thermoplasmonic functionalisation method holds great potential for applications requiring precise spatial control over chemical activity at the nanoscale, particularly in biosensing. The ability to selectively tune the chemical properties across large areas ( $> \text{mm}^2$ ) with this high-throughput process is a promising avenue for scaling metamaterial technologies to commercial applications.

In future work, more complicated structures could be investigated in applications such as biosensing, further demonstrating the validity of this technique. Additionally, the thermoplasmonic behaviour of chiral NPs exposed to CPL could be studied and harvested to achieve selective functionalisation. Alternatively, this functionalisation technique could be studied in the context of photothermal therapy, which has seen a surge in interest, particularly in cancer treatment. It is especially relevant because *p-NIPAAm* has been extensively studied for this specific application owing to its ideal phase transition properties (low LCST) adapted for drug delivery and its biocompatibility [332]. Integrating these concepts could enhance the efficiency of cancer therapies, as suggested by a recent study [333].

**Chapter 5** presents a new near-field probing technique based on photoluminescence (PL), enabling enhanced bio-detection compared to traditional light-scattering methods. This technique, named plasmonic circularly polarised luminescence (PCPL), was able to detect a chiral response from a monolayer quantity of de novo peptide adsorbed at the surface of the shuriken metafilm TPS, while traditional reflectance-based measurements showed no detection capability. This improvement in the sensitivity was attributed to the fact that PL is directly linked to the local density of optical states (LDOS) of the EM near field at the surface of the plasmonic sample, while the light scattering measurements are based on a far larger EM field volume. This hypothesis is supported by simulation work on *COMSOL*, reproducing the experimental observations by considering two different volumes above the plasmonic metamaterial. Enhancing the sensitivity of metamaterials is key in applications such as point-of-care diagnostics and nanometrology, the PCPL technique represents a significant advancement in this direction.

This work could be taken further by investigating different avenues to enhance the PL signal generated by the shuriken metafilm. In this study, much of the observed signal enhancement was attributed to the Purcell effect, as the near-UV laser does not directly excite the plasmonic shuriken template at its LSPR frequency. Adapting the geometry of the metamaterial to maximise the PL yield could further increase the sensitivity of this technique. Additionally, using QDs with a strong PL intensity and high quantum efficiency could improve the results observed with the TPS employed in this study. Future work could also explore the potential enantioselectivity of this nanophotonic platform by employing time-resolved fluorescence microscopy, providing deeper insights into its chiral sensing capabilities and expanding the scope of biosensing applications.

In **Chapter 6** of this thesis, another application of the shuriken metafilm sample was explored using SERS to detect the handedness of chiral NPs (HNPs) attached to the metasurface by an achiral Raman molecule reporter (BPDT) in a SAM. The simulation work successfully explained the experimental observations by looking at the electric field enhancement between the HNP and the chiral shuriken cavity for all the combinations. Three different models were studied with a HNP at different positions/orientations with respect to the shuriken nanocavity. The findings revealed that the symmetry of the combination between the HNP and the shuriken cavity produces a drastically different EM environment. Specifically, the pairs of matching handedness show a near twofold increase in field enhancement ( $|E_{loc}/E_0|^4$ ) compared to the mismatching pairs. This technique benefits from its simplicity and sensitivity, using a conventional Raman spectrometer with the ability to detect monolayer amount of analyte.

Improvements could be made to this technique, such as matching the plasmonic resonance with the Raman laser wavelength to maximise the chiral SERS effect. The addition of nanogaps in the plasmonic design could further enhance the SERS signal by creating intense plasmonic hotspots. This SERS method can also be extended to chiral molecular analytes instead of the HNPs, which would similarly influence the EM near field, broadening its use in biosensing applications. Further work conducted after this project has provided additional evidence of this by using this technique in the ultrasensitive biomolecular conformation detection of poly-L/D-lysine [326].

In **Chapter 7**, chiral metamaterials are studied in the IR range using two different setups: an FTIR and a VCD spectrometer. These analytical techniques are routinely used in research to identify molecular analytes through their specific vibrational bands. An FTIR spectrometer measures the light transmitted through the metamaterial sample from an unpolarised incident beam in a wide wavelength range. A VCD spectrometer is more specialised, measuring the difference in absorbance between circularly polarised light (CPL) of both handedness, making it enantio-sensitive. In this study, the cysteine amino acid was chosen to be analysed in

conjunction with chiral shuriken metamaterials of different sizes (1000 and 1500 nm) and therefore different plasmonic resonances. The plasmonic resonances were tailored to coincide with different vibrational bands of cysteine.

A SAM layer of the L- and D-cysteine enantiomers, as well as the racemate mixture, was deposited on the gold shuriken structures and the samples were studied with the FTIR setup. The results revealed a distinct broadening of the plasmonic peak at the position of the most intense vibrational bands of cysteine, and a smaller response was also detected at the smaller mode on the other shuriken size. This effect could not be explained by previous studies using intense electric field enhancement to significantly increase the absorption at the molecular vibrational mode of molecules through a technique called SEIRA. Indeed, the simulation work showed that the plasmonic structures studied here produced a modest electric field enhancement  $|E/E_0|^2 \approx 8$  in the vicinity of the plasmonic structures. This is too low to observe SEIRA effects given the negligible absorption of a monolayer of cysteine (0.1 %). This new effect was instead attributed to plasmonic damping mediated by the vibration of the molecular layer, causing a shorter plasmon lifetime. Although this technique was able to detect the molecular vibration of a monolayer amount of analyte, no enantioselectivity was observed, highlighting the necessity of using a VCD spectrometer.

The VCD spectrometer was used on the 1000 nm shuriken size only, with a higher amount of cysteine dried on top of the metamaterial. In this experiment, discrimination of the cysteine enantiomers was obtained through two distinct plasmonic effects. The first was observed at the plasmonic VCD resonance, where the intensity of the peak was correlated with the enantiomeric form of cysteine. Simulation work replicated this effect, which was explained by a difference in dichroic coupling of the plasmonic near field with the chiral molecules, leading to a difference in light absorption ( $\Delta A$ ). The second effect occurred directly at the position of the vibrational band, where a mirror response was obtained between the two shuriken handedness for a given cysteine enantiomer. This was rationalised and reproduced by numerical simulation through the variation in the electric field induced by the change in the value of the chirality parameter at the VCD band of the molecule.

This work demonstrated the potential of chiral metamaterials in vibrational spectroscopy. Studying trace amounts of material is crucial in many applications, including pharmaceutical quality control, environmental monitoring, and biomedical diagnostics. Future research should focus on enhancing enantioselectivity at the single molecular layer level and extending the technique to other chiral biomolecules relevant in both research and industrial settings. These requirements will necessitate a new metamaterial design with higher electric field enhancement, which can be achieved through the use of nanogaps or increased surface roughness, for example.

The work presented in this thesis contributes to the knowledge in the field of plasmonic metamaterials applied to sensing technologies, showcasing a novel functionalisation technique and three chiral biosensing applications. It is my hope that this research will participate to the development of better sensing devices, which will lead to more reliable and timely diagnoses in healthcare and improve the quality of pharmaceutical products.

As a final note, metamaterials have provided new solutions to a wide range of scientific fields, captivating the curiosity of researchers with unlimited design possibilities and enhanced optical properties. Future work is essential to develop reliable and competitive platforms for real-world biosensing applications, especially as other techniques, such as molecularly imprinted polymers (MIP), are also being developed. The analysis of complex samples containing various analytes and interferent compounds requires exceptional sensitivity and selectivity from next-generation nanophotonic platforms. These challenges can be addressed by developing novel functionalisation techniques, increasing the chemical selectivity of surfaces, and leveraging advances in machine learning and artificial neural networks. These computational approaches would enable both the design of new plasmonic architectures tailored for specific analytes, and the ability to precisely analyse the measured resonance spectra, leading to more efficient metamaterial-based plasmonic biosensors.



# References

- [1]. NGUYEN LA, HE H, PHAM-HUY C. CHIRAL DRUGS: AN OVERVIEW. *INT J BIOMED SCI.* 2006;2(2):85.
- [2]. MURRAY WA, BARNES WL. PLASMONIC MATERIALS. *ADV. MATER.* 2007;19(22):3771–82.
- [3]. TANG Y, COHEN AE. OPTICAL CHIRALITY AND ITS INTERACTION WITH MATTER. *PHYS REV LETT.* 2010;104(16):163901.
- [4]. HENDRY E, CARPY T, JOHNSTON J, POPLAND M, MIKHAYLOVSKIY R V, LAPTHORN AJ, ET AL. ULTRASENSITIVE DETECTION AND CHARACTERIZATION OF BIOMOLECULES USING SUPERCHIRAL FIELDS. *NAT NANOTECHNOL.* 2010;5(11):783–7.
- [5]. LI Z, GUO P, ZHOU Y. DIP-PEN NANOLITHOGRAPHY ENABLED FUNCTIONAL NANOMATERIALS AND THEIR APPLICATIONS. *ADV MATER TECHNOL.* 2021;6(4):2000897.
- [6]. NAYAK L, MOHANTY S, NAYAK SK, RAMADOSS A. A REVIEW ON INKJET PRINTING OF NANOPARTICLE INKS FOR FLEXIBLE ELECTRONICS. *JOURNAL OF MATERIALS CHEMISTRY C.* 2019;7(29):8771–95.
- [7]. RUHOFF VT, ARASTOO MR, MORENO-PESCADOR G, BENDIX PM. BIOLOGICAL APPLICATIONS OF THERMOPLASMONICS. *NANO LETT.* 2024;24(3):777–89.
- [8]. GUGLIEMELLI A, PIERINI F, TABIRYAN N, UMETON C, BUNNING TJ, DE SIO L. THERMOPLASMONICS WITH GOLD NANOPARTICLES: A NEW WEAPON IN MODERN OPTICS AND BIOMEDICINE. *ADV PHOTONICS RES.* 2021;2(8):2000198.
- [9]. DUBI Y, UN IW, SIVAN Y. THERMAL EFFECTS—AN ALTERNATIVE MECHANISM FOR PLASMON-ASSISTED PHOTOCATALYSIS. *CHEM SCI.* 2020;11(19):5017–27.
- [10]. SHIN D, KANG G, GUPTA P, BEHERA S, LEE H, URBAS AM, ET AL. THERMOPLASMONIC AND PHOTOTHERMAL METAMATERIALS FOR SOLAR ENERGY APPLICATIONS. *ADV OPT MATER.* 2018;6(18):1800317.
- [11]. MAXWELL JC. VIII. A DYNAMICAL THEORY OF THE ELECTROMAGNETIC FIELD. *PHILOS TRANS R SOC LOND.* 1865;(155):459–512.
- [12]. HURAY PG. MAXWELL'S EQUATIONS. JOHN WILEY & SONS; 2009.
- [13]. FLEISCH D. A STUDENT'S GUIDE TO MAXWELL'S EQUATIONS. CAMBRIDGE UNIVERSITY PRESS; 2008.
- [14]. GREINER W. CLASSICAL ELECTRODYNAMICS. SPRINGER SCIENCE & BUSINESS MEDIA; 2012.
- [15]. GRIFFITHS DJ. INTRODUCTION TO ELECTRODYNAMICS. CAMBRIDGE UNIVERSITY PRESS; 2023.
- [16]. ELLIS GFR, UZAN JP. C IS THE SPEED OF LIGHT, ISN'T IT? *AM J PHYS.* 2005;73(3):240–7.
- [17]. FRESNEL AJ. MÉMOIRE SUR LA DOUBLE RÉFRACTION. VOL. 7. CHEZ FIRMIN DIDOT, PÈRE ET FILS, LIBRAIRES; 1827.
- [18]. GOLDSTEIN DH. POLARIZED LIGHT. CRC PRESS; 2017.
- [19]. CLOUDE S. POLARISATION: APPLICATIONS IN REMOTE SENSING. OUP OXFORD; 2009.
- [20]. BARRON LD. FROM COSMIC CHIRALITY TO PROTEIN STRUCTURE: LORD KELVIN'S LEGACY. *CHIRALITY.* 2012;24(11):879–93.
- [21]. THOMSON W, KELVIN B. BALTIMORE LECTURES ON MOLECULAR DYNAMICS AND THE WAVE THEORY OF LIGHT. CAMBRIDGE UNIVERSITY PRESS; 2010.
- [22]. PRELOG V. CHIRALITY IN CHEMISTRY. *SCIENCE* (1979). 1976;193(4247):17–24.

- [23]. SCHÄFERLING M. CHIRAL NANOPHOTONICS–CHIRAL OPTICAL PROPERTIES OF PHASMONIC SYSTEMS. SPRINGER SERIES IN OPTICAL SCIENCES. 205.
- [24]. WAINER I. DRUG STEREOCHEMISTRY: ANALYTICAL METHODS AND PHARMACOLOGY. VOL. 18. CRC PRESS; 1993.
- [25]. CALDWELL J. DO SINGLE ENANTIOMERS HAVE SOMETHING SPECIAL TO OFFER? HUMAN PSYCHOPHARMACOLOGY: CLINICAL AND EXPERIMENTAL. 2001;16(S2):S67–71.
- [26]. RIEHL JP. MIRROR-IMAGE ASYMMETRY: AN INTRODUCTION TO THE ORIGIN AND CONSEQUENCES OF CHIRALITY. JOHN WILEY & SONS; 2010.
- [27]. BREWSTER JH. THE DISTINCTION OF DIASTEREOMERS IN THE CAHN-INGOLD-PRELOG (RS) NOTATION. J ORG CHEM. 1986;51(25):4751–3.
- [28]. WILLIAMS K, LEE E. IMPORTANCE OF DRUG ENANTIOMERS IN CLINICAL PHARMACOLOGY. DRUGS. 1985;30:333–54.
- [29]. PLUM E, LIU XX, FEDOTOV VA, CHEN Y, TSAI DP, ZHELUDEV NI. METAMATERIALS: OPTICAL ACTIVITY WITHOUT CHIRALITY. PHYS REV LETT. 2009;102(11):113902.
- [30]. BARRON LD. MOLECULAR LIGHT SCATTERING AND OPTICAL ACTIVITY. CAMBRIDGE UNIVERSITY PRESS; 2009.
- [31]. SLINEY DH. WHAT IS LIGHT? THE VISIBLE SPECTRUM AND BEYOND. EYE. 2016;30(2):222–9.
- [32]. MCCALL MW, HODGKINSON IJ, WU Q. BIREFRINGENT THIN FILMS AND POLARIZING ELEMENTS. WORLD SCIENTIFIC; 2014.
- [33]. YANG JT. OPTICAL ROTATORY DISPERSION OF POLYPEPTIDES AND PROTEINS. TETRAHEDRON. 1961;13(1–3):143–65.
- [34]. WOODY RW. [4] CIRCULAR DICHROISM. METHODS ENZYMOL. 1995;246:34–71.
- [35]. RANJBAR B, GILL P. CIRCULAR DICHROISM TECHNIQUES: BIOMOLECULAR AND NANOSTRUCTURAL ANALYSES-A REVIEW. CHEM BIOL DRUG DES. 2009;74(2):101–20.
- [36]. BEROVA N, NAKANISHI K, WOODY RW. CIRCULAR DICHROISM: PRINCIPLES AND APPLICATIONS. JOHN WILEY & SONS; 2000.
- [37]. LOWRY TM. THE COTTON EFFECT. NATURE PUBLISHING GROUP UK LONDON; 1933.
- [38]. LUCARINI V, SAARINEN JJ, PEIPONEN KE, VARTIAINEN EM. KRAMERS-KRONIG RELATIONS IN OPTICAL MATERIALS RESEARCH. VOL. 110. SPRINGER SCIENCE & BUSINESS MEDIA; 2005.
- [39]. POLAVARAPU PL. KRAMERS–KRONIG TRANSFORMATION FOR OPTICAL ROTATORY DISPERSION STUDIES. J PHYS CHEM A. 2005;109(32):7013–23.
- [40]. GILROY C, HASHIYADA S, ENDO K, KARIMULLAH AS, BARRON LD, OKAMOTO H, ET AL. ROLES OF SUPERCHIRALITY AND INTERFERENCE IN CHIRAL PLASMONIC BIODETECTION. THE JOURNAL OF PHYSICAL CHEMISTRY C. 2019;123(24):15195–203.
- [41]. GREENFIELD JL, WADE J, BRANDT JR, SHI X, PENFOLD TJ, FUCHTER MJ. PATHWAYS TO INCREASE THE DISSYMMETRY IN THE INTERACTION OF CHIRAL LIGHT AND CHIRAL MOLECULES. CHEM SCI. 2021;12(25):8589–602.
- [42]. LIPKIN DM. EXISTENCE OF A NEW CONSERVATION LAW IN ELECTROMAGNETIC THEORY. J MATH PHYS. 1964;5(5):696–700.
- [43]. VÁZQUEZ-LOZANO JE, MARTÍNEZ A. OPTICAL CHIRALITY IN DISPERSIVE AND LOSSY MEDIA. PHYS REV LETT. 2018;121(4):043901.

- [44]. TANG Y, COHEN AE. ENHANCED ENANTIOSELECTIVITY IN EXCITATION OF CHIRAL MOLECULES BY SUPERCHIRAL LIGHT. *SCIENCE* (1979). 2011;332(6027):333–6.
- [45]. DAVIS TJ, HENDRY E. SUPERCHIRAL ELECTROMAGNETIC FIELDS CREATED BY SURFACE PLASMONS IN NONCHIRAL METALLIC NANOSTRUCTURES. *PHYSICAL REVIEW B—CONDENSED MATTER AND MATERIALS PHYSICS*. 2013;87(8):085405.
- [46]. BABICHEVA VE. OPTICAL PROCESSES BEHIND PLASMONIC APPLICATIONS. *NANOMATERIALS*. 2023;13(7):1270.
- [47]. MARADUDIN AA, SAMBLES JR, BARNES WL. *MODERN PLASMONICS*. ELSEVIER; 2014.
- [48]. KREIBIG U, VOLLMER M. *OPTICAL PROPERTIES OF METAL CLUSTERS*. VOL. 25. SPRINGER SCIENCE & BUSINESS MEDIA; 2013.
- [49]. JAIN PK, EL-SAYED MA. PLASMONIC COUPLING IN NOBLE METAL NANOSTRUCTURES. *CHEM PHYS LETT*. 2010;487(4–6):153–64.
- [50]. SOLIS DM, TABOADA J, LANDESA L, RODRIGUEZ JL, OBELLEIRO F. SQUEEZING MAXWELL’S EQUATIONS INTO THE NANOSCALE. *PROGRESS IN ELECTROMAGNETICS RESEARCH*. 2015;154:35–50.
- [51]. MAIER SA. *PLASMONICS: FUNDAMENTALS AND APPLICATIONS*. VOL. 1. SPRINGER; 2007.
- [52]. KOLWAS K, DERKACHOVA A. IMPACT OF THE INTERBAND TRANSITIONS IN GOLD AND SILVER ON THE DYNAMICS OF PROPAGATING AND LOCALIZED SURFACE PLASMONS. *NANOMATERIALS*. 2020;10(7):1411.
- [53]. JOHNSON PB, CHRISTY RWJP. OPTICAL CONSTANTS OF THE NOBLE METALS. *PHYS REV B*. 1972;6(12):4370.
- [54]. NOVOTNY L, HECHT B. *PRINCIPLES OF NANO-OPTICS*. CAMBRIDGE UNIVERSITY PRESS; 2012.
- [55]. FRYDENDAHL C. THESIS: EXPERIMENTAL EXPLORATION OF GOLD SEMI-CONTINUOUS FILMS IN THE NEAR-AND FAR-FIELD. ARXIV PREPRINT ARXIV:1906.01375. 2019 JUN 4.
- [56]. ZHANG J, ZHANG L, XU W. SURFACE PLASMON POLARITONS: PHYSICS AND APPLICATIONS. *J PHYS D APPL PHYS*. 2012;45(11):113001.
- [57]. LI L. *MANIPULATION OF NEAR FIELD PROPAGATION AND FAR FIELD RADIATION OF SURFACE PLASMON POLARITON*. SPRINGER; 2017.
- [58]. HOMOLA J, YEE SS, GAUGLITZ G. SURFACE PLASMON RESONANCE SENSORS. *SENS ACTUATORS B CHEM*. 1999;54(1–2):3–15.
- [59]. WILLETS KA, VAN DUYN RP. LOCALIZED SURFACE PLASMON RESONANCE SPECTROSCOPY AND SENSING. *ANNU REV PHYS CHEM*. 2007;58(1):267–97.
- [60]. KLEINMAN SL, SHARMA B, BLABER MG, HENRY AI, VALLEY N, FREEMAN RG, ET AL. STRUCTURE ENHANCEMENT FACTOR RELATIONSHIPS IN SINGLE GOLD NANOANTENNAS BY SURFACE-ENHANCED RAMAN EXCITATION SPECTROSCOPY. *J AM CHEM SOC*. 2013;135(1):301–8.
- [61]. MIE G. BEITRÄGE ZUR OPTIK TRÜBER MEDIEN, SPEZIELL KOLLOIDALER METALLLÖSUNGEN. *ANN PHYS*. 1908;330(3):377–445.
- [62]. RIVERA VAG, FERRI FA, MAREGA JR E. LOCALIZED SURFACE PLASMON RESONANCES: NOBLE METAL NANOPARTICLE INTERACTION WITH RARE-EARTH IONS. *PLASMONICS-PRINCIPLES AND APPLICATIONS*. 2012;1(11):283–312.
- [63]. BOHREN CF, HUFFMAN DR. *ABSORPTION AND SCATTERING OF LIGHT BY SMALL PARTICLES*. JOHN WILEY & SONS; 2008.
- [64]. GERSTEN JI, NITZAN A. PHOTOPHYSICS AND PHOTOCHEMISTRY NEAR SURFACES AND SMALL PARTICLES. *SURF SCI*. 1985;158(1–3):165–89.



- [65]. PRODAN E, RADLOFF C, HALAS NJ, NORDLANDER P. A HYBRIDIZATION MODEL FOR THE PLASMON RESPONSE OF COMPLEX NANOSTRUCTURES. *SCIENCE (1979)*. 2003;302(5644):419–22.
- [66]. SCHÄFERLING M. *CHIRAL NANOPHOTONICS*. SPRINGER SERIES IN OPTICAL SCIENCES. 2017;205:159.
- [67]. PARK W. OPTICAL INTERACTIONS IN PLASMONIC NANOSTRUCTURES. *NANO CONVERG*. 2014;1:1–27.
- [68]. HALL WP, MODICA J, ANKER J, LIN Y, MRKSICH M, VAN DUYN RP. A CONFORMATION-AND ION-SENSITIVE PLASMONIC BIOSENSOR. *NANO LETT*. 2011;11(3):1098–105.
- [69]. HALL WP, ANKER JN, LIN Y, MODICA J, MRKSICH M, VAN DUYN RP. A CALCIUM-MODULATED PLASMONIC SWITCH. *J AM CHEM SOC*. 2008;130(18):5836–7.
- [70]. BAFFOU G, CICHOS F, QUIDANT R. APPLICATIONS AND CHALLENGES OF THERMOPLASMONICS. *NAT MATER*. 2020;19(9):946–58.
- [71]. HUTTMANN G, BIRNGRUBER R. ON THE POSSIBILITY OF HIGH-PRECISION PHOTOTHERMAL MICROEFFECTS AND THE MEASUREMENT OF FAST THERMAL DENATURATION OF PROTEINS. *IEEE JOURNAL OF SELECTED TOPICS IN QUANTUM ELECTRONICS*. 1999;5(4):954–62.
- [72]. BOYER D, TAMARAT P, MAALI A, LOUNIS B, ORRIT M. PHOTOTHERMAL IMAGING OF NANOMETER-SIZED METAL PARTICLES AMONG SCATTERERS. *SCIENCE (1979)*. 2002;297(5584):1160–3.
- [73]. HIRSCH LR, STAFFORD RJ, BANKSON JA, SERSHEN SR, RIVERA B, PRICE RE, ET AL. NANOSHELL-MEDIATED NEAR-INFRARED THERMAL THERAPY OF TUMORS UNDER MAGNETIC RESONANCE GUIDANCE. *PROCEEDINGS OF THE NATIONAL ACADEMY OF SCIENCES*. 2003;100(23):13549–54.
- [74]. CAO L, BARSIC DN, GUICHARD AR, BRONGERSMA ML. PLASMON-ASSISTED LOCAL TEMPERATURE CONTROL TO PATTERN INDIVIDUAL SEMICONDUCTOR NANOWIRES AND CARBON NANOTUBES. *NANO LETT*. 2007;7(11):3523–7.
- [75]. ZHOU Z, SAKR E, SUN Y, BERMEL P. SOLAR THERMOPHOTOVOLTAICS: RESHAPING THE SOLAR SPECTRUM. *NANOPHOTONICS*. 2016;5(1):1–21.
- [76]. BAFFOU G, GIRARD C, QUIDANT R. MAPPING HEAT ORIGIN IN PLASMONIC STRUCTURES. *PHYS REV LETT*. 2010;104(13):136805.
- [77]. BAFFOU G, QUIDANT R. THERMO-PLASMONICS: USING METALLIC NANOSTRUCTURES AS NANO-SOURCES OF HEAT. *LASER PHOTON REV*. 2013;7(2):171–87.
- [78]. BAFFOU GT. *HEATING METAL NANOPARTICLES USING LIGHT*. CAMBRIDGE UNIVERSITY PRESS; 2017.
- [79]. BRONGERSMA ML, HALAS NJ, NORDLANDER P. PLASMON-INDUCED HOT CARRIER SCIENCE AND TECHNOLOGY. *NAT NANOTECHNOL*. 2015;10(1):25–34.
- [80]. YANG B, LI C, WANG Z, DAI Q. THERMOPLASMONICS IN SOLAR ENERGY CONVERSION: MATERIALS, NANOSTRUCTURED DESIGNS, AND APPLICATIONS. *ADV. MATER*. 2022;34(26):2107351.
- [81]. BAFFOU G, BERTO P, BERMÚDEZ UREÑA E, QUIDANT R, MONNERET S, POLLEUX J, ET AL. PHOTOINDUCED HEATING OF NANOPARTICLE ARRAYS. *ACS NANO*. 2013;7(8):6478–88.
- [82]. KIM M, LEE J, NAM J. PLASMONIC PHOTOTHERMAL NANOPARTICLES FOR BIOMEDICAL APPLICATIONS. *ADVANCED SCIENCE*. 2019;6(17):1900471.
- [83]. MANJAVACAS A, LIU JG, KULKARNI V, NORDLANDER P. PLASMON-INDUCED HOT CARRIERS IN METALLIC NANOPARTICLES. *ACS NANO*. 2014;8(8):7630–8.
- [84]. VESELAGO VG. THE ELECTRODYNAMICS OF SUBSTANCES WITH SIMULTANEOUSLY NEGATIVE VALUES OF  $\epsilon$  AND  $\mu$ . *USP FIZ NAUK*. 1967;92(3):517–26.
- [85]. CUI TJ, SMITH DR, LIU R. *METAMATERIALS*. SPRINGER; 2010.

- [86]. PENDRY JB, HOLDEN AJ, STEWART WJ, YOUNGS I. EXTREMELY LOW FREQUENCY PLASMONS IN METALLIC MESOSTRUCTURES. *PHYS REV LETT*. 1996;76(25):4773.
- [87]. PENDRY JB, HOLDEN AJ, ROBBINS DJ, STEWART WJ. MAGNETISM FROM CONDUCTORS AND ENHANCED NONLINEAR PHENOMENA. *IEEE TRANS MICROW THEORY TECH*. 1999;47(11):2075–84.
- [88]. SMITH DR, PADILLA WJ, VIER DC, NEMAT-NASSER SC, SCHULTZ S. COMPOSITE MEDIUM WITH SIMULTANEOUSLY NEGATIVE PERMEABILITY AND PERMITTIVITY. *PHYS REV LETT*. 2000;84(18):4184.
- [89]. PRINZ VY. ELECTROMAGNETIC "MAGIC" OF SUPERMATERIALS. *SCIENCE FIRST HAND*. 2012;(3):24–7.
- [90]. PENDRY JB. NEGATIVE REFRACTION MAKES A PERFECT LENS. *PHYS REV LETT*. 2000;85(18):3966.
- [91]. WOOD B. METAMATERIALS AND INVISIBILITY. *C R PHYS*. 2009;10(5):379–90.
- [92]. SCHURIG D, MOCK JJ, JUSTICE BJ, CUMMER SA, PENDRY JB, STARR AF, ET AL. METAMATERIAL ELECTROMAGNETIC CLOAK AT MICROWAVE FREQUENCIES. *SCIENCE (1979)*. 2006;314(5801):977–80.
- [93]. CAI W, SHALAEV V. OPTICAL METAMATERIALS. FUNDAMENTALS AND. 2010;
- [94]. COLLINS JT, KUPPE C, HOOPER DC, SIBILIA C, CENTINI M, VALEV VK. CHIRALITY AND CHIROPTICAL EFFECTS IN METAL NANOSTRUCTURES: FUNDAMENTALS AND CURRENT TRENDS. *ADV OPT MATER*. 2017;5(16):1700182.
- [95]. GANSEL JK, THIEL M, RILL MS, DECKER M, BADE K, SAILE V, ET AL. GOLD HELIX PHOTONIC METAMATERIAL AS BROADBAND CIRCULAR POLARIZER. *SCIENCE (1979)*. 2009;325(5947):1513–5.
- [96]. WU Z, ZHENG Y. MOIRÉ CHIRAL METAMATERIALS. *ADV OPT MATER*. 2017;5(16):1700034.
- [97]. ABDULRAHMAN NA, FAN Z, TONOOKA T, KELLY SM, GADEGAARD N, HENDRY E, ET AL. INDUCED CHIRALITY THROUGH ELECTROMAGNETIC COUPLING BETWEEN CHIRAL MOLECULAR LAYERS AND PLASMONIC NANOSTRUCTURES. *NANO LETT*. 2012;12(2):977–83.
- [98]. ZHAO Y, ASKARPOUR AN, SUN L, SHI J, LI X, ALÙ A. CHIRALITY DETECTION OF ENANTIOMERS USING TWISTED OPTICAL METAMATERIALS. *NAT COMMUN*. 2017;8(1):14180.
- [99]. LIN D, HUANG JS. SLANT-GAP PLASMONIC NANOANTENNAS FOR OPTICAL CHIRALITY ENGINEERING AND CIRCULAR DICHROISM ENHANCEMENT. *OPT EXPRESS*. 2014;22(7):7434–45.
- [100]. GRAF F, FEIS J, GARCIA-SANTIAGO X, WEGENER M, ROCKSTUHL C, FERNANDEZ-CORBATON I. ACHIRAL, HELICITY PRESERVING, AND RESONANT STRUCTURES FOR ENHANCED SENSING OF CHIRAL MOLECULES. *ACS PHOTONICS*. 2019;6(2):482–91.
- [101]. MA W, XU L, WANG L, XU C, KUANG H. CHIRALITY-BASED BIOSENSORS. *ADV FUNCT MATER*. 2019;29(1):1805512.
- [102]. BOCHENKOV VE, SHABATINA TI. CHIRAL PLASMONIC BIOSENSORS. *BIOSENSORS (BASEL)*. 2018;8(4):120.
- [103]. SCHÄFERLING M, YIN X, GIessen H. FORMATION OF CHIRAL FIELDS IN A SYMMETRIC ENVIRONMENT. *OPT EXPRESS*. 2012;20(24):26326–36.
- [104]. KERN W. THE EVOLUTION OF SILICON WAFER CLEANING TECHNOLOGY. *J ELECTROCHEM SOC*. 1990;137(6):1887.
- [105]. BUSNAINA AA, KASHKOUSH II, GALE GW. AN EXPERIMENTAL STUDY OF MEGASONIC CLEANING OF SILICON WAFERS. *J ELECTROCHEM SOC*. 1995;142(8):2812.
- [106]. HABUKA H, FUKUMOTO R, OKADA Y, KATO M. DOMINANT FORCES FOR DRIVING BUBBLES IN A WET CLEANING BATH USING MEGASONIC WAVE. *J ELECTROCHEM SOC*. 2010;157(6):H585.
- [107]. STROBEL M, LYONS CS, MITTAL KL. PLASMA SURFACE MODIFICATION OF POLYMERS: RELEVANCE TO ADHESION. 1994;

- [108]. BELKIND A, GERSHMAN S. PLASMA CLEANING OF SURFACES. VACUUM COATING AND TECHNOLOGY NOVEMBER. 2008;46-57.
- [109]. YANG XM, ZHONG ZW, DIALLO EM, WANG ZH, YUE WS. SILICON WAFER WETTABILITY AND AGING BEHAVIORS: IMPACT ON GOLD THIN-FILM MORPHOLOGY. MATER SCI SEMICOND PROCESS. 2014;26:25-32.
- [110]. SUNI T, HENTTINEN K, SUNI I, MÄKINEN J. EFFECTS OF PLASMA ACTIVATION ON HYDROPHILIC BONDING OF Si AND SiO<sub>2</sub>. J ELECTROCHEM SOC. 2002;149(6):G348.
- [111]. BHUSHAN B. ENCYCLOPEDIA OF NANOTECHNOLOGY. SPRINGER DORDRECHT, THE NETHERLANDS;; 2012.
- [112]. CARBAUGH DJ, WRIGHT JT, PARTHIBAN R, RAHMAN F. PHOTOLITHOGRAPHY WITH POLYMETHYL METHACRYLATE (PMMA). SEMICOND SCI TECHNOL. 2015;31(2):025010.
- [113]. CHEN Y. NANOFABRICATION BY ELECTRON BEAM LITHOGRAPHY AND ITS APPLICATIONS: A REVIEW. MICROELECTRON ENG. 2015;135:57-72.
- [114]. STEPANOVA M, DEW S. NANOFABRICATION: TECHNIQUES AND PRINCIPLES. SPRINGER SCIENCE & BUSINESS MEDIA; 2011.
- [115]. ARAT KT, KLIMPEL T, ZONNEVYLLE AC, KETELAARS WSMM, HEERKENS CTH, HAGEN CW. CHARGE-INDUCED PATTERN DISPLACEMENT IN E-BEAM LITHOGRAPHY. JOURNAL OF VACUUM SCIENCE & TECHNOLOGY B. 2019;37(5).
- [116]. PRAKASH S, YEOM J. NANOFUIDICS AND MICROFLUIDICS: SYSTEMS AND APPLICATIONS. WILLIAM ANDREW; 2014.
- [117]. FELDMAN M. NANOLITHOGRAPHY: THE ART OF FABRICATING NANOELECTRONIC AND NANOPHOTONIC DEVICES AND SYSTEMS. WOODHEAD PUBLISHING; 2014.
- [118]. CHOI JO, MOORE JA, CORELLI JC, SILVERMAN JP, BAKHRU H. DEGRADATION OF POLY (METHYLMETHACRYLATE) BY DEEP ULTRAVIOLET, X-RAY, ELECTRON BEAM, AND PROTON BEAM IRRADIATIONS. JOURNAL OF VACUUM SCIENCE & TECHNOLOGY B: MICROELECTRONICS PROCESSING AND PHENOMENA. 1988;6(6):2286-9.
- [119]. LEHOCKEY EM, REID I, HILL I. THE RADIATION CHEMISTRY OF POLY (METHYL METHACRYLATE) POLYMER RESISTS. JOURNAL OF VACUUM SCIENCE & TECHNOLOGY A: VACUUM, SURFACES, AND FILMS. 1988;6(4):2221-5.
- [120]. GREENEICH JS. DEVELOPER CHARACTERISTICS OF POLY-(METHYL METHACRYLATE) ELECTRON RESIST. J ELECTROCHEM SOC. 1975;122(7):970.
- [121]. GONZÁLEZ-BENITO J, KOENIG JL. NATURE OF PMMA DISSOLUTION PROCESS BY MIXTURES OF ACETONITRILE/ALCOHOL (POOR SOLVENT/NONSOLVENT) MONITORED BY FTIR-IMAGING. POLYMER (GUILDF). 2006;47(9):3065-72.
- [122]. ALI MOHAMMAD M, POULOSE SANTO K, DEW SK, STEPANOVA M. STUDY OF THE INTERACTION OF POLYMETHYLMETHACRYLATE FRAGMENTS WITH METHYL ISOBUTYL KETONE AND ISOPROPYL ALCOHOL. JOURNAL OF VACUUM SCIENCE & TECHNOLOGY B. 2012;30(6).
- [123]. ROOKS MJ, KRATSCHEMER E, VISWANATHAN R, KATINE J, FONTANA JR RE, MACDONALD SA. LOW STRESS DEVELOPMENT OF POLY (METHYLMETHACRYLATE) FOR HIGH ASPECT RATIO STRUCTURES. JOURNAL OF VACUUM SCIENCE & TECHNOLOGY B: MICROELECTRONICS AND NANOMETER STRUCTURES PROCESSING, MEASUREMENT, AND PHENOMENA. 2002;20(6):2937-41.
- [124]. GILMOUR S, KERSHAW S V, PETHRICK RA, PANTELIS P, CASSIDY S, SHERWOOD JN. DEVELOPMENT OF LITHOGRAPHIC TECHNIQUES FOR METALLISATION OF ORGANIC SUBSTRATES. ADV. MATER. FOR OPTICS AND ELECTRONICS. 1992;1(4):197-201.
- [125]. GOLDEN J, MILLER H, NAWROCKI D, ROSS J. OPTIMIZATION OF BI-LAYER LIFT-OFF RESIST PROCESS. CS MANTECH TECHNICAL DIGEST. 2009;

- [126]. KAKKAR T, KEIJZER C, RODIER M, BUKHAROVA T, TALIANSKY M, LOVE AJ, ET AL. SUPERCHIRAL NEAR FIELDS DETECT VIRUS STRUCTURE. *LIGHT SCI APPL*. 2020;9(1):195.
- [127]. FISA B, FAVIS BD, BOURGEOIS S. INJECTION MOLDING OF POLYPROPYLENE/POLYCARBONATE BLENDS. *POLYM ENG SCI*. 1990;30(17):1051–5.
- [128]. VOIGTLÄNDER B. SCANNING PROBE MICROSCOPY: ATOMIC FORCE MICROSCOPY AND SCANNING TUNNELING MICROSCOPY. SPRINGER; 2015.
- [129]. GAN Y. ATOMIC AND SUBNANOMETER RESOLUTION IN AMBIENT CONDITIONS BY ATOMIC FORCE MICROSCOPY. *SURF SCI REP*. 2009;64(3):99–121.
- [130]. SHEN J, ZHANG D, ZHANG FH, GAN Y. AFM TIP-SAMPLE CONVOLUTION EFFECTS FOR CYLINDER PROTRUSIONS. *APPL SURF SCI*. 2017;422:482–91.
- [131]. ZHOU W, APKARIAN R, WANG ZL, JOY D. FUNDAMENTALS OF SCANNING ELECTRON MICROSCOPY (SEM). SCANNING MICROSCOPY FOR NANOTECHNOLOGY: TECHNIQUES AND APPLICATIONS. 2007;1–40.
- [132]. CARTER CB, WILLIAMS DB. TRANSMISSION ELECTRON MICROSCOPY: DIFFRACTION, IMAGING, AND SPECTROMETRY. SPRINGER; 2016.
- [133]. KANNAN M. SCANNING ELECTRON MICROSCOPY: PRINCIPLE, COMPONENTS AND APPLICATIONS. A TEXTBOOK ON FUNDAMENTALS AND APPLICATIONS OF NANOTECHNOLOGY. 2018;81–92.
- [134]. GOLDSTEIN JI. SCANNING ELECTRON AND X-RAY MICROANALYSIS. A TEXT FOR BIOLOGISTS, MATERIALS SCIENTISTS, AND GEOLOGISTS. 1992;395–416.
- [135]. THEETEN JB, ASPNES DE. ELLIPSOMETRY IN THIN FILM ANALYSIS. *ANNUAL REVIEW OF MATERIALS SCIENCE*. 1981;11(1):97–122.
- [136]. TOMPKINS H, IRENE EA. HANDBOOK OF ELLIPSOMETRY. WILLIAM ANDREW; 2005.
- [137]. TOMPKINS HG. A USER'S GUIDE TO ELLIPSOMETRY. COURIER CORPORATION; 2006.
- [138]. COLLETT E. FIELD GUIDE TO POLARIZATION. IN SPIE BELLINGHAM, WA; 2005.
- [139]. TABOUILLOT V, KUMAR R, LALAGUNA PL, HAJJI M, CLARKE R, KARIMULLAH AS, ET AL. NEAR-FIELD PROBING OF OPTICAL SUPERCHIRALITY WITH PLASMONIC CIRCULARLY POLARIZED LUMINESCENCE FOR ENHANCED BIO-DETECTION. *ACS PHOTONICS*. 2022;9(11):3617–24.
- [140]. RAHMAN BMA, AGRAWAL A. FINITE ELEMENT MODELING METHODS FOR PHOTONICS. ARTECH HOUSE; 2013.
- [141]. RAO SS. THE FINITE ELEMENT METHOD IN ENGINEERING. BUTTERWORTH-HEINEMANN; 2017.
- [142]. COMSOL AB. WAVE OPTICS MODULE USER'S GUIDE, COMSOL MULTIPHYSICS® v. 5.3 A. STOCKHOLM, SWEDEN. 2017;38–46.
- [143]. BASSIRI S, PAPAS CH, ENGHETA N. ELECTROMAGNETIC WAVE PROPAGATION THROUGH A DIELECTRIC-CHIRAL INTERFACE AND THROUGH A CHIRAL SLAB. *JOSA A*. 1988;5(9):1450–9.
- [144]. WANG B, ZHOU J, KOSCHNY T, KAFESAKI M, SOUKOULIS CM. CHIRAL METAMATERIALS: SIMULATIONS AND EXPERIMENTS. *JOURNAL OF OPTICS A: PURE AND APPLIED OPTICS*. 2009;11(11):114003.
- [145]. GOVOROV AO, FAN Z. THEORY OF CHIRAL PLASMONIC NANOSTRUCTURES COMPRISING METAL NANOCRYSTALS AND CHIRAL MOLECULAR MEDIA. *CHEMPHYSCHEM*. 2012;13(10):2551–60.
- [146]. GOVOROV AO. PLASMON-INDUCED CIRCULAR DICHROISM OF A CHIRAL MOLECULE IN THE VICINITY OF METAL NANOCRYSTALS. APPLICATION TO VARIOUS GEOMETRIES. *THE JOURNAL OF PHYSICAL CHEMISTRY C*. 2011;115(16):7914–23.
- [147]. SCHELLMAN JA. CIRCULAR DICHROISM AND OPTICAL ROTATION. *CHEM REV*. 1975;75(3):323–31.

- [148]. PRYOR RW. MULTIPHYSICS MODELING USING COMSOL®: A FIRST PRINCIPLES APPROACH. JONES & BARTLETT PUBLISHERS; 2009.
- [149]. COMSOL AB. HEAT TRANSFER MODULE USER'S GUIDE COMSOL. INC, BURLINGTON, MA. 2006;
- [150]. VAJDI M, MOGHANLOU FS, SHARIFIANJAZI F, ASL MS, SHOKOUHIMEHR M. A REVIEW ON THE COMSOL MULTIPHYSICS STUDIES OF HEAT TRANSFER IN ADVANCED CERAMICS. JOURNAL OF COMPOSITES AND COMPOUNDS. 2020;2(2):35–43.
- [151]. GOVOROV AO, RICHARDSON HH. GENERATING HEAT WITH METAL NANOPARTICLES. NANO TODAY. 2007;2(1):30–8.
- [152]. BV C, OY C. COMSOL MULTIPHYSICS USER'S GUIDE© COPYRIGHT 1998–2010 COMSOL AB. 1998;
- [153]. FAISAL FHM, KAMIŃSKI JZ. FLOQUET-BLOCH THEORY OF HIGH-HARMONIC GENERATION IN PERIODIC STRUCTURES. PHYS REV A (COLL PARK). 1997;56(1):748.
- [154]. CHANG H, RHO WY, SON BS, KIM J, LEE SH, JEONG DH, ET AL. PLASMONIC NANOPARTICLES: BASICS TO APPLICATIONS (I). NANOTECHNOLOGY FOR BIOAPPLICATIONS. 2021;133–59.
- [155]. SINGH M, HAVERINEN HM, DHAGAT P, JABBOUR GE. INKJET PRINTING—PROCESS AND ITS APPLICATIONS. ADV. MATER. 2010;22(6):673–85.
- [156]. LIU G, PETROSKO SH, ZHENG Z, MIRKIN CA. EVOLUTION OF DIP-PEN NANOLITHOGRAPHY (DPN): FROM MOLECULAR PATTERNING TO MATERIALS DISCOVERY. CHEM REV. 2020;120(13):6009–47.
- [157]. LASAGNI AF, GACHOT C, TRINH KE, HANS M, ROSENKRANZ A, ROCH T, ET AL. DIRECT LASER INTERFERENCE PATTERNING, 20 YEARS OF DEVELOPMENT: FROM THE BASICS TO INDUSTRIAL APPLICATIONS. IN: LASER-BASED MICRO-AND NANOPROCESSING XI. SPIE; 2017. P. 186–96.
- [158]. WANG Q, ZHANG G, ZHANG H, DUAN Y, YIN Z, HUANG Y. HIGH-RESOLUTION, FLEXIBLE, AND FULL-COLOR PEROVSKITE IMAGE PHOTODETECTOR VIA ELECTROHYDRODYNAMIC PRINTING OF IONIC-LIQUID-BASED INK. ADV FUNCT MATER. 2021;31(28):2100857.
- [159]. MONDAL K, McMURTREY MD. PRESENT STATUS OF THE FUNCTIONAL ADVANCED MICRO-, NANO-PRINTINGS—A MINI REVIEW. MATER TODAY CHEM. 2020;17:100328.
- [160]. SALAITA K, WANG Y, MIRKIN CA. APPLICATIONS OF DIP-PEN NANOLITHOGRAPHY. NAT NANOTECHNOL. 2007;2(3):145–55.
- [161]. SERRA P, PIQUÉ A. LASER-INDUCED FORWARD TRANSFER: FUNDAMENTALS AND APPLICATIONS. ADV MATER TECHNOL. 2019;4(1):1800099.
- [162]. JACK C, KARIMULLAH AS, TULLIUS R, KHORASHAD LK, RODIER M, FITZPATRICK B, ET AL. SPATIAL CONTROL OF CHEMICAL PROCESSES ON NANOSTRUCTURES THROUGH NANO-LOCALIZED WATER HEATING. NAT COMMUN. 2016;7(1):10946.
- [163]. OU W, ZHOU B, SHEN J, ZHAO C, LI YY, LU J. PLASMONIC METAL NANOSTRUCTURES: CONCEPTS, CHALLENGES AND OPPORTUNITIES IN PHOTO-MEDIATED CHEMICAL TRANSFORMATIONS. ISCIENCE. 2021 FEB 19;24(2).
- [164]. FLEMMING P, MÜNCH AS, FERY A, UHLMANN P. CONSTRAINED THERMORESPONSIVE POLYMERS—NEW INSIGHTS INTO FUNDAMENTALS AND APPLICATIONS. BEILSTEIN J. ORG. CHEM. 2021;17(1):2123–63.
- [165]. YANG L, FAN X, ZHANG J, JU J. PREPARATION AND CHARACTERIZATION OF THERMORESPONSIVE POLY (N-ISOPROPYLACRYLAMIDE) FOR CELL CULTURE APPLICATIONS. POLYMERS (BASEL). 2020;12(2):389.
- [166]. LIU L, PENG P, HU A, ZOU G, DULEY WW, ZHOU YN. HIGHLY LOCALIZED HEAT GENERATION BY FEMTOSECOND LASER INDUCED PLASMON EXCITATION IN AG NANOWIRES. APPL PHYS LETT. 2013;102(7).
- [167]. JAUFFRED L, SAMADI A, KLINGBERG H, BENDIX PM, ODDERSHEDE LB. PLASMONIC HEATING OF NANOSTRUCTURES. CHEM REV. 2019;119(13):8087–130.

- [168]. CHEN X, CHEN Y, YAN M, QIU M. NANOSECOND PHOTOTHERMAL EFFECTS IN PLASMONIC NANOSTRUCTURES. *ACS NANO*. 2012;6(3):2550–7.
- [169]. CHEN G, HUI P. THERMAL CONDUCTIVITIES OF EVAPORATED GOLD FILMS ON SILICON AND GLASS. *APPL PHYS LETT*. 1999;74(20):2942–4.
- [170]. QIU TQ, TIEN CL. SHORT-PULSE LASER HEATING ON METALS. *INT J HEAT MASS TRANSF*. 1992;35(3):719–26.
- [171]. ZHANG Q, WEBER C, SCHUBERT US, HOOGENBOOM R. THERMORESPONSIVE POLYMERS WITH LOWER CRITICAL SOLUTION TEMPERATURE: FROM FUNDAMENTAL ASPECTS AND MEASURING TECHNIQUES TO RECOMMENDED TURBIDIMETRY CONDITIONS. *MATER HORIZ*. 2017;4(2):109–16.
- [172]. NASSERI R, DEUTSCHMAN CP, HAN L, POPE MA, TAM KC. CELLULOSE NANOCRYSTALS IN SMART AND STIMULI-RESPONSIVE MATERIALS: A REVIEW. *MATER TODAY ADV*. 2020;5:100055.
- [173]. DAI S, RAVI P, TAM KC. THERMO-AND PHOTO-RESPONSIVE POLYMERIC SYSTEMS. *SOFT MATTER*. 2009;5(13):2513–33.
- [174]. HOFFMAN AS. “INTELLIGENT” POLYMERS IN MEDICINE AND BIOTECHNOLOGY. *ARTIF ORGANS*. 1995;19(5):458–67.
- [175]. LIU MS, TAYLOR C, CHONG B, LIU L, BILIC A, TEREFE NS, ET AL. CONFORMATIONAL TRANSITIONS AND DYNAMICS OF THERMAL RESPONSIVE POLY (N-ISOPROPYLACRYLAMIDE) POLYMERS AS REVEALED BY MOLECULAR SIMULATION. *EUR POLYM J*. 2014;55:153–9.
- [176]. HAN F, SOERİYADI AH, VIVEKCHAND SRC, GOODING JJ. SIMPLE METHOD FOR TUNING THE OPTICAL PROPERTIES OF THERMORESPONSIVE PLASMONIC NANOGELS. *ACS MACRO LETT*. 2016;5(5):626–30.
- [177]. YESHCHENKO OA, NAUMENKO AP, KUTSEVOL N V, MASKOVA DO, HARAHUTS II, CHUMACHENKO VA, ET AL. ANOMALOUS INVERSE HYSTERESIS OF PHASE TRANSITION IN THERMOSENSITIVE DEXTRAN-GRAFT-PNIPAM COPOLYMER/AU NANOPARTICLES HYBRID NANOSYSTEM. *THE JOURNAL OF PHYSICAL CHEMISTRY C*. 2018;122(14):8003–10.
- [178]. BAFFOU G, QUIDANT R. THERMOPLASMONICS. IN: *WORLD SCIENTIFIC HANDBOOK OF METAMATERIALS AND PLASMONICS: VOLUME 4: RECENT PROGRESS IN THE FIELD OF NANOPLASMONICS*. WORLD SCIENTIFIC; 2018. p. 379–407.
- [179]. DE SIO L, PLACIDO T, COMPARELLI R, CURRI ML, STRICCOLI M, TABIRYAN N, ET AL. NEXT-GENERATION THERMO-PLASMONIC TECHNOLOGIES AND PLASMONIC NANOPARTICLES IN OPTOELECTRONICS. *PROG QUANTUM ELECTRON*. 2015;41:23–70.
- [180]. KASHYAP RK, DWIVEDI I, ROY S, ROY S, RAO A, SUBRAMANIAM C, ET AL. INSIGHTS INTO THE UTILIZATION AND QUANTIFICATION OF THERMOPLASMONIC PROPERTIES IN GOLD NANOROD ARRAYS. *CHEMISTRY OF MATERIALS*. 2022;34(16):7369–78.
- [181]. HAJJI M, CARIELLO M, GILROY C, KARTAU M, SYME CD, KARIMULLAH A, ET AL. CHIRAL QUANTUM METAMATERIAL FOR HYPERSENSITIVE BIOMOLECULE DETECTION. *ACS NANO*. 2021;15(12):19905–16.
- [182]. SCHILD HG. POLY (N-ISOPROPYLACRYLAMIDE): EXPERIMENT, THEORY AND APPLICATION. *PROG POLYM SCI*. 1992;17(2):163–249.
- [183]. KLOUDA L, MIKOS AG. THERMORESPONSIVE HYDROGELS IN BIOMEDICAL APPLICATIONS. *EUROPEAN JOURNAL OF PHARMACEUTICS AND BIOPHARMACEUTICS*. 2008;68(1):34–45.
- [184]. HEMRAZ UD, LU A, SUNASEE R, BOLUK Y. STRUCTURE OF POLY (N-ISOPROPYLACRYLAMIDE) BRUSHES AND STERIC STABILITY OF THEIR GRAFTED CELLULOSE NANOCRYSTAL DISPERSIONS. *J COLLOID INTERFACE SCI*. 2014;430:157–65.

- [185]. MURPHY S, JABER S, RITCHIE C, KARG M, MULVANEY P. LASER FLASH PHOTOLYSIS OF Au-PNIPAM CORE-SHELL NANOPARTICLES: DYNAMICS OF THE SHELL RESPONSE. *LANGMUIR*. 2016;32(47):12497–503.
- [186]. WEBER PC, OHLENDORF DH, WENDOLOSKI JJ, SALEMME FR. STRUCTURAL ORIGINS OF HIGH-AFFINITY BIOTIN BINDING TO STREPTAVIDIN. *SCIENCE (1979)*. 1989;243(4887):85–8.
- [187]. GRIGORENKO AN, ROBERTS NW, DICKINSON MR, ZHANG Y. NANOMETRIC OPTICAL TWEEZERS BASED ON NANOSTRUCTURED SUBSTRATES. *NAT PHOTONICS*. 2008;2(6):365–70.
- [188]. QUIDANT R, GIRARD C. SURFACE-PLASMON-BASED OPTICAL MANIPULATION. *LASER PHOTON REV*. 2008;2(1-2):47–57.
- [189]. ANKER JN, HALL WP, LYANDRES O, SHAH NC, ZHAO J, VAN DUYN RP. BIOSENSING WITH PLASMONIC NANOSENSORS. *NAT MATER*. 2008;7(6):442–53.
- [190]. HOLMAN JP & BSS. HEAT TRANSFER. MCGRAW-HILL, EDITOR. 2002.
- [191]. SUN T, WANG G, FENG L, LIU B, MA Y, JIANG L, ET AL. REVERSIBLE SWITCHING BETWEEN SUPERHYDROPHILICITY AND SUPERHYDROPHOBICITY. *ANGEWANDTE CHEMIE INTERNATIONAL EDITION*. 2004;43(3):357–60.
- [192]. GARNER BW, CAI T, GHOSH S, HU Z, NEOGI A. REFRACTIVE INDEX CHANGE DUE TO VOLUME-PHASE TRANSITION IN POLYACRYLAMIDE GEL NANOSPHERES FOR OPTOELECTRONICS AND BIO-PHOTONICS. *APPLIED PHYSICS EXPRESS*. 2009;2(5):057001.
- [193]. KURT H, PISHVA P, PEHLIVAN ZS, ARSOY EG, SALEEM Q, BAYAZIT MK, ET AL. NANOPLASMONIC BIOSENSORS: THEORY, STRUCTURE, DESIGN, AND REVIEW OF RECENT APPLICATIONS. *ANAL CHIM ACTA*. 2021;1185:338842.
- [194]. LI B, ZHANG Y, ZOU R, WANG Q, ZHANG B, AN L, ET AL. SELF-ASSEMBLED WO<sub>3</sub>-X HIERARCHICAL NANOSTRUCTURES FOR PHOTOTHERMAL THERAPY WITH A 915 NM LASER RATHER THAN THE COMMON 980 NM LASER. *DALTON TRANSACTIONS*. 2014;43(16):6244–50.
- [195]. DAI M, GUO W, LIU X, ZHANG M, WANG Y, WEI LF, ET AL. MEASUREMENT OF OPTICAL CONSTANTS OF TiN AND TiN/Ti/TiN MULTILAYER FILMS FOR MICROWAVE KINETIC INDUCTANCE PHOTON-NUMBER-RESOLVING DETECTORS. *J Low Temp Phys*. 2019;194:361–9.
- [196]. RAJABPOUR V, ABBASIAN K, ERTUGRUL M. CORE-SHELL PLASMONIC NANOSTRUCTURES FOR HYPERTHERMIA OF CANCER AND TUMOR CELLS. *PLASMONICS*. 2024;1–13.
- [197]. ZHAO Y, HUBAREVICH A, IAROSI M, BORZDA T, TANTUSSI F, HUANG J, ET AL. HYPERBOLIC NANOPARTICLES ON SUBSTRATE WITH SEPARATE OPTICAL SCATTERING AND ABSORPTION RESONANCES: A DUAL FUNCTION PLATFORM FOR SERS AND THERMOPLASMONICS. *ADV OPT MATER*. 2021;9(20):2100888.
- [198]. LEE SG, PASCAL TA, KOH W, BRUNELLO GF, GODDARD III WA, JANG SS. DESWELLING MECHANISMS OF SURFACE-GRAFTED POLY (NIPAAm) BRUSH: MOLECULAR DYNAMICS SIMULATION APPROACH. *THE JOURNAL OF PHYSICAL CHEMISTRY C*. 2012;116(30):15974–85.
- [199]. JIANG K, SMITH DA, PINCHUK A. SIZE-DEPENDENT PHOTOTHERMAL CONVERSION EFFICIENCIES OF PLASMONICALLY HEATED GOLD NANOPARTICLES. *THE JOURNAL OF PHYSICAL CHEMISTRY C*. 2013;117(51):27073–80.
- [200]. MING T, ZHAO L, YANG Z, CHEN H, SUN L, WANG J, ET AL. STRONG POLARIZATION DEPENDENCE OF PLASMON-ENHANCED FLUORESCENCE ON SINGLE GOLD NANORODS. *NANO LETT*. 2009;9(11):3896–903.
- [201]. HAMZA ME, OTHMAN MA, SWILLAM MA. PLASMONIC BIOSENSORS. *BIOLOGY (BASEL)*. 2022;11(5):621.
- [202]. PELTON M, AIZPURUA J, BRYANT G. METAL-NANOPARTICLE PLASMONICS. *LASER PHOTON REV*. 2008;2(3):136–59.
- [203]. LAKOWICZ JR. PRINCIPLES OF FLUORESCENCE SPECTROSCOPY. SPRINGER; 2006.

- [204]. MOORADIAN A. PHOTOLUMINESCENCE OF METALS. *PHYS REV LETT.* 1969;22(5):185.
- [205]. BOYD GT, YU ZH, SHEN YR. PHOTOINDUCED LUMINESCENCE FROM THE NOBLE METALS AND ITS ENHANCEMENT ON ROUGHENED SURFACES. *PHYS REV B.* 1986;33(12):7923.
- [206]. THOMAS M, GREFFET JJ, CARMINATI R, ARIAS-GONZALEZ JR. SINGLE-MOLECULE SPONTANEOUS EMISSION CLOSE TO ABSORBING NANOSTRUCTURES. *APPL PHYS LETT.* 2004;85(17):3863–5.
- [207]. WILCOXON JP, MARTIN JE, PARSAPOUR F, WIEDENMAN B, KELLEY DF. PHOTOLUMINESCENCE FROM NANOSIZE GOLD CLUSTERS. *J CHEM PHYS.* 1998;108(21):9137–43.
- [208]. MOHAMED MB, VOLKOV V, LINK S, EL-SAYED MA. THE LIGHTNING'GOLD NANORODS: FLUORESCENCE ENHANCEMENT OF OVER A MILLION COMPARED TO THE GOLD METAL. *CHEM PHYS LETT.* 2000;317(6):517–23.
- [209]. WANG QQ, HAN JB, GUO DL, XIAO S, HAN YB, GONG HM, ET AL. HIGHLY EFFICIENT AVALANCHE MULTIPHOTON LUMINESCENCE FROM COUPLED AU NANOWIRES IN THE VISIBLE REGION. *NANO LETT.* 2007;7(3):723–8.
- [210]. DONG J, GAO W, HAN Q, WANG Y, QI J, YAN X, ET AL. PLASMON-ENHANCED UPCONVERSION PHOTOLUMINESCENCE: MECHANISM AND APPLICATION. *REVIEWS IN PHYSICS.* 2019;4:100026.
- [211]. TER HUURNE SET, PEETERS DBL, SÁNCHEZ-GIL JA, RIVAS JG. DIRECT MEASUREMENT OF THE LOCAL DENSITY OF OPTICAL STATES IN THE TIME DOMAIN. *ACS PHOTONICS.* 2023;10(8):2980–6.
- [212]. GIRARD C, DEREUX A. NEAR-FIELD OPTICS THEORIES. *REPORTS ON PROGRESS IN PHYSICS.* 1996;59(5):657.
- [213]. ANGER P, BHARADWAJ P, NOVOTNY L. ENHANCEMENT AND QUENCHING OF SINGLE-MOLECULE FLUORESCENCE. *PHYS REV LETT.* 2006;96(11):113002.
- [214]. PURCELL EM, TORREY HC, POUND R V. RESONANCE ABSORPTION BY NUCLEAR MAGNETIC MOMENTS IN A SOLID. *PHYSICAL REVIEW.* 1946;69(1–2):37.
- [215]. XU D, XIONG X, WU L, REN XF, PNG CE, GUO GC, ET AL. QUANTUM PLASMONICS: NEW OPPORTUNITY IN FUNDAMENTAL AND APPLIED PHOTONICS. *ADV OPT PHOTONICS.* 2018;10(4):703–56.
- [216]. RYBIN M V, MINGALEEV SF, LIMONOV MF, KIVSHAR YS. PURCELL EFFECT AND LAMB SHIFT AS INTERFERENCE PHENOMENA. *SCI REP.* 2016;6(1):20599.
- [217]. KRASNOK AE, SLOBOZHANYUK AP, SIMOVSKI CR, TRETYAKOV SA, PODDUBNY AN, MIROSHNICHENKO AE, ET AL. AN ANTENNA MODEL FOR THE PURCELL EFFECT. *SCI REP.* 2015;5(1):12956.
- [218]. MAIER SA. PLASMONIC FIELD ENHANCEMENT AND SERS IN THE EFFECTIVE MODE VOLUME PICTURE. *OPT EXPRESS.* 2006;14(5):1957–64.
- [219]. PARK W, LU D, AHN S. PLASMON ENHANCEMENT OF LUMINESCENCE UPCONVERSION. *CHEM SOC REV.* 2015;44(10):2940–62.
- [220]. RIEHL JP, RICHARDSON FS. CIRCULARLY POLARIZED LUMINESCENCE SPECTROSCOPY. *CHEM REV.* 1986;86(1):1–16.
- [221]. BRITTAI HG. EXCITED-STATE OPTICAL ACTIVITY, 1987–1995. *CHIRALITY.* 1996;8(5):357–63.
- [222]. MERTENS H, BITEEN JS, ATWATER HA, POLMAN A. POLARIZATION-SELECTIVE PLASMON-ENHANCED SILICON QUANTUM-DOT LUMINESCENCE. *NANO LETT.* 2006;6(11):2622–5.
- [223]. MEINZER N, HENDRY E, BARNES WL. PROBING THE CHIRAL NATURE OF ELECTROMAGNETIC FIELDS SURROUNDING PLASMONIC NANOSTRUCTURES. *PHYS REV B.* 2013;88(4):041407.
- [224]. MORGAN TA, JOSEPH DW. TENSOR LAGRANGIANS AND GENERALIZED CONSERVATION LAWS FOR FREE FIELDS. *IL NUOVO CIMENTO (1955-1965).* 1965;39:494–503.



- [225]. COTRUFO M, OSORIO CI, KOENDERINK AF. SPIN-DEPENDENT EMISSION FROM ARRAYS OF PLANAR CHIRAL NANOANTENNAS DUE TO LATTICE AND LOCALIZED PLASMON RESONANCES. *ACS NANO*. 2016;10(3):3389–97.
- [226]. SOLOMON ML, ABENDROTH JM, POULIKAKOS L V, HU J, DIONNE JA. FLUORESCENCE-DETECTED CIRCULAR DICHROISM OF A CHIRAL MOLECULAR MONOLAYER WITH DIELECTRIC METASURFACES. *J AM CHEM SOC*. 2020;142(43):18304–9.
- [227]. TULLIUS R, PLATT GW, KHOSRAVI KHORASHAD L, GADEGAARD N, LAPTHORN AJ, ROTELLO VM, ET AL. SUPERCHIRAL PLASMONIC PHASE SENSITIVITY FOR FINGERPRINTING OF PROTEIN INTERFACE STRUCTURE. *ACS NANO*. 2017;11(12):12049–56.
- [228]. RODIER M, KEIJZER C, MILNER J, KARIMULLAH AS, BARRON LD, GADEGAARD N, ET AL. PROBING SPECIFICITY OF PROTEIN–PROTEIN INTERACTIONS WITH CHIRAL PLASMONIC NANOSTRUCTURES. *J PHYS CHEM LETT*. 2019;10(20):6105–11.
- [229]. KARIMULLAH AS, JACK C, TULLIUS R, ROTELLO VM, COOKE G, GADEGAARD N, ET AL. DISPOSABLE PLASMONICS: PLASTIC TEMPLATED PLASMONIC METAMATERIALS WITH TUNABLE CHIRALITY. *ADV. MATER*. 2015;27(37):5610–6.
- [230]. KELLY C, KHOSRAVI KHORASHAD L, GADEGAARD N, BARRON LD, GOVOROV AO, KARIMULLAH AS, ET AL. CONTROLLING METAMATERIAL TRANSPARENCY WITH SUPERCHIRAL FIELDS. *ACS PHOTONICS*. 2018;5(2):535–43.
- [231]. KELLY C, TULLIUS R, LAPTHORN AJ, GADEGAARD N, COOKE G, BARRON LD, ET AL. CHIRAL PLASMONIC FIELDS PROBE STRUCTURAL ORDER OF BIOINTERFACES. *J AM CHEM SOC*. 2018;140(27):8509–17.
- [232]. RODIER M, KEIJZER C, MILNER J, KARIMULLAH AS, ROSZAK AW, BARRON LD, ET AL. BIOMACROMOLECULAR CHARGE CHIRALITY DETECTED USING CHIRAL PLASMONIC NANOSTRUCTURES. *NANOSCALE HORIZ*. 2020;5(2):336–44.
- [233]. GILROY C, MCKAY K, DEVINE M, WEBSTER RWH, GADEGAARD N, KARIMULLAH AS, ET AL. ACTIVE CHIRAL PLASMONICS: FLEXOELECTRIC CONTROL OF NANOSCALE CHIRALITY. *ADV PHOTONICS RES*. 2021;2(1):2000062.
- [234]. TULLIUS R, KARIMULLAH AS, RODIER M, FITZPATRICK B, GADEGAARD N, BARRON LD, ET AL. “SUPERCHIRAL” SPECTROSCOPY: DETECTION OF PROTEIN HIGHER ORDER HIERARCHICAL STRUCTURE WITH CHIRAL PLASMONIC NANOSTRUCTURES. *J AM CHEM SOC*. 2015;137(26):8380–3.
- [235]. THOMSON AR, WOOD CW, BURTON AJ, BARTLETT GJ, SESSIONS RB, BRADY RL, ET AL. COMPUTATIONAL DESIGN OF WATER-SOLUBLE A-HELICAL BARRELS. *SCIENCE (1979)*. 2014;346(6208):485–8.
- [236]. GREENFIELD NJ. USING CIRCULAR DICHROISM COLLECTED AS A FUNCTION OF TEMPERATURE TO DETERMINE THE THERMODYNAMICS OF PROTEIN UNFOLDING AND BINDING INTERACTIONS. *NAT PROTOC*. 2006;1(6):2527–35.
- [237]. MACLAREN DA, JOHNSTON J, DUNCAN DA, MARCHETTO H, DHESI SS, GADEGAARD N, ET AL. ASYMMETRIC PHOTOELECTRON TRANSMISSION THROUGH CHIRALLY-SCULPTED, POLYCRYSTALLINE GOLD. *PHYSICAL CHEMISTRY CHEMICAL PHYSICS*. 2009;11(38):8413–6.
- [238]. POULIKAKOS L V, GUTSCHE P, MCPKAM KM, BURGER S, NIEGEMANN J, HAFNER C, ET AL. OPTICAL CHIRALITY FLUX AS A USEFUL FAR-FIELD PROBE OF CHIRAL NEAR FIELDS. *ACS PHOTONICS*. 2016;3(9):1619–25.
- [239]. KOYROYTSALTIS-MCQUIRE DJP, GILROY C, BARRON LD, GADEGAARD N, KARIMULLAH AS, KADODWALA M. DETECTING ANTIBODY–ANTIGEN INTERACTIONS WITH CHIRAL PLASMONS: FACTORS INFLUENCING CHIRAL PLASMONIC SENSING. *ADV PHOTONICS RES*. 2022;3(1):2100155.
- [240]. RAMAN CV. A NEW RADIATION. *INDIAN JOURNAL OF PHYSICS*. 1928;2:387–98.
- [241]. ROSTRON P, GABER S, GABER D. RAMAN SPECTROSCOPY, REVIEW. *LASER*. 2016;21:24.

- [242]. FLEISCHMANN M, HENDRA PJ, MCQUILLAN AJ. RAMAN SPECTRA OF PYRIDINE ADSORBED AT A SILVER ELECTRODE. *CHEM PHYS LETT.* 1974;26(2):163–6.
- [243]. JEANMAIRE DL, VAN DUYN RP. SURFACE RAMAN SPECTROELECTROCHEMISTRY: PART I. HETEROCYCLIC, AROMATIC, AND ALIPHATIC AMINES ADSORBED ON THE ANODIZED SILVER ELECTRODE. *J ELECTROANAL CHEM INTERFACIAL ELECTROCHEM.* 1977;84(1):1–20.
- [244]. GERSTEN JI. THE EFFECT OF SURFACE ROUGHNESS ON SURFACE ENHANCED RAMAN SCATTERING. *J CHEM PHYS.* 1980;72(10):5779–80.
- [245]. MCCALL SL, PLATZMAN PM. RAMAN SCATTERING FROM CHEMISORBED MOLECULES AT SURFACES. *PHYS REV B.* 1980;22(4):1660.
- [246]. MAI QD, NGUYEN HA, PHUNG TLH, XUAN DINH N, TRAN QH, DOAN TQ, ET AL. SILVER NANOPARTICLES-BASED SERS PLATFORM TOWARDS DETECTING CHLORAMPHENICOL AND AMOXICILLIN: AN EXPERIMENTAL INSIGHT INTO THE ROLE OF HOMO–LUMO ENERGY LEVELS OF THE ANALYTE IN THE SERS SIGNAL AND CHARGE TRANSFER PROCESS. *THE JOURNAL OF PHYSICAL CHEMISTRY C.* 2022;126(17):7778–90.
- [247]. MOSIER-BOSS PA. REVIEW OF SERS SUBSTRATES FOR CHEMICAL SENSING. *NANOMATERIALS.* 2017;7(6):142.
- [248]. EFRIMA S. RAMAN OPTICAL ACTIVITY OF MOLECULES ADSORBED ON METAL SURFACES: THEORY. *J CHEM PHYS.* 1985;83(3):1356–62.
- [249]. ABDALI S, BLANCH EW. SURFACE ENHANCED RAMAN OPTICAL ACTIVITY (SEROA). *CHEM SOC REV.* 2008;37(5):980–92.
- [250]. THEOPHILE T. INFRARED SPECTROSCOPY: MATERIALS SCIENCE, ENGINEERING AND TECHNOLOGY. *BOD–BOOKS ON DEMAND;* 2012.
- [251]. MADEY TE, YATES JR JT. *VIBRATIONAL SPECTROSCOPY OF MOLECULES ON SURFACES. VOL. 1.* SPRINGER SCIENCE & BUSINESS MEDIA; 2013.
- [252]. SMITH E, DENT G. *MODERN RAMAN SPECTROSCOPY: A PRACTICAL APPROACH.* JOHN WILEY & SONS; 2019.
- [253]. JAYASOORIYA UA, JENKINS RD. INTRODUCTION TO RAMAN SPECTROSCOPY. IN: *AN INTRODUCTION TO LASER SPECTROSCOPY: SECOND EDITION.* SPRINGER; 2002. p. 77–104.
- [254]. LONG DA. *THE RAMAN EFFECT. THE RAMAN EFFECT: A UNIFIED TREATMENT OF THE THEORY OF RAMAN SCATTERING BY MOLECULES.* 2002;
- [255]. HAHN DW. *RAMAN SCATTERING THEORY.* DEPARTMENT OF MECHANICAL AND AEROSPACE ENGINEERING, UNIVERSITY OF FLORIDA. 2007;
- [256]. KERESZTURY G, CHALMERS JM, GRIFFITH PR. RAMAN SPECTROSCOPY: THEORY. *HANDBOOK OF VIBRATIONAL SPECTROSCOPY.* 2002;1:71–87.
- [257]. ZHAO Y. ON THE MEASUREMENTS OF THE SURFACE-ENHANCED RAMAN SCATTERING SPECTRUM: EFFECTIVE ENHANCEMENT FACTOR, OPTICAL CONFIGURATION, SPECTRAL DISTORTION, AND BASELINE VARIATION. *NANOMATERIALS.* 2023;13(23):2998.
- [258]. PROCHÁZKA M. SURFACE-ENHANCED RAMAN SPECTROSCOPY. *BIOLOGICAL AND MEDICAL PHYSICS, BIOMEDICAL ENGINEERING.* 2016;1–221.
- [259]. AROCA R. *SURFACE-ENHANCED VIBRATIONAL SPECTROSCOPY.* JOHN WILEY & SONS; 2006.
- [260]. BARRON LD, BUCKINGHAM AD. RAYLEIGH AND RAMAN SCATTERING FROM OPTICALLY ACTIVE MOLECULES. *MOL PHYS.* 1971;20(6):1111–9.
- [261]. ER E, CHOW TH, LIZ-MARZÁN LM, KOTOV NA. CIRCULAR POLARIZATION-RESOLVED RAMAN OPTICAL ACTIVITY: A PERSPECTIVE ON CHIRAL SPECTROSCOPIES OF VIBRATIONAL STATES. *ACS NANO.* 2024;18(20):12589–97.

- [262]. NIE S, EMORY SR. PROBING SINGLE MOLECULES AND SINGLE NANOPARTICLES BY SURFACE-ENHANCED RAMAN SCATTERING. *SCIENCE* (1979). 1997;275(5303):1102–6.
- [263]. LE RU EC, ETCHEGOIN PG. SINGLE-MOLECULE SURFACE-ENHANCED RAMAN SPECTROSCOPY. *ANNU REV PHYS CHEM*. 2012;63(1):65–87.
- [264]. KARTAU M, SKVORTSOVA A, TABOUILLOT V, CHAUBEY SK, BAINOVA P, KUMAR R, ET AL. CHIRAL METAFILMS AND SURFACE ENHANCED RAMAN SCATTERING FOR ENANTIOMERIC DISCRIMINATION OF HELICOID NANOPARTICLES. *ADV OPT MATER*. 2023;11(9):2202991.
- [265]. LEE HE, KIM RM, AHN HY, LEE YY, BYUN GH, IM SW, ET AL. CYSTEINE-ENCODED CHIRALITY EVOLUTION IN PLASMONIC RHOMBIC DODECAHEDRAL GOLD NANOPARTICLES. *NAT COMMUN*. 2020;11(1):263.
- [266]. LEE HE, AHN HY, MUN J, LEE YY, KIM M, CHO NH, ET AL. AMINO-ACID-AND PEPTIDE-DIRECTED SYNTHESIS OF CHIRAL PLASMONIC GOLD NANOPARTICLES. *NATURE*. 2018;556(7701):360–5.
- [267]. LEE YR, KIM MS, KWON CH. SURFACE-ENHANCED RAMAN SCATTERING AND DFT STUDY OF 4, 4'-BIPHENYLDITHIOL ON SILVER SURFACE. *BULL KOREAN CHEM SOC*. 2013;34(2):470–4.
- [268]. LANGER J, JIMENEZ DE ABERASTURI D, AIZPURUA J, ALVAREZ-PUEBLA RA, AUGUIÉ B, BAUMBERG JJ, ET AL. PRESENT AND FUTURE OF SURFACE-ENHANCED RAMAN SCATTERING. *ACS NANO*. 2019;14(1):28–117.
- [269]. DING SY, YOU EM, TIAN ZQ, MOSKOVITS M. ELECTROMAGNETIC THEORIES OF SURFACE-ENHANCED RAMAN SPECTROSCOPY. *CHEM SOC REV*. 2017;46(13):4042–76.
- [270]. XIAO TH, CHENG Z, LUO Z, ISOZAKI A, HIRAMATSU K, ITOH T, ET AL. ALL-DIELECTRIC CHIRAL-FIELD-ENHANCED RAMAN OPTICAL ACTIVITY. *NAT COMMUN*. 2021;12(1):3062.
- [271]. EL-AZAZY M. INTRODUCTORY CHAPTER: INFRARED SPECTROSCOPY-A SYNOPSIS OF THE FUNDAMENTALS AND APPLICATIONS. *INFRARED SPECTROSCOPY-PRINCIPLES, ADVANCES, AND APPLICATIONS*. 2018;1–10.
- [272]. VOGT C, WONDERGEM CS, WECKHUYSEN BM. ULTRAVIOLET-VISIBLE (UV-Vis) SPECTROSCOPY. IN: *SPRINGER HANDBOOK OF ADVANCED CATALYST CHARACTERIZATION*. SPRINGER; 2023. P. 237–64.
- [273]. TRANTER GE, LE PEVELEN DD. CHIROPTICAL SPECTROSCOPY AND THE VALIDATION OF CRYSTAL STRUCTURE STEREOCHEMICAL ASSIGNMENTS. *TETRAHEDRON ASYMMETRY*. 2017;28(10):1192–8.
- [274]. WESOLOWSKI SS, PIVONKA DE. A RAPID ALTERNATIVE TO X-RAY CRYSTALLOGRAPHY FOR CHIRAL DETERMINATION: CASE STUDIES OF VIBRATIONAL CIRCULAR DICHROISM (VCD) TO ADVANCE DRUG DISCOVERY PROJECTS. *BIOORG MED CHEM LETT*. 2013;23(14):4019–25.
- [275]. BARRON LD. THE DEVELOPMENT OF BIOMOLECULAR RAMAN OPTICAL ACTIVITY SPECTROSCOPY. *BIOMED SPECTROSC IMAGING*. 2015;4(3):223–53.
- [276]. BATISTA JR JM, BLANCH EW, DA SILVA BOLZANI V. RECENT ADVANCES IN THE USE OF VIBRATIONAL CHIROPTICAL SPECTROSCOPIC METHODS FOR STEREOCHEMICAL CHARACTERIZATION OF NATURAL PRODUCTS. *NAT PROD REP*. 2015;32(9):1280–302.
- [277]. BOGAERTS J, AERTS R, VERMEYEN T, JOHANNESSEN C, HERREBOUT W, BATISTA JR JM. TACKLING STEREOCHEMISTRY IN DRUG MOLECULES WITH VIBRATIONAL OPTICAL ACTIVITY. *PHARMACEUTICALS*. 2021;14(9):877.
- [278]. NAFIE LA, DIEM M, VIDRINE DW. FOURIER TRANSFORM INFRARED VIBRATIONAL CIRCULAR DICHROISM. *J AM CHEM SOC*. 1979;101(2):496–8.
- [279]. KEIDERLING TA, LAKHANI A. MINI REVIEW: INSTRUMENTATION FOR VIBRATIONAL CIRCULAR DICHROISM SPECTROSCOPY, STILL A ROLE FOR DISPERSIVE INSTRUMENTS. *CHIRALITY*. 2018;30(3):238–53.
- [280]. KUROUSKI D. ADVANCES OF VIBRATIONAL CIRCULAR DICHROISM (VCD) IN BIOANALYTICAL CHEMISTRY. A REVIEW. *ANAL CHIM ACTA*. 2017;990:54–66.

- [281]. ALPERT NL, KEISER WE, SZYMANSKI HA. IR: THEORY AND PRACTICE OF INFRARED SPECTROSCOPY. SPRINGER SCIENCE & BUSINESS MEDIA; 2012.
- [282]. SATHYANARAYANA DN. VIBRATIONAL SPECTROSCOPY: THEORY AND APPLICATIONS. NEW AGE INTERNATIONAL; 2015.
- [283]. FERRARO JR. INTRODUCTORY RAMAN SPECTROSCOPY. ELSEVIER; 2003.
- [284]. RODRIGO D, LIMAJ O, JANNER D, ETEZADI D, GARCÍA DE ABAJO FJ, PRUNERI V, ET AL. MID-INFRARED PLASMONIC BIOSENSING WITH GRAPHENE. SCIENCE (1979). 2015;349(6244):165–8.
- [285]. HARTSTEIN A, KIRTLEY JR, TSANG JC. ENHANCEMENT OF THE INFRARED ABSORPTION FROM MOLECULAR MONOLAYERS WITH THIN METAL OVERLAYERS. PHYS REV LETT. 1980;45(3):201.
- [286]. ADATO R, ALTUG H. IN-SITU ULTRA-SENSITIVE INFRARED ABSORPTION SPECTROSCOPY OF BIOMOLECULE INTERACTIONS IN REAL TIME WITH PLASMONIC NANOANTENNAS. NAT COMMUN. 2013;4(1):2154.
- [287]. YANG X, SUN Z, LOW T, HU H, GUO X, GARCÍA DE ABAJO FJ, ET AL. NANOMATERIAL-BASED PLASMON-ENHANCED INFRARED SPECTROSCOPY. ADV. MATER. 2018;30(20):1704896.
- [288]. AUTSCHBACH J. COMPUTING CHIROPTICAL PROPERTIES WITH FIRST-PRINCIPLES THEORETICAL METHODS: BACKGROUND AND ILLUSTRATIVE EXAMPLES. CHIRALITY: THE PHARMACOLOGICAL, BIOLOGICAL, AND CHEMICAL CONSEQUENCES OF MOLECULAR ASYMMETRY. 2009;21(1E):E116–52.
- [289]. ALKIRE RC, KOLB DM, LIPKOWSKI J, ROSS PN. DIFFRACTION AND SPECTROSCOPIC METHODS IN ELECTROCHEMISTRY. VOL. 18. JOHN WILEY & SONS; 2006.
- [290]. DONG L, YANG X, ZHANG C, CERJAN B, ZHOU L, TSENG ML, ET AL. NANOGAPPED AU ANTENNAS FOR ULTRASENSITIVE SURFACE-ENHANCED INFRARED ABSORPTION SPECTROSCOPY. NANO LETT. 2017;17(9):5768–74.
- [291]. NEUBRECH F, HUCK C, WEBER K, PUCCI A, GIESSEN H. SURFACE-ENHANCED INFRARED SPECTROSCOPY USING RESONANT NANOANTENNAS. CHEM REV. 2017;117(7):5110–45.
- [292]. KOPPENS FHL, CHANG DE, GARCÍA DE ABAJO FJ. GRAPHENE PLASMONICS: A PLATFORM FOR STRONG LIGHT-MATTER INTERACTIONS. NANO LETT. 2011;11(8):3370–7.
- [293]. GINN JC, JARECKI RL, SHANER EA, DAVIDS PS. INFRARED PLASMONS ON HEAVILY-DOPED SILICON. J APPL PHYS. 2011;110(4).
- [294]. SEMENYSHYN R, HENTSCHEL M, STANGLMAIR C, TEUTSCH T, TARIN C, PACHOLSKI C, ET AL. IN VITRO MONITORING CONFORMATIONAL CHANGES OF POLYPEPTIDE MONOLAYERS USING INFRARED PLASMONIC NANOANTENNAS. NANO LETT. 2018;19(1):1–7.
- [295]. MAHMOUDI M, LYNCH I, EJTEHADI MR, MONOPOLI MP, BOMBELLI FB, LAURENT S. PROTEIN– NANOPARTICLE INTERACTIONS: OPPORTUNITIES AND CHALLENGES. CHEM REV. 2011;111(9):5610–37.
- [296]. SOTO C, PRITZKOW S. PROTEIN MISFOLDING, AGGREGATION, AND CONFORMATIONAL STRAINS IN NEURODEGENERATIVE DISEASES. NAT NEUROSCI. 2018;21(10):1332–40.
- [297]. BAUMRUK V, KEIDERLING TA. VIBRATIONAL CIRCULAR DICHROISM OF PROTEINS IN WATER SOLUTION. J AM CHEM SOC. 1993;115(15):6939–42.
- [298]. DOBROWOLSKI JC, LIPINSKI PJF, RODE JE, SADLEJ J. A-AMINO ACIDS IN WATER: A REVIEW OF VCD AND ROA SPECTRA. OPTICAL SPECTROSCOPY AND COMPUTATIONAL METHODS IN BIOLOGY AND MEDICINE. 2014;83–160.
- [299]. VÁZQUEZ-GUARDADO A, CHANDA D. SUPERCHIRAL LIGHT GENERATION ON DEGENERATE ACHIRAL SURFACES. PHYS REV LETT. 2018;120(13):137601.

- [300]. KNIPPER R, KOPECKY JR V, HUEBNER U, POPP J, MAYERHÖFER TG. SLIT-ENHANCED CHIRAL-AND BROADBAND INFRARED ULTRA-SENSING. *ACS PHOTONICS*. 2018;5(8):3238–45.
- [301]. IIDA T, ISHIKAWA A, TANAKA T, MURANAKA A, UCHIYAMA M, HAYASHI Y, ET AL. SUPER-CHIRAL VIBRATIONAL SPECTROSCOPY WITH METASURFACES FOR HIGH-SENSITIVE IDENTIFICATION OF ALANINE ENANTIOMERS. *APPL PHYS LETT*. 2020;117(10).
- [302]. XU C, REN Z, ZHOU H, ZHOU J, HO CP, WANG N, ET AL. EXPANDING CHIRAL METAMATERIALS FOR RETRIEVING FINGERPRINTS VIA VIBRATIONAL CIRCULAR DICHROISM. *LIGHT SCI APPL*. 2023;12(1):154.
- [303]. BISWAS A, CENCILLO-ABAD P, SHABBIR MW, KARMAKAR M, CHANDA D. TUNABLE PLASMONIC SUPERCHIRAL LIGHT FOR ULTRASENSITIVE DETECTION OF CHIRAL MOLECULES. *SCI ADV*. 2024;10(8):EADK2560.
- [304]. GHARABEKYAN HH, KOETZ J, POGHOSYAN AH. A PROTONATED L-CYSTEINE ADSORPTION ON GOLD SURFACE: A MOLECULAR DYNAMICS STUDY. *COLLOIDS SURF A PHYSICOCHEM ENG ASP*. 2021;629:127452.
- [305]. MATEO-MARTÍ E, ROGERO C, GONZÁLEZ C, SOBRADO JM, DE ANDRÉS PL, MARTÍN-GAGO JA. INTERPLAY BETWEEN FAST DIFFUSION AND MOLECULAR INTERACTION IN THE FORMATION OF SELF-ASSEMBLED NANOSTRUCTURES OF S-CYSTEINE ON Au (111). *LANGMUIR*. 2010;26(6):4113–8.
- [306]. BROGLY M, BISTAC S, BINDEL D. ADSORPTION AND STRUCTURATION OF PEG THIN FILMS: INFLUENCE OF THE SUBSTRATE CHEMISTRY. *POLYMERS (BASEL)*. 2024;16(9):1244.
- [307]. BRETZLAFF RS, BAHDER TB. APODIZATION EFFECTS IN FOURIER TRANSFORM INFRARED DIFFERENCE SPECTRA. *REVUE DE PHYSIQUE APPLIQUÉE*. 1986;21(12):833–44.
- [308]. HE Y, BO W, DUKOR RK, NAFIE LA. DETERMINATION OF ABSOLUTE CONFIGURATION OF CHIRAL MOLECULES USING VIBRATIONAL OPTICAL ACTIVITY: A REVIEW. *APPL SPECTROSC*. 2011;65(7):699–723.
- [309]. NAFIE LA. VIBRATIONAL CD SPECTROMETERS. IN: LINDON JC, TRANTER GE, KOPPENAAAL DW, EDITORS. *ENCYCLOPEDIA OF SPECTROSCOPY AND SPECTROMETRY (THIRD EDITION)* [INTERNET]. OXFORD: ACADEMIC PRESS; 2017. P. 524–33. AVAILABLE FROM: [HTTPS://WWW.SCIENCEDIRECT.COM/SCIENCE/ARTICLE/PII/B9780128032244000819](https://www.sciencedirect.com/science/article/pii/B9780128032244000819)
- [310]. JALILEHVAND F, MAH V, LEUNG BO, MINK J, BERNARD GM, HAJBA L. CADMIUM (II) CYSTEINE COMPLEXES IN THE SOLID STATE: A MULTISPECTROSCOPIC STUDY. *INORG CHEM*. 2009;48(9):4219–30.
- [311]. MIN'KOV VS, CHESALOV YA, BOLDYREVA E V. STUDY OF THE TEMPERATURE EFFECT ON IR SPECTRA OF CRYSTALLINE AMINO ACIDS, DIPEPTIDES, AND POLYAMINO ACIDS. IV. L-CYSTEINE AND DL-CYSTEINE. *JOURNAL OF STRUCTURAL CHEMISTRY*. 2008;49:1022–34.
- [312]. RINNAN Å, VAN DEN BERG F, ENGELSEN SB. REVIEW OF THE MOST COMMON PRE-PROCESSING TECHNIQUES FOR NEAR-INFRARED SPECTRA. *TRAC TRENDS IN ANALYTICAL CHEMISTRY*. 2009;28(10):1201–22.
- [313]. TALSKY G, MAYRING L, KREUZER H. HIGH-RESOLUTION, HIGHER-ORDER UV/VIS DERIVATIVE SPECTROPHOTOMETRY. *ANGEWANDTE CHEMIE INTERNATIONAL EDITION IN ENGLISH*. 1978;17(11):785–99.
- [314]. TOFT J, SÁNCHEZ FC, VAN DEN BOGAERT B, LIBNAU FO, MASSART DL. RESOLUTION OF OVERLAPPING MID-INFRARED SPECTRA USING SIMPLISMA AND A SECOND-ORDER DERIVATIVE APPROACH. *VIB SPECTROSC*. 1996;10(2):125–38.
- [315]. FLACH CR, BRAUNER JW, TAYLOR JW, BALDWIN RC, MENDELSON R. EXTERNAL REFLECTION FTIR OF PEPTIDE MONOLAYER FILMS IN SITU AT THE AIR/WATER INTERFACE: EXPERIMENTAL DESIGN, SPECTRA-STRUCTURE CORRELATIONS, AND EFFECTS OF HYDROGEN-DEUTERIUM EXCHANGE. *BIOPHYS J*. 1994;67(1):402–10.
- [316]. HALE GM, QUERRY MR. OPTICAL CONSTANTS OF WATER IN THE 200-NM TO 200-MM WAVELENGTH REGION. *APPL OPT*. 1973;12(3):555–63.

- [317]. VIEIRA LG. INFRARED OPTICAL FUNCTIONS OF WATER RETRIEVED USING ATTENUATED TOTAL REFLECTION SPECTROSCOPY. *APPL SPECTROSC.* 2023;77(2):178–86.
- [318]. PAI PG, CHAO SS, TAKAGI Y, LUCOVSKY G. INFRARED SPECTROSCOPIC STUDY OF SiO<sub>2</sub> FILMS PRODUCED BY PLASMA ENHANCED CHEMICAL VAPOR DEPOSITION. *JOURNAL OF VACUUM SCIENCE & TECHNOLOGY A: VACUUM, SURFACES, AND FILMS.* 1986;4(3):689–94.
- [319]. BOYD IW, WILSON JIB. A STUDY OF THIN SILICON DIOXIDE FILMS USING INFRARED ABSORPTION TECHNIQUES. *J APPL PHYS.* 1982;53(6):4166–72.
- [320]. IHS A, LIEDBERG B. CHEMISORPTION OF L-CYSTEINE AND 3-MERCAPTOPROPIONIC ACID ON GOLD AND COPPER SURFACES: AN INFRARED REFLECTION-ABSORPTION STUDY. *J COLLOID INTERFACE SCI.* 1991;144(1):282–92.
- [321]. MATEO MARTI E, METHIVIER C, PRADIER CM. (S)-CYSTEINE CHEMISORPTION ON Cu (110), FROM THE GAS OR LIQUID PHASE: AN FT-RAIRS AND XPS STUDY. *LANGMUIR.* 2004;20(23):10223–30.
- [322]. NEUMAN T, HUCK C, VOGT J, NEUBRECH F, HILLENBRAND R, AIZPURUA J, ET AL. IMPORTANCE OF PLASMONIC SCATTERING FOR AN OPTIMAL ENHANCEMENT OF VIBRATIONAL ABSORPTION IN SEIRA WITH LINEAR METALLIC ANTENNAS. *THE JOURNAL OF PHYSICAL CHEMISTRY C.* 2015;119(47):26652–62.
- [323]. ADATO R, ARTAR A, ERRAMILI S, ALTUG H. ENGINEERED ABSORPTION ENHANCEMENT AND INDUCED TRANSPARENCY IN COUPLED MOLECULAR AND PLASMONIC RESONATOR SYSTEMS. *NANO LETT.* 2013;13(6):2584–91.
- [324]. DONATI G, LINGERFELT DB, AIKENS CM, LI X. MOLECULAR VIBRATION INDUCED PLASMON DECAY. *THE JOURNAL OF PHYSICAL CHEMISTRY C.* 2017;121(28):15368–74.
- [325]. LEE SA, LINK S. CHEMICAL INTERFACE DAMPING OF SURFACE PLASMON RESONANCES. *ACC CHEM RES.* 2021;54(8):1950–60.
- [326]. CHAUBEY SK, KUMAR R, LALAGUNA PL, KARTAU M, BIANCO S, TABOUILLOT V, ET AL. ULTRASENSITIVE RAMAN DETECTION OF BIOMOLECULAR CONFORMATION AT THE ATTOMOLE SCALE USING CHIRAL NANOPHOTONICS. *SMALL.* 2024;2404536.
- [327]. GAUTIER C, BÜRGI T. VIBRATIONAL CIRCULAR DICHROISM OF N-ACETYL-L-CYSTEINE PROTECTED GOLD NANOPARTICLES. *CHEMICAL COMMUNICATIONS.* 2005;(43):5393–5.
- [328]. GAUTIER C, BÜRGI T. CHIRAL N-ISOBUTYRYL-CYSTEINE PROTECTED GOLD NANOPARTICLES: PREPARATION, SIZE SELECTION, AND OPTICAL ACTIVITY IN THE UV–VIS AND INFRARED. *J AM CHEM SOC.* 2006;128(34):11079–87.
- [329]. LU W. CHIRALLY FUNCTIONALIZED METAL NANOPARTICLES. 2009;
- [330]. NESTEROV ML, YIN X, SCHÄFERLING M, GIESSEN H, WEISS T. THE ROLE OF PLASMON-GENERATED NEAR FIELDS FOR ENHANCED CIRCULAR DICHROISM SPECTROSCOPY. *ACS PHOTONICS.* 2016;3(4):578–83.
- [331]. YAO K, ZHENG Y. NEAR-ULTRAVIOLET DIELECTRIC METASURFACES: FROM SURFACE-ENHANCED CIRCULAR DICHROISM SPECTROSCOPY TO POLARIZATION-PRESERVING MIRRORS. *THE JOURNAL OF PHYSICAL CHEMISTRY C.* 2019;123(18):11814–22.
- [332]. THROAT S, BHATTACHARYA S. MACROMOLECULAR POLY (N-ISOPROPYLACRYLAMIDE)(PNIPAM) IN CANCER TREATMENT AND BEYOND: APPLICATIONS IN DRUG DELIVERY, PHOTOTHERMAL THERAPY, GENE DELIVERY AND BIOMEDICAL IMAGING. *ADV. POLYM. TECH.* 2024;2024(1):1444990.
- [333]. LI Y, MIAO Z, SHANG Z, CAI Y, CHENG J, XU X. A VISIBLE-AND NIR-LIGHT RESPONSIVE PHOTOTHERMAL THERAPY AGENT BY CHIRALITY-DEPENDENT MoO<sub>3</sub>-x NANOPARTICLES. *ADV. FUNCT. MATER.* 2020 JAN;30(4):1906311.

# Appendix A

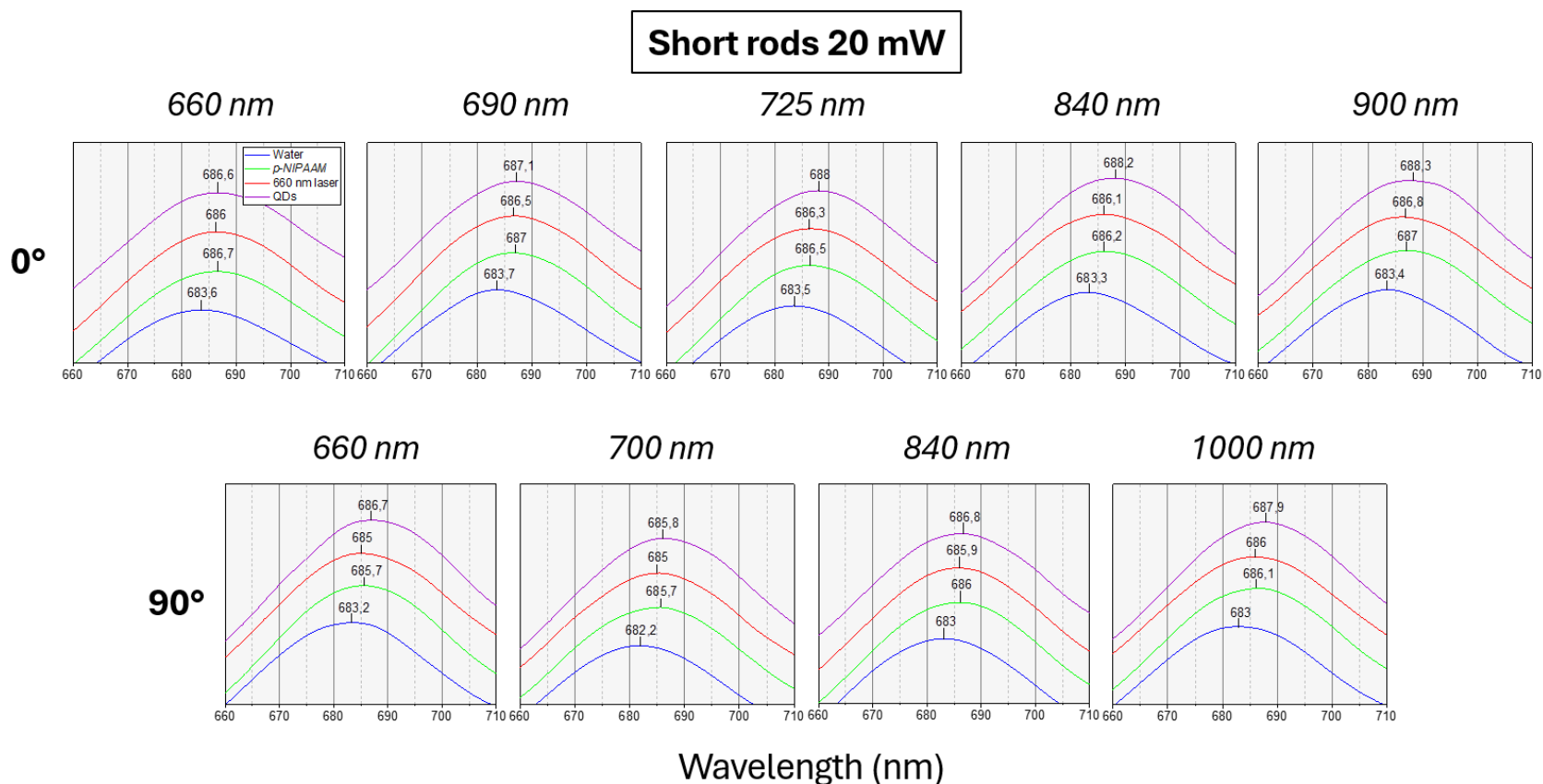


**Figure A.1: Short rods reflectance spectra of the 20 mW experiment of all the illuminated arrays at different wavelengths (upper label) and for both polarisations (labelled on the left of each row) taken in water (blue), after *p*-NIPAAM deposition (green), following the laser heating at the wavelength indicated (red) and finally after the QD functionalisation (purple). The wavelength position of resonance is labelled for each curves.**

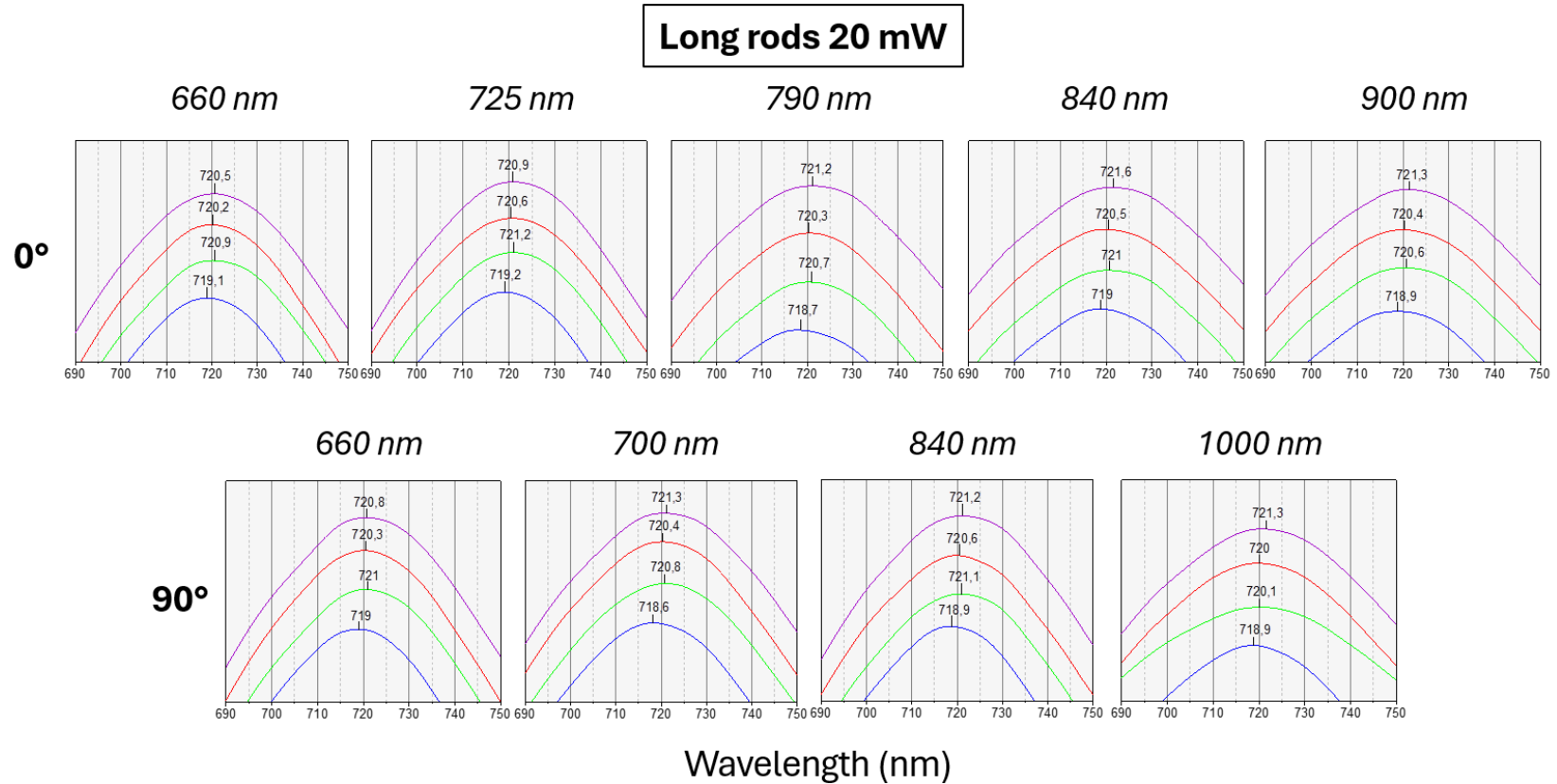


**Figure A.2: Long rods reflectance spectra of the 20 mW experiment of all the illuminated arrays at different wavelengths (upper label) and for both polarisations (labelled on the left of each row) taken in water (blue), after *p*-NIPAAM deposition (green), following the laser heating at the wavelength indicated (red) and finally after the QD functionalisation (purple). The wavelength position of resonance is labelled for each curves.**



# Appendix B

**Table B: Number of QDs counted on the SEM of each rods for the 20 mW experiment, the red numbers were excluded from the results because they were taken outside the middle part of the array (exposed to a lower intensity of the laser).**

| <i>700 nm Unilluminated Summary</i> |       |       |       |       |       |       |         |     |         |    |
|-------------------------------------|-------|-------|-------|-------|-------|-------|---------|-----|---------|----|
| $\lambda$                           | SEM # | Rod 1 | Rod 2 | Rod 3 | Rod 4 | Rod 5 | Average | SD  | Average | SD |
| Unilluminated                       | 1     | 23    | 28    | 28    | 22    | 23    | 24.8    | 2.9 | 29.1    | 5  |
|                                     | 2     | 27    | 30    | 29    | 21    | 42    | 29.8    | 7.7 |         |    |
|                                     | 3     | 27    | 32    | 25    | 27    | 30    | 28.2    | 2.8 |         |    |
|                                     | 4     | 37    | 39    | 32    | 37    | 33    | 35.6    | 3   |         |    |
|                                     | 5     | 29    | 28    | 25    | 25    | 24    | 26.2    | 2.2 |         |    |
|                                     | 6     | 31    | 30    | 26    | 33    | 30    | 30      | 2.5 |         |    |

| <i>700 nm 0° Summary</i> |       |       |       |       |       |       |         |     |         |     |
|--------------------------|-------|-------|-------|-------|-------|-------|---------|-----|---------|-----|
| $\lambda$                | SEM # | Rod 1 | Rod 2 | Rod 3 | Rod 4 | Rod 5 | Average | SD  | Average | SD  |
| 660 nm                   | 1     | 3     | 2     | 4     | 6     | 1     | 3,2     | 1,9 | 6.3     | 3.3 |
|                          | 2     | 9     | 11    | 11    | 5     | 5     | 8,2     | 3,0 |         |     |
|                          | 3     | 11    | 5     | 7     | 5     | 9     | 7,4     | 2,6 |         |     |
|                          | 4     | 7     | 2     | 3     | 7     | 4     | 4,6     | 2,3 |         |     |
|                          | 5     | 4     | 8     | 7     | 2     | 6     | 5,4     | 2,4 |         |     |
|                          | 6     | 12    | 9     | 14    | 5     | 5     | 9       | 4,1 |         |     |
| 690 nm                   | 1     | 2     | 3     | 5     | 8     | 8     | 5,2     | 2,8 | 8.3     | 3.5 |
|                          | 2     | 6     | 7     | 4     | 10    | 6     | 6,6     | 2,2 |         |     |
|                          | 3     | 10    | 7     | 4     | 9     | 7     | 7,4     | 2,3 |         |     |
|                          | 4     | 7     | 7     | 5     | 6     | 6     | 6,2     | 0,8 |         |     |
|                          | 5     | 8     | 10    | 13    | 12    | 11    | 10,8    | 1,9 |         |     |
|                          | 6     | 14    | 15    | 12    | 12    | 15    | 13,6    | 1,5 |         |     |
| 725 nm                   | 1     | 17    | 18    | 12    | 29    | 18    | 18,8    | 6,2 | 21      | 5   |
|                          | 2     | 21    | 19    | 21    | 25    | 17    | 20,6    | 3,0 |         |     |
|                          | 3     | 14    | 24    | 20    | 14    | 20    | 18,4    | 4,3 |         |     |
|                          | 4     | 18    | 12    | 19    | 20    | 22    | 18,2    | 3,8 |         |     |
|                          | 5     | 26    | 26    | 24    | 19    | 23    | 23,6    | 2,9 |         |     |
|                          | 6     | 24    | 27    | 21    | 25    | 34    | 26,2    | 4,9 |         |     |
| 840 nm                   | 1     | 17    | 20    | 21    | 19    | 18    | 19      | 1,6 | 19.7    | 4.3 |
|                          | 2     | 24    | 18    | 20    | 11    | 17    | 18      | 4,7 |         |     |
|                          | 3     | 18    | 16    | 21    | 15    | 21    | 18,2    | 2,8 |         |     |
|                          | 4     | 21    | 16    | 16    | 16    | 17    | 17,2    | 2,2 |         |     |
|                          | 5     | 22    | 19    | 20    | 17    | 19    | 19,4    | 1,8 |         |     |
|                          | 6     | 26    | 22    | 26    | 34    | 24    | 26,4    | 4,6 |         |     |
| 900 nm                   | 1     | 23    | 22    | 22    | 22    | 17    | 21,2    | 2,4 | 22.9    | 5.4 |
|                          | 2     | 21    | 24    | 17    | 19    | 28    | 21,8    | 4,3 |         |     |
|                          | 3     | 30    | 17    | 23    | 21    | 20    | 22,2    | 4,9 |         |     |
|                          | 4     | 18    | 18    | 22    | 19    | 20    | 19,4    | 1,7 |         |     |
|                          | 5     | 22    | 20    | 17    | 21    | 22    | 20,4    | 2,1 |         |     |
|                          | 6     | 30    | 31    | 35    | 36    | 31    | 32,6    | 2,7 |         |     |

| <i>700 nm 90° Summary</i> |       |       |       |       |       |       |         |     |         |     |
|---------------------------|-------|-------|-------|-------|-------|-------|---------|-----|---------|-----|
| $\lambda$                 | SEM # | Rod 1 | Rod 2 | Rod 3 | Rod 4 | Rod 5 | Average | SD  | Average | SD  |
| 660 nm                    | 1     | 5     | 6     | 7     | 5     | 7     | 6       | 1,0 | 10.2    | 4.7 |
|                           | 2     | 9     | 6     | 8     | 5     | 9     | 7,4     | 1,8 |         |     |
|                           | 3     | 13    | 6     | 9     | 10    | 16    | 10,8    | 3,8 |         |     |
|                           | 4     | 4     | 7     | 5     | 7     | 7     | 6       | 1,4 |         |     |
|                           | 5     | 14    | 11    | 13    | 19    | 14    | 14,2    | 2,9 |         |     |
|                           | 6     | 19    | 18    | 15    | 15    | 17    | 16,8    | 1,8 |         |     |
| 700 nm                    | 1     | 7     | 7     | 2     | 3     | 4     | 4,6     | 2,3 | 9.6     | 4.5 |
|                           | 2     | 8     | 4     | 7     | 5     | 9     | 6,6     | 2,1 |         |     |
|                           | 3     | 9     | 8     | 7     | 5     | 6     | 7       | 1,6 |         |     |
|                           | 4     | 9     | 9     | 11    | 14    | 10    | 10,6    | 2,1 |         |     |
|                           | 5     | 14    | 11    | 14    | 16    | 8     | 12,6    | 3,1 |         |     |
|                           | 6     | 17    | 15    | 16    | 17    | 17    | 16,4    | 0,9 |         |     |
| 840 nm                    | 1     | 11    | 18    | 18    | 11    | 12    | 14      | 3,7 | 23.9    | 7.5 |
|                           | 2     | 25    | 19    | 25    | 17    | 26    | 22,4    | 4,1 |         |     |
|                           | 3     | 28    | 27    | 35    | 34    | 29    | 30,6    | 3,6 |         |     |
|                           | 4     | 22    | 28    | 21    | 25    | 32    | 25,6    | 4,5 |         |     |
|                           | 5     | 19    | 22    | 16    | 32    | 22    | 22,2    | 6,0 |         |     |
|                           | 6     | 40    | 28    | 32    | 29    | 14    | 28,6    | 9,4 |         |     |
| 1000 nm                   | 1     | 14    | 19    | 21    | 19    | 17    | 18      | 2,6 | 25.3    | 4.7 |
|                           | 2     | 26    | 27    | 24    | 20    | 24    | 24,2    | 2,7 |         |     |
|                           | 3     | 31    | 24    | 24    | 25    | 30    | 26,8    | 3,4 |         |     |
|                           | 4     | 37    | 31    | 26    | 27    | 27    | 29,6    | 4,6 |         |     |
|                           | 5     | 32    | 28    | 26    | 25    | 23    | 26,8    | 3,4 |         |     |
|                           | 6     | 23    | 28    | 27    | 26    | 27    | 26,2    | 1,9 |         |     |

| <b>800 nm Unilluminated Summary</b> |       |       |       |       |       |       |             |            |             |          |
|-------------------------------------|-------|-------|-------|-------|-------|-------|-------------|------------|-------------|----------|
| $\lambda$                           | SEM # | Rod 1 | Rod 2 | Rod 3 | Rod 4 | Rod 5 | Average     | SD         | Average     | SD       |
| Unilluminated                       | 1     | 36    | 30    | 31    | 34    | 31    | <b>32.4</b> | <b>2.5</b> | <b>32.6</b> | <b>6</b> |
|                                     | 2     | 28    | 28    | 24    | 32    | 23    | <b>27</b>   | <b>3.6</b> |             |          |
|                                     | 3     | 33    | 29    | 31    | 32    | 30    | <b>31</b>   | <b>1.6</b> |             |          |
|                                     | 4     | 25    | 30    | 26    | 27    | 29    | <b>27.4</b> | <b>2.1</b> |             |          |
|                                     | 5     | 32    | 34    | 39    | 38    | 40    | <b>36.6</b> | <b>3.4</b> |             |          |
|                                     | 6     | 39    | 35    | 50    | 43    | 39    | <b>41.2</b> | <b>5.7</b> |             |          |

| <b>800 nm 0° Summary</b> |       |           |           |           |           |           |             |            |             |            |
|--------------------------|-------|-----------|-----------|-----------|-----------|-----------|-------------|------------|-------------|------------|
| $\lambda$                | SEM # | Rod 1     | Rod 2     | Rod 3     | Rod 4     | Rod 5     | Average     | SD         | Average     | SD         |
| 660 nm                   | 1     | 1         | 1         | 0         | 4         | 3         | <b>1,8</b>  | <b>1,6</b> | <b>6.4</b>  | <b>4.8</b> |
|                          | 2     | 3         | 3         | 0         | 1         | 2         | <b>1,8</b>  | <b>1,3</b> |             |            |
|                          | 3     | 7         | 2         | 0         | 4         | 2         | <b>3</b>    | <b>2,6</b> |             |            |
|                          | 4     | <b>6</b>  | <b>10</b> | <b>11</b> | <b>12</b> | <b>9</b>  | <b>9,6</b>  | <b>2,3</b> |             |            |
|                          | 5     | <b>12</b> | <b>12</b> | <b>6</b>  | <b>8</b>  | <b>10</b> | <b>9,6</b>  | <b>2,6</b> |             |            |
|                          | 6     | <b>13</b> | <b>13</b> | <b>15</b> | <b>8</b>  | <b>13</b> | <b>12,4</b> | <b>2,6</b> |             |            |
| 725 nm                   | 1     | 9         | 6         | 5         | 7         | 3         | <b>6</b>    | <b>2,2</b> | <b>9.6</b>  | <b>4.8</b> |
|                          | 2     | 3         | 8         | 7         | 7         | 12        | <b>7,4</b>  | <b>3,2</b> |             |            |
|                          | 3     | 11        | 10        | 7         | 10        | 9         | <b>9,4</b>  | <b>1,5</b> |             |            |
|                          | 4     | 6         | 5         | 11        | 4         | 11        | <b>7,4</b>  | <b>3,4</b> |             |            |
|                          | 5     | 8         | 9         | 11        | 13        | 9         | <b>10</b>   | <b>2,0</b> |             |            |
|                          | 6     | <b>21</b> | <b>11</b> | <b>22</b> | <b>21</b> | <b>12</b> | <b>17,4</b> | <b>5,4</b> |             |            |
| 790 nm                   | 1     | 13        | 8         | 8         | 16        | 17        | <b>12,4</b> | <b>4,3</b> | <b>15.6</b> | <b>4</b>   |
|                          | 2     | 13        | 8         | 10        | 10        | 16        | <b>11,4</b> | <b>3,1</b> |             |            |
|                          | 3     | 20        | 14        | 14        | 17        | 15        | <b>16</b>   | <b>2,5</b> |             |            |
|                          | 4     | 13        | 19        | 17        | 15        | 17        | <b>16,2</b> | <b>2,3</b> |             |            |
|                          | 5     | 20        | 21        | 16        | 22        | 15        | <b>18,8</b> | <b>3,1</b> |             |            |
|                          | 6     | 20        | 19        | 20        | 14        | 21        | <b>18,8</b> | <b>2,8</b> |             |            |
| 840 nm                   | 1     | 13        | 15        | 7         | 17        | 14        | <b>13,2</b> | <b>3,8</b> | <b>16.3</b> | <b>5.3</b> |
|                          | 2     | 14        | 17        | 8         | 8         | 15        | <b>12,4</b> | <b>4,2</b> |             |            |
|                          | 3     | 16        | 11        | 12        | 9         | 13        | <b>12,2</b> | <b>2,6</b> |             |            |
|                          | 4     | <b>16</b> | <b>19</b> | <b>12</b> | <b>20</b> | <b>24</b> | <b>18,2</b> | <b>4,5</b> |             |            |
|                          | 5     | <b>24</b> | <b>25</b> | <b>20</b> | <b>13</b> | <b>17</b> | <b>19,8</b> | <b>5,0</b> |             |            |
|                          | 6     | <b>23</b> | <b>20</b> | <b>20</b> | <b>22</b> | <b>26</b> | <b>22,2</b> | <b>2,5</b> |             |            |
| 900 nm                   | 1     | 27        | 18        | 24        | 22        | 24        | <b>23</b>   | <b>3,3</b> | <b>21.8</b> | <b>3.9</b> |
|                          | 2     | 22        | 16        | 24        | 18        | 19        | <b>19,8</b> | <b>3,2</b> |             |            |
|                          | 3     | 23        | 26        | 25        | 28        | 22        | <b>24,8</b> | <b>2,4</b> |             |            |
|                          | 4     | 26        | 19        | 20        | 25        | 20        | <b>22</b>   | <b>3,2</b> |             |            |
|                          | 5     | 19        | 24        | 21        | 13        | 28        | <b>21</b>   | <b>5,6</b> |             |            |
|                          | 6     | 16        | 17        | 18        | 27        | 22        | <b>20</b>   | <b>4,5</b> |             |            |

| <i>800 nm 90° Summary</i> |       |       |       |       |       |       |         |     |         |     |
|---------------------------|-------|-------|-------|-------|-------|-------|---------|-----|---------|-----|
| $\lambda$                 | SEM # | Rod 1 | Rod 2 | Rod 3 | Rod 4 | Rod 5 | Average | SD  | Average | SD  |
| 660 nm                    | 1     | 6     | 5     | 3     | 4     | 8     | 5,2     | 1,9 | 11.9    | 5.6 |
|                           | 2     | 6     | 8     | 8     | 11    | 5     | 7,6     | 2,3 |         |     |
|                           | 3     | 16    | 10    | 6     | 8     | 14    | 10,8    | 4,1 |         |     |
|                           | 4     | 20    | 10    | 13    | 15    | 12    | 14      | 3,8 |         |     |
|                           | 5     | 16    | 12    | 12    | 14    | 13    | 13,4    | 1,7 |         |     |
|                           | 6     | 19    | 22    | 22    | 18    | 21    | 20,4    | 1,8 |         |     |
| 700 nm                    | 1     | 11    | 13    | 20    | 18    | 12    | 14,8    | 4,0 | 17.3    | 5.2 |
|                           | 2     | 5     | 14    | 14    | 13    | 12    | 11,6    | 3,8 |         |     |
|                           | 3     | 15    | 15    | 18    | 15    | 12    | 15      | 2,1 |         |     |
|                           | 4     | 21    | 29    | 18    | 14    | 24    | 21,2    | 5,7 |         |     |
|                           | 5     | 25    | 26    | 18    | 23    | 19    | 22,2    | 3,6 |         |     |
|                           | 6     | 16    | 24    | 16    | 20    | 19    | 19      | 3,3 |         |     |
| 840 nm                    | 1     | 19    | 14    | 12    | 26    | 20    | 18,2    | 5,5 | 19.2    | 4.5 |
|                           | 2     | 27    | 16    | 12    | 19    | 12    | 17,2    | 6,2 |         |     |
|                           | 3     | 25    | 16    | 18    | 17    | 24    | 20      | 4,2 |         |     |
|                           | 4     | 18    | 18    | 19    | 19    | 21    | 19      | 1,2 |         |     |
|                           | 5     | 15    | 18    | 15    | 17    | 19    | 16,8    | 1,8 |         |     |
|                           | 6     | 24    | 21    | 25    | 30    | 19    | 23,8    | 4,2 |         |     |
| 1000 nm                   | 1     | 28    | 30    | 26    | 21    | 22    | 25,4    | 3,8 | 27.2    | 5   |
|                           | 2     | 29    | 26    | 27    | 30    | 20    | 26,4    | 3,9 |         |     |
|                           | 3     | 26    | 22    | 30    | 14    | 20    | 22,4    | 6,1 |         |     |
|                           | 4     | 24    | 27    | 30    | 33    | 26    | 28      | 3,5 |         |     |
|                           | 5     | 20    | 31    | 34    | 29    | 32    | 29,2    | 5,4 |         |     |
|                           | 6     | 33    | 28    | 35    | 33    | 29    | 31,6    | 3,0 |         |     |

# Appendix C

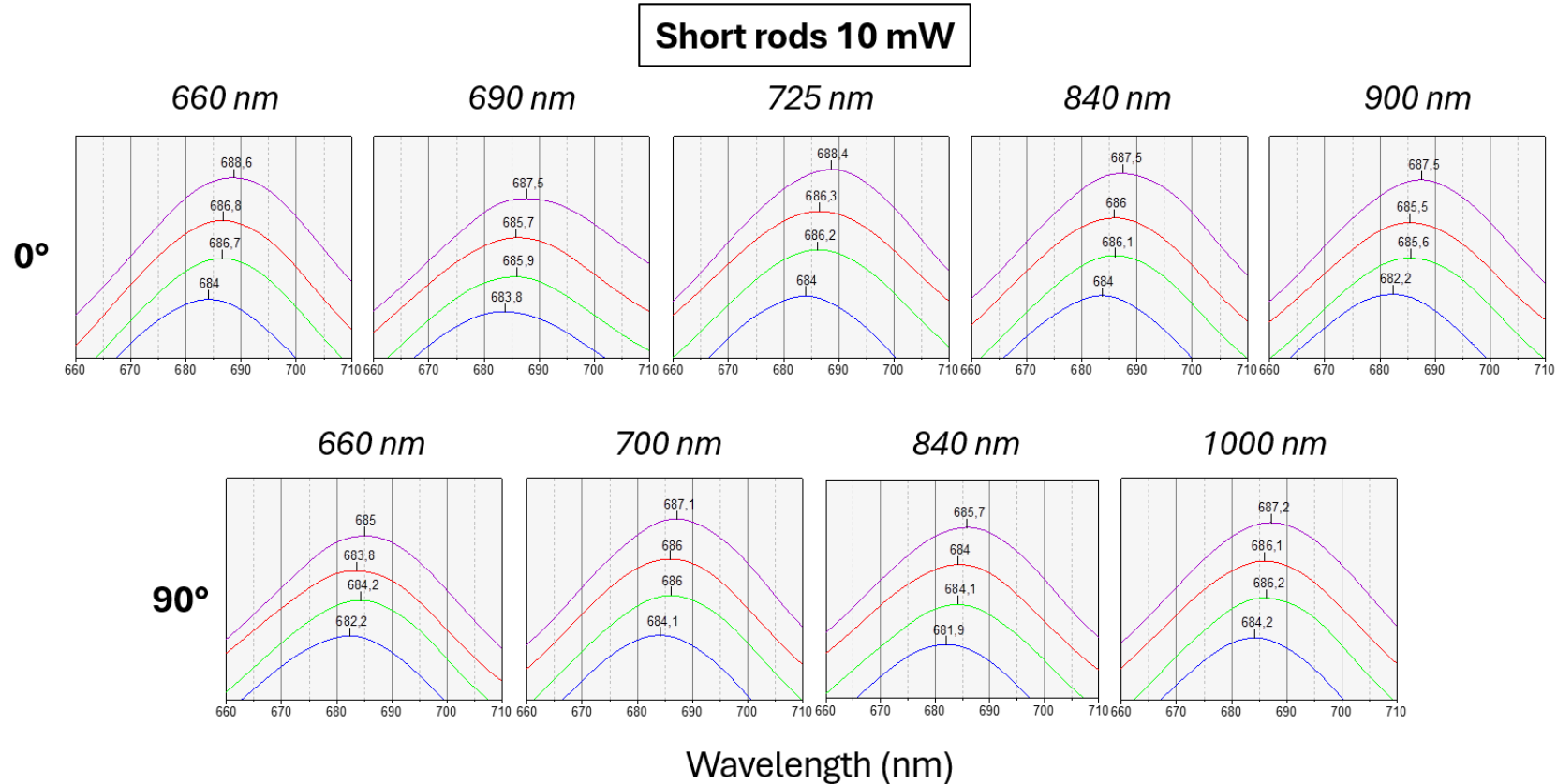


**Figure C.1: Short rods reflectance spectra of the 10 mW experiment of all the illuminated arrays at different wavelengths (upper label) and for both polarisations (labelled on the left of each row) taken in water (blue), after *p*-NIPAAM deposition (green), following the laser heating at the wavelength indicated (red) and finally after the QD functionalisation (purple). The wavelength position of resonance is labelled for each curves.**

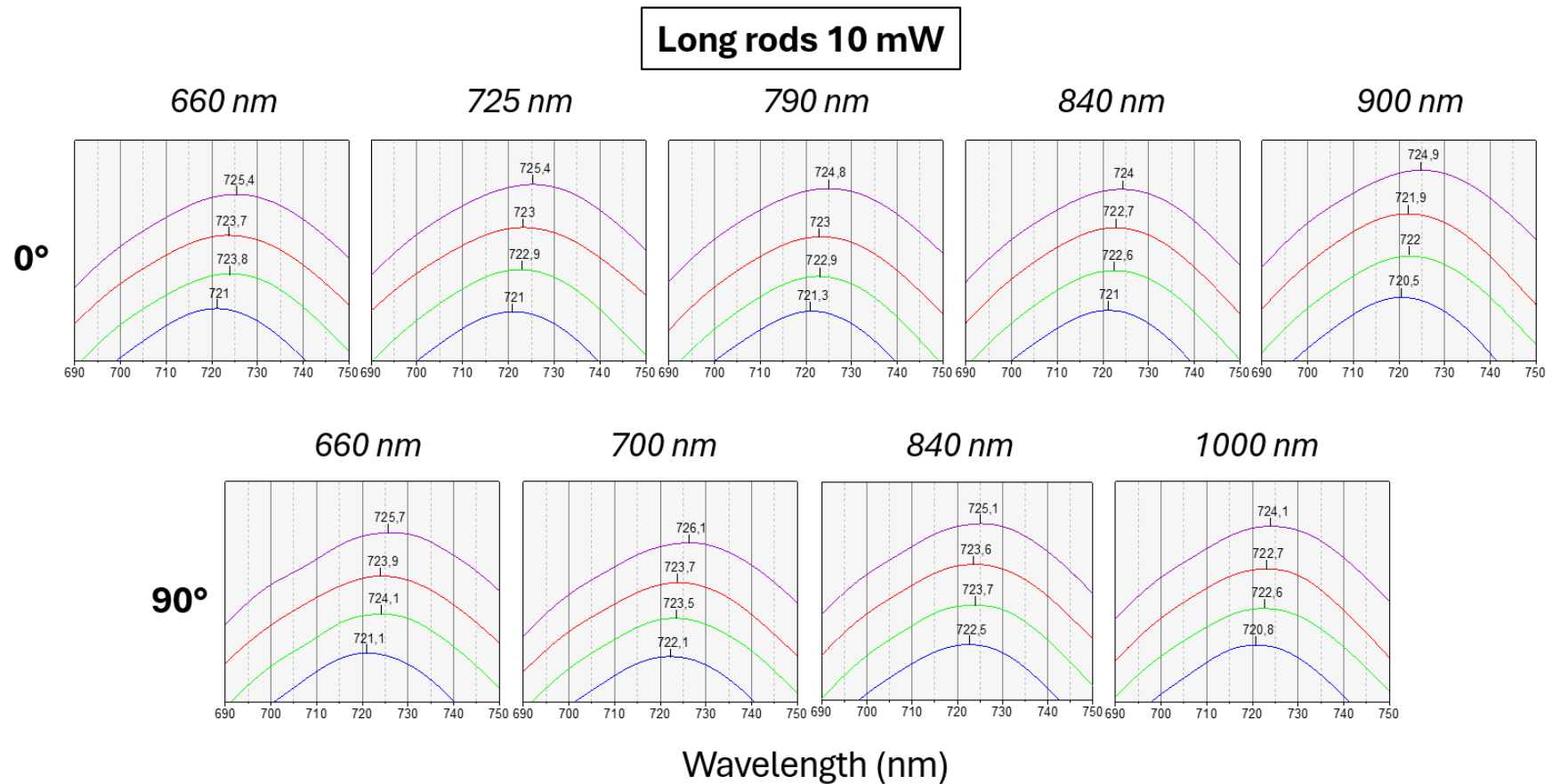


**Figure C.2:** Long rods reflectance spectra of the 10 mW experiment of all the illuminated arrays at different wavelengths (upper label) and for both polarisations (labelled on the left of each row) taken in water (blue), after *p*-NIPAAM deposition (green), following the laser heating at the wavelength indicated (red) and finally after the QD functionalisation (purple). The wavelength position of resonance is labelled for each curves.

# Appendix D

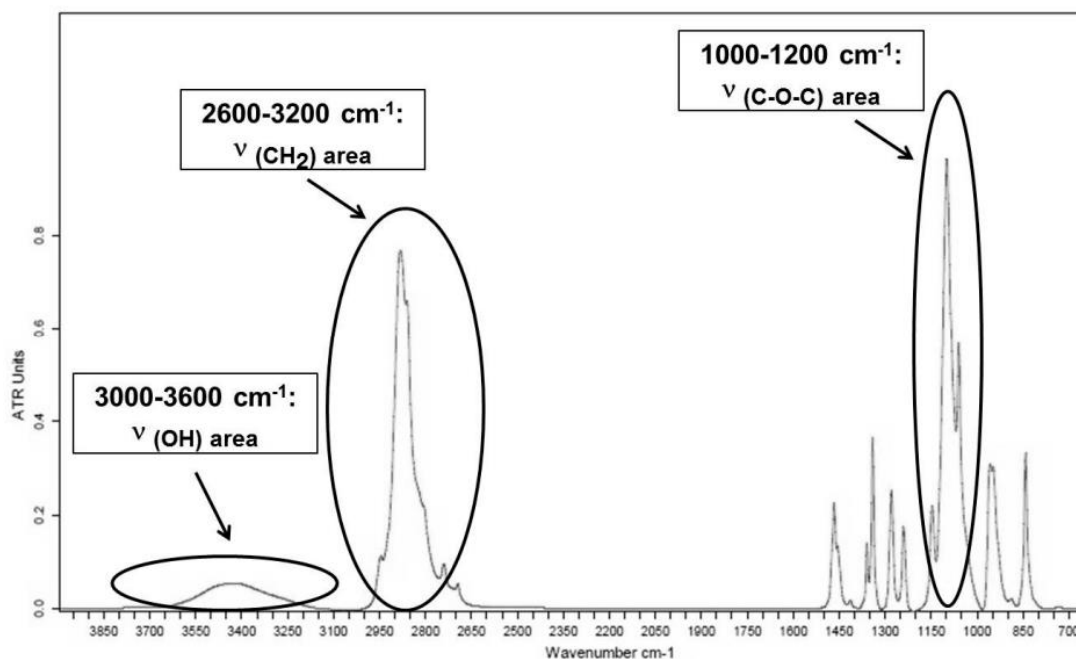


Figure D.1: IR spectrum of solid PEG in the 4000 to 700  $\text{cm}^{-1}$  region taken by attenuated total reflection (ATR) (from [306]).

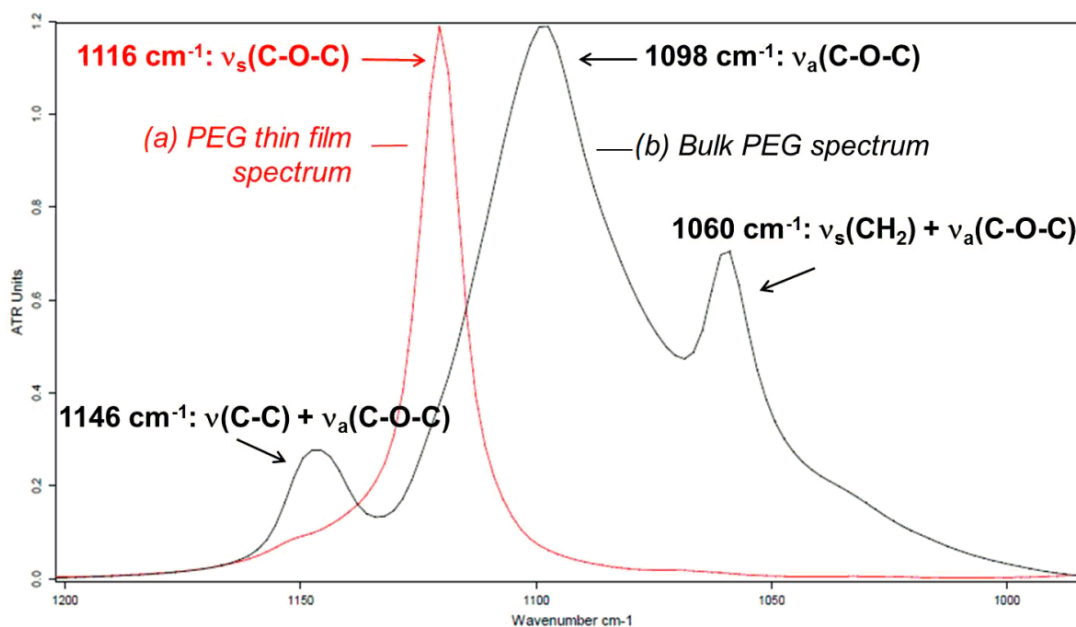


Figure D.2: IR spectrum of PEG (a) adsorbed in a thin layer on a gold substrate (red line), compared to (b) bulk PEG (black line) in the 1200 to 1000  $\text{cm}^{-1}$  region measured by polarisation modulation IR reflection-absorption spectroscopy (PM-IRRAS) and ATR, respectively (from [306]).

Simulation middle cut

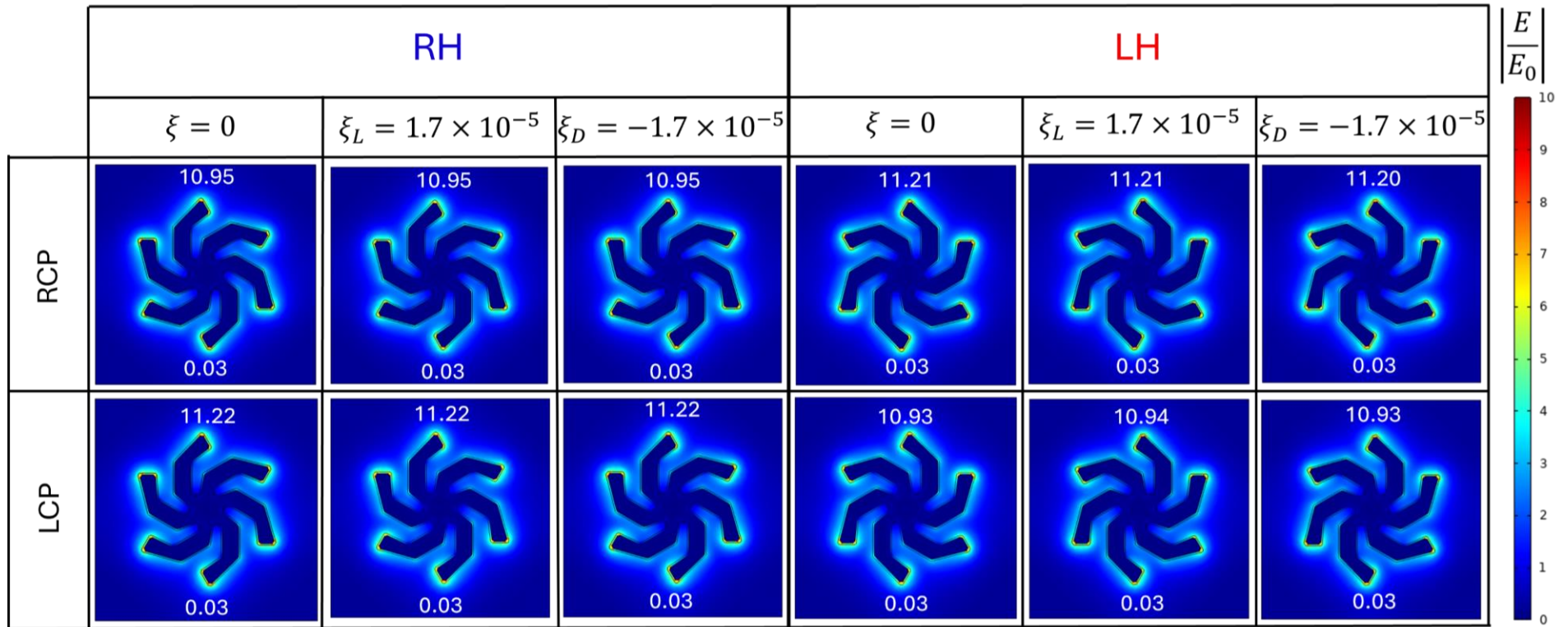


Figure E.1: Simulated maps of the electric field enhancement  $|E/E_0|$  obtained for a circularly polarised incident light (RCP and LCP) at  $1628 \text{ cm}^{-1}$ , at the middle surface of the RH and LH shuriken structure. An achiral dielectric medium ( $\xi = 0$ ) is compared to a small *Pasteur* coefficient of  $\xi_{L(D)} = (-)1.7 \times 10^{-5}$ . The maximum and minimum values obtained in each cut maps are displayed on the top and bottom, respectively.



## Simulation middle cut

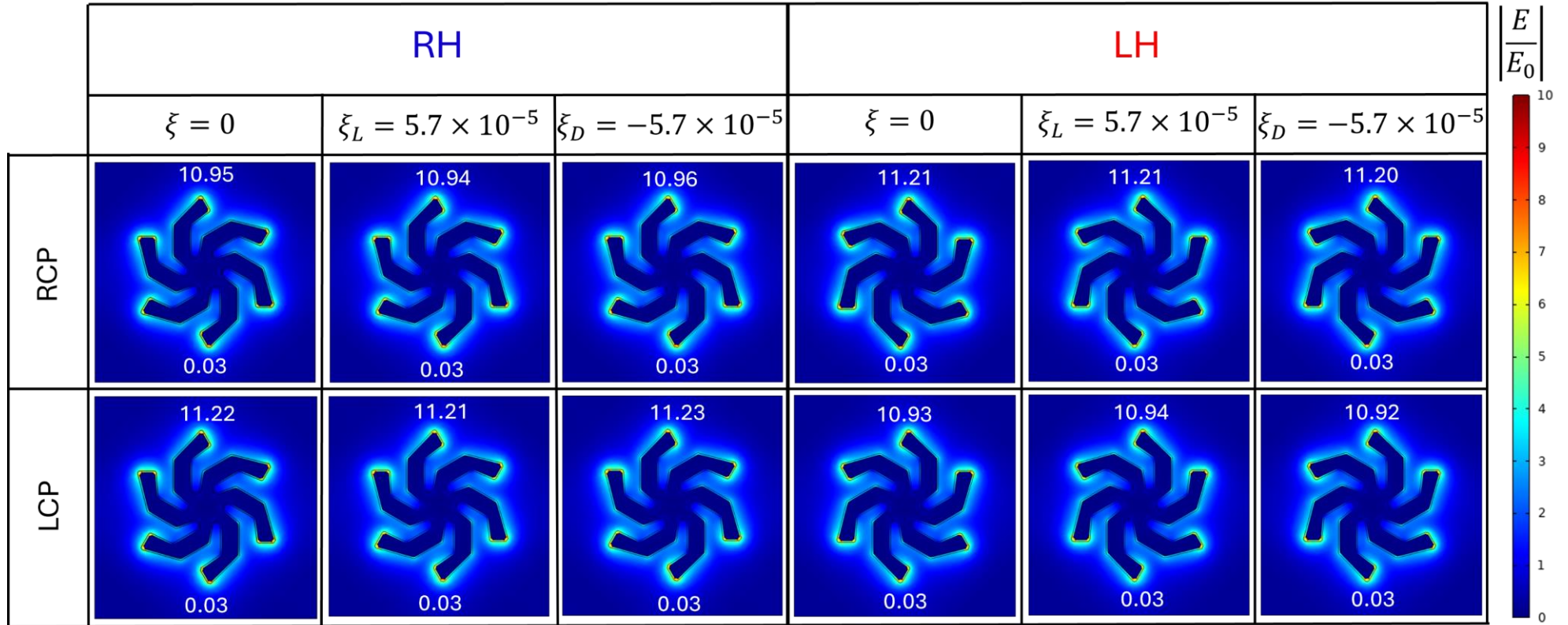


Figure E.2: Simulated maps of the electric field enhancement  $|E/E_0|$  obtained for a circularly polarised incident light (RCP and LCP) at  $1628 \text{ cm}^{-1}$ , at the middle surface of the RH and LH shuriken structure. An achiral dielectric medium ( $\xi = 0$ ) is compared to a higher *Pasteur* coefficient of  $\xi_{L(D)} = (-)5.7 \times 10^{-5}$ . The maximum and minimum values obtained in each cut maps are displayed on the top and bottom, respectively.

## Simulation middle cut

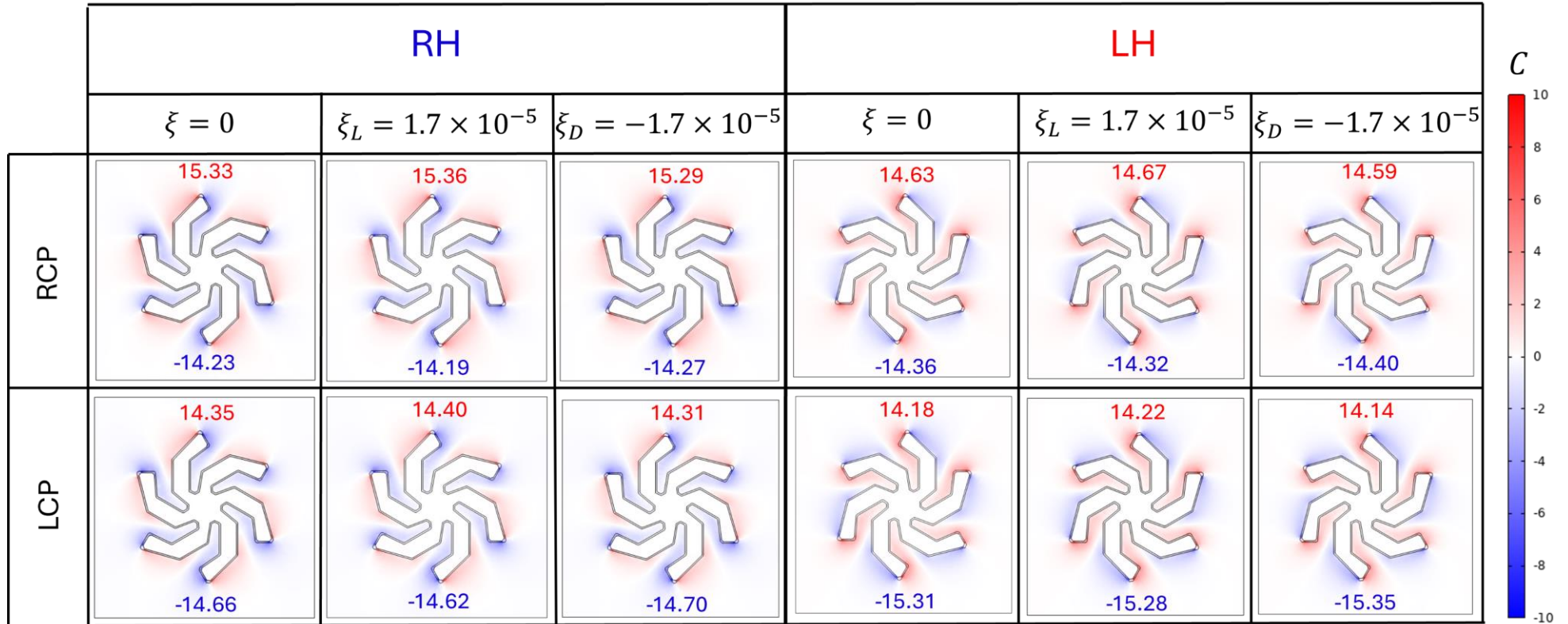


Figure E.3: Simulated maps of the optical chirality  $C$  obtained for a circularly polarised incident light (RCP and LCP) at  $1628 \text{ cm}^{-1}$ , at the middle surface of the RH and LH shuriken structures. An achiral dielectric medium ( $\xi = 0$ ) is compared to a small *Pasteur* coefficient of  $\xi_{L(D)} = (-)1.7 \times 10^{-5}$ . The maximum and minimum values obtained in each cut map are displayed on the top and bottom, respectively.

## Simulation middle cut

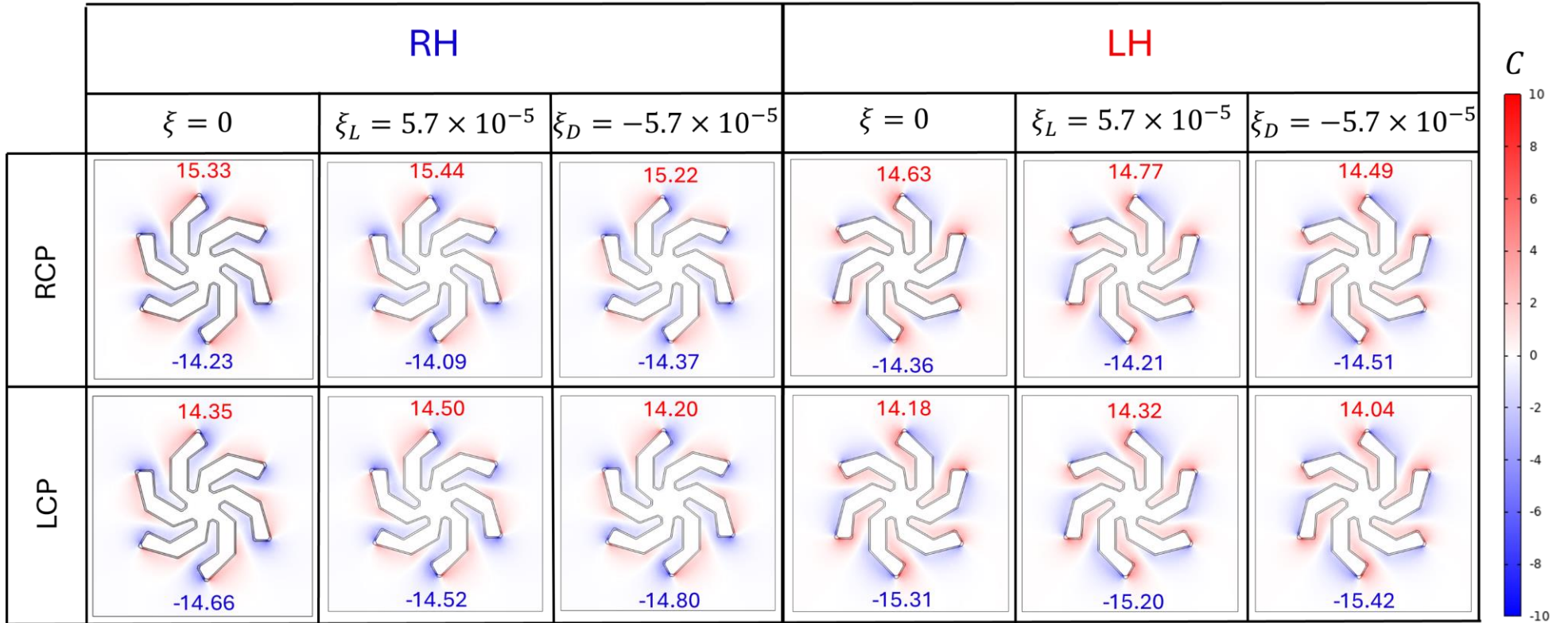


Figure E.4: Simulated maps of the optical chirality  $C$  obtained for a circularly polarised incident light (RCP and LCP) at  $1628 \text{ cm}^{-1}$ , at the middle surface of the RH and LH shuriken structures. An achiral dielectric medium ( $\xi = 0$ ) is compared to a higher *Pasteur* coefficient of  $\xi_{L(D)} = (-)5.7 \times 10^{-5}$ . The maximum and minimum values obtained in each cut map are displayed on the top and bottom, respectively.



## Simulation bottom cut

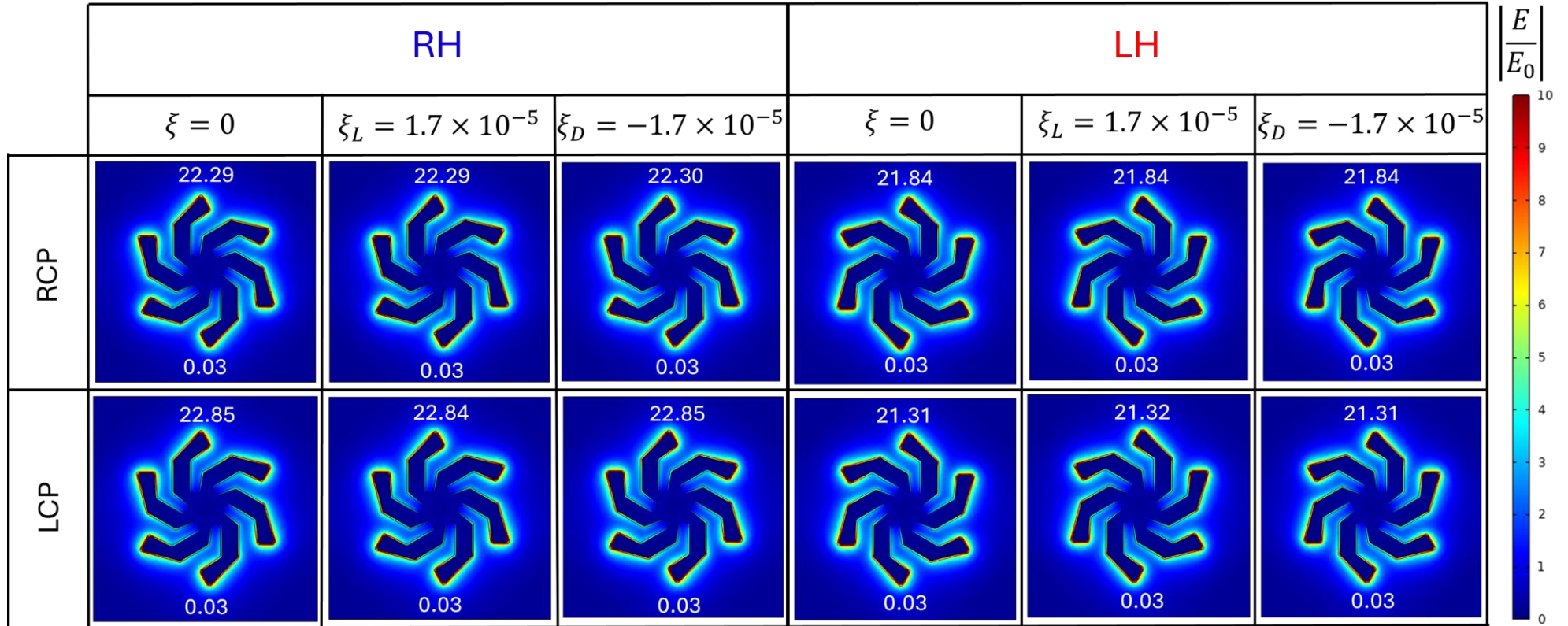


Figure E.5: Simulated maps of the electric field enhancement  $|E/E_0|$  obtained for a circularly polarised incident light (RCP and LCP) at  $1628 \text{ cm}^{-1}$ , at the bottom surface of the RH and LH shuriken structure. An achiral dielectric medium ( $\xi = 0$ ) is compared to a small *Pasteur* coefficient of  $\xi_{L(D)} = (-)1.7 \times 10^{-5}$ . The maximum and minimum values obtained in each cut maps are displayed on the top and bottom, respectively.

## Simulation bottom cut

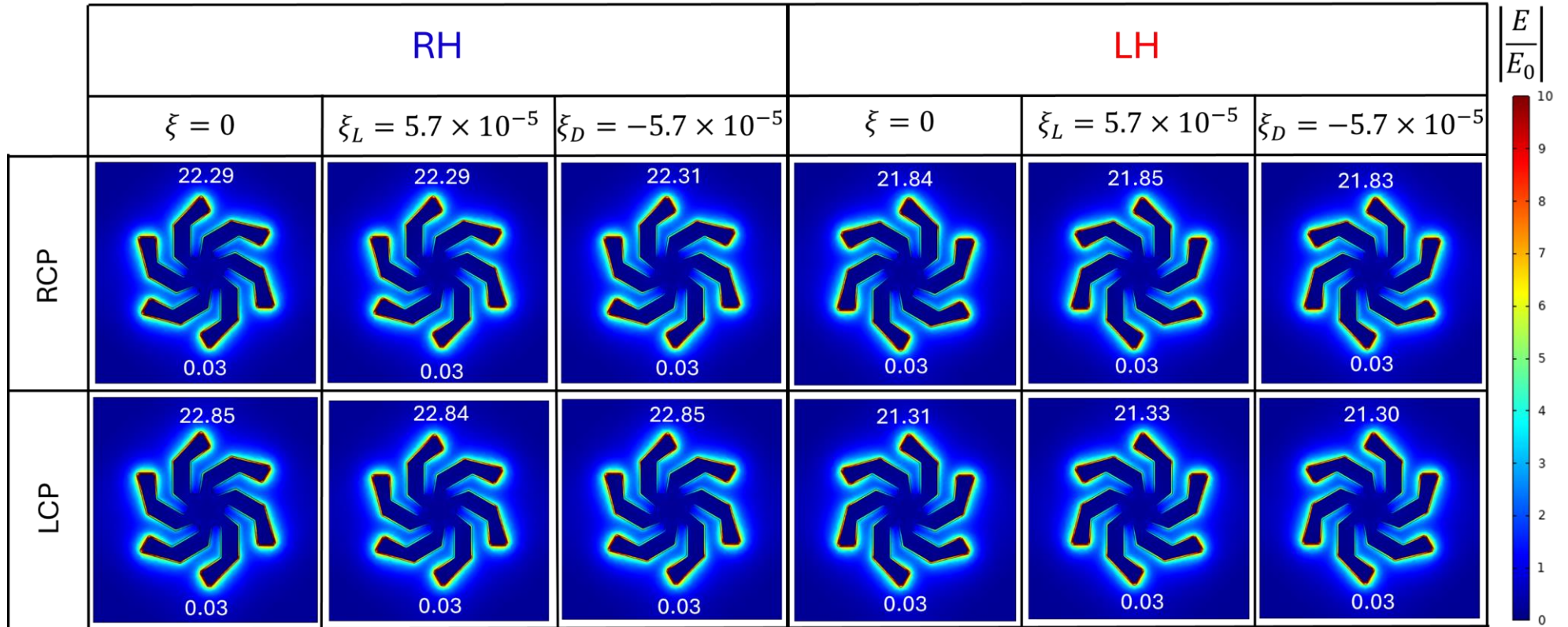


Figure E.6: Simulated maps of the electric field enhancement  $|E/E_0|$  obtained for a circularly polarised incident light (RCP and LCP) at  $1628 \text{ cm}^{-1}$ , at the bottom surface of the RH and LH shuriken structure. An achiral dielectric medium ( $\xi = 0$ ) is compared to a higher *Pasteur* coefficient of  $\xi_{L(D)} = (-)5.7 \times 10^{-5}$ . The maximum and minimum values obtained in each cut maps are displayed on the top and bottom, respectively.

## Simulation bottom cut

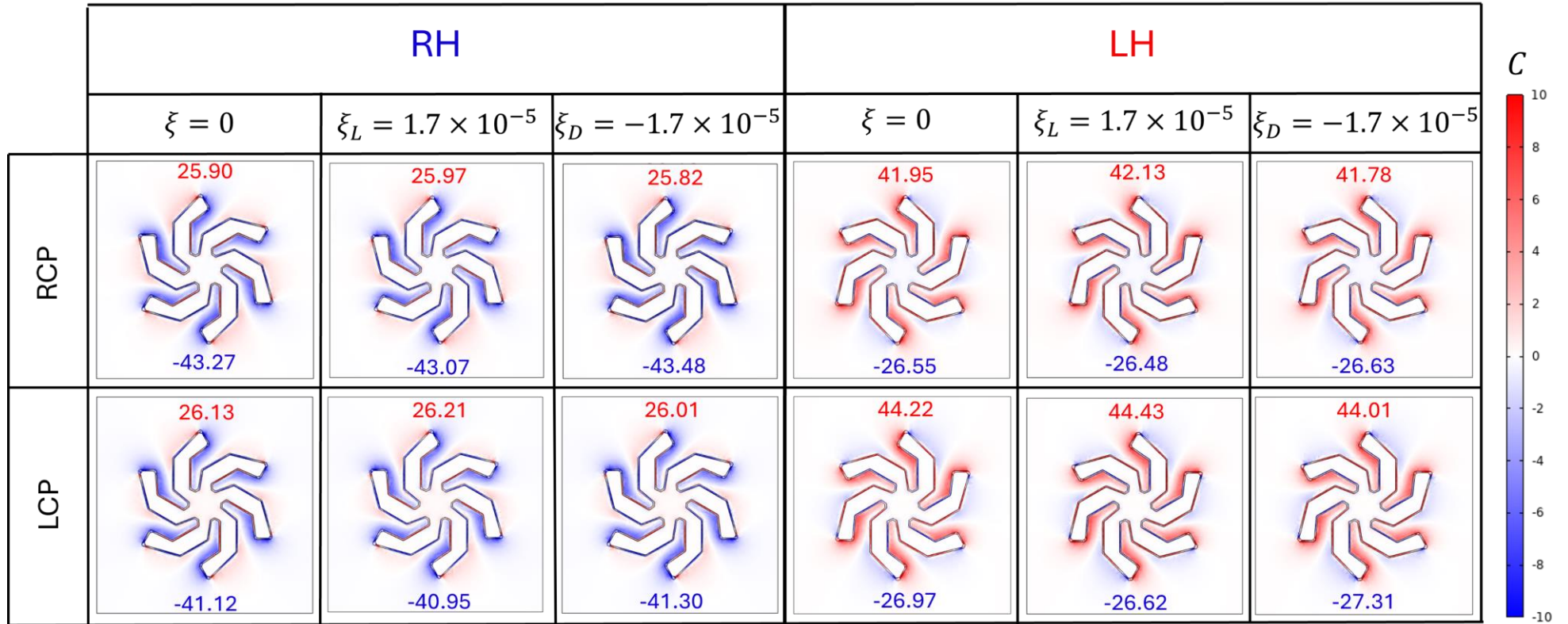


Figure E.7: Simulated maps of the optical chirality  $C$  obtained for a circularly polarised incident light (RCP and LCP) at  $1628 \text{ cm}^{-1}$ , at the bottom surface of the RH and LH shuriken structures. An achiral dielectric medium ( $\xi = 0$ ) is compared to a small *Pasteur* coefficient of  $\xi_{L(D)} = (-)1.7 \times 10^{-5}$ . The maximum and minimum values obtained in each cut map are displayed on the top and bottom, respectively.



## Simulation bottom cut

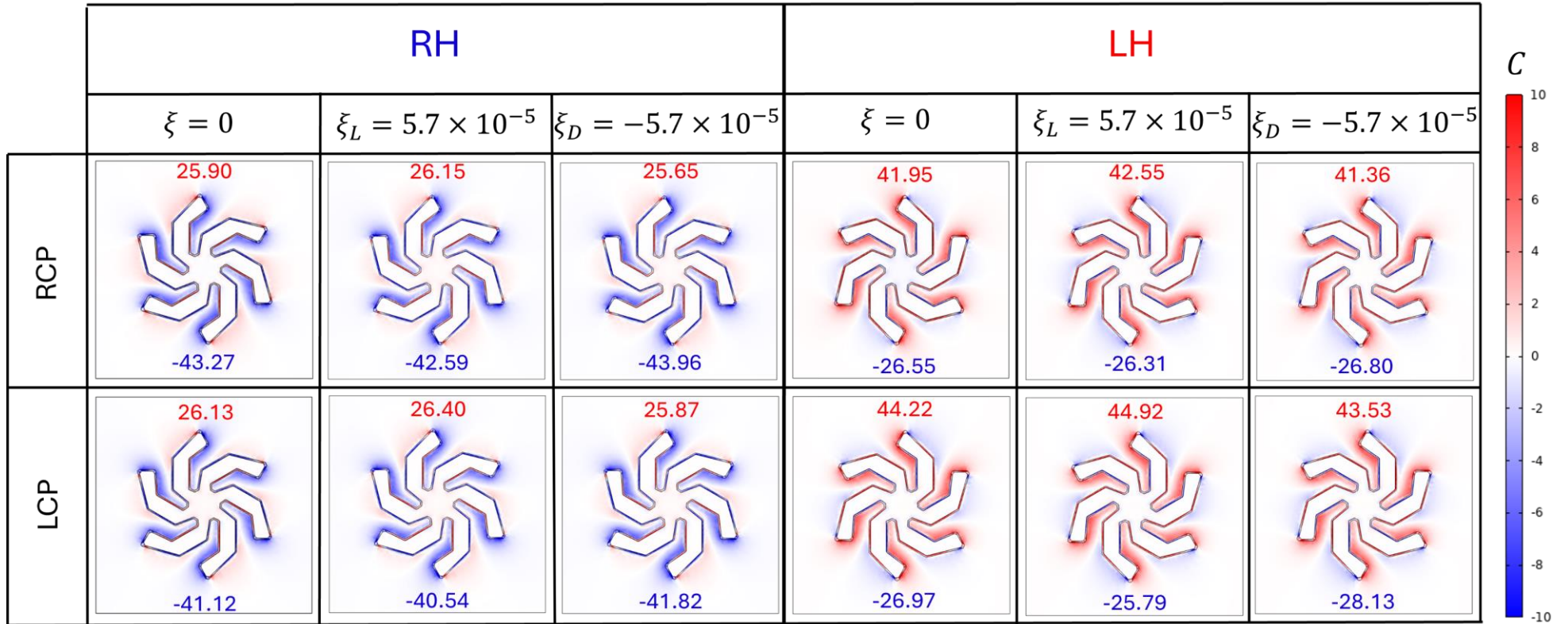


Figure E.8: Simulated maps of the optical chirality  $C$  obtained for a circularly polarised incident light (RCP and LCP) at  $1628 \text{ cm}^{-1}$ , at the bottom surface of the RH and LH shuriken structures. An achiral dielectric medium ( $\xi = 0$ ) is compared to a higher *Pasteur* coefficient of  $\xi_{L(D)} = (-)5.7 \times 10^{-5}$ . The maximum and minimum values obtained in each cut map are displayed on the top and bottom, respectively.